EXPLORING THE RELATIONSHIP BETWEEN SOIL STRUCTURE AND SOIL FUNCTIONS VIA PORE-SCALE IMAGING

A habilitation thesis for the purpose of obtaining the academic degree

Dr. agr. habil

submitted to the

Faculty of Natural Sciences III – Agronomy and Nutrition Science, Geoscience and Computer Science

of the

Martin Luther University Halle-Wittenberg

by

Dr. rer. nat. Steffen Schlüter

Born on March 23rd 1983 in Schlema

Reviewers:

1. Prof. Dr. Hans-Jörg Vogel

2. Prof. Dr. Nicolas Jarvis

3. Prof. Dr. Iain Young

Halle (Saale), 17.12.2019

To Ina and Johannes

Summary

Soil structure is shaped by various biotic and abiotic processes in soil and in turn governs many important soil functions. The advent of non-invasive image techniques has enabled a shift in soil structure assessment from the aggregate perspective towards the pore perspective. The direct characterization of the undisturbed pore structure is beneficial for a better understanding of the functional behavior of soil, as it is the complex pore system at various scales that provides the pathways for matter fluxes, the habitats for soil biota and the space for chemical reactions.

The research presented here aims on the one hand at method improvement to advance the characterization of soil structure and soil structure dynamics through novel imaging processing protocols (four papers) and on the other at unraveling the relationship between soil structure and soil functions with field and laboratory experiments (three papers). Method developments are focused on three-dimensional image processing of X-ray microtomography images and its combination with biochemical microscopy. This includes (i) the optimization of image segmentation for multi-class soil images, (ii) the quantification of three-dimensional soil deformations, (iii) the analysis of soil structure turnover through a new structure labeling approach and (iv) the development of a correlative imaging protocol to merge three-dimensional soil structure data with two-dimensional microscopy data. The experimental studies comprise (i) the investigation of soil structure changes due to different tillage practices in a long-term field trial and its implications on important soil functions like water storage, plant growth and habitat maintenance. The two remaining incubation studies investigate the role of physical constraints to matter cycling, in particular respiration and denitrification in microbial hotspots, through (ii) changes in aggregate size and oxygen concentration or (iii) water saturation and hotspots distribution in space.

The thesis concludes with some general observations that were common to all studies. The range of spatial scales at which soil structure is representatively captured with a specific imaging technique is quite small. The most appropriate scale depends on the soil function of interest, e.g. large for water transport, but small for microbial habitats. Approaches to extend the range of spatial scales through hierarchical sampling and correlative imaging have been introduced and applied in this thesis. The second general observations that resonated through all studies is the non-linearity in the relationship between pore space attributes and the non-linear response of soil functions to change in pore space attributes. The non-linearity is in fact one of the reasons why soil structure is such a suitable indicator for the soil ecological status and the detoriation of soil functions. The thesis ends with an outlook at potential extensions or applications of the methods that have been introduced here, most of which are already ongoing.

Contents

Table of Figures

List of Tables

1. Introduction

1.1. Two Perspectives on Soil Structure[1]

Soil is a precious resource with crucial ecosystem functions such as water and nutrient cycling, food production and maintaining habitat biodiversity. These functions result from complex interactions of physical, chemical and biological processes. Soil structure is a manifestation of these interactions under given environmental conditions and can be interpreted as an integral indicator of the soil ecological status, i.e., the capacity to host organisms, to sustain the production of biomass, and to recover from external perturbation (Kibblewhite et al., 2008; Rabot et al., 2018; Young and Crawford, 2004). Soil structure is defined here as three-dimensional arrangement of solid soil constituents and voids across different scales (Rabot et al., 2018), resulting from interactions of biotic and abiotic factors, including climate, mineral composition, organic matter (OM), roots, fungal hyphae, soil fauna, and tillage. This definition already highlights the dichotomy in soil structure assessment through the aggregate perspective or pore space perspective (Figure 1).

The traditional approach has always been to characterize soil structure through the size, shape, grade and stability of soil aggregates (Ad-hoc-AG Boden, 2005; Jahn et al., 2006). This is standard procedure in soil surveys worldwide and common practice for farmers to evaluate the soil ecological status from quick field observations. The fastest and cheapest soil structure assessment is achieved with drop-shatter tests, for which a spade-full of topsoil is dropped from a certain height, e.g 1m, and a score is derived from the size distribution, and shape of aggregates as well as earthworm and root abundance (Ball et al., 2007; McKenzie, 2001; Shepherd et al., 2008). The scoring results have been shown to correlate with soil compaction and the associated decrease in gas exchange, infiltration and agricultural production (Guimarães et al., 2013; Mueller et al., 2009; Pulido Moncada et al., 2014; Shepherd, 2003). However, scoring methods are rarely used in basic research because the assessment is somewhat subjective and the results depend on texture as well as time-variant soil moisture and biological activity (Guimarães et al., 2011; Mueller et al., 2009; Newell-Price et al., 2013).

Soil structure can be measured more objectively with laboratory methods. The most common method is to measure bulk density and derive porosity from the dry weight of undisturbed soil cores with a given volume. The soil core extraction in the field, might not capture the field variability representatively, is known to induce some disturbance along the wall and can become impossible for high rock content and in the presence of woody roots (Page-Dumroese et al., 1999; Schlüter et al., 2011; Vincent and Chadwick, 1994). Another common approach to characterize soil structure through aggregate size distribution and stability according to various protocols grouped into wet-sieving and dry-sieving (Díaz-Zorita et al., 2002). The results are highly sensitive to specific details of each protocol (energy, duration, repetition) and antecedent soil moisture (Almajmaie et al., 2017; Beare and Bruce, 1993). Despite these drawbacks aggregative sieving and stability tests remain as they can inform about the susceptibility to slaking (wet-sieving) and resistance to mechanical disturbance (dry-sieving) and are relatively easy to perform. Moreover the fragmentation of soil into different aggregate size classes supports the concept of an aggregate hierarchy which assumes that macroaggregates (>250µm) form around particulate organic matter and microaggregates (<250µm) are released upon breakdown of macroaggregates (Angers et al., 1997; Tisdall and Oades, 1982). The macroaggregates are supposed to be relatively short-lived as their binding agents are less persistent than those within microaggregates.

This aggregate perspective on soil structure has frequently been criticized as the associated methods rather aim at measuring the stability of soil structure than soil structure itself and the outcome of these measurements highly depend on the applied energy (Baveye, 2006; Letey, 1991; Pagliai and Vignozzi,

[1] This paragraph is loosely based on the paper: Rabot et al.(2018): Geoderma 314, 122-137.

2002; Young et al., 2001). Moreover, it is the pore space and not the solid space that constitute the spatial domain for water flow, matter fluxes and gas exchange, the habitat for soil biota and the reactor of a multitude of reactions. Therefore, the characterization of pore space attributes in undisturbed soil seems more promising to relate it to soil functions. Methods for pore space characterization can be roughly grouped into indirect methods and direct methods. Indirect methods (e.g. mercury porosimetry, pressure chamber) derive pore attributes like the pore size distribution from functional behavior like water retention curves. Direct observations of pore structure are based on imaging (e.g. thin section microscopy, X-ray tomography). They allow for a qualitative assessment of pore structure according to its formation (packing voids, microcracks, root channels, earthworm burrows) as shown in Figure 1 and for a quantitative assessment through image analysis resulting in properties like pore size distribution, pore connectivity or pore distances. Both direct and indirect methods for pore structure assessment tend to be more time-consuming and labor-sensitive than aggregate structure assessment. Imaging methods, in particular, suffer from limited access and some degree of subjectivity in the image processing protocols (Baveye et al., 2010).

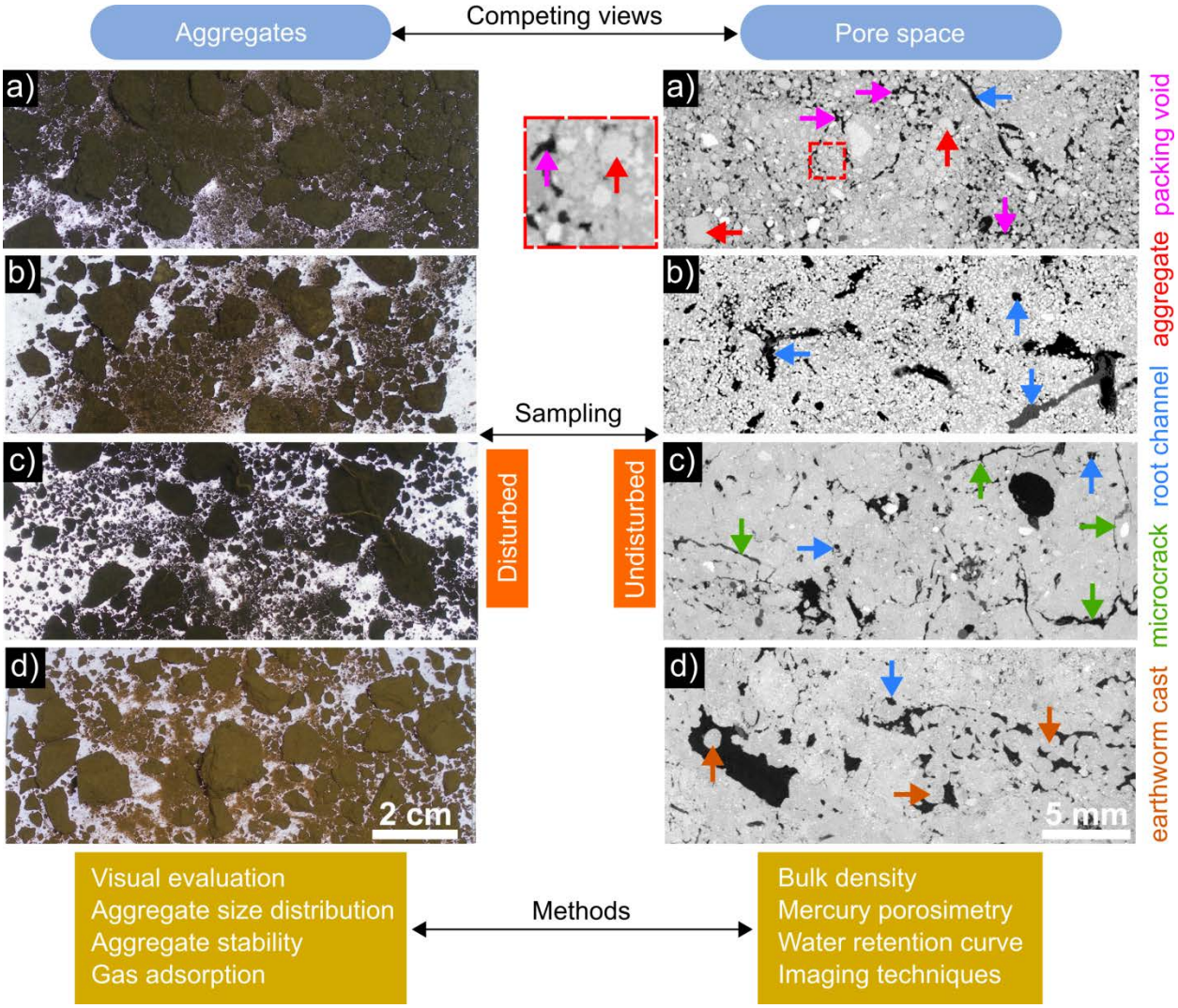

Figure 1: Summary of two competing views: the aggregate perspective and the pore space perspective. (a) Kühnfeld, Halle, Germany (continuous maize, conventional tillage, 63% sand, 25% silt, 12% clay), (b) Hadera, Israel (orchard, 65% sand, 16% silt, 19% clay), (c) Bad Lauchstädt, Germany (grassland, 12% sand, 68% silt, 20% clay), (d) Garzweiler,

Germany (crop rotation, below plow layer, 5% sand, 81% silt, 14% clay); modified from Rabot et al. (2018)

Relevance of soil structure for soil functioning

Soil structure exerts a major control on many important soil functions like storage and filtering of water, carbon and nutrient cycling, as well as habitat for biological activity. A comprehensive review of soil structure effects on these soil functions is beyond the scope of this introduction, but can be found elsewhere (Kravchenko and Guber, 2017; Rabot et al., 2018). Instead we use an illustrative example to demonstrate the role of soil structure for a few fundamental soil processes and their implications for the abovementioned soil functions.

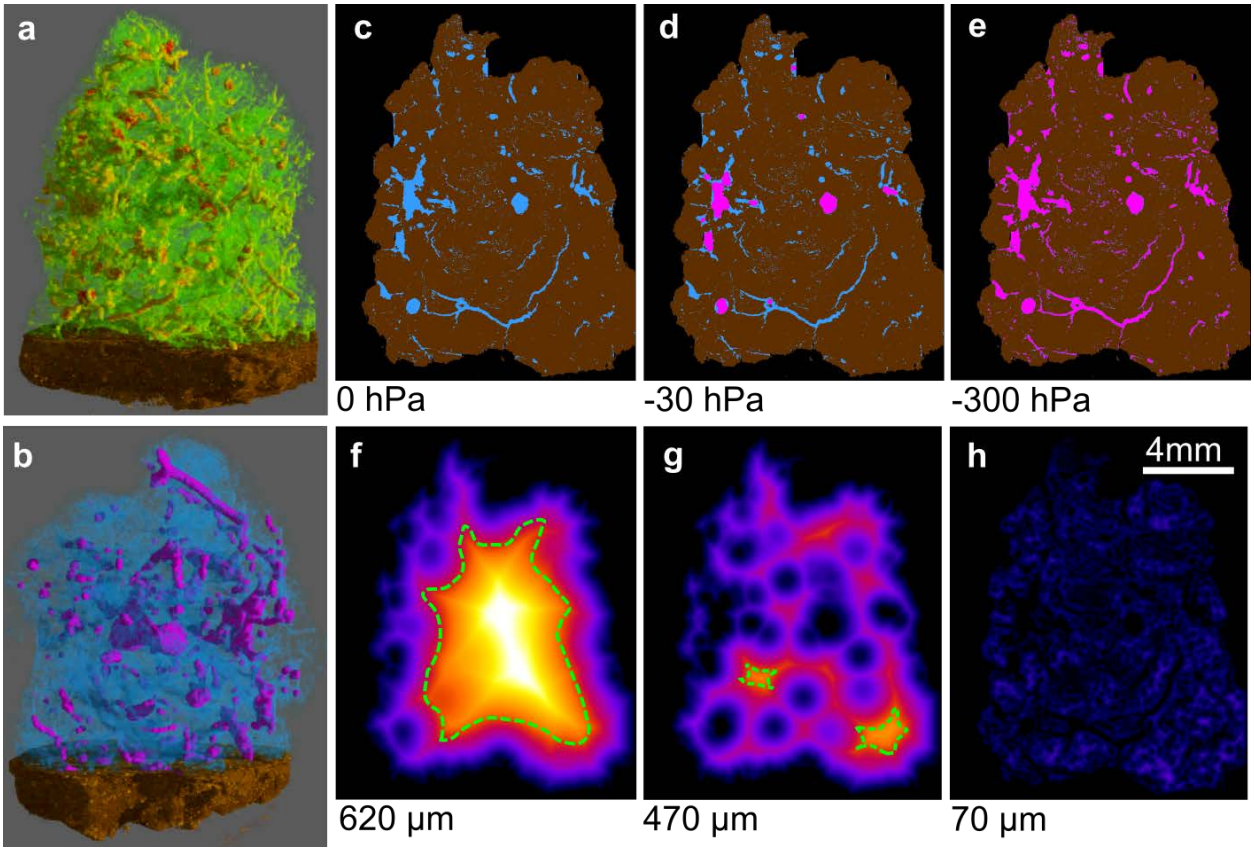

Figure 2: X-ray CT scans of a 1cm thick aggregate from a topsoil in Bad Lauchstädt scanned at a resolution of 8µm: (a) the pore size distribution is depicted from small (green) to large (red) diameters; (b) the 3D distribution of air and water at -30hPa modeled with the maximum inscribed sphere method; (c-d) 2D sections of the modeling results at different matric potentials; (f-h) air distances within the aggregate at the same potentials. The values represent average distances and the green frames delineate hypothetic perimeters of anoxic centers.

Figure 2(a) shows the pore architecture of a 1cm large soil aggregate from Bad Lauchstädt scanned with X-ray CT at a voxel resolution of 8µm. The pore size distribution is obtained with the maximum inscribed sphere method and depicted from small (green) to large (red) diameters. This pore size information can be used to model water retention and the distribution of water and air at a certain matric potential by employing Young-Laplace law and the capillary rise equation that is derived from it:

$$h = \frac{2\,\gamma\,cos(\alpha)}{\varrho_w\,g\,r} \quad (1)$$

where h is the rise above a free water table in a cylindrical capillary with radius r, γ is interfacial tension between water and air, α contact angle, ϱ_w is the density of water and g is gravitational acceleration. In

hydraulic equilibrium this height above the free water table can be directly interpreted as pressure head h_m (or capillary pressure P_c or matric potential ψ_m) in that soil depth. Assuming a capillary bundle model Eq. (1) can be recast to directly infer whether a pore with a certain radius will be water or air-filled at a certain matric potential. This pore morphology based simulation of water retention is done in Figure 2(b) for a matric potential of -30hPa assuming pure water and perfect wettability. Note that the capillary bundle assumption is a severe oversimplification, because in order to drain a pore it is not only important whether its radius is large enough, but also whether there exists a continuous path towards the atmosphere through which air can invade (Hazlett, 1995; Hilpert and Miller, 2001). However, for the following example this difference is not important. Repeating this analysis for decreasing matric potentials resembles a drainage process (Figure 2c-e). The soil moisture characteristic (or water retention curve or moisture release curve or pF curve) could be directly estimated from the water content at each drainage step. Larger packing pores and root channels are drained first, whereas air invades microcracks and smaller intra-aggregate pores at a more negative matric potential. At a matric potential of -300cm ≈ pF 2.5 all macropores (>50µm) and narrow macropores (>10µm) are drained and the soil has reached field capacity (Figure 2e). The unresolved mesopores (>0.2µm) act as a reservoir for root water uptake as they hold the water against gravity by capillary forces. The visible macropores, in turn, are essential for soil aeration at field capacity or for preferential flow and solute transport when the soil is fully saturated (Rabot et al., 2018). Note that a large part of the unresolved mesopores are textural pores between primary particles, whereas all visible pores are structural pores.

In summary, water retention and soil aeration patterns are a direct imprint of the underlying pore architecture. But this also has important ramifications into matter cycles as they govern diffusion pathways, microhabitats and reaction patterns. This is demonstrated with contact distances to the closest air-filled pore at different matric potentials (Figure 2f-h). At full saturation, air is only present outside the aggregate so that on average dissolved oxygen has to diffuse 620µm from the aggregate boundary to reach any location within the soil matrix. For sake of simplicity this contact distance is estimated by direct Euclidean distances, whereas pores are tortuos and real diffusion trajectories along a concentration gradient are not straight but chaotic due to Brownian motion. When the aggregate is drained this average air distance decreases substantially. At field capacity it already decreased by one order of magnitude (70µm), which entails a much better supply with dissolved oxygen in the water-filled soil matrix. This dissolved oxygen will be consumed through aerobic respiration in the soil matrix. If this oxygen consumption exceeds the oxygen supply through diffusion along the oxygen gradient, then anoxic zones may form in the aggregate center (Figure 2f-g). Their extent depends on local respiration rates and contact distances.

The implications of these micro-environmental conditions for carbon and nitrogen turnover are manifold. Carbon mineralization rate through anaerobic respiration are about one order of magnitude smaller than through aerobic respiration (Keiluweit et al., 2017). This leads to the well-known saturation dependence of bulk soil respiration with an optimal respiration rate at intermediate soil moisture and a decline towards full saturation and complete dryness(Moyano et al., 2013; Skopp et al., 1990). Under very dry conditions a substrate diffusion limit arises, because the continuity in the water phase is lost and microbes become separated from resources and may fall into metabolic arrest (Manzoni and Katul, 2014; Tecon and Or, 2017). Under very wet conditions an oxygen diffusion limit may arise, when oxygen consumption exceeds the diffusive flux towards the location of oxygen consumption, so that anaerobic respiration with alternative electron acceptors sets in (Linn and Doran, 1984b). The susceptibility of organic matter to mineralization therefore does not only depend on the chemical structure of the organic compounds, which defines the electron donator-dependent energy gain, but also on the moisture regime and resulting redox conditions which controls the electron acceptor-dependent energy gain of the reaction (Keiluweit et al., 2016). Soil structure does not only have an indirect effect carbon turnover through the regulation of water retention and soil aeration, but also exerts a direct control on carbon stabilization in soil through physical protection against mineralization, when organic compounds are located in pores that are not accessible to

microorganisms. In fact, this physical protection seems to be the main mechanism for long-term carbon storage next to protection in organo-mineral associations, whereas the important of chemical recalcitrance might have been overstated in the past (Lehmann and Kleber, 2015; Schmidt et al., 2011). This physical protection might occur in pores that are smaller than a microorganism itself, or when they are separated by discontinuous water films, though this limitation is more relevant for bacteria than for fungi as they can overcome these barriers via hyphae (Ritz and Young, 2004). There are indications that this physical carbon protection is most relevant in fine-textured, structured soils, but less relevant in sandy soils (Christensen, 2001). There is an important feedback loop because soil structure does not only affect carbon turnover. Organic carbon is also a key driver in the formation of soil structure by acting directly as binding agent for mineral particles and indirectly by stimulating soil biota that modify soil structure (Rillig and Mummey, 2006; Six et al., 2004; Tisdall and Oades, 1982).

Soil structure is not only important for carbon turnover, but also for nutrient cycling, in particular nitrogen. Reactive nitrogen exists in many soluble and gaseous forms in soil. Transformations between them are regulated by environmental conditions (pH, temperature, moisture) and different transformations may occur simultaneously in different niches and microsites in structured soil. This is again demonstrated with the aggregate example in Figure 2. Denitrification, i.e. the reduction of nitrate through anaerobic respiration, will occur in anoxic aggregate centers. Nitrification, i.e. the biological oxidation of ammonium to nitrite and nitrate, in turn, is an aerobic process as it requires oxygen and will therefore occur in direct vicinity to air-filled pores. The relative importance of both processes depends in soil moisture. Nitrification rates increase with soil moisture in line with overall microbial activity until it drops when aeration becomes a limiting factor. Denitrification emerges at saturations around 60-70% and peaks around 90% (Linn and Doran, 1984a). It does not only depend on the moisture-dependent diffusion distances in soil, but also on the distribution of organic carbon in soil. In a seminal study Parkin (1987) demonstrated that 25-85% of denitrification activity was associated with particulate organic matter that comprised less than 1% of the soil volume. The concentration of microbial activity in microbial hotspots is therefore not only immanent to carbon cycling but also to nitrogen cycling (Kuzyakov and Blagodatskaya, 2015) and their distribution in space is controlled by soil structure.

1.3. Brief thesis outline

This cumulative thesis summarizes the findings from seven peer-reviewed papers (one still in revision) published between 2014 and 2019. The common scope of all papers is the quantification of soil structure and soil structure dynamics and its impact on the functional behavior of soils. The papers are structured according to their main focus, which is either method development to advance soil structure characterization (chapter 2 Methods) or experimental studies on the role of soil structure for various soil functions (chapter 3 Results and Discussion). Both chapters are briefly outlined in the following.

1.3.1. Method development

All four papers in this chapter describe methods to analyze soil structure and its dynamics via imaging and image processing. The main imaging method used in all papers is X-ray computed microtomography (X-ray CT or µCT). The principles of X-ray CT are not explained in detail here, but have been reviewed elsewhere (Wildenschild and Sheppard, 2013). In brief, the physical principle of X-ray imaging is the attenuation of X-rays as the function of electron density according to Beer-Lambert's law, which is a function of local bulk density and the blend of atomic numbers based on the local element composition. The X-ray attenuation along the path through a 3D object is projected onto a 2D radiogram. The internal structure of the 3D object is then recovered by reconstruction of a 3D tomogram based on a multitude of radiograms acquired at different rotation angles of the 3D objects via mathematic reconstruction algorithms. X-ray CT has developed into a standard method for analyzing porous media like soils and rocks in three dimensions (Cnudde and Boone, 2013; Wildenschild and Sheppard, 2013). The raw data rarely serves as a basis for retrieving quantitative information of soil structure, but has to undergo several

image processing steps before it can be analyzed towards different ends. The main image processing methods applied in this thesis are summarized in a workflow in Figure 3. The content of each paper is briefly described in the following.

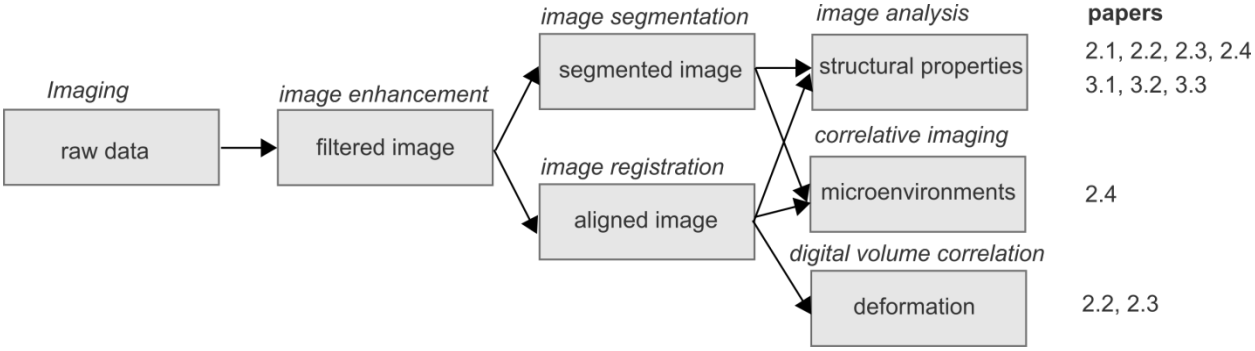

Figure 3: Image processing workflow applied in all papers. The workflow contains methods (cursive) and their outcomes (gray boxes). The papers are listed according to the methods used using their chapter numbers.

The first paper (chapter 2.1) is a comprehensive review of image processing methods for X-ray CT images with an emphasis on multi-phase images. Special segmentation algorithms are required, if the sample contains more than two material classes, i.e. not only pores and soil matrix, but in addition particulate organic matter or water and air within pores. The review paper surveys combinations of image enhancement and image segmentation methods and evaluates their suitability for multi-phase segmentation by visual assessment and by comparing structural properties derived from the segmented images. The image processing protocols developed in that paper are used in all subsequent papers.

The second paper (chapter 2.2) introduces a protocol for digital volume correlation to study internal soil deformation during centrifugation. Centrifugation is a method for measuring soil water retention curves. However, the bias induced by structural damage at high pressures is typically ignored. By looking at deformation patterns and changes in pore structure properties we show that soil structure is modified by the interplay between desiccation and compaction. Considerable damage is only induced when a critical pressure is reached. Digital volume correlation is also applied in another paper (chapter 2.3) to determine the internal deformation during compaction.

The third paper (chapter 2.3) introduces a new conceptual approach for estimating soil structure turnover and explains the required experimental setup as well as image processing protocol. The basic idea is to label soil structure by coating aggregate surfaces with small particles and to measure how fast the position of particles is randomized with respect to pore distances. That is, these distances are minimal initially as there are located directly at the aggregate surfaces. However, as old pores are destroyed and new pores are formed through biotic or abiotic agents the particle-pore distance may gradually evolve towards a dynamic equilibrium. The methodology is tested for compaction, as a typical example of an abiotic structure changing process. Implications for biotic structure modification and the coupling of organic matter turnover and soil structure turnover are discussed.

The fourth paper (chapter 2.4) demonstrates correlative imaging as a tool for studying microenvironments in soil. Image registration is introduces as a method to combine 3D structural information of an intact soil core obtained with X-ray CT with 2D biochemical information measured on exposed surfaces with various microscopy methods (light microscopy, fluorescence microscopy, electron microscopy, secondary ion microscopy). The spatial distribution of bacteria is registered to the 3D soil structure to demonstrate that bacteria are mostly located in mesopores and have a tendency to forage near macropore surfaces and near particulate organic matter. The spatial distribution of minerals and organic matter within the 3D pore space is also discussed.

1.3.2. Experimental studies on soil structure and soil functions

The relationship between soil structure and soil functions like water storage or maintenance of microbial diversity is already analyzed on a few occasions in the papers on method development in chapter 2. The remaining three papers in chapter 3 are based on these image-processing methods and combine them with other laboratory methods to investigate the role of soil structure for other important soil functions.

The fifth paper (chapter 3.1) analyzes a long-term tillage trial with respect to soil structure changes in two soil depths induced by 25 years of different management (conventional tillage vs. reduced tillage). The functional behavior of these differently tilled soils is investigated in terms of aeration (air capacity), water filtration (hydraulic conductivity), habitat for soil biota (earthworm abundance) and plant growth (grain yield). It is shown that 25 years of reduced tillage has led to a compaction of the topsoil underneath the cultivator but did not loosen the old plow pan, despite the higher earthworm abundance. Grain yields are not affected, since the observed compaction has not reached a critical threshold that would affect plant growth.

The sixth paper (chapter 3.2) investigates the role of aggregate size and oxygen concentration at the aggregate boundary for microbial growth and denitrification in anoxic centers of fully saturated porous glass beads that serve as analogues for soil aggregate. This is the only paper in this thesis that does not involve X-ray CT, except for visualization, as the structural properties of the artificial aggregates are known a priori. With gas chromatography it is shown that bacteria grow faster in small aggregates through better oxygen supply due to a favorable surface-to-volume ratio, thus inducing denitrification earlier. However, the total N-gas production through denitrification is higher in large aggregates due to a higher anaerobic soil volume fraction evolving in the course of incubation. The protocol for preparing artificial aggregates as well as the experimental setup for gas kinetics measurement is adopted in the subsequent paper.

The seventh and final paper (chapter 3.3) explores physical limitations to microbial respiration and denitrification imposed by oxygen diffusion and substrate diffusion. The porous glass beads serve as artificial microbial hotspots that are placed in different spatial configurations into a sterile sand matrix with different water saturations. Microbial growth in these hotspots depends on the distribution of hotspots as it governs the local competition for oxygen. These different growth rates also cause different N gas kinetics especially at low and intermediate saturation. At high water saturation the supply of hotspots with oxygen is impaired irrespective of hotspot distribution. The total magnitude of denitrification mainly depends on water saturation. 3D image analysis indicates that the steep increase in denitrification is not caused by a loss in connectivity of air-filled pores but rather by an increase in diffusion length towards and within air-filled pores.

2. Methods

2.1. Image processing of multiphase images obtained via X-ray microtomography: A review (Schlüter et al. 2014, Water Resources Research, 50(4), 3615-3639, doi: 10.1002/2014WR015256)

Abstract

Easier access to x-ray microtomography (µCT) facilities has provided much new insight from high-resolution imaging for various problems in porous media research. Pore space analysis with respect to functional properties usually requires segmentation of the intensity data into different classes. Image segmentation is a non-trivial problem that may have a profound impact on all subsequent image analyses. This review deals with two issues that are neglected in most of the recent studies on image segmentation: (i) focus on multi-class segmentation and (ii) detailed descriptions as to why a specific method may fail together with strategies for preventing the failure by applying suitable image enhancement prior to segmentation. In this way, the presented algorithms become very robust and are less prone to operator bias. Three different test images are examined: a synthetic image with ground-truth information, a synchrotron image of precision beads with three different fluids residing in the pore space, and a µCT image of a soil sample containing macropores, rocks, organic matter, and the soil matrix. Image blur is identified as the major cause for poor segmentation results. Other impairments of the raw data like noise, ring artifacts, and intensity variation can be removed with current image enhancement methods. Bayesian Markov random field segmentation, watershed segmentation, and converging active contours are well suited for multi-class segmentation, yet with different success to correct for partial volume effects and conserve small image features simultaneously.

Introduction

The last decade has seen a tremendous progress in x-ray tomography and imaging techniques providing new means to analyze a multitude of research problems in porous media research. In the scope of water resources research, applications range from soil-water-root interactions, mechanical and hydraulic properties of rocks, to pore-scale modelling of multi-phase flow and continue to appear in related fields of research (Anderson and Hopmans, 2013; Blunt et al., 2013; Wildenschild and Sheppard, 2013). Progress in image progressing has kept a comparable pace in terms of new developments in image enhancement, image analysis, and hardware architectures (Kaestner et al., 2008; Ketcham and Carlson, 2001; Porter and Wildenschild, 2010; Sheppard et al., 2004; Tuller et al., 2013). Since x-ray tomography is becoming a standard technique available to an increasing number of research groups in water resources research, more and more scientists have a need for information on how to process their data. Not everyone new to the field has the resources to develop their own image processing toolbox, tailored for the research question at hand, nor the budget to take advantage of powerful image processing software that often has a rather comprehensive scope. A relief in this regard are software toolboxes which are freely available to the scientific community like *ImageJ* (Ferreira and Rasband, 2012), *ITK* (Ibanez et al., 2005), *QuantIm* (Vogel et al., 2010), Blob3d (Ketcham, 2005), *OpenCV*[2] or *scikit-image*[3], just to name a few. Their multi-phase segmentation capabilities are somewhat limited and may require substantial operator input. The software used in this study is described in the appendix.

However, comparing the performance of different image processing methods on the same set of test images often leads to very different results. A notorious example is image segmentation of a gray value image into objects and background (Baveye et al., 2010; Iassonov et al., 2009; Sezgin and Sankur, 2004).

[2] http://opencv.org/
[3] http://scikit-image.org/

Yet, these comparative studies often merely list the performance of several segmentation methods with respect to a certain quality measure or highlight the user-dependency of the segmentation result, but lack in useful information as to why a specific method fails under certain circumstances and how this may be avoided by suitable preprocessing. Another shortcoming is that many recent review papers on image segmentation with a focus on soil images deal with binary segmentation only (Baveye et al., 2010; Houston et al., 2013b; Wang et al., 2011) and do not provide solutions to multi-class segmentation problems.

This review paper has two main objectives. First, we survey various segmentation methods with respect to multi-class segmentation. We focus on methods that operate on a single image, i.e. coupled images scanned at different x-ray energy levels (Armstrong et al., 2012; Costanza-Robinson et al., 2008; Rogasik et al., 1999) or in a wet and dry state (Culligan et al., 2004; Wildenschild et al., 2005) are not discussed here. We refer the reader to Brown et al. (2014) where we demonstrate that a single-energy method outperforms a three-energy method and discuss the potential shortcomings of either approach. All of the surveyed methods are locally-adaptive, i.e. in addition to global histogram information they consider some neighborhood statistic for class assignment. In particular, we will examine hysteresis segmentation (Vogel and Kretzschmar, 1996), indicator kriging (Oh and Lindquist, 1999), converging active contours (Sheppard et al., 2004), watershed segmentation (Vincent and Soille, 1991) and Bayesian Markov random field segmentation (Kulkarni et al., 2012). As quality measures we will use misclassification error, volume fraction, specific interfacial area, and a connectivity measure. Second, we point out that the performance of image segmentation cannot be examined independently of image enhancement prior to classification. To do so, we compare the impact of different denoising methods on the segmentation results. We have chosen standard noise removal methods that were reviewed for application in µCT data of porous media before (Kaestner et al., 2008; Tuller et al., 2013). Moreover, we apply efficient algorithms for image artifact removal, such as intensity bias (Iassonov and Tuller, 2010) and ring artifacts (Sijbers and Postnov, 2004). Finally, we illustrate the impairment of proper threshold detection that is due to low contrast and imbalanced histograms, and present methods to correct it.

The performance of different segmentation methods is evaluated by means of three test images. We start with a synthetic test image of a partially saturated packing of spheres, where the volume fractions and interfacial areas of the wetting, non-wetting and solid phase are known exactly. The true image is superimposed with ring artifacts, blur, and noise, and the success of different combinations of denoising and segmentation in recovering the morphological properties of the true image is compared. Subsequently, the most suitable combinations are applied to two real images of quite different scopes. The first is a synchrotron image of a three-fluid medium impaired by intensity variation and noise (Brown et al., 2014), the second is a µCT image of a soil with macropores, organic matter and rocks impaired by noise and blur (Houston et al., 2013a).

The paper is organized as follows: In Section *Material & Methods* we provide the details for each image processing method, while image enhancement and segmentation results are compared in terms of visual appearance and morphology measures in Section *Results*. In Section *Discussion* we discuss the results and provide recommendations for best practices, and our findings are summarized in Section *Conclusions*.

Methods

Artifact Removal

Due to shortcomings in the image acquisition process, the base signal of an x-ray scan is often superimposed by different kinds of image artifacts (Ketcham and Carlson, 2001; Wildenschild et al., 2002). The most frequent impairments are image noise due to a low count of incoming radiation at the detector, and image blur due to movement, hardware constraints, or suboptimal image reconstruction. As

discussed below, there are powerful denoising methods that efficiently remove noise in homogeneous locations and at the same time conserve edges between objects. Other image artifacts which are less trivial to remove *a posteriori* are ring artifacts, due to defective diodes in the detector panel, or beam hardening of polychromatic beams, which manifests itself in the reconstructed image as streakings around high attenuation objects and intensity variation with distance to the sample center. Note that there are means to avoid some of these artifacts already during image acquisition or image reconstruction like a slightly altering detector panel position during scanning and wedge calibration (Ketcham and Carlson, 2001). Here we focus on methods that can be directly applied to the reconstructed volume.

Ring artifacts can be removed separately for each image slice z after transforming the image from Cartesian coordinates $\mathbf{x} = (x, y)$ into polar coordinates $\mathbf{x} = (r, \varphi)$, where $\mathbf{x}$ is the location vector, (x, y) is the horizontal and vertical coordinate and (r, φ) are radius and angle. In this way, the rings appear as vertical lines that can be removed with a moving window W of width $w \ll R$, where R is the radius of the sample. The window detects average variations in gray value median $\tilde{I}(r)$ along r and normalizes them subsequently (Sijbers and Postnov, 2004). Only homogeneous rows within W contribute to the median $\tilde{I}(r)$ at column r, where the homogeneity threshold H has to be set by the user. This method has some shortcomings since objects aligned to a certain radius may also be removed.

To our knowledge, the removal of streaking artifacts due to beam hardening is an unresolved problem. Intensity bias, on the other hand, can be removed rather easily given that it is not superimposed by changing attenuation coefficients due to variable fluid saturation or matrix porosity. To do so, requires an iterative procedure (Iassonov and Tuller, 2010): (i) the image is segmented into the class with the highest attenuation and background by simple, histogram-based thresholding. (ii) The mean gray value within the highest-density class is stored as a function of radius. (iii) A smooth function is fitted to the data:

$$I(r) = a + b\cos(2\pi r/R) + c\exp(r/R) \quad (2)$$

where a, b and c are fitting parameters. (iv) The smooth function is used to normalize the data. Steps (i-iv) are repeated until convergence is achieved after 2-4 iterations.

Denoising

Median Filter

A good noise removal algorithm should exert significant smoothing in homogeneous regions (i.e. zones with low intensity gradient $\nabla I(\mathbf{x})$ and minimal modification of edges (i.e. high $\nabla I(\mathbf{x})$ zones), where ∇ is the differential operator with respect to three dimensions ($\nabla = \frac{\partial}{\partial x} + \frac{\partial}{\partial y} + \frac{\partial}{\partial z}$). The simplest method for non-linear denoising is a median filter (MD) with a cubic kernel of diameter d:

$$\hat{I}_{\mathrm{MD}}(\mathbf{x}) = I'(\mathbf{x}) * M_d(\mathbf{x}) \quad (3)$$

where $*$ denotes convolution, I' is the raw image and $\hat{I}$ is the denoised result. The gray value that divides the set of d^3 sorted gray values within M_d into equal halves is assigned to the current voxel at location $\mathbf{x}$ (Gonzalez and Woods, 2002). Note that this routine is usually applied in one loop and is rather slow for large kernel sizes, mainly due to sorting. However, a tremendous increase in speed is achieved by applying lookup tables and a moving median, i.e. for a kernel shift of one position only a small amount of d^2 gray values has to be replaced in a table (Huang et al., 1979).

Anisotropic Diffusion Filter

Another popular, nonlinear denoising method is the anisotropic diffusion (AD) filter (Catté et al., 1992; Perona and Malik, 1990). The rationale of this method is that the Gaussian distribution is the solution to the diffusion equation with a constant diffusion coefficient D. In the same way, applying the diffusion equation with a non-linear diffusion coefficient amounts to smoothing with a Gaussian kernel of strongly varying standard deviation. Obviously, D should depend on the local intensity gradient $\nabla I(\mathbf{x})$. Hence, anisotropic diffusion calls for a numerical solution of the following partial differential equation (PDE):

$$\begin{aligned} \hat{I}^0 &= I' \\ \frac{\partial \hat{I}_{\mathrm{AD}}}{\partial t} &= \nabla[D(|\nabla(G_\sigma * \hat{I}_{\mathrm{AD}})|)\nabla \hat{I}_{\mathrm{AD}}] \end{aligned} \qquad (4)$$

where t is numerical time, $\hat{I}_{\mathrm{AD}}$ is short for $\hat{I}_{\mathrm{AD}}(\mathbf{x}, t)$ and the gradient of smoothed intensity values, convolved by a Gaussian G_σ of standard deviation σ, serve as an edge detector. The simplest implementation is:

$$D(|\nabla(G_\sigma * \hat{I})|) = \begin{cases} 1, |\nabla(G_\sigma * \hat{I})| \leq \kappa \\ 0, |\nabla(G_\sigma * \hat{I})| > \kappa \end{cases} \qquad (5)$$

where κ is a diffusion stop criterion. The number of iterations is another important parameter that has to be set manually, because the solution would eventually converge to uniform intensity.

Total Variation Filter

Another PDE-based approach is total variation (TV) denoising (Rudin et al., 1992). The rationale behind this method is to minimize the intensity variation in the image by means of the following cost function:

$$\hat{I}_{\mathrm{TV}} = \underset{\hat{I}}{\operatorname{argmin}} \left\{ \underbrace{\int |\nabla \hat{I}(\mathbf{x})| d\mathbf{x}}_{\text{regularization}} + \lambda \underbrace{\int |I'(\mathbf{x}) - \hat{I}(\mathbf{x})|^2 d\mathbf{x}}_{\text{fidelity}} \right\} \qquad (6)$$

where λ is a scale parameter that controls the trade-off between regularization, i.e. smoothing, and fidelity to the raw data I'. The solution is achieved with the following set of coupled PDE's:

$$\begin{aligned} \hat{I}^0 &= I' \\ \frac{\partial \hat{I}_{\mathrm{TV}}}{\partial t} &= \nabla\left(\frac{\nabla \hat{I}_{\mathrm{TV}}}{|\nabla \hat{I}_{\mathrm{TV}}|}\right) + \lambda(I' - \hat{I}_{\mathrm{TV}} + K) \\ \frac{\partial K}{\partial t} &= \alpha(I' - \hat{I}_{\mathrm{TV}}) \end{aligned} \qquad (7)$$

where $\hat{I}_{\mathrm{TV}}$ is short for $\hat{I}_{\mathrm{TV}}(\mathbf{x}, t)$. The time step control α can be made adaptive to $\partial K/\partial t$. The number of iterations, used as a stopping criterion, is less crucial as compared to $\hat{I}_{\mathrm{AD}}$, because the solution does not converge to uniform intensity due to the fidelity term.

Non-Local Means Filter

Unlike the previous methods, the non-local means filter (NL) is a linear filter, i.e. the gray value at the current location is the average of gray values at other locations, assigned with some suitable weighting factors w. However, in contrast to standard linear filters (Gaussian filter, mean filter, etc.) it does not use a small-sized kernel, but potentially the entire image as a search window. The rationale is to compare the neighborhoods of all voxels $\mathbf{y} \in I$ with the neighbors of the current voxel at location $\mathbf{x}$ (Buades et al., 2005):

$$\hat{I}_{\mathrm{NL}}(\mathbf{x}) = \sum_{\mathbf{y}\in I} w(\mathbf{x},\mathbf{y}) I'(\mathbf{y}) \qquad (8)$$

Thus, the similarity of a whole neighborhood with fixed size determines the weight $w(\mathbf{x},\mathbf{y})$ with which a distant voxel will influence the new value of the current voxel. More specifically, the weights are significant only if a Gaussian kernel G_σ with standard deviation σ around **y** looks like the corresponding Gaussian kernel around **x**:

$$w(\mathbf{x},\mathbf{y}) = \frac{1}{Z(\mathbf{x})} \exp\left(-\frac{\int G_\sigma(\mathbf{n}) * |I'(\mathbf{x}+\mathbf{n}) - I'(\mathbf{y}+\mathbf{n})|^2 d\mathbf{n}}{h^2}\right), \qquad (9)$$

where **n** scans the neighborhood, h acts as a filtering parameter that can be adapted to the level of image noise and $Z(\mathbf{x})$ is the normalizing factor. Note that the computational cost for the neighborhood search in the entire image can become excessive, so restricting the search to a certain window size ($\mathbf{y} \in \boldsymbol{S}$ instead of $\mathbf{y} \in I$) is required (Buades et al., 2008).

Edge Enhancement

A notorious problem in image processing is partial volume effects due to image blur. That is, image edges do not manifest themselves as crisp intensity steps, but rather as gradual intensity changes spanning several voxels. A standard method to sharpen the image, i.e. to enhance the intensity gradient locally, is unsharp masking (Sheppard et al., 2004):

$$\hat{I}_{\mathrm{UM}}(\mathbf{x}) = I'(\mathbf{x}) - \frac{w(G_\sigma * I'(\mathbf{x}))}{1-w} \qquad (10)$$

where σ should roughly match the half-width of blurry edges and w defines the degree of edge enhancement, where $[0.1,0.9]$ is a suitable range. In the context of the last section, this corresponds to the inverse diffusion equation. Evidently, unsharp masking will also enhance noise, so the image should be denoised first. Alternative edge enhancement methods like a difference of Gaussians or a Laplacian of Gaussian filter (Gonzalez and Woods, 2002; Russ, 2006) have a very similar concept and are not further discussed here.

Image Segmentation

Histogram bias correction

The frequency distribution of gray values can have an unfavorable shape for threshold detection. Typical examples are low contrast, imbalanced class proportions, class skewnesses or class variances. Here we list three methods that can partially remove these histogram traits and thus facilitate more reliable threshold estimates:

1. Gradient Mask:

Partial volume effects due to blurred phase edges can cause long tailings in the histogram, which lead to skewed distributions for the lowest and highest intensity class. Partial volume voxels can be identified through high gradient intensities and treated by different strategies (Panda and Rosenfeld, 1978). One is to calculate the average gray value of partial volume voxels and use it as an optimal threshold (Schlüter et al., 2010), another is to mask them out and only calculate the histogram for low gradient regions. The mask is generated by unimodal thresholding (Rosin, 2001) of the histogram of intensity gradients.

2. Histogram equilization:

Image contrast is often enhanced by linear or non-linear intensity rescaling, sometimes also denoted as histogram stretching (Gonzalez and Woods, 2002; Russ, 2006). An alternative approach to contrast enhancement is contrast-limited adaptive histogram equalization (CLAHE) (Pizer et al., 1987). Image contrast can be defined as the slope of the cumulative density function of gray values. Limiting this contrast corresponds to clipping the histogram at a certain cutoff. The histogram area thus removed is uniformly distributed over the range of gray values that occur in the image. In principle, this algorithm operates on the histogram of a certain search window to obtain a locally adaptive contrast enhancement. The method can be generalized such that any transition between global and local contrast enhancement is achieved (Stark, 2000). In this study, histogram clipping is only applied to the global histogram to improve threshold detection and is not mapped to the corresponding image.

3. ROI dilations

Some images exhibit unimodal histograms due to very imbalanced class proportions, i.e. a very small volume fraction of a certain phase and a very large volume fraction of the background. A balanced frequency distribution can be obtained with a new, semi-automatic algorithm: (i) pick a threshold manually that detects the class with lowest volume fraction as the region of interest (ROI) and binarize the image. (ii) Dilate the thus obtained mask. (iii) multiply the original image with the mask in order to compute the ROI histogram. (iv) if it is not yet clearly bimodal (multimodal) return to step (ii).

Global Thresholding

Image segmentation is a crucial step in image processing and affects all subsequent image analyses. In this context, it is common to refer to global thresholding as approaches where classes are assigned to voxels by histogram evaluation only, without considering how the gray values are spatially arranged in the corresponding image. A multitude of different thresholding methods exist today which have been reviewed by various authors (Pal and Pal, 1993; Sahoo et al., 1988; Sezgin and Sankur, 2004; Trier and Jain, 1995). The general conclusion, if any, is that none of the reviewed methods excel at all segmentation problems. A comprehensive survey by Sezgin and Sankur (2004) compared 40 different thresholding methods, most of them global, and classified them according to fundamental principles. Five out of those methods were chosen for implementation in this study as well as an additional one:

1. G1 - Maximum Variance:

This is a classic method based on discriminant analysis (Otsu, 1975). Consider the histogram as an estimator of the probability of a certain gray value and $n-1$ thresholds to divide the histogram into n classes $(C_0, C_1, \dots, C_n)$. The total variance σ_T^2 of the population of gray values can be divided into the sum of within-class variances σ_W^2 and the between-class variance σ_B^2 of class means. The objective is to find the set of $n-1$ thresholds $(t_0, t_1, \dots, t_{n-1})$ that maximizes this between-class variance.

2. G2 - Minimum Error:

Minimum Error Thresholding assumes the histogram to be composed of normal distributions for each class (Kittler and Illingworth, 1986). The Gaussian modes that are fitted to the histogram usually overlap at certain gray values. As a consequence, assigning those voxels to only one class will deliberately lead to a certain misclassification error for the other class. The objective is to set the thresholds $(t_0, t_1, \dots, t_{n-1})$ such that the misclassification error is minimal.

3. G3 - Maximum Entropy:

This method exists in various modifications. The classic approach, which is implemented here, relies on Shannon Entropy as a measure of the information content of a signal (Kapur et al., 1985). Assume a threshold to be close to the maximum or minimum gray value. Objects will barely appear in the output image and will be almost completely surrounded by background. Hence the information content of the resulting image is low. A set of thresholds $(t_0, t_1, \dots, t_{n-1})$ can be adjusted such that the image has the richest detail, i.e. the information transfer is optimal. This is achieved by maximizing the sum of class entropies.

4. G4 - Fuzzy C-means:

This method combines the classic k-means algorithm (Ridler and Calvard, 1978) with fuzzy set theory (Jawahar et al., 1997). Membership functions $M_0, M_1, \dots, M_n$ are assigned to each gray value depending on the distance to each class mean $\mu_0, \mu_1, \dots, \mu_n$ and a fuzziness index τ. The optimal set of thresholds $(t_0, t_1, \dots, t_{n-1})$ is detected at the intersections of adjacent M.

5. G5 - Shape:

This method detects the thresholds $(t_0, t_1, \dots, t_{n-1})$ at the local minimum between two adjacent histogram peaks (Tsai, 1995). If the number of peaks n_p exceeds the predefined number of classes n, iterative Gaussian smoothing is first applied to the histogram, until $n_p = n$. If $n_p < n$, the missing thresholds are set at the location of maximum histogram curvature instead.

6. G6 - Average:

It can be shown that some methods are optimal under certain conditions (Kurita et al., 1992), e.g. equal class probabilities, equal class variances, etc. However, these conditions are hardly ever met in a real image and all methods will be biased to some degree. Assuming that the bias of different methods may partly cancel out due to the different criteria that they optimize, an averaged threshold over all methods may lie closer to the true, unknown optimum. Since some methods may fail completely, outliers have to be removed, i.e. only thresholds within $(\overline{t}_k - \sigma_{t_k}, \overline{t}_k + \sigma_{t_k})$ contribute to the final value, where $k = 0, \dots, n-1$.

Note that in the first three methods the computational cost for an exhaustive search over all sets of thresholds in a n -dimensional search space increases exponentially with increasing number of classes n. Therefore, the methods are implemented in an efficient way by using look-up tables to store each term of a specific objective function for every possible pair of class boundaries, and employ these tables to calculate the objective function for an arbitrary number of classes (Liao et al., 2001). For the fuzzy c-means the exhaustive search is replaced by an iterative search (Jawahar et al., 1997). The search space for the shape method is one-dimensional irrespective of the number of classes.

Local Segmentation

In contrast to global, histogram-based thresholding, locally adaptive segmentation methods also account for some kind of neighborhood statistic for class assignment in order to smooth object boundaries, avoid noise objects, or compensate for local intensity changes. Due to the added flexibility, local segmentation methods often result in more satisfying segmentation results (Iassonov et al., 2009; Wang et al., 2011). Five different local segmentation methods, which have all been successfully applied to porous media images in the past, will be used in this study:

1. L1 - Hysteresis:

Hysteresis segmentation, which is sometimes also denoted as bi-level segmentation or region growing, was introduced as a method to improve edge continuity in gradient images (Canny, 1986). In the same way it improves the class assignment of partial volume voxels in soil images (Schlüter et al., 2010; Vogel and Kretzschmar, 1996). Two thresholds have to be set by the user, a lower threshold that identifies voxels which definitely belong to a low intensity class and an upper threshold for which the uncertainty of class assignment is highest. A voxel in the intermediate gray value range is only assigned to the low intensity class, if a neighbor voxel already belongs to the low intensity class. In other words, low intensity voxels serve as seed regions for iterations of conditional dilations. Unassigned voxels which cannot be accessed by this region growing process are assigned to the high intensity class. Hysteresis thresholding is not a multi-class segmentation method in its strictest sense as the procedure has to be repeated $n-1$ times for n classes.

2. L2 - Indicator kriging:

In this geostatistical method, spatial correlation is used as a local assignment criterion (Houston et al., 2013b; Oh and Lindquist, 1999). Again, two thresholds are specified by the user to define two *a priori* classes. The upper threshold of the unclassified range is extended towards gray values that definitely belong to a high-intensity class. The class assignment at an unclassified location depends on the weighted average of indicator values in its neighborhood, where the weights are obtained by kriging. Indicator kriging has to be repeated $n-1$ times for n classes as well.

3. L3 - Bayesian Markov Random Field:

The rationale of this probabilistic segmentation method is to find a spatial arrangement of class labels $\hat{C}$ with minimum boundary surface that at the same time honors the gray value data in the best possible way (Berthod et al., 1996; Kulkarni et al., 2012). This is a combinatorial optimization problem which is solved in the framework of Markov random fields (MRF), i.e. by only evaluating the interaction between direct neighbors:

$$\hat{C} = \underset{\hat{C}}{\operatorname{argmin}} \left\{ \underbrace{\int_{\Omega} \left(\sqrt{2\pi\sigma_c^2} + \frac{I'_{\mathbf{x}} - \mu_c}{2\sigma_c^2} \right)}_{\text{class statistics}} + \underbrace{\beta \int_{\Pi} \gamma(c_{\mathbf{x}}, c_{\mathbf{y}})}_{\text{class boundaries}} \right\} \tag{11}$$

with

$$\gamma(c_{\mathbf{x}}, c_{\mathbf{y}}) = \begin{cases} -1, & c_{\mathbf{x}} = c_{\mathbf{y}} \\ +1, & c_{\mathbf{x}} \neq c_{\mathbf{y}} \end{cases} \tag{12}$$

where Ω is the population of all voxels, Π is the population of all pairs of neighboring voxels $\mathbf{x}$ and $\mathbf{y}$, $c_{\mathbf{x}}$ is the class label at $\mathbf{x}$, μ_c and σ_c^2 are class mean and variance and β is a homogeneity parameter that determines the weight of the penalty term for class boundaries. Class updating is achieved in a deterministic order denoted with iterative conditional modes (ICM) (Besag, 1986) where sufficient convergence is usually achieved after 3-5 loops.

4. L4 - Watershed:

The watershed algorithm uses lines of highest gradient to demarcate class borders locally (Beucher and Lantuejoul, 1979; Roerdink and Meijster, 2000; Vincent and Soille, 1991). The image is preclassified with simple thresholding to set markers for the immersion process. High gradient zones are subsequently set to unclassified again, as they will be assigned by the watershed algorithm. These high gradient zones

are either identified by edge detection (Sobel, Canny, etc.) or by a small cubic kernel that detects neighborhoods with non-uniform class assignment. The latter method produced the better results for the images examined in this study. The unclassified zones are filled from different ends using the intensity gradient as a pseudo-height until the watershed line is reached. Finally, the voxels located directly on the separation line and on plateaus are filled with the most representative class in their neighborhood.

5. L5 - Converging Active Contours:

This approach is a combination of the watershed method and active contour methods which uses gradient and intensity information simultaneously (Sheppard et al., 2004). The method is initialized by identifying seed regions for each class; as in the methods above, this means that each voxel is either assigned to one of the classes or left unassigned, to be classified during the main segmentation step. Like the watershed method described above, this initial classification is normally done by thresholding in both intensity and gradient space; each class has an upper and a lower threshold along with an upper gradient threshold. The main classification algorithm proceeds by simultaneously growing the boundaries of these seed regions towards each other. The speed at which the boundaries advance varies spatially and temporally, depending on the local gradient and optionally on the distance of the local gray value to its class mean. The algorithm ends when all boundaries have converged. The final separation line assignment problem described above that affects some watershed methods is not an issue because every non-seed voxel is traversed by one class boundary before any others. The advancement of the boundaries is implemented efficiently using the fast marching algorithm; despite this, the method is quite computationally intensive and requires parallel implementations to operate on large 3D images.

Postprocessing

Denoising and boundary refinement can also be applied to the class image C as postprocessing instead of smoothing the raw image I'. Among the most popular postprocessing methods for binary images are morphological operators like erosion and dilation (Serra, 1982). However, in multi-class images they would correspond to a minimum and maximum filter, which are not suited for this purpose at all. A median filter, on the other hand, removes segmentation noise and rugged class boundaries rather well. It does however, have the unwanted feature that the results happen to depend on the order in which the classes are numbered. This is avoided by applying a majority filter $\hat{C}_{\mathrm{MA}}$, which assigns the most representative class among all neighbors in a cubic kernel to the central voxel. It is common to enforce two criteria to prevent unwanted features where more than two phases meet: (i) the most representative class exceeds a certain volume fraction and (ii) the volume fraction of the most representative class exceeds the volume fraction of the old class at the central voxel by a certain percentage.

An alternative post-processing method is size-dependent object removal. For this method, each object of each class has to be labeled. Volumes are then determined by voxel counting and objects smaller than a user-dependent threshold are filled with the class that completely surrounds the object. Consequently, rugged surfaces of big objects are conserved. Small deleted objects at the boundary between two materials are filled by simultaneous dilation of both materials.

Structural analysis

The list of tools with which complex structures like porous media can be analyzed is virtually endless. This study is constrained to only four very simple, but meaningful metrics. If ground truth information is available from a true image I, a misclassification error ME can be determined:

$$ME = \frac{1}{N_{\mathbf{x}}} \sum_{i=1}^{N_{\mathbf{x}}} \delta(c_i, \hat{c_i}), \qquad (13)$$

$$\delta(c_i, \widehat{c_i}) = \begin{cases} 1, & c_i = \widehat{c_i} \\ 0, & c_i \neq \widehat{c_i} \end{cases} \quad (14)$$

where c_i and $\widehat{c_i}$ are the true and current class at location i and $N_{\mathbf{x}}$ is the number of all voxels. Bulk volumes V and surface areas a are examined for each individual phase. Specific interfacial areas between two phases (a and b) are obtained by the following relation:

$$a_{ab} = \frac{1}{2}(a_a + a_b - a_c) \quad (15)$$

where c is the union of all other classes. Both V and a are determined with Minkowski functionals (Vogel et al., 2010). In this way, surface area estimates are directly obtained from the segmented voxel image and problems associated with aligning isosurfaces of each indivdual phase are avoided. Finally, a dimensionless connectivity indicator for a specific phase is calculated (Renard and Allard, 2013):

$$\Gamma_a = \frac{1}{N_a^2} \sum_{i=1}^{N_l} n_i^2 \quad (16)$$

where each cluster of phase a has a label l_i and a size n_i, N_l is the number of clusters and N_a is the number of all phase a voxels. Cluster labeling is typically achieved with a fast method by Hoshen and Kopelman (1976). Γ_a has the edge over the popular Euler number that it is bounded by (0,1] and less sensitive to noise.

Results

Synthetic Test Image

Image Generation

Synthetic images provide ground truth data against which different image enhancement and segmentation methods can be compared. The test image in this study is generated to resemble a partially saturated sand packing. To this end, a volume of $512 \times 512 \times 128$ voxels is filled by non-overlapping spheres with a radius of $r = 50$ voxels placed at random locations. If a new sphere does not fit at a given location, the radius decreases in steps until the overlap vanishes. The location is completely abandoned when $r = 20$ is reached. The procedure stops after 250 spheres have successfully been placed resulting in a porosity of 0.412. Subsequently, an opening transform (Serra, 1982) is applied to the pore space with a spherical structure element of $r = 15$. The pore space which has been removed by this opening is considered to be filled with the wetting phase (w) and the remaining, larger pore bodies are assigned to the non-wetting phase (n). This does not necessarily produce a physically realistic fluid distribution, but evokes fluid configurations that are similar enough to serve as a test scenario. The resulting volume fractions are $V_w = 0.279$ and $V_n = 0.133$. Gray values of 50, 125 and 205 are assigned to non-wetting, wetting and solid phase, respectively, resulting in the true image I. An axial image slice of I is depicted in Figure 1(a).

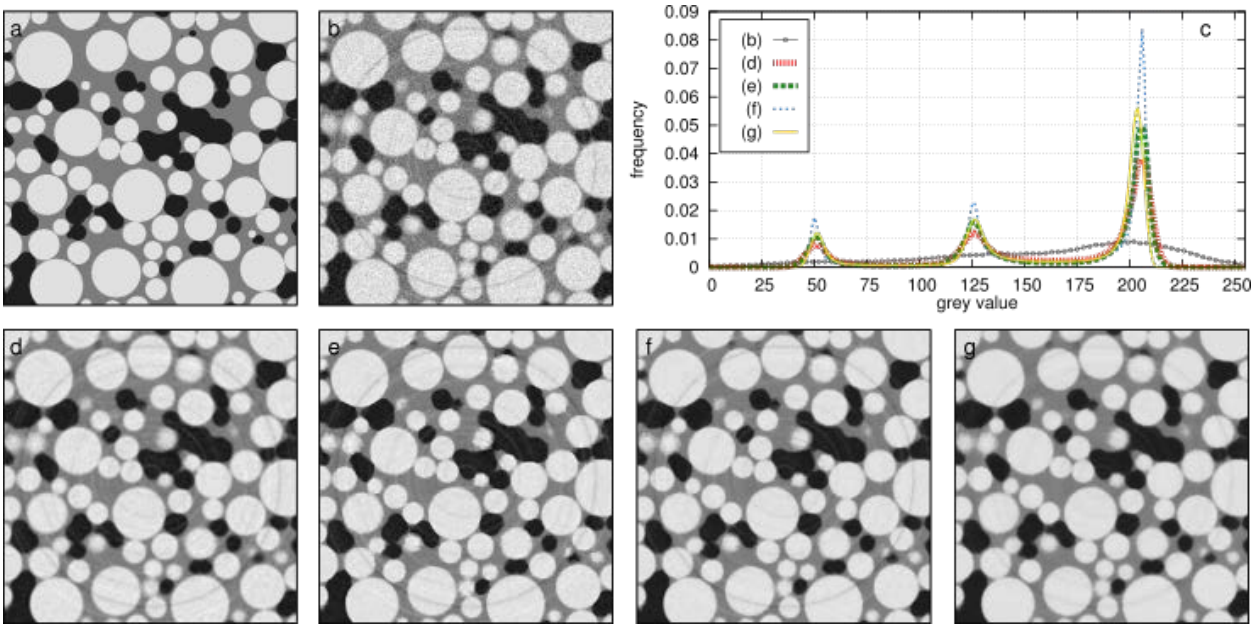

Figure 4: Comparison of denoising methods: (a) True image I with spheres and size-dependent distribution of wetting and non-wetting phase, (b) raw image I' exhibiting ring artifacts, blur and noise, (c) histograms before and after image enhancement. Lower row depicts image enhancement results with different denoising methods in combination with unsharp masking: (d) $\hat{I}_{\mathrm{ME+UM}}$, (e) $\hat{I}_{\mathrm{AD+UM}}$, (f) $\hat{I}_{\mathrm{TV+UM}}$, (g) $\hat{I}_{\mathrm{NL+UM}}$.

Subsequently, the image is superimposed with ring artifacts, blur and noise in order to obtain a more realistic, raw image I' (Figure 1(b)). The ring artifacts are additive with random height and random radius. The rings manifest themselves as a random gray value offset in the range [-100,100], where the resulting gray value is limited at [0,255]. Subsequently, blurring is achieved with a cubic mean kernel of five voxels on a side. Finally, uncorrelated Gaussian noise is added with a signal-to-noise ratio of $\sigma_b/\sigma_n = 2$, where σ_b and σ_n are the standard deviations of gray values in the blurred image and the noise model, respectively.

Denoising and Edge enhancement

Four different denoising methods (Figure 1(d-g)) are applied to the raw image I' in (Figure 1(b)) in order to remove noise followed by an edge-enhancement step to mitigate partial volume effects caused by blur. The median filter was applied one time with a cubic convolution kernel with a side length of $d = 7$ voxels. The anisotropic diffusion filter was applied with $\kappa = 15$, $\sigma = 1.0$ and $t = 1.5$ (9 iterations). The total variation filter was applied with $\lambda = 2$stopping after $t = 0.12$ (30 iterations). For the non-local means filter a cubic kernel of $d = 7$ was used for neighborhood search with a Gaussian convolution kernel of $\sigma = 2$ in a reduced search window S of $d = 23$ voxels. The two criteria for the majority filter are set to an absolute majority of 0.33 and a higher occurence than the class of the central voxel of 0.05.

The settings of each denoising method have been carefully chosen to achieve strong denoising, deliberately accepting some degree of edge smoothing. Subsequently, an unsharp mask filter for edge enhancement with a Gaussian kernel of $\sigma = 1.5$ and a weighting factor of $w = 0.7$ was applied to each denoising result. Finally, the results of the unsharp mask after anisotropic diffusion $\hat{I}_{\mathrm{AD+UM}}$and total variation denoising $\hat{I}_{\mathrm{TV+UM}}$ had to be cleaned by a median filter with a $d = 5$ kernel to smooth rough surfaces that were enhanced during unsharp masking.

The histograms in (Figure 1(c)) and visual appearances in (Figure 1(d-g)) indicate different success in noise removal and edge-preservation. The edges in the median image $\hat{I}_{\mathrm{ME+UM}}$ appear slightly more blurry than in the images for the other three denoising methods. Moreover, we observe that the non-local means filter $\hat{I}_{\mathrm{NL+UM}}$ is superior in removing ring artifacts during the denoising step alone and does not require the additional cleanup of rough edges by a median filter mentioned above.

Ring Artifact Removal

The ring artifact routine of Sijbers and Postnov (2004) is applied slice-wise with a window size of $w = 27$ pixels and a homogeneity threshold H adapted to the noise level in Figure 1 (d-g). The outcome is depicted for the enhanced image $\hat{I}_{\mathrm{NL+UM}}$ after TV denoising and unsharp mask edge enhancement (Figure 2(c)). Obviously, the ring artifact removal works well for some rings, but is incomplete for others even after carefully testing different w and H. For instance, the white ring within the green window exhibits a varying magnitude after denoising (Figure 2(a)). Since the high artifact magnitude in the pore space contributes less than half to the window height in Figure 2(b), it remains undetected by the median $\tilde{I}(r)$. Stretching the window over more than one slice as suggested by Ketcham (2006) does not improve the results. In addition, the back transform from polar into Cartesian coordinates introduces additional blur for high radii (yellow frame).

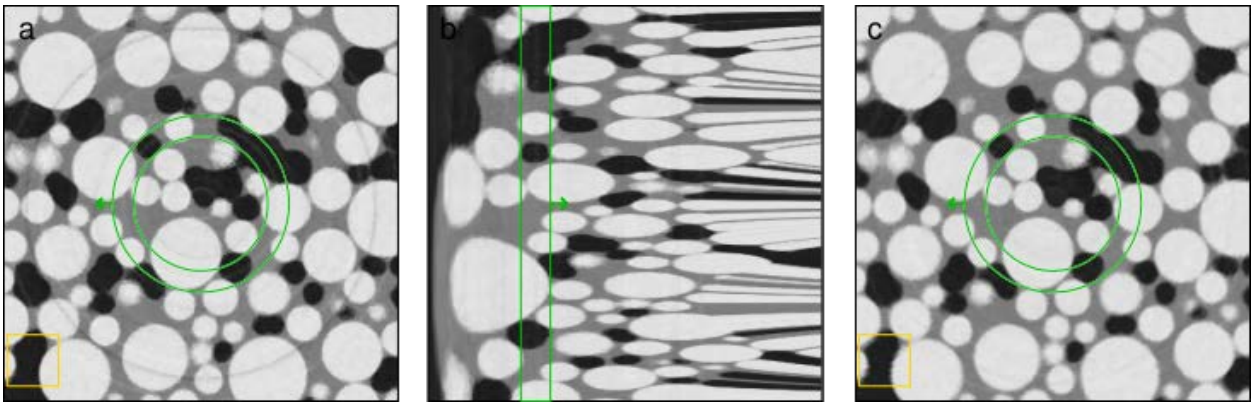

Figure 5: Ring artifact removal: (a) Test image after a combination of TV denoising and unsharp masking $\hat{I}_{\mathrm{NL+UM}}$ (corresponds to Figure 1(f)). Yellow frame marks sharp boundaries before ring artifact removal and the green ring corresponds to the window in polar coordinates. (b) Same image in polar coordinates after line removal. Green rectangle depicts the moving window W. (c) Same image after ring artifact removal. The yellow frame highlights blur due to the back transform into Cartesian coordinates.

Global Thresholding

In Figure 3(a) the well-known Otsu method (G1) is applied as an example to the histogram of $\hat{I}_{\mathrm{NL+UM}}$after ring artifact removal. Results for the other denoising methods are similar (not shown). The exhaustive search for each pair of thresholds detects the optimum at $t^{\max} = (95; 166)$. Percentiles of this objective criterion can be used to obtain fuzzy threshold ranges (Oh and Lindquist, 1999), i.e. t_1 is held constant and t_0 decreases (or increases) until in this case $\sigma_b^2/\langle\sigma_b^2\rangle_{max} = 0.992$ is reached at t_0^l (or t_0^h). The procedure is repeated for t_1 where t_0 kept is constant. Applying these thresholds and associated ranges to the underlying histogram (Figure 3(b)) reveals a bias of Otsu's method towards the class with highest volume fraction. Note that the true optimum, which is estimated by the intersection points of the individual gray value frequencies within in each class of the true image, is at $t^{\mathrm{true}} = (91; 162)$. Some other thresholding methods are also afflicted by bias, yet in different directions (Figure 3(c)). Fuzzy c-means (G3) show the same bias due to imbalanced class probabilities. The shape analysis (G5) performs

well since the local histogram minima happen to coincide with the intersection points in Figure 3(b). The minimum error method (G2) is biased due to imbalanced skewness, i.e. only the wetting phase exhibits two long tailings due to partial volume effects in both directions, which increases the probability of being assigned to that class. The maximum entropy method (G4) fails completely in identifying meaningful thresholds. Figure 3(c) also depicts the arithmetic mean of thresholds and associated ranges after outlier removal (G6). This average set of thresholds at $t = (88; 165)$ is closer to the true optimum. Note that the specific percentiles for each thresholding method have to be set individually, as each objective criterion exhibits very different ranges, i.e. some are bounded and yet others are logarithmic. A large part of the bias in Figure 3(c) can be removed easily. First, the impact of imbalanced skewness is mitigated by masking out partial volume voxels at phase edges (Panda and Rosenfeld, 1978). Second, the impact of imbalanced class probabilities is reduced by histogram clipping (Pizer et al., 1987). In this way the skewness of the non-wetting and solid phase is also efficiently removed. The combination of both methods leads to a well-balanced histogram for which each of the surveyed thresholding methods ends up at similar values (Figure 3(d)). The average after outlier removal at $t = \{90; 162\}$ matches the true optimum almost perfectly.

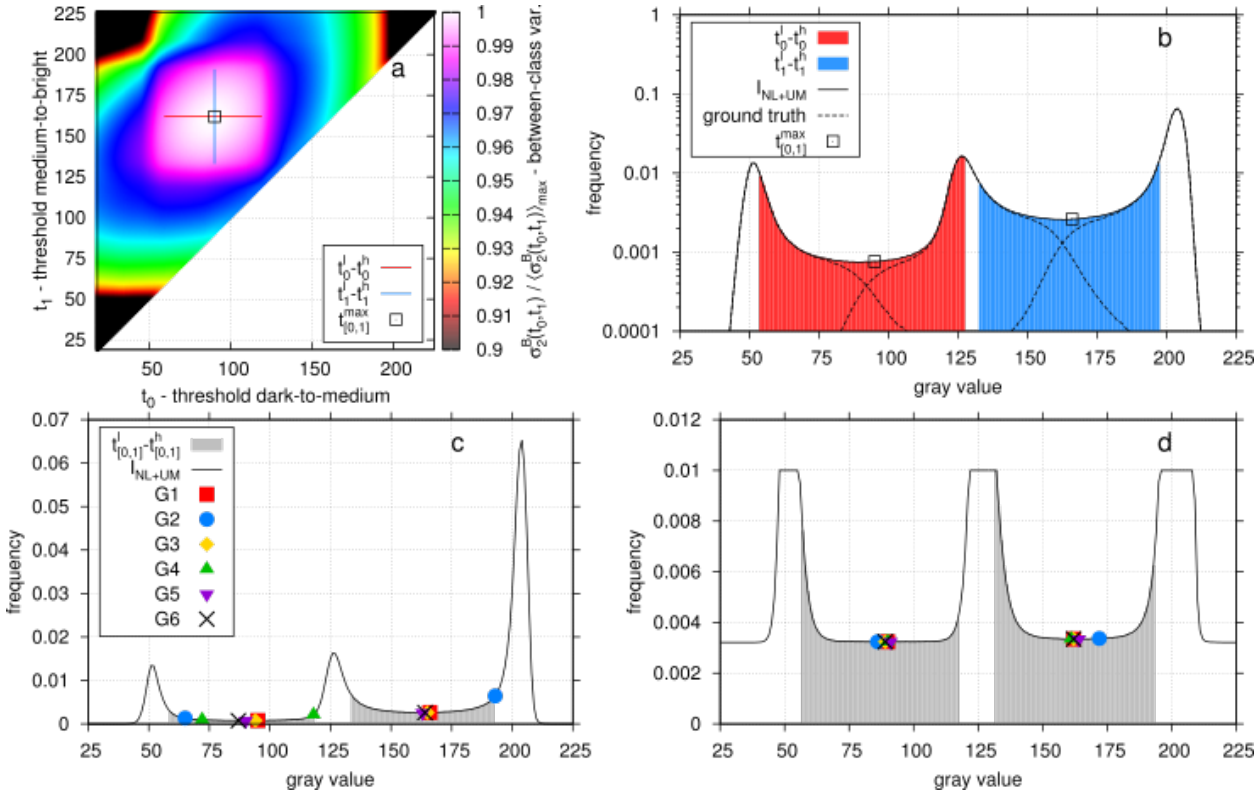

Figure 6: Threshold detection methods: (a) normalized objective function of Otsu's method (G1) with the thresholds detected at the maximum between-class variance and the transition regions stopping at the 0.992 percentile. (b) Histogram of $\hat{I}_{\mathrm{NL+UM}}$ after ring artifact removal with thresholds $t_0^{\max}$ and $t_1^{\max}$ and transition ranges (t_0^l, t_0^h and t_1^l, t_1^h) detected with Otsu's method (G1). (c) Threshold pairs for five different methods (G1-G5) and the corresponding averages after outlier removal (G6). The transition regions $[t_{[0,1]}^l, t_{[0,1]}^h]$ are obtained accordingly. (d) Same averaging method after edge masking and histogram clipping.

Local Segmentation

The average set of thresholds (Figure 3(d)) are determined for each denoising method individually and then used for global thresholding as an initial step in all local segmentation methods. Note that *a priori*

segmentation with Bayesian Markov random field (L3) and watershed segmentation (L4) requires single thresholds $t_k^{\max}$ only, hysteresis segmentation (L1) uses the range $\left[t_k^{\mathrm{l}}, t_k^{\max}\right]$, and indicator kriging (L2) and converging active contours (L5) use $\left[t_k^{\mathrm{l}}, t_k^{\mathrm{h}}\right]$, with $k = \{0; 1\}$. In addition, converging active contours requires a gradient threshold, which is determined automatically by unimodal thresholding of the gradient histogram.

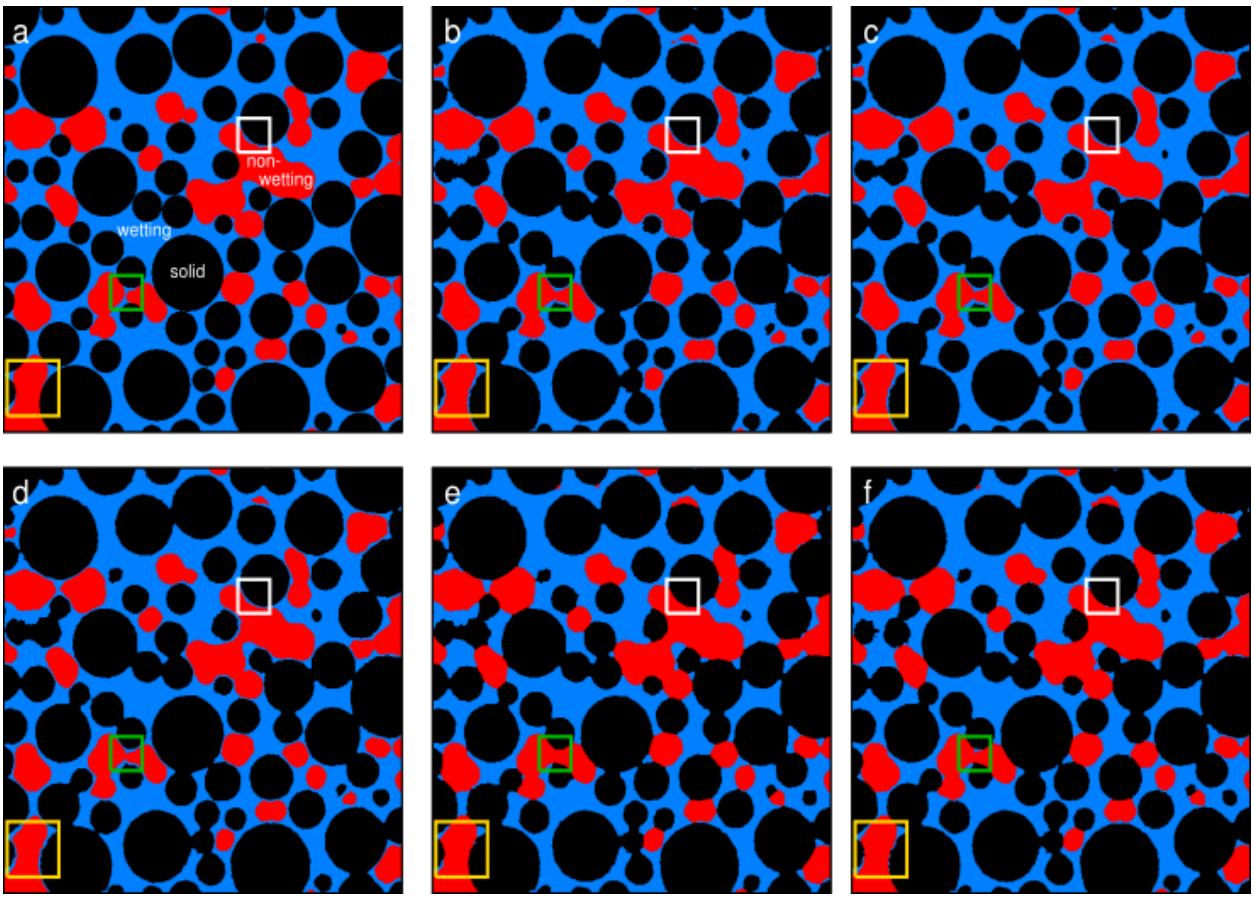

Figure 7: Segmentation results for different local segmentation methods applied on the image after non-local means denoising and unsharp masking $\hat{I}_{\mathrm{NL+UM}}$: (a) original image, (b) global thresholding, (c) indicator kriging, (d) Bayesian MRF, (e) watershed, (f) converging active contours. Differently colored frames highlight failures of various methods.

The results of each local segmentation method on $\hat{I}_{\mathrm{NL+UM}}$ are depicted in Figure 4. The segmentation result for hysteresis segmentation (L1) is left out, because it is indistinguishable from the outcome of global thresholding (G6). All segmentation results are free of ring artifacts and noise and exhibit smooth object boundaries which can be mainly credited to successful preprocessing. However, some segmentation results perform better than others in the way they recover image features impaired by blur. Incorrectly identified, apparent wetting films that are due to partial volume voxels at class boundaries between the non-wetting and solid phases (yellow frame) can be mainly attributed to image blur. Indicator kriging (L2) and hysteresis segmentation (L1) cannot cope with this problem, since these are iterative methods, i.e. the segmentation between wetting and non-wetting phase is independent of the segmentation between wetting and solid phase.

In principle, Bayesian MRF segmentation (L3) has a mechanism to remove these films. To do so, the homogeneity factor β has to be set high, thus also removing true features of similar size. A moderate

value of $\beta = 0.5$ is used here. Yet, no matter how high β is set only direct neighbors are evaluated in the MRF paradigm and since the films are thicker than two voxels they cannot be penalized. Another fundamental shortcoming of Bayesian MRF segmentation that has previously gone unnoticed is its tendency towards bias in the class statistics (Eq.11). The histogram of the wetting phase exhibits long tailing towards both directions in contrast to only one tail for the other classes (Figure 3(c)). Consequently, σ_w is much higher than σ_n and the probability of a voxel in the intermediate intensity range to be assigned to the wetting phase increases accordingly, resulting in even thicker apparent wetting films. This bias is mitigated here by a quick and rather inelegant fix to use $\sigma_w/2$ for the class statistics instead. In this way, the gray values at which the penalty functions for adjacent classes cross each other coincide much better with the previously detected thresholds (Figure 8).

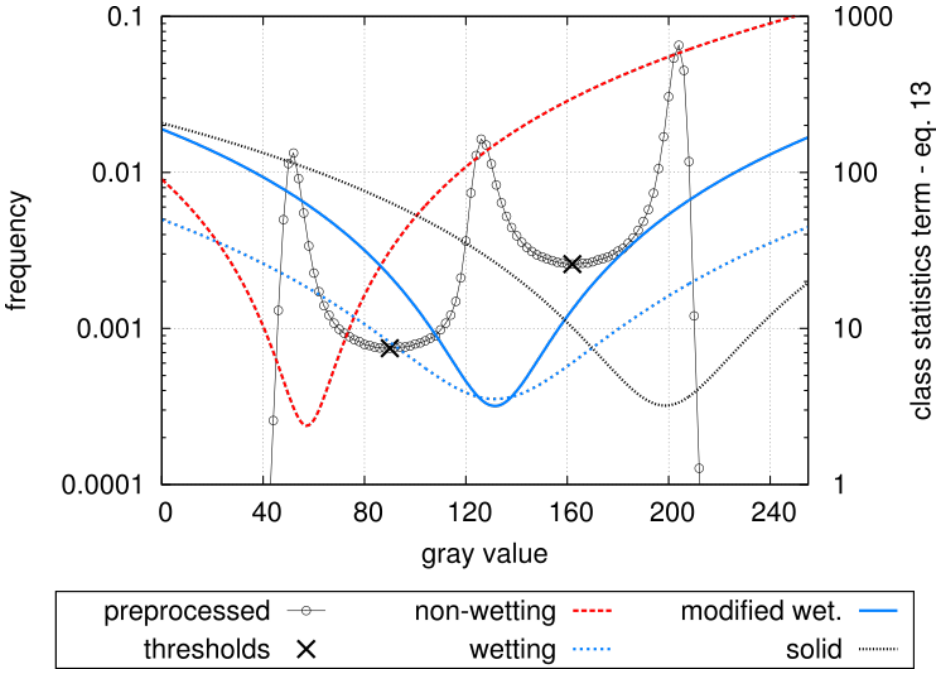

Figure 8: First term of the objective function for MRF segmentation (Eq.11) as a function of gray value for each class. In the modified class statistics σ_w is replaced by $\sigma_w/2$ for the wetting phase.

The watershed method (L4) successfully removes apparent wetting films in the yellow frame (Figure 4 (e)). However, true wetting films are also being removed (white frame). Segmentation with converging active contours (L5 - Figure 4(f)) exhibit excessive wetting film removal as well. Finally, no method is capable of restoring the small wetting phase bridge (green frame) in Figure 4, because its intensity is highly smoothed due to image blur.

Structural Analysis

The shortcomings of the different segmentation methods are corroborated by structural properties of the non-wetting phase listed in Table 1. The misclassification error ME is roughly$3-4\%$ for all methods including global thresholding. However, the lowest ME does not guarantee the best recovery of morphological properties. The bulk volume V_n of the non-wetting phase is slightly underestimated by all segmentation methods, except for watershed segmentation and converging active contours which show a tendency for overestimation, due to the way partial volume voxels are treated. Surprisingly, simple thresholding and hysteresis thresholding match the true a_n value best, whereas indicator kriging and Bayesian MRF underestimate it and watershed segmentation and converging active contours overestimate

it as a consequence of partial volume voxel treatment. More importantly, the specific interface between fluids a_{wn} only diverges from the total non-wetting surface a_n if false wetting films are successfully supressed. Simple thresholding, hysteresis thresholding, indicator kriging, and Bayesian MRF segmentation all fail in this respect. The only exception is Bayesian MRF segmentation on the raw data if combined with postprocessing $\hat{C}_{\mathrm{MA}}$, simply because the majority filter removes partial volume voxels. Watershed segmentation and converging active contours underestimate a_{wn} because a lot of true wetting films are removed as well. The connectivity index of the true image Γ_n is matched well by most segmentation methods, because the bubbles remain rather isolated no matter how wetting films are treated. Oversegmentation of the non-wetting phase with watershed segmentation and converging active contours may lead to lower Γ_n, however, because (i) the denominator N_a in Eq. (16) increases and (ii) the increase in bubble volume is evenly distributed among all clusters in the numerator. The differences in structural properties due to different denoising methods are also listed in Table 1. Obviously, no denoising at all produced the worst results in all respects. Moreover, the structural properties do not vary much among the different denoising methods. Surprisingly, a simple majority filter $\hat{C}_{\mathrm{MA}}$, applied on the segmented raw data without any preprocessing results in the best agreement with the true bulk properties. This is because any kind of preprocessing, i.e. denoising and edge enhancement, removes structural information to some degree.

Table 1: Structural properties of segmented images for different combinations of denoising and segmentation methods: unsharp mask (UM), median (MD), anisotropic diffusion (AD), total variation (TV), non-local means (NL), majority (MA). *ME* is misclassification error, V_n is volume fraction of non-wetting phase, a_n is surface area density of non-wetting phase, a_{wn} is surface area density between non-wetting and wetting phase and Γ_n is connectivity index of non-wetting phase.

denoising	ME	V_n	a_n	a_{wn}	Γ_n
	[−]	[−]	[pix^{-1}]	[pix^{-1}]	[−]
true image					
	.000	.133	.0169	.0140	.355
G6 - global thresholding					
I'	.140	.141	.1005	.0954	.312
$\hat{I}_{MD+UM}$	.028	.128	.0168	.0167	.355
$\hat{I}_{AD+UM}$	.029	.124	.0165	.0165	.355
$\hat{I}_{TV+UM}$	.027	.127	.0169	.0169	.355
$\hat{I}_{NL+UM}$	.027	.130	.0172	.0170	.354
$\hat{C}_{MA}$	.024	.129	.0169	.0168	.355
L1 - hysteresis					
I'	.107	.131	.0722	.0695	.346
$\hat{I}_{MD+UM}$	.027	.127	.0167	.0167	.355
$\hat{I}_{AD+UM}$	.029	.123	.0164	.0164	.355
$\hat{I}_{TV+UM}$	.027	.127	.0169	.0169	.355
$\hat{I}_{NL+UM}$	.027	.129	.0171	.0170	.354
$\hat{C}_{MA}$	.024	.128	.0167	.0167	.355
L2 - indicator kriging					
I'	.037	.131	.0202	.0201	.386
$\hat{I}_{MD+UM}$	.033	.128	.0166	.0166	.351
$\hat{I}_{AD+UM}$	.037	.122	.0162	.0162	.353
$\hat{I}_{TV+UM}$	.032	.125	.0165	.0165	.352
$\hat{I}_{NL+UM}$	.033	.127	.0166	.0166	.352
$\hat{C}_{MA}$	.029	.131	.0167	.0167	.352

L3 - Bayesian MRF (β=0.5)					
I'	.049	.133	.0282	.0272	.385
$\hat{I}_{MD+UM}$	.027	.124	.0163	.0163	.356
$\hat{I}_{AD+UM}$	.033	.119	.0160	.0160	.357
$\hat{I}_{TV+UM}$	.028	.124	.0165	.0165	.356
$\hat{I}_{NL+UM}$	.028	.127	.0166	.0165	.356
$\hat{C}_{MA}$	.038	.134	.0170	.0140	.356
L4 – watershed					
I'	.041	.136	.0184	.0112	.358
$\hat{I}_{MD+UM}$	.029	.135	.0172	.0110	.355
$\hat{I}_{AD+UM}$	.025	.134	.0170	.0117	.355
$\hat{I}_{TV+UM}$	.029	.135	.0174	.0111	.355
$\hat{I}_{NL+UM}$	.032	.137	.0175	.0102	.322
$\hat{C}_{MA}$	.037	.136	.0174	.0101	.359
L5 - converging active contours					
I'	.046	.136	.0241	.0178	.390
$\hat{I}_{MD+UM}$	.042	.136	.0173	.0108	.324
$\hat{I}_{AD+UM}$	.042	.137	.0172	.0107	.324
$\hat{I}_{TV+UM}$	.042	.136	.0174	.0110	.324
$\hat{I}_{NL+UM}$	.043	.138	.0175	.0108	.324
$\hat{C}_{MA}$	.043	.136	.0175	.0105	.360

Final Workflow

At this point, some preliminary conclusions about a suitable image processing protocol can already be drawn in order to set the workflow for the remaining images:

1. The variability in structural properties among the different denoising methods was rather small. Qualitatively, all filters reduce noise in homogeneous areas well. In addition, only the non-local means filter sufficiently denoises along edges while smoothing across the edges is inhibited. In this way, an additional treatment of rugged surfaces after edge enhancement is not necessary. Thus, in the remainder of the paper, only the non-local means filter will be used.

2. A combination of methods for histogram bias correction causes a better agreement between different threshold detection methods. The outlier-corrected average of five different threshold detection methods reproduced ground truth information well and will be used for global thresholding.

3. Hysteresis thresholding and indicator kriging are not capable of multi-class segmentation, which leads to misclassifaction errors where more than two phases meet locally. Therefore, only converging active contours, watershed and Bayesian MRF segmentation will be applied to the remaining images. Simple thresholding will also be applied for sake of comparison.

4. Segmentation of the raw data with a subsequent majority filter performed slightly better in terms of structural properties than denoising the intensity data in advance. Both approaches will be compared with each other.

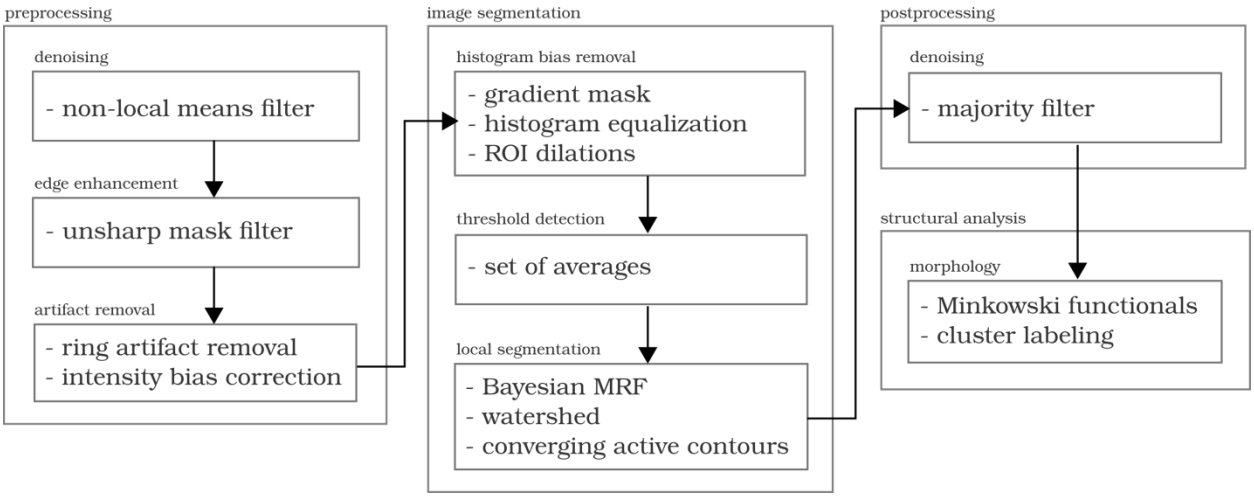

Figure 9: Workflow diagram for multi-class segmentation of the remaining multi-fluid image and soil image. Headlines denote image processing steps and gray boxes the specific methods.

These findings translate into the workflow diagram shown in Figure 6. Some steps are optional, e.g. the need for edge enhancement depends on the sharpness of the raw image, ROI dilations are only necessary, if the volume fraction of the phase of interest is very low, etc.

Synchrotron Image of Three-Fluid Phases in a Porous Medium

Image Enhancement

A sample of sintered glass beads with a porosity of roughly 32% has been scanned at a resolution of 9.24µm. The pore space was partially saturated with air (14%), oil (39%) and water (47%). The cylindrical region of interest has a diameter of 665 voxels and height of 210 voxels. The image is free of ring artifacts and is sharp, without noticeable blur (Figure 7(a)). The reconstruction method caused a slight decrease in mean intensity for large radii which is evident in the denoised image after non-local means denoising. (Figure 7(b)). This radial intensity variation can be removed almost completely (Figure 7(c)) with intensity bias correction (Iassonov and Tuller, 2010). This has a considerable impact on the histogram (Figure 7(d)). The frequency distributions for each class turns from broad and multi-peaked into a narrow band. For the same reasons as discussed for the synthetic test image, edges are masked out and the histogram is clipped into a well-balanced frequency distribution, so that five different global threshold detection methods (G1-G5) yield very similar sets of thresholds. Again, the average after outlier removal (G6) is used for final segmentation using local methods. Note that edge enhancement with unsharp mask filtering has not been applied, as there are hardly any partial volume voxels in this image.

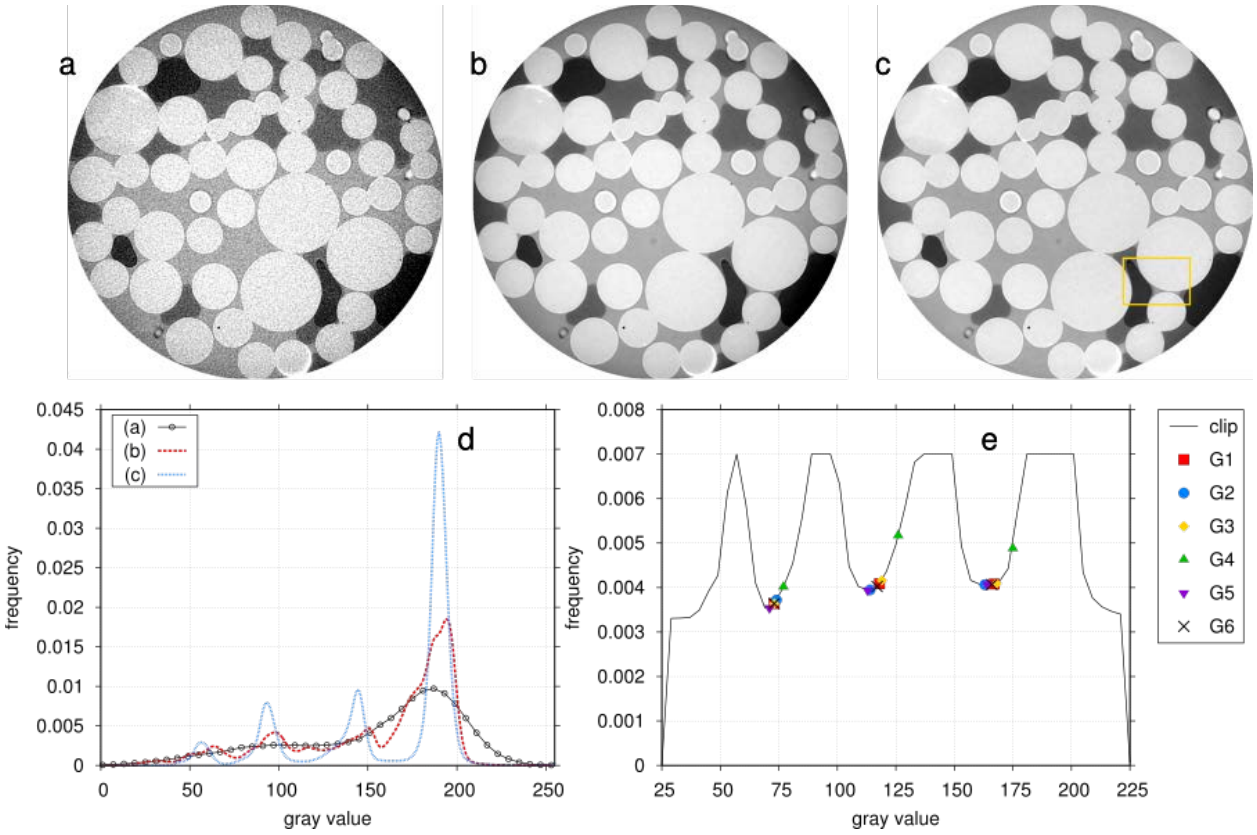

Figure 10: Image enhancement of multi-fluid image: (a) raw image I', (b) non-local means filter $\hat{I}_{\mathrm{NL}}$ on I', (c) beam hardening removal on $\hat{I}_{\mathrm{NL}}$. The yellow frame outlines the subset in Figure 8. (d) Histograms of (a), (b) and (c), (e) global threshold detection after histogram clipping.

Image Segmentation

Simple thresholding (G6), Bayesian MRF segmentation (L3), watershed segmentation (L4) and converging active contours (L5) are applied to the multi-fluid image, either on the preprocessed $\hat{I}_{\mathrm{NL}}$ or on the raw I' followed by a majority filter. A small subset of the segmentation results are depicted in Figure 8. Since the exact arrangement of interfaces is unknown, it is difficult to judge objectively what combination of methods performs best. The edge between beads and air is roughly two voxels thick. In the smooth $\hat{I}_{\mathrm{NL}}$ image, the edge is assigned to oil films, water films or both (Figure 8(d,f,h,j)), whereas in the noisy image edge voxels are equally assigned to all four classes but subsequently assigned to air or beads since they constitute the most representative class in the neighborhood of an edge (Figure 8(c,e,g,i)). It is almost impossible to conclusively determine whether a fluid film thicker than the image resolution really covers the beads entirely. However, small isolated water voxels between solid voxels and oil film are highly unlikely, and should be suppressed. Global thresholding without postprocessing has no mechanism to achieve this. Bayesian MRF segmentation of $\hat{I}_{\mathrm{NL}}$ only succeeded in doing so with a relatively high homogeneity parameter ($\beta = 10$). In turn, watershed segmentation fails to detect an oil film at the left side of the pendular water ring, either because of a lacking seed voxel for oil or because the underlying gradient image is not sharp enough to evoke two distinct edges within such a short distance. Converging active contours result in subjectively plausible results for both I' and $\hat{I}_{\mathrm{NL}}$.

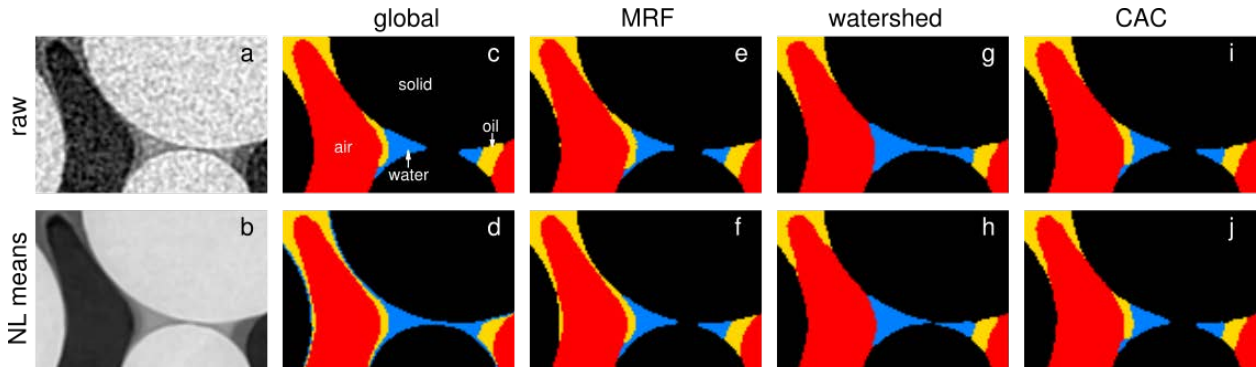

Figure 11: Segmentation results for multi-fluid image: (a) raw image I', (b) non-local means filter $\hat{I}_{\mathrm{NL}}$, global thresholding on I' with postprocessing (c) or on $\hat{I}_{\mathrm{NL}}$ (d), Bayesian MRF segmentation with $\beta = 0.1$ on I' with postprocessing (e) or with $\beta = 10$ on $\hat{I}_{\mathrm{NL}}$ (f), watershed segmentation on I' with postprocessing (g) or on $\hat{I}_{\mathrm{NL}}$ (h), converging active contours on I' with postprocessing (i) or on $\hat{I}_{\mathrm{NL}}$ (j).

Image Analysis

The qualitative analysis illustrated in Figure 8 is corroborated by the results with respect to structural analysis in Table 2. The bulk volumes of air and oil, V_a and V_o, remain largely unaffected by the choice of segmentation methods. The surface area densities a_o, a_a and a_{ao}, however, vary considerably among different segmentation methods. This is because small image objects like films, meniscii and ganglia exhibit large surface-to-volume ratios and at the same time are associated with the highest uncertainty in terms of class assignment. A majority filter $\hat{C}_{\mathrm{MA}}$ leads to a general reduction in surface areas and to very similar results for all segmentation methods. The surface areas increase with a decreasing boundary penalty factor β for Bayesian MRF segmentation on $\hat{I}_{\mathrm{NL}}$ and are highest for global thresholding on $\hat{I}_{\mathrm{NL}}$, where there is no penalty term at all. The a_o and a_a values for $\beta = 10$ are very similar to all postprocessed class images $\hat{C}_{\mathrm{MA}}$, to the outcome of converging active contours on $\hat{I}_{\mathrm{NL}}$, and to the result after watershed segmentation on $\hat{I}_{\mathrm{NL}}$. Yet, the specific surface area between air and oil ($a_{ao} = 0.149$) is as much as $\approx 27\%$ higher than the average of other methods ($a_{ao} = [0.107 - 0.130]$). Eventually, a decision as to which image is closer to reality needs to be made. But without an analytical solution or other ground truth information such a decision will suffer from a certain level of subjectivity.

Table 2: Volume fractions V and surface area densities a of air (a) and oil (o) for the segmented multi-fluid image. Denoising is either applied prior to segmentation with a non-local means filter ($\hat{I}_{\mathrm{NL}}$) or as postprocessing with a majority filter ($\hat{C}_{\mathrm{MA}}$).

denoising	V_a	a_a	V_o	a_o	a_{ao}
	[−]	[mm^{-1}]	[−]	[mm^{-1}]	[mm^{-1}]
G6 - global thresholding					
$\hat{C}_{\mathrm{MA}}$	.047	.400	.125	1.621	.120
$\hat{I}_{\mathrm{NL}}$	.046	.545	.125	2.281	.384
L3 - Bayesian MRF					
(†β=0.1; ‡β=1; §β=10)					
$\hat{C}_{\mathrm{MA}}$ †	.047	.482	.125	1.840	.215
$\hat{I}_{\mathrm{NL}}$ †	.046	.505	.124	2.214	.369
$\hat{I}_{\mathrm{NL}}$ ‡	.046	.459	.125	2.063	.327
$\hat{I}_{\mathrm{NL}}$ §	.046	.397	.125	1.686	.149

L4 - watershed					
$\hat{C}_{\mathrm{MA}}$	.048	.403	.127	1.646	.107
$\hat{I}_{\mathrm{NL}}$	.048	.406	.127	1.631	.109
L5 - converging active contours					
$\hat{C}_{\mathrm{MA}}$	.047	.421	.121	1.642	.130
$\hat{I}_{\mathrm{NL}}$	.048	.407	.123	1.650	.119

µCT image of soil

Image Enhancement

The soil image corresponds to image 2 in Houston et al. (2013b) with a size of $256 \times 256 \times 256$ voxels and a resolution of 32µm. The sample consists of macropores ($V_p \approx 12\%$), organic matter ($V_o \approx 13\%$), soil matrix ($V_m \approx 72\%$) and dense particles like rocks ($V_r \approx 3\%$). The raw data I' (Figure 9(a)) is again denoised with a non-local means filter $\hat{I}_{\mathrm{NL}}$ (Figure 9(b)). Afterwards edges are enhanced by an unsharp mask $\hat{I}_{\mathrm{NL+UM}}$ with $\sigma = 1$ and $w = 0.5$ so that intensity values of partial volume voxels are forced closer to their respective class means (Figure 9(c)). The gradient mask in (Figure 9(d)) detects partial volume voxels at phase edges which are excluded from subsequent threshold detection. Each of these methods has a favorable impact on the intensity histogram (Figure 9(e)) in that valleys between the class peaks are much more pronounced. The combination of all methods, i.e., edge masking on $\hat{I}_{\mathrm{NL+UM}}$, together with histogram clipping leads to a modified histogram for which all five threshold detection methods (G1-G5) lead to similar results (Figure 9(e)). The average after outlier removal (G6) is again used for all locally-adaptive segmentation methods.

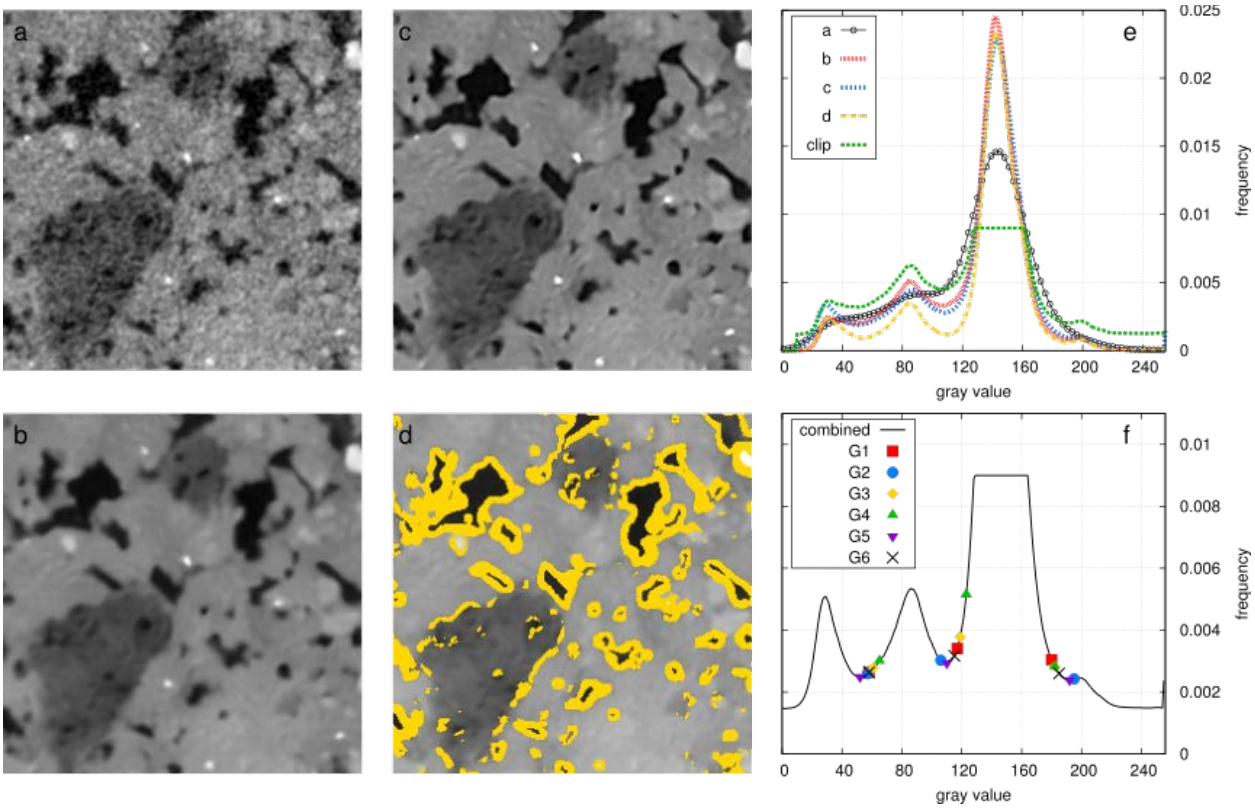

Figure 12: Image enhancement of a soil image: (a) raw image I' (Houston et al., 2013b), (b) $\hat{I}_{\mathrm{NL}}$ after non-local means denoising, (c) $\hat{I}_{\mathrm{NL+UM}}$ after unsharp mask, (d) gradient mask on $\hat{I}_{\mathrm{NL+UM}}$, (e) histogram of (b), (c), (d) and histogram clipping of (b), (f) histogram after combined postprocessing (b+c+d+clip) together with the corresponding thresholds obtained by various global thresholding methods.

Image Segmentation

Only some of the segmentation methods introduced in this paper are applied to the soil image. Global thresholding of the raw data I' in combination with a majority filter $\hat{C}_{\mathrm{MA}}$ (Figure 10(a)) shall serve as a reference to which the other methods can be compared. Evidently, simple thresholding already leads to rather satisfying results if it is accompanied by suitable postprocessing. However, the segmented image clearly suffers from false organic coatings around macropores which can be attributed to incorrect assignment of partial volume voxels (violet frame). This misclassification of boundary voxels can be avoided with watershed segmentation (Figure 10(b)) and converging active contours (Figure 10(c)) both applied to denoised and edge-enhanced image $\hat{I}_{\mathrm{NL+UM}}$. In addition, even thin macropores are correctly detected (green frame). Bayesian MRF segmentation is applied to $\hat{I}_{\mathrm{NL+UM}}$ with $\beta = 0.1$, $\beta = 1$ and $\beta = 10$, respectively (Figure 10(d-f)). We observe that the segmented images look very different for different β. If the penalty term for class boundaries (Eq. 11) has a low weight ($\beta = 0.1$), the image looks very similar to (Figure 10(a)), i.e. all image objects are well preserved, yet all macropores exhibit false coatings of organic matter. In turn, if the homogeneity parameter is set very high ($\beta = 10$), partial volume effects are suppressed and so are small image objects in general, like the thin macropore in the green frame. A moderate value ($\beta = 1$) leads to an unsatisfactory trade-off between the two problems.

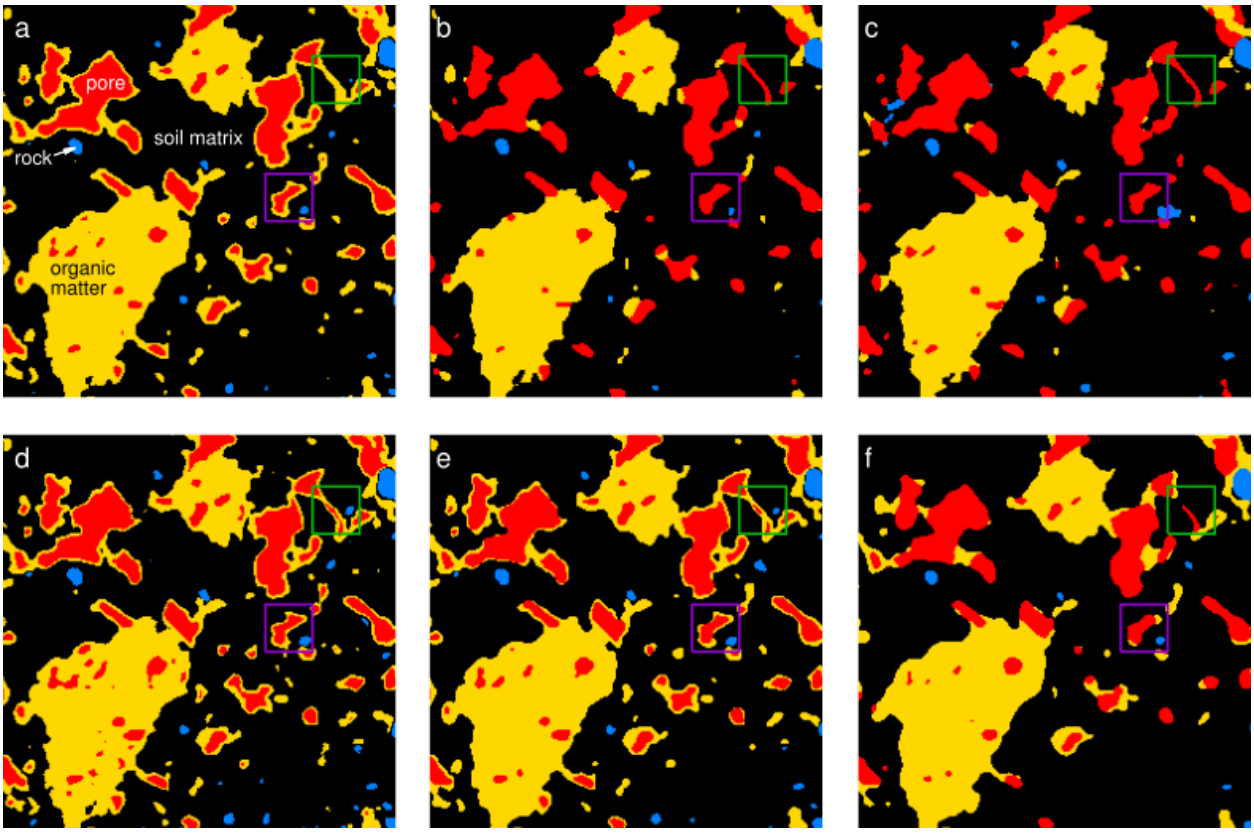

Figure 13: Image segmentation of the soil image: (a) global thresholding on I' with postprocessing, (b) watershed segmentation on $\hat{I}_{\mathrm{NL+UM}}$, (c) converging active contours on $\hat{I}_{\mathrm{NL+UM}}$, (d-f) Bayesian MRF segmentation on $\hat{I}_{\mathrm{NL+UM}}$ with $\beta = (0.1, 1, 10)$, respectively.

Image Analysis

The qualitative interpretation is again corroborated by structural properties of macropores and organic matter summarized in Table 3. Bulk volume and surface area vary much more among different segmentation methods as compared to the multi-fluid image. For instance, the surface area density a_{op} between organic matter and macropores decreases by a factor of 2.5 if the homogeneity parameter for Bayesian MRF segmentation is increased from $\beta = 0.1$ (Figure 13(d)) to $\beta = 10$ (Figure 13(f)), and is even smaller for watershed segmentation (Figure 13(b)) and converging active contours (Figure 13(c)). In addition, the connectivity indicator Γ is also sensitive to the choice of segmentation method, because small objects close to the image resolution have a high impact on the continuity of a phase. Therefore, macropore connectivity increases from $\Gamma_p = [0.72 - 0.80]$ to $\Gamma_p = [0.83 - 0.84]$ if thin macropores that connect larger pore bodies are correctly identified, e.g. the green frame in Figure 10. At the same time the connectivity of organic matter decreases drastically from $\Gamma_o = [0.94 - 0.96]$ to $\Gamma_o = [0.64 - 0.74]$ if false organic coatings of macropores (violet frame) are successfully suppressed.

Table 3: Volume fractions *V*, surface area densities *a* and connectivity indices Γ of pores *p* and organic residues *o* for the soil image. Denoising is either applied prior to segmentation with a non-local means filter ($\hat{I}_{\mathrm{NL}}$) or as postprocessing with a majority filter ($\widehat{C}_{\mathrm{MA}}$).

denoising	V_p	V_o	a_o	a_{op}	Γ_p	Γ_o

	[−]	[−]	[mm^{-1}]	[mm^{-1}]	[−]	[−]
G6 - global thresholding						
$\hat{C}_{\mathrm{MA}}$	.082	.213	2.74	0.91	.721	.953
$\hat{I}_{\mathrm{NL}}$	.096	.190	3.30	1.29	.777	.940
L3 - Bayesian MRF						
($^{\dagger}\beta$*=0.1;* $^{\ddagger}\beta$*=1;* $^{\S}\beta$*=10)*						
$\hat{C}_{\mathrm{MA}}$ †	.085	.208	2.63	0.91	.734	.953
$\hat{I}_{\mathrm{NL}}$ †	.093	.197	2.97	1.12	.787	.950
$\hat{I}_{\mathrm{NL}}$ ‡	.086	.193	2.13	0.71	.795	.961
$\hat{I}_{\mathrm{NL}}$ §	.087	.176	1.46	0.44	.822	.963
L4 - watershed						
$\hat{C}_{\mathrm{MA}}$	.110	.137	1.05	0.30	.802	.652
$\hat{I}_{\mathrm{NL}}$	.117	.127	0.84	0.25	.834	.644
L5 - converging active contours						
$\hat{C}_{\mathrm{MA}}$	.088	.135	1.24	0.40	.730	.744
$\hat{I}_{\mathrm{NL}}$	.129	.116	0.66	0.24	.825	.681

Discussion

Image enhancement

We have demonstrated how essential a suitable combination of image enhancement methods can be for subsequent image segmentation. The correction of intensity bias due to beam hardening was adequately corrected by the method of Iassonov and Tuller (2010), since the examined sample was cylindrical and fairly homogeneous. If the intensity bias had a more complex shape, which cannot be readily described as function of radius, the bias model could have been obtained by interpolation instead. For instance, the approach of Yanowitz and Bruckstein (1989) to use the Laplace equation to interpolate a threshold surface between slowly varying gray values along phase boundaries can be adapted to interpolate a bias surface between objects of the highest intensity class. Even better results can be expected by using the Poisson equation for this purpose (Pérez et al., 2003). The ring artifact removal routine (Sijbers and Postnov, 2004) succeeded in removing most of the rings. However, the ring artifact removal is incomplete if the artifact magnitude is not constant along rotation angle φ. Moreover, the back-transfrom from polar into Cartesian coordinates introduces additional blur that increases with radius r. Thus, the performance is always somewhat worse as compared to line removal directly applied on the sinograms when this is possible (Ketcham, 2006). Also, some methods operate on rings in Cartesian space directly (Freundlich, 1987). Finally, Fourier and wavelet filters generally lead to improved ring removal (Münch et al., 2009; Raven, 1998).

The surveyed denoising methods were efficient in removing noise while keeping the blurring of edges at a minimum, given that the associated parameters are set adequately. In fact, image noise today has become a secondary issue for successful image analysis. Instead, image blur has been identified as more of a pitfall for the success of the various segmentation methods in this study. Edge enhancement with unsharp masks partly mitigates image blur, but is not capable of removing partial volume effects completely. Surely, future advances in x-ray tomography hardware and reconstruction software will lead to steady improvements in image quality, so that sharper images can be acquired on a routine basis.

One of our significant findings was that even though image enhancement is often indispensable for robust threshold detection, it does not necessarily imply that the segmentation itself also has to be applied to the enhanced image. Instead, segmenting the raw data with the thus obtained thresholds may lead to fewer misclassification errors if suitable postprocessing is applied to the segmentated images. This is because any image enhancement inevitably destroys some structural information in the raw data. For the images examined in this study, a majority filter on the segmented raw data produced good results, mostly because the objects had rather smooth, convex boundaries. In turn, a majority filter can be a less desirable option if true objects are thin, concave, have rough surfaces or acute angles. It is up to the user to always compare and decide which is the most favorable option.

Global thresholding

We have demonstrated that every histogram-based thresholding method relies on certain assumptions about the histogram shape. This introduces some bias if the class modes have different variance, skewness, or proportion. Many bias correction techniques for the standard methods used here have been suggested. For instance, minimum error thresholding can be corrected for imbalanced overlap (Cho et al., 1989) or can be used with Poisson distributions for each class instead of Gaussian distributions (Pal and Bhandari, 1993). Shannon entropy can be replaced by Tsallis entropy for maximum entropy thresholding, allowing for an additional degree of freedom that can be used to tune the results (de Albuquerque et al., 2004). Fuzzy c-means can be corrected for imbalanced class proportions (Jawahar et al., 1997). The list is virtually endless. However, we found it more useful to (i) put some effort into suitable image enhancement prior to thresholding, (ii) alleviate the impact of bias by histogram clipping, and (iii) use the average after outlier removal to determine thresholds for subsequent segmentation. Even with this preprocessing methodology there might be soil images that still exhibit unimodal histograms due to a lot of unresolved porosity or very imbalanced class proportions (Baveye et al., 2010; Wang et al., 2011). The second problem can be avoided with a semi-automatic algorithm based on ROI dilations (Figure 11). For instance, small rocks constitute only 3% to volume in the soil image and are hard to distinguish as an individual class in the histogram. The threshold for the region of interest (ROI) is set to the class mean ($t = \mu_s = 203$). Consecutive dilations of the ROI mask lead to a clearly bimodal histogram for which a threshold between the soil and rock class can be easily identified. Note that the thus obtained local histogram minimum at 182 is very close to $t = 185$ in Figure 9(f), but much easier to identify. An alternative to deal with unimodal histograms, which is, however, restricted to two-class segmentation, is to estimate a threshold from the mean gray value within edge regions (Panda and Rosenfeld, 1978; Schlüter et al., 2010). The problem of too much unresolved porosity or too gradual intensity changes is more severe and puts the entire concept of segmentation into question. In this case, some morphology analysis can be deployed to the intensity data directly, including distance transforms (Jang and Hong, 2001), isosurfaces (McClure et al., 2007), skeletonization (Chung and Sapiro, 2000) or tortuosity (Gommes et al., 2009).

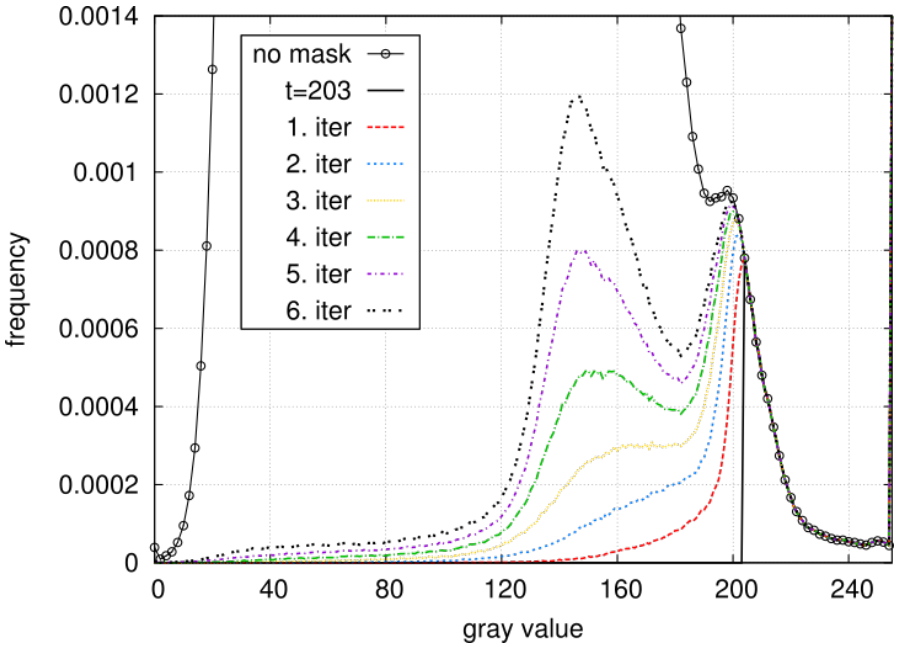

Figure 14: Iterative algorithm to identify a truly bimodal histogram at high gray values in the soil image.

Local segmentation

We have corroborated the importance of using locally adaptive methods truly capable of multi-class segmentation instead of applying iterations of binarizations (Tuller et al., 2013). Methods that fulfill this criterion are Bayesian MRF segmentation (Berthod et al., 1996; Kulkarni et al., 2012), watershed segmentation (Beucher and Lantuejoul, 1979; Roerdink and Meijster, 2000; Vincent and Soille, 1991) and converging active contours (Sheppard et al., 2004). Bayesian MRF segmentation was originally developed for image classification in the presence of additive noise and is based on the assumption that individual class modes follow a Gaussian distribution. This causes failure of the method for denoised images with pronounced partial volume effects due to image blur, which leads to either one-sided or two-sided tailings in the histogram. As a consequence, special care has to be taken to correct for this histogram bias. In addition, the results depend heavily on the homogeneity parameter β. Erroneous assignment of partial volume voxels could only be suppressed with a high penalty on class boundaries (β =10), which at the same time removed true image features of similar size. A promising improvement of the Bayesian MRF segmentation, especially if applied to fluid images, would be to replace the unspecified penalty term (Eq. 16) with real surface tensions (Knight et al., 1990; Silverstein and Fort, 2000). In fact, any non-invasive laboratory technique which provides independent measurements about a structural property of the same sample can potentially help to condition segmentation parameters. This has been recently demonstrated for three-phase segmentation of limestone via hysteresis thresholding, where the region growing parameters were conditioned by independent porosity measurements (Mangane et al., 2013).

For the watershed segmentation in its current implementation, a benefit is that it only requires simple thresholding and a gradient image. However, the lack of additional parameters also hampers flexibility. Therefore, excessive elimination of wetting films in the synthetic image could not be avoided. In contrast, the somewhat similar converging active contours method honors local gradient and intensity information at the same time. A reported drawback of this method is its sensitivity to seed region detection and the adjustment of parameters for the speed function (Iassonov et al., 2009). In this paper, we demonstrated strategies to define the seed regions automatically. In addition, the parameters for the speed function can be obtained directly by a careful evaluation of the gradient histogram (Figure 12). The frequency of local

gradients is almost always unimodal and therefore difficult to threshold with standard methods. Yet, every unimodal histogram exhibits some characteristic features such as a point of maximum curvature (Tsai, 1995) or the point of maximum distance from an auxiliary line between the histogram mode and the maximum bin (Rosin, 2001) (Figure 12, inset). In addition, some gradient histograms may exhibit secondary shoulders if the intensity data comprises fairly constant edge heights. Picking one of these points as a gradient threshold would result in a fully objective segmentation method. In this study we always used the gradient cutoff detection with Rosin's method. In turn, adjusting this cutoff adds some flexibility to the speed function in the same way as β scales the penalty term in the Bayesian MRF method. For instance, we achieved a very good reproduction of the true interfacial area between fluids a_{wn} in the synthetic test image by setting the gradient cutoff to a higher value.

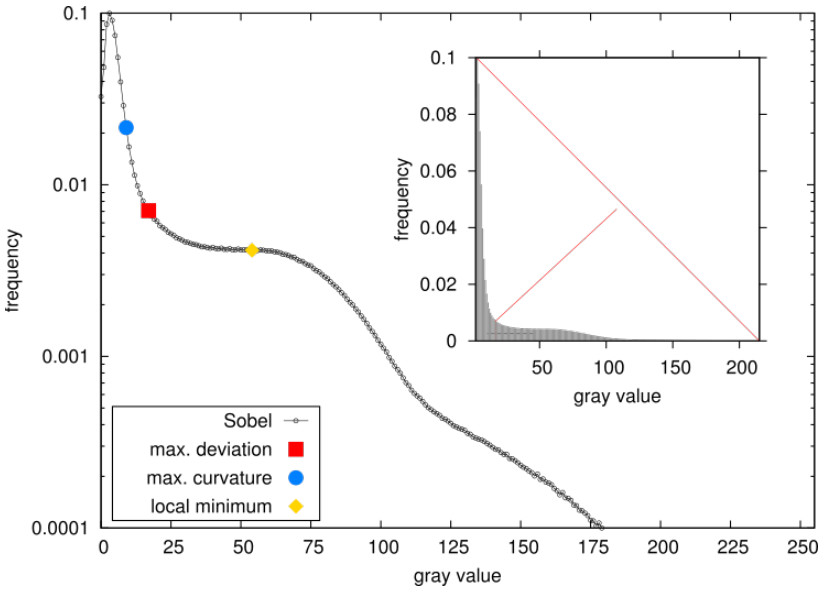

Figure 15: Gradient histogram computed on a Sobel image of $\hat{I}_{\mathrm{NL+UM}}$ for the synthetic image. Each unimodal histogram has a unique point of maximum curvature and maximum distance from the auxiliary line depicted in the inset. In addition, the shoulder in the histogram produces a local minimum, which can be detected as well.

As expected, objects that are close in size to the image resolution were associated with the highest uncertainty in all test images. Five voxels in diameter has been suggested as a rough estimate for an object size limit for which image analysis is reliable (Lehmann et al., 2006; Vogel et al., 2010). Features like the thin oil films and pendular rings at grain contacts in the synchrotron image clearly do not meet this criterion. Brown et al. (2014) compared surface area densities of smooth fluid interfaces for the same kind of three-fluid samples when improving the image resolution from 10.6µm to 5.3µm and observed an increase in the range of 5-16%, depending on the specific fluid pair. An improvement in resolution usually comes at the cost of a smaller field of view as far as industrial scanners are concerned, as well as increased noise unless the scan time is increased as well. For heterogeneous media, especially, there is a trade-off between a representative image size and sufficient resolution to capture important details. However, the scale window can also be extended towards smaller objects by scanning the same sample at different resolutions, even with different imaging techniques, and merging the images with image registration (Latham et al., 2008), statistical fusion of images (Mohebi et al., 2009) or scale fusion applied to structure analysis data only (Schlüter et al., 2011; Vogel et al., 2010). Finally, for this study we have merely compared the outcome of different local segmentation methods with each other. Of course, several methods can also be combined. For instance, Bayesian MRF segmentation with surface tensions could be used for postprocessing the outcome of converging active contours. If necessary, postprocessing with a

majority filter could also be applied in addition to denoising prior to segmentation. After all, the choice of a suitable protocol always depends on characteristics of the raw data.

Conclusions

We have surveyed recent advances in image enhancement and image segmentation of multi-phase x-ray microtomography data. Image enhancement methods included ring artifact removal, intensity bias correction, edge enhancement, image denoising and contrast enhancement. Image segmentation methods comprised six global segmentation and five different locally adaptive segmentation methods. Some general conclusions can be drawn from our findings:

1. Image blur is the major cause of poor segmentation results in this study, since image noise and other image artifacts could be removed with current image processing methods.

2. A lot of uncertainty in threshold detection can be removed by suitable preprocessing and correction of histograms for bias in the class statistics prior to thresholding.

3. Bayesian Markov randomfield segmentation, watershed segmentation and converging active contours are suited for multi-class segmentation. The converging active contour method has potentially the highest flexibility to correct for partial volume effects and simultaneously conserve small image features.

Acknowledgments

We thank Alasdair Houston (SIMBIOS, Abertay, UK) for providing the µCT soil image and three anonymous reviewers for their helpful comments. S. Schlüter is grateful to the Alexander-von-Humboldt Foundation for granting a Feodor-Lynen scholarship. A. Sheppard acknowledges the support of an Australian Research Council Future Fellowship.

Appendix A

Most image processing steps presented in this study can be done with freely available software. The only exceptions are the nonlocal means filter for denoising and the watershed method for segmentation, which were carried out with Avizo® Fire(http://www.vsg3d.com/avizo/fire). Moreover, the converging active contours method for segmentation was performed with Mango (http://physics.anu.edu.au/appmaths/capabilities/mango.php).

The conversion between Cartesian and polar coordinates for ring artifact removal was performed with the freely available Polar Transformer (http://rsbweb.nih.gov/ij/plugins/polar-transformer.html) plug-in for ImageJ. All other image processing steps are either built on or directly implemented in the QuantIm (http://www.quantim.ufz.de) open-source image processing library.

2.2. X-ray microtomography analysis of soil structure deformation caused by centrifugation (Schlüter et al. 2016, Solid Earth, 7(1), 129-140, doi: 10.5194/se-7-129-2016)

Abstract

Centrifugation provides a fast method to measure soil water retention curves over a wide moisture range. However, deformation of soil structure may occur at high angular velocities in the centrifuge. The objective of this study was to capture these changes in soil structure with X-ray microtomography and to measure local deformations via digital volume correlation. Two samples were investigated that differ in texture and rock content. A detailed analysis of the pore space reveals an interplay between shrinkage due to drying and soil compaction due to compression. Macroporosity increases at moderate angular velocity because of crack formation due to moisture release. At higher angular velocities, corresponding to capillary pressure of $\psi < -100\,\mathrm{kPa}$, macroporosity decreases again because of structure deformation due to compression. While volume changes due to swelling clay minerals are immanent in any drying process, the compaction of soil is a specific drawback of the centrifugation method. A new protocol for digital volume correlation was developed to analyze the spatial heterogeneity of deformation. In both samples the displacement of soil constituents is highest in the top part of the sample and exhibits high lateral variability explained by the spatial distribution of macropores in the sample. Centrifugation should therefore only be applied after the completion of all other hydraulic or thermal experiments, or any other analysis that depends on the integrity of soil structure.

Introduction

Soils, rocks and sediments are assumed to be rigid bodies in many modeling applications. Yet, the internal structure of these porous media is modified through a variety of technical and natural processes. The internal changes can either be gradual, e.g., through dissolution, biological activity or swelling/shrinking, or abrupt, e.g., landslides or tillage. Conventional laboratory methods can only provide a limited set of structural properties, such as bulk density and porosity, or provide indirect information through functional properties that are governed by the internal structure, such as gas diffusion, permeability or stress–strain relationships. Direct information on the deformation of the internal pore architecture is typically missing. X-ray microtomography has turned into a standard technique to fill this gap and measure the three-dimensional internal structure of porous media (Cnudde and Boone, 2013; Ketcham and Carlson, 2001; Wildenschild and Sheppard, 2013). There is a huge variety of image processing and image analysis methods that are all tailored for the ultimate goal to quantify the complex, structural heterogeneity based on a few meaningful parameters (Kaestner et al., 2008; Schlüter et al., 2014; Vogel et al., 2010). The changes in the internal structure can be assessed statistically, e.g., by comparing the pore size distribution or pore connectivity averaged over different samples at two points in time (Jégou et al., 2002; Schlüter et al., 2011). Evidently, spatially explicit information about the internal displacement of particles or aggregates is excluded from analysis in such an approach. However, this local deformation information is of particular interest, e.g., in soil mechanics (Terzaghi et al., 1996). So far there are only a few approaches to measure the deformation explicitly via imaging and image analysis. One method would obviously be to manually identify identical objects in two consecutive images and measure their separation distance. Repeating this measurement for many objects would then populate the deformation field. However, this is impractical for large, three-dimensional data sets, because of the large number of measurements required to reach an appropriate density of displacement information. Therefore, automatic methods are needed.

Automated methods to detect deformation are usually based on digital volume correlation (Bay et al., 1999; Hall, 2010; Lenoir et al., 2007; Peth et al., 2010; Son et al., 2012). The rationale of this method is to recover the displacement field by finding a geometric transformation of a deformed image that optimizes

a correlation coefficient with the original, undeformed target image. The method usually comprises three steps (Bay et al., 1999): (1) the acquisition of X-ray microtomography image before and after the perturbation, (2) image registration of one image onto the other to obtain a discrete deformation vector field and (3) calculation of the strain tensor field from the displacement vector field. Another popular method for change detection is called particle image velocimetery (PIV)(White, 2003). PIV was originally developed to visualize flow paths within a fluid by tracking small, yet visible particles over time (Adrian, 1991). In this method the image is divided into a large number of sub-windows, and the displacement vector for each window is calculated via cross-correlation between two consecutive images, which results in a local velocity for the given time lag. The particles can be substituted by any moving feature such as a growing root (Bengough et al., 2010), soil displacement along an earthworm burrow (Barnett et al., 2009) or soil creeping along slopes (Baba and Peth, 2012). A serious shortcoming of PIV is that so far it can only be applied to two-dimensional sections, in which case any displacement out of plane into the third dimension is excluded.

The objective of this paper is to measure local deformations in a soil core caused by centrifugation with digital volume correlation. We put special emphasis on common pitfalls and best practices for image registration, which is the critical step for a successful application of this method. Centrifugation has been chosen for the deformation analysis in this study because it is suitable to evoke structure deformation under controlled conditions. Measuring the water loss through centrifugation of a soil is a rather old method for determining the water retention curve of a soil (Gardner, 1937; Oden, 1975; Reatto et al., 2008; Russell and Richards, 1939). It has obvious advantages over other conventional methods like multi-step outflow (Van Dam et al., 1994; Vogel et al., 2008) or evaporation (Peters and Durner, 2008; Simunek et al., 1998) in that the method is less time consuming, it captures a wide moisture range of the retention curve and provides a good reproducibility through defined experimental conditions (angular velocity, temperature, pressure). More recently, the steady state centrifugation method was also used to measure the unsaturated hydraulic conductivity of soils (McCartney and Zornberg, 2010; Šimůnek and Nimmo, 2005; Van den Berg et al., 2009). However, a serious drawback is that soil can get compacted through the centrifugal force, i.e., the inertia that acts on the sample during rotation (Khanzode et al., 2002; Wedler and Boguslawski, 1965). The spatial variability of compaction within a sample will be investigated in this study.

Materials & Methods

Overview of core concepts

Since image registration is the backbone of our deformation detection method, we provide a brief overview over the core concepts. Optimal spatial alignment of an altered image with a target image is usually achieved by minimizing an objective function that quantifies the mismatch in terms of a predefined metric. A standard metric would be the correlation coefficient between co-localized voxels (Hapca et al., 2011; Latham et al., 2008). More advanced metrics are based on information theory like mutual information criteria (Mattes et al., 2001). Composite metrics are also possible, e.g., with an additional regularization term in case of elastic registration or an additional term for the mismatch of manually defined point pairs, so-called landmarks. The geometrical transform that produces an optimized alignment can be grouped according to the degrees of freedom by which the image can move. The simplest transform is rigid registration with six degrees of freedom, i.e., rotation around three axes and translation in three directions. A similarity transform includes isotropic scaling as one additional parameter. Affine transformations possess 12 degrees of freedom through rotation, translation, shearing in three directions and anisotropic scaling. All aforementioned transforms are global in that a single transformation matrix is uniformly applied to the entire image. Thus they do not allow for non-uniform deformation. Elastic registration with a B-spline transform, in turn, requires a regular grid of control

points over the image where each performs independent, affine registrations. As a consequence, the control points move relative to each other in the course of registration. Image registration is achieved by an iterative optimization scheme with standard methods like gradient descent or more involved methods like adaptive stochastic gradient descent (Klein et al., 2010) with optimal trade-off between speed and robustness. This completes the description of the core methodology of automated image registration. However, based on our own experience a straightforward implementation can lead to a failure of the method without following some best practices.

Initialization

Salient objects in the altered and the target image need to have substantial overlap to identify a meaningful correspondence of features. This is facilitated by a manually edited transformation matrix, in which the resolution of the altered image is adapted to the resolution of the target image and an offset between the images is corrected by some initial translation or rotation of the altered image. This manual procedure can be avoided by exhaustive sampling, where all combinations of translations (and rotations if required) are tested at a coarse grid representation (Latham et al., 2008). A different kind of user input is provided by landmarks placed on the salient features in both images. The cumulative Euclidean distance between point pairs is then added as a second term to the objective function. In all cases, the correct orientation of the sample has to be ensured a priori, because a flipped orientation cannot be recovered by rotation.

Concatenation

It is often useful to combine several consecutive image registration steps with each other, especially when an elastic registration with thousands of degrees of freedom is involved. Then a rigid registration can place the altered image already close to the global minimum and thus anticipate a collective movement of all control points in the subsequent B-spline transform. In our example, a two-step procedure will first match the position of the cylindrical container in the original sample with that of deformed sample after centrifugation, by aligning corresponding landmarks on the core wall. Then, a B-spline transform of the centrifuged sample onto the original sample will recover the remaining internal deformations.

Pyramid schedule

As mentioned above, a coarse representation of both images at reduced resolution vastly reduces the processing time so that it may even allow for exhaustive sampling of all transform parameter combinations. At the same time the coarsening reduces the iterations necessary to achieve a certain translation in physical space. This can be achieved with a so-called pyramid schedule. That is, the registration is started at a coarse representation and when convergence is reached the registration is continued at the next pyramid level with higher resolution. Finer details, e.g., small rocks that did not appear at a coarse level are then used to refine the registration results.

Contrast enhancement

The success of image registration depends on the existence of salient features in the two corresponding images. Here, a particular problem for structure deformation in soil may take effect that macropores are not rigid and may disappear completely due to compression. Likewise, cracks may form in dry soil that were not present at high moisture content. However, a lack of corresponding features may impair the success of image registration. To avoid this, the gray values in both images can be rescaled such that pore and soil matrix voxels have zero gray value and all rigid rocks are depicted with optimal contrast. In this way only the rock matrix is used for registration, i.e., an assemblage of bodies that change their position but not their shape. This raises the questions, what the minimum amount of rocks has to be in order to still

get good image registration results. Therefore, registration results will be compared for soils with high and low rock content and also with and without contrast enhancement.

Soil sampling

Undisturbed soil was sampled from two locations using a custom-made drill for undisturbed sampling of cylindrical soil cores (UGT GmbH, Germany). One sample was taken from the upper soil layer (in 5 to 15 cm depth) of a meadow in Köllme near Halle (Saale), Germany. The second sample stems from the plow horizon of a fallow plot (in 5 to 15 cm depth) at the experimental station of the Helmholtz-Centre for Environmental Research – UFZ in Bad Lauchstädt, Germany. The samples were covered with a lid, carefully transported to the laboratory and stored in a refrigerator at 4 °C to prevent the soil from drying and to reduce biological activity. The soil samples had a mean height of 7.9 cm, a diameter of 9.4 cm. The Köllme soil had an initial bulk density of 1.24 g cm^{-3} and a rock content of 3 %. The bulk density in the Bad Lauchstädt soil was higher (1.32 g cm^{-3}) and the rock content was much lower (0.2 %). The Köllme soil has a slightly coarser texture with 24 % sand, 58 % silt and 18 % clay as compared to 5 % sand, 71 % silt and 24 % clay for the Bad Lauchstädt soil (disregarding organic matter and rocks > 2 mm in diameter).

Centrifugation

A perforated aluminum plate covered with a filter paper (pore size 10 µm) was installed in between the lower boundary of the sample and a reservoir that collects the drained water. This setup was placed in a centrifuge (Cryofuge 6000i, Heraeus GmbH, Germany) and covered with a plastic film to prevent evaporation. The capillary pressure was initially adjusted to full saturation. Afterwards, the sample was centrifuged at increasing angular velocities. The equivalent capillary pressure of water ψ in equilibrium with the gravitational field written in differential form is as follows (Gardner, 1937; Russell and Richards, 1939):

$$\frac{\partial \psi}{\partial r} = \rho \omega^2 r \qquad (17)$$

Integrating Eq. (17) between the inner ($r_i = 0.136$m) and outer ($r_o = 0.22$m) boundaries of the soil core one obtains

$$\psi = \frac{\rho \omega^2}{2}(r_o^2 - r_i^2) \qquad (18)$$

where normalizing by the density of water ρ results in work per unit mass of water and hence pressure [Pa]. The angular velocity ω was calculated by $\omega = 2\pi N$, where N is the revolution frequency [rad s^{-1}].

X-ray microtomography

The soil cores were scanned with an X-ray microtomograph (X-TEk XCT 225, Nikon Metrology) with slightly different energy settings for the Köllme soil (150 keV, 425 µA) and the Bad Lauchstädt soil (160 keV, 500 µA). In both cases we used a 1 mm copper filter to reduce beam hardening artifacts and prevent overexposure at the lateral margins of the detector panel. An entire scan comprised 2749 projections with an exposure time of 708 mS (one frame per projection) which resulted in a scan time of roughly half an hour. A detector panel (Elmer-Perkin 1620) with 1750 × 2000 pixels (200 µm resolution) captures projections with 16-bit precision. The reconstruction of three-dimensional images via filtered back projection was done with the CT Pro 3-D software package (version 3.1) at a spatial resolution of 61 µm and 8 bit grayscale resolution.

Image processing

The deformation of soil structure is analyzed in two ways. First, the changes in the macropore structure are analyzed by comparing pore size distributions as well as depth profiles of macroporosity for images before and after centrifugation. Second, the displacement of soil constituents is explored with digital image correlation, i.e., via image registration of the deformed soil to the original soil prior to centrifugation. The entire image processing workflow for pore space analysis (top row) and digital image correlation (bottom row) is summarized in Figure 13.

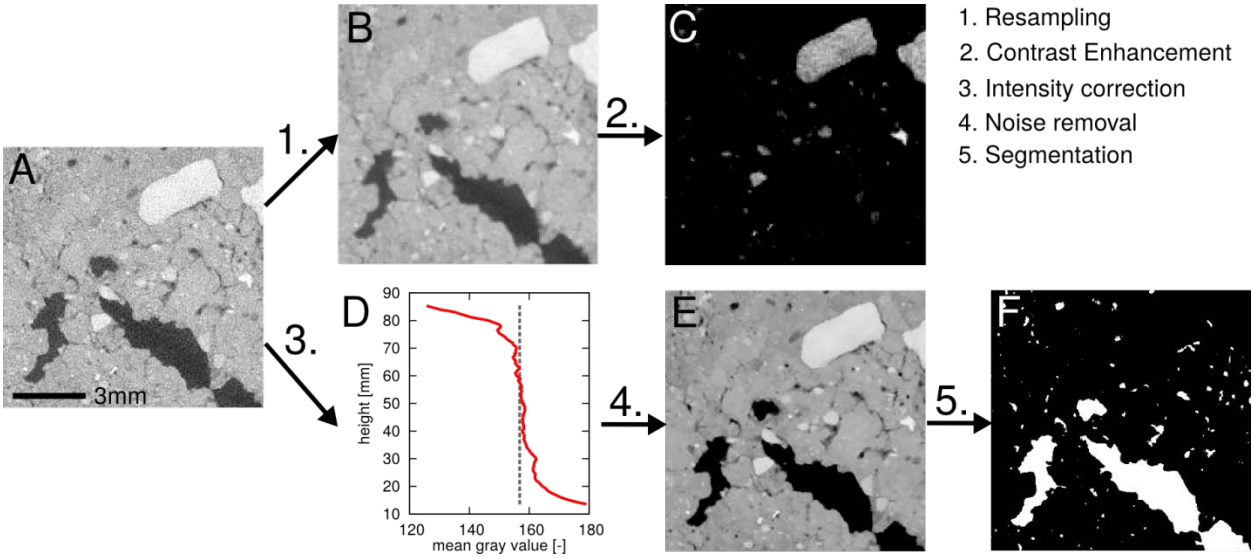

Figure 16: Image processing workflow for this study depicted for a small two-dimensional subset (a)**. Noise is removed with a non-local means filter** (b)**. Shading and cone beam artifacts evoke differences in image intensity which are corrected by subtracting the difference between the depth-dependent gray value average of the soil matrix from the mean gray value of the entire soil matrix** (c)**. Subsequently, image segmentation is performed with multi-level Otsu thresholding** (d)**. For digital image correlation all images are resampled from a voxel size of 61 to 183 µm to reduce memory consumption** (e)**. Optionally, the grayscale range is adapted such that rocks are depicted with optimal contrast and macropores vanish** (f)**.**

As a first step for the pore space analysis, noise in the raw images is removed with a non-local means filter implemented in ITK (image registration tool) (Buades et al., 2005; Tristán-Vega et al., 2012). This version of the non-local means filter requires two parameters: (1) the radius of the search window is set to four pixels and an estimate of the noise level expressed as a standard deviation of noise is set to 60; (2) vertical differences in average image intensity due to shading and cone beam artifacts are removed. To do so, the mean gray value of the soil matrix in a specific z-slice is measured and the difference to the mean gray value of the soil matrix in the entire image is subtracted from each voxel in that depth (Iassonov and Tuller, 2010). The two thresholds that separate the soil matrix from darker pore voxels and brighter rock voxels are chosen manually and do not affect the results much as long as they cover the entire grayscale range of soil without adding pores and rocks to the average. The main purpose of noise removal and intensity drift correction is to improve the robustness of automatic, histogram-based threshold detection methods. In this study the multi-level version of the popular Otsu method was used (Liao et al., 2001) to obtain the thresholds between four classes (pores, soil matrix, low density rocks and high density rocks), of which only the pore class is analyzed subsequently. Segmentation into pores and background was carried out with simple thresholding. The resulting pore space was analyzed towards two different directions. First, pore size distributions were calculated with the maximum inscribed sphere method using the BoneJ plugin (version 1.3.12) in Fiji (Doube et al., 2010). Second, depth profiles of porosity were computed in equidistant steps of 10 pixels to monitor the depth dependent changes of macroporosity caused by drying and compaction. All image processing steps except noise removal and pore size analysis were performed with the QuantIm image processing library (Schlüter et al., 2014; Vogel et al., 2010).

Digital image correlation is applied to the raw image with only little preprocessing. The images are resampled at a 3-times coarser resolution of 183 µm via simple averaging in order to reduce memory consumption. Optionally, the contrast is stretched such that macropores and soil are binned to zero and the rocks are displayed with optimal contrast so that only the rock matrix is used for subsequent image registration. The lower boundary under which all gray values are set to zero is chosen manually. Image registration was carried out with elastix[4] (Klein et al., 2010), an open-source image registration tool based on ITK (Ibanez et al., 2005) which was tailored for medical imaging applications. The image of the original soil structure was registered to the deformed soil in two steps. First, we applied a rigid registration that minimizes the sum of Euclidean distances between corresponding landmarks which we placed at four notches in the container wall. The mutual information criterion (Mattes et al., 2001) between images is added to the objective function as a second term with a low weighting factor because the manual selection of landmarks is typically afflicted with an imprecision of a few pixels. This rigid registration forces the cylindrical containers of both images to be well aligned. Then we applied elastic registration with a B-spline transform that optimizes the mutual information criterion to recover internal deformations. A regularization term, called bending energy penalty, was added to the objective function which ascertains that local transitions in deformation magnitude and direction are smooth (Klein et al., 2010). The success of image registration is evaluated via visual comparison of the target image and the aligned image. The outcome of an image registration process is a parameter file that stores the global transformation matrix (for rigid registration) or the transformation matrix of all grid nodes (for elastic registration). This parameter file is then applied to the input image in order to construct a new image that is perfectly aligned with the target image. This transformation matrix can also be applied to other images that were not used in the image registration process. This is essential since the image registration is optimized with auxiliary images which only contain rocks while the resulting transformation matrix is applied to the raw images that display the original soil structure. Two sample images and all parameter files to reproduce the entire workflow are available from the authors upon request.

Results

X-ray microtomography

The three-dimensional structure of the Köllme soil before centrifugation is depicted in Figure 14a. Rocks of different sizes are embedded in a loamy soil matrix and large macropores are present in all depths. After centrifugation down to a capillary pressure of $\psi = -100$ kPa the structure is markedly deteriorated (Figure 14b). The shape and position of macropores have changed, and desiccation cracks have formed in the vicinity of macropores. A perforated, rigid plate is visible, which was mounted at the bottom of the sample to prevent soil loss during centrifugation and transport. At a capillary pressure of $\psi = -500$ kPa the soil is severely compacted as can been seen by the larger head space above the soil surface (Figure 14c). Macropores are almost absent especially in the lower part of the sample and only a few desiccation cracks with vertical orientation remain in the upper part of the profile.

[4] http://elastix.isi.uu.nl/

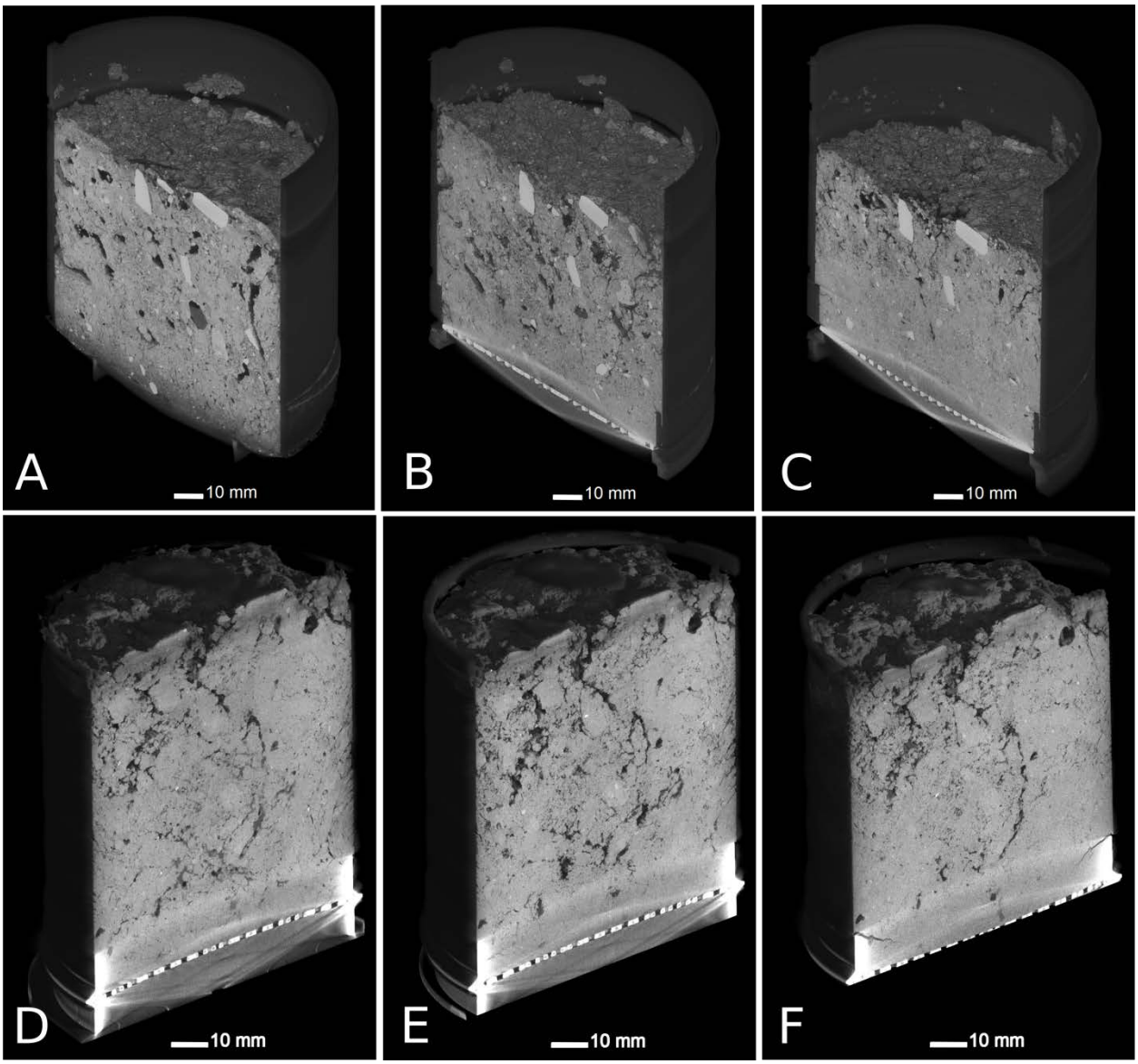

Figure 17: X-ray microtomography images of the soil structure in the Köllme soil (a) **at full water saturation (ψ=0 kPa) and** (b) **at ψ =−100 kPa and** (c) **at ψ =−500 kPa and in the Bad Lauchstädt soil** (d) **at full water saturation (ψ =0 kPa) and** (e) **at ψ =−50 kPa and** (f) **at ψ =−300 kPa.**

The low rock content of the Bad Lauchstädt soil is evident in Figure 14d–f. After centrifugation down to a capillary pressure of ψ=−50 kPa all macropores are intact and have even slightly increased in size due to shrinkage of clay minerals in the course of drying. At a capillary pressure of ψ=−300 kPa the original macropore network is still visible but some macropores are partially compressed.

These visual observations are confirmed by quantitative analysis of the pore space (Figure 15a). The total visible macroporosity (>61 µm) in the Köllme soil at full saturation is 6.6 %. At ψ=−100 kPa, macroporosity increased to slightly (8.1 %) due to crack formation. These new desiccation cracks due to soil drying mainly formed in that size range of 0.1–1 mm. Macropores >1 mm in diameter are less abundant in the soil at ψ=−100 kPa because larger macropores were partially compressed. The subsequent centrifugation to a capillary pressure of ψ=−500 kPa reduced visible macroporosity to 2.0 % and removed

porosity in all size ranges. A similar trend is evident in the Bad Lauchstädt soil (Figure 15b) though with lower magnitude. The visible porosity (>61 µm) at full saturation (9.4%) increases slightly when centrifuged to ψ=−50 kPa and decreases to 7.6% at a capillary pressure of ψ=−300 kPa. The changes in the pore size distribution are smaller in the Bad Lauchstädt soil due to less negative capillary pressures and a lower abundance of big macropores > 1 mm in diameter which are most easily compressed.

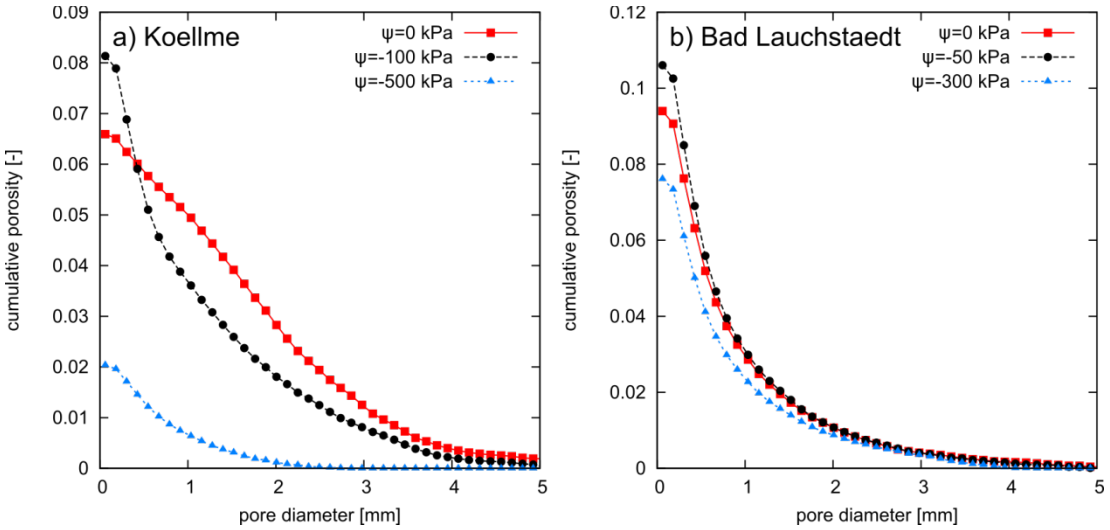

Figure 18: Cumulative pore size distribution (> 61 µm) in the Köllme soil (a) **and the Bad Lauchstädt soil** (b) **at three different capillary pressures. Values are derived with the maximum inscribed sphere method and correspond to porosity larger than a specific pore diameter.**

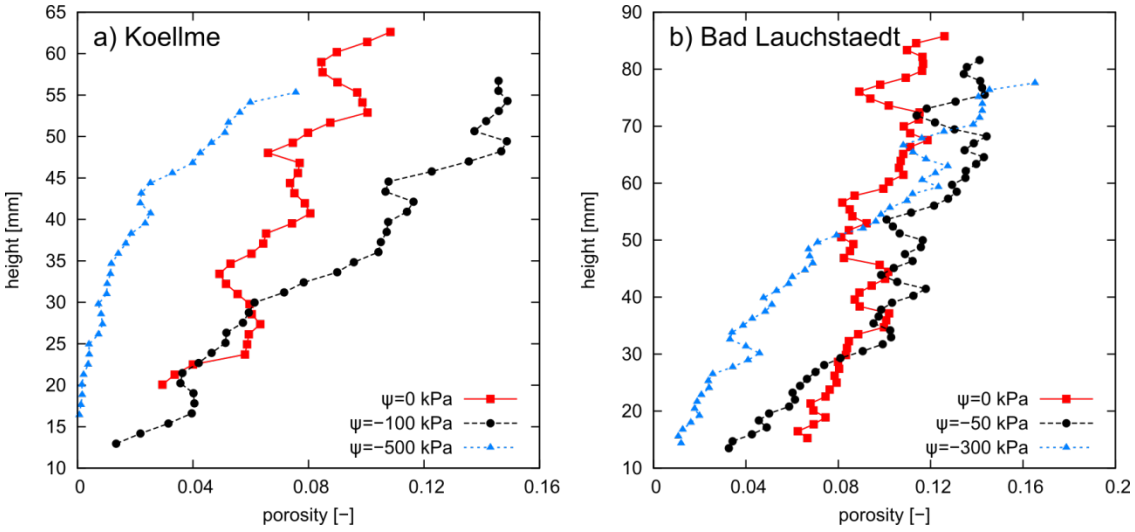

Figure 19: Depth profile of macroporosity (> 61 µm) at three different capillary pressures in the Köllme soil (a) **and Bad Lauchstädt soil** (b)**. All images cover slightly different field of views and are normalized to a reference height at the bottom of the sample.**

The change in porosity through centrifugation is not evenly distributed across the sample (Figure 16a). In the Köllme soil desiccation cracks at ψ=−100 kPa mainly formed in the top part of the sample, whereas the bottom part of the sample exhibits lower porosity than the reference sample due to compaction. The sample in its driest state is compacted across the entire profile. The decline in macroporosity increases with depth. A specific rock close to the soil surface served as a cut-off height for the profile. Its position

changed from 68 to 58 mm and to 55 mm, respectively. In the Bad Lauchstädt soil (Figure 16b) the same trends apply though at different magnitude. At ψ=−50 kPa macroporosity increases in the top part of the sample due to drying, whereas the bottom exhibits slightly smaller macroporosity due to compression. Further drying down to ψ=−300 kPa reduces macroporosity in all depths. The height of the sample as measured by the position of a reference rock decreases from 85 to 81 mm for ψ=−50 kPa, followed by 77 mm for ψ=−300 kPa.

Deformation

Rocks are especially suited to track internal deformations as they change in position, but not in shape. The poor spatial alignment of rocks between the saturated (green) and the centrifuged soil at a capillary pressure of ψ=−500 kPa (red) after the Euler transform is depicted in Figure 17(a) (results for deformation at ψ=−100 kPa not shown). Elastic registration with a B-spline transform leads to a very good spatial alignment of rocks in all soil depths (Figure 17b). In both images (original and deformed soil) the contrast had been optimized for rocks prior to image registration. Figure 17(c) shows the registration results for the resampled raw images. That is, the full grayscale range including soil matrix and macropores is used for digital volume correlation and the contrast is optimized for rocks only afterwards for visualization. This results in a less accurate spatial alignment of the rock matrix especially in the lower part of the sample where deformation is strongest and macropores are compressed. Even though the rock content in the Bad Lauchstädt soil is very low (0.2 %), it is sufficient to achieve a good spatial alignment when only the rock matrix is used for image registration (Figure 17e). Results are shown for the most compacted state only (ψ=−300 kPa). The spatial alignment of the rock matrix works comparably well, if the entire grayscale range including soil and macropores is used for image registration (Figure 17f). Hence, taking the spatial alignment of macropores also into account does not impair the spatial alignment of the rock matrix, as most of the macropores persist during the centrifugation process. A general advice whether to use the whole grayscale range or not will be discussed below.

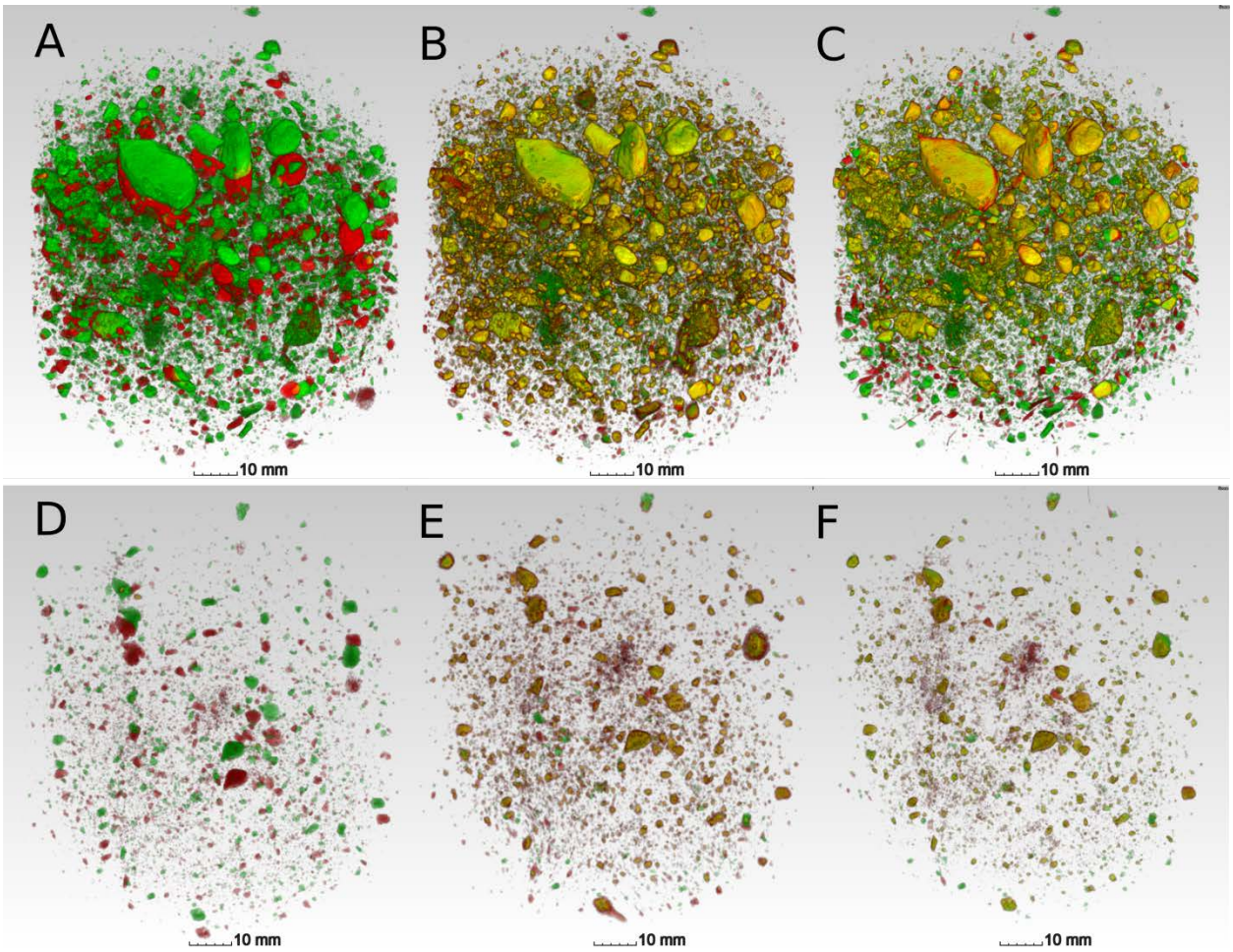

Figure 20: The spatial alignment of rocks between the saturated soil (green) and the soil at ψ=−500 kPa (red) before (a) **and after** (b) **elastic registration image registration of the rock matrix in the Köllme soil. Note that the co-occurrence of rocks results in a composite, yellowish color. The spatial alignment of rocks is less accurate in the bottom of the sample, when the entire grayscale range is used for image registration** (c)**. Same is shown for the Bad Lauchstädt soil** (d–f)**. There, both strategies, with and without contrast enhancement for rocks, lead to equally good spatial alignment of the rock matrix.**

An important result of the registration procedure is the displacement vector field. There is a clear trend towards a downward movement of soil constituents in the Köllme soil as a consequence of compaction and its magnitude increases from ψ=−100 kPa to ψ=−500 kPa (Figure 18a–b). However, the direction and length of local displacement does not only vary with depth but also laterally. Furthermore, there is a substantial horizontal component of displacement in many locations. This lateral movement can have two different origins. First, the formation of mainly vertically aligned cracks displaces the soil normally into the crack but not along it. Secondly, regions of high macroporosity are preferential failure zones during compaction. Filling these macropores during compression with soil material from above evokes a lateral displacement component because they are not evenly distributed across the soil. The Bad Lauchstädt soil at ψ=−50 kPa exhibits a rather uniform downward displacement of soil constituents of about 3–5 mm (Figure 18c) that is in line with the reduction of sample height shown in Figure 16. A pressure of ψ=−300 kPa evokes lateral differences in downward displacement again (Figure 18d), as already discussed for the Köllme soil.

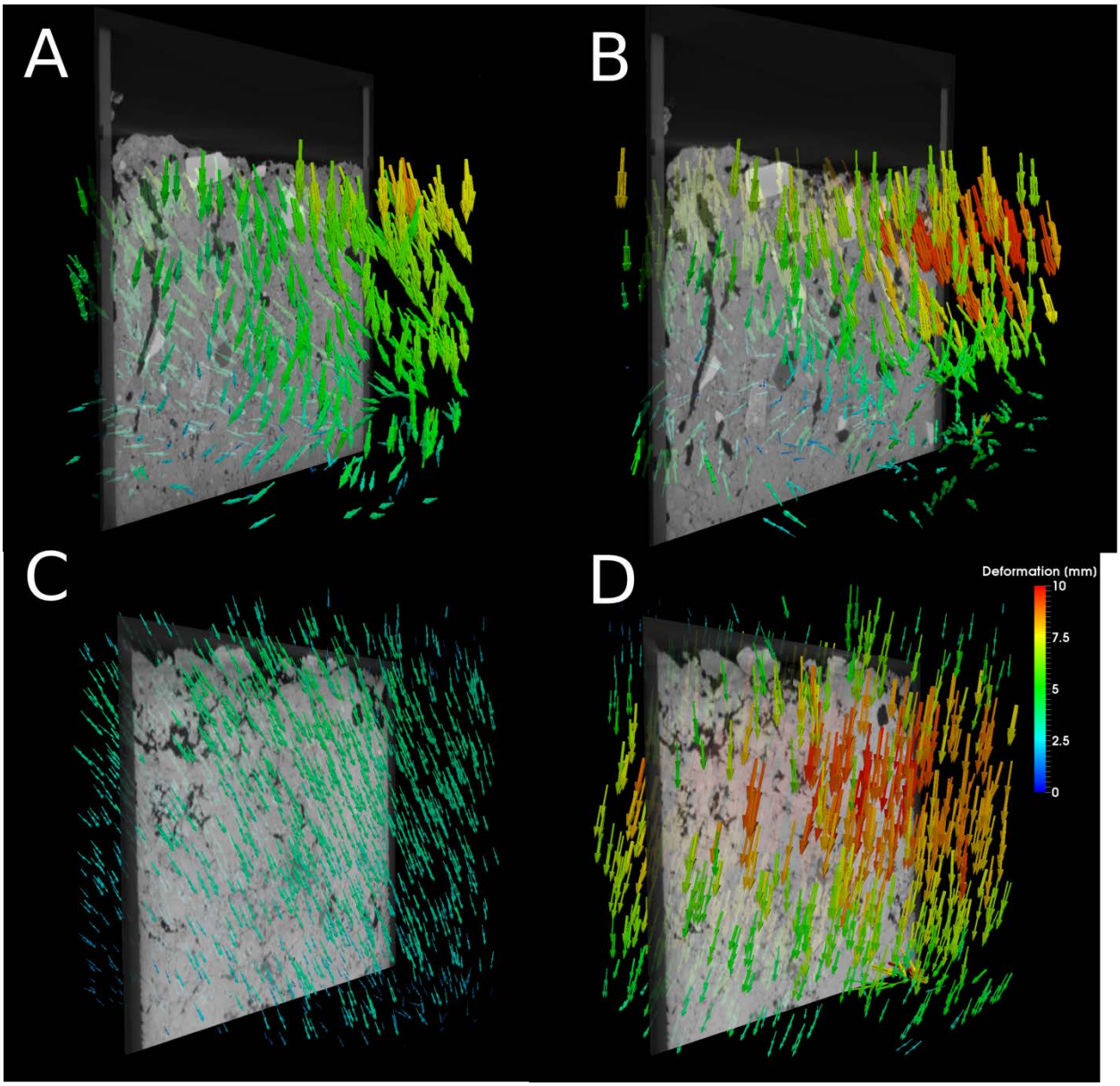

Figure 21: Displacement vector field for the Köllme soil for the deformation (a) **from ψ=0 kPa to ψ=−100 kPa and** (b) **from ψ=0 kPa to ψ=−500 kPa. Only a small percentage of all vectors is displayed to improve visibility. The vector length corresponds to the physical displacement. The two-dimensional section of the undisturbed soil is for orientation. Same is shown for the Bad Lauchstädt soil for the deformation** (a) **from ψ=0 kPa to ψ=−50 kPa and** (b) **from ψ=0 kPa to ψ=−300 kPa.**

Discussion

Pore scale processes during centrifugation

The analysis of macroporosity at 61 µm resolution revealed substantial alterations of the pore space architecture during centrifugation. Without such a detailed X-ray microtomography analysis the only measurable, macroscopic changes in soil structure would have been an increase in bulk density and a decrease in sample height. The conventional, quantitative image analysis of the pore space revealed a depth-dependent increase or decrease of macroporosity that resulted from the interplay of soil shrinkage due to drying and soil compaction due to compression. The reduction of macroporosity due to compaction

was most severe in the lower part of the samples. Evidently this is because the inertial force that acts on the soil in a given depth, i.e., $F_z = m\omega^2 r$, increases both with increasing overburden m and increasing absolute acceleration (due to $r_o > r_i$) (McCartney, 2007). This was corroborated by displacement vector fields obtained from digital volume correlation which showed an increase of vertical displacement with sample height. Evidently, this is due to the fact that the local displacement integrates over the distance to the lower boundary.

The deformation of the soil due to shrinkage is immanent in any drying process in presence of swelling clay minerals and capillary forces that pull unconsolidated grains closer together (Or and Ghezzehei, 2002; Stange and Horn, 2005). So it would have also occurred if drying is induced by another process, e.g., by evaporation. The compaction of the soil through centrifugal forces, however, is obviously caused by the centrifugation process and represents a severe drawback of the method. A significant breakdown of structure through centrifugation was previously reported for an equivalent capillary pressure of ψ=−100 kPa (Wedler and Boguslawski, 1965) using a loess soil with a texture (5 % sand, 77 % silt, 18 % clay) comparable to the Bad Lauchstädt soil. The deformation field analysis of the Bad Lauchstädt soil confirmed that at a capillary pressure of ψ=−50 kPa, the soil structure is still intact with fairly uniform downward displacement of all soil constituents by a few mm, whereas centrifugation at ψ=−300 kPa caused stronger lateral heterogeneity in deformation caused by the compression of heterogeneously distributed macropores. Though this critical threshold certainly depends on soil texture and bulk density it also compares well with the critical value found for the Köllme soil. In the deformation field at ψ=−100 kPa lateral heterogeneity in local displacement already emerged but is only fully developed at ψ=−500 kPa. Studies with repacked clay of low plasticity in centrifuge samples of comparable dimensions (71 mm diameter, 127 mm height) only showed marginal settlement of the sample (< 1 mm) in a suction range down to ψ≈−50 kPa due to the absence of natural macropores (McCartney, 2007; McCartney and Zornberg, 2010). It is clear that the susceptibility to compaction during centrifugation, just like the stress–strain relationship of any soil heavily depends on the pore size distribution and the stress history of the sample (Horn and Baumgartl, 2002; Or and Ghezzehei, 2002).

The question is, how this structure deformation changes the measured water retention curve. Presumably, those macropores with the lowest mechanical stability are also the pores that drain first. That is, they have released their water before they got deformed. Comparisons between water retention curves obtained with different laboratory methods for various soils with different initial compaction states indicate that centrifugation often results in higher water content for a given suction than a pressure chamber or hanging water column test (Khanzode et al., 2002; McCartney, 2007; McCartney and Zornberg, 2010; Wedler and Boguslawski, 1965). The interpretation whether the offset is still tolerable differs among these authors. The offset emerges because soil compaction leads to a general shift of the pore size distribution, during which the absolute abundance of smaller pores grows on the expense of bigger pores (Assouline, 2006; Leij et al., 2002). However, these pores cannot be captured with X-ray microtomography. An appropriate discussion of this effect is therefore beyond the scope of this paper.

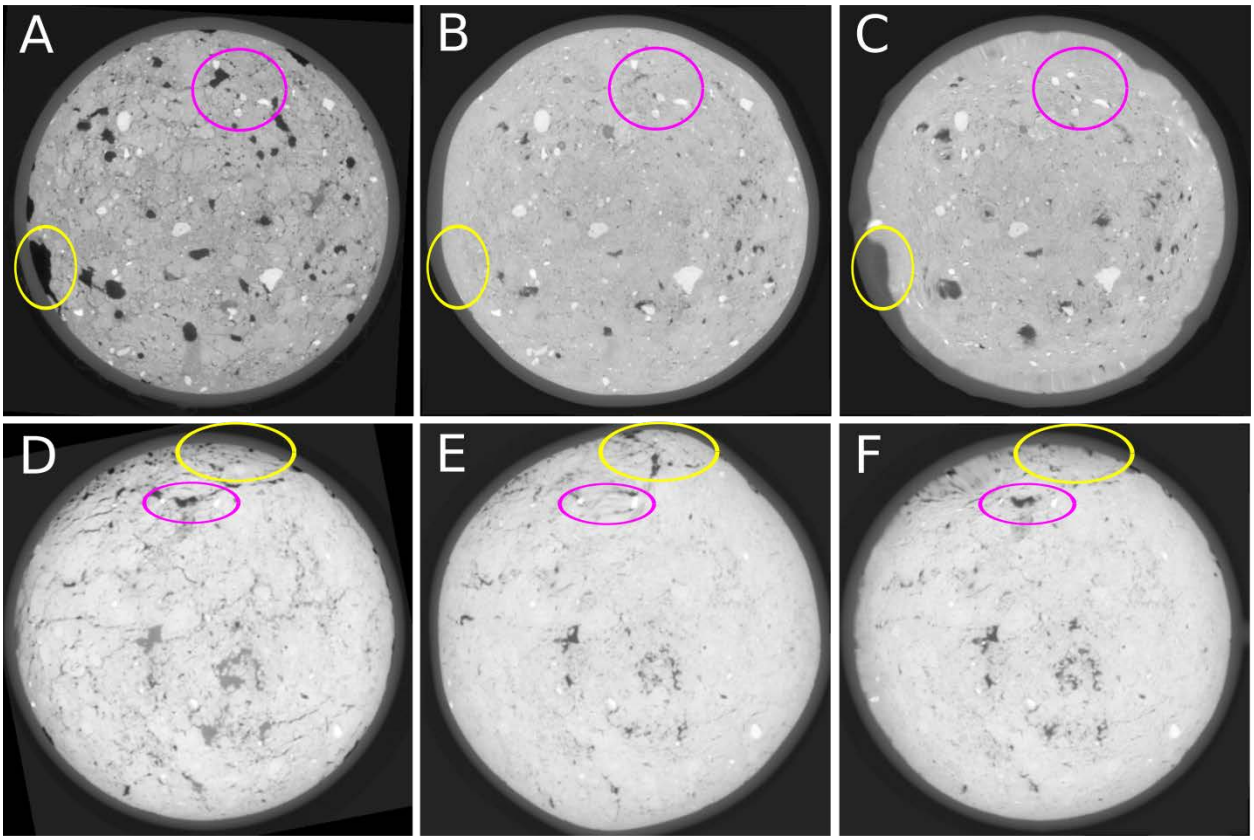

Figure 22: Comparison between registration results using the entire gray scale range or the rock matrix only: Representative slice of the Köllme soil close to saturation (a)**. The B-spline transformation matrix of the rock matrix in the Köllme soil at ψ=−500 kPa is applied to the corresponding grayscale image** (b)**. B-spline transform of the original Köllme soil at ψ=−500 kPa** (c)**. Same comparison for the Bad Lauchstädt soil close to saturation** (d) **and at ψ=−500 kPa** (e, f)**. Pink and yellow frame highlight salient features.**

As general advice, centrifugation should not be used to measure water retention curves down to very low pressure ranges if the sample is prone to soil compaction. For practical purposes the reduction in sample height can be used as a suitable indicator to identify the critical pressure beyond which deformation has to be expected. If this method still has to be applied beyond this critical point, it should be performed at the end of all envisaged hydraulic or thermal experiments, as it causes irreversible damages to the internal soil structure.

Methodological limitations

We have developed a workflow for the automatic detection of soil structure deformation by means of free image registration software and outlined best practices in order to optimize the registration results. By imposing a pyramid schedule the image registration of resampled images with roughly 400^3 voxels took approximately 1 min for the Euler transform and 150 min for the B-spline transform on a Linux work station (32 GB RAM, 12 cores with 1.2 GHz). A maximum number of iterations on each pyramid scale is the conventional stopping criterion of the program (in the range of 100–5000), which could have easily been reduced to save time, as the improvement in the last iterations is usually small. We resampled the images from 61 to 183 µm in order to reduce memory use which can reach up to 10 times the image size, depending on data type of both working copies in memory (float vs. short), interpolation type, number of pyramid scales and other internal settings of elastix. As a consequence of resampling, registration cannot

be more accurate than the resolution of the final pyramid (183 µm in this case), which is still sufficient as the local deformations in our samples where in the mm range.

The benefits of focusing on the rock matrix during image registration was shown in Figure 17. Rocks change position and orientation, but in contrast to macropores they do not change their shape. Therefore, they are more easily recovered by the B-spline transform. Taking macropores into account during image registration impaired the spatial alignment of rocks in the lower part of the Köllme soil, because many macropores disappeared completely in that depth which caused wrong feature alignment. This is corroborated by comparing the registration results for the full grayscale range in a representative slice (Figure 19a–c). Figure 19(b) is the result of applying the transformation matrix that was obtained from a B-spline transform of the rock matrix to the original grayscale image, whereas Figure 19(c) was obtained by computing a B-spline transform with the original grayscale image directly. The pink frame highlights the perfect alignment of a set of rocks if only the rock matrix is considered for image registration, while the position of some rocks was not fully recovered without contrast adjustment. The yellow frame highlights that the disappearance of a macropore at the boundary produces a distortion of the core wall into the soil. This flaw is avoided by focusing on the rock matrix only. A critical question is the following: what is the minimum amount of rock content to guarantee a good recovery of the deformation field? In spite of a very low rock content (0.2 %) in the Bad Lauchstädt soil, the spatial alignment of the rock matrix was satisfactory both with and without contrast adjustment for rocks. This is supported by comparing the registration results in a representative slice (Figure 19d–f). The position of rocks, e.g., in the pink frame and elsewhere, is correct. In this case taking the full grayscale range into account even improves the spatial alignment of salient features like the macropore in the pink frame. Moreover, the yellow frame highlights poor spatial alignment of the core wall after contrast adjustment because there are no rocks in the vicinity to constrain the registration result. Therefore, focusing on the rock matrix is in fact not advisable for this particular soil.

In summary, a general lack of rocks or other salient, rigid features may render elastic registration useless depending on the severity of deformation. Only additional landmarks can help to improve the registration result in that case. In turn, if the focus is not on natural soil, but on repacked substrates, then the addition of easily trackable features like rocks or metal particles is an easy way to improve the accurate detection of internal deformation.

Conclusions

Measuring the water release through soil centrifugation is a fast method to obtain soil water retention curves. Using X-ray microtomography we have corroborated previous findings that the soil structure starts to deteriorate at a capillary pressure of about ψ=−100 kPa. Moreover, quantitative analysis of the pore space at 61 µm resolution revealed that the soil deformation is caused by the interplay of shrinkage and compaction. Local deformation was detected by a novel workflow for digital volume correlation based on elastic image registration. This method enables a detailed look at local soil deformation and its spatial variability. We applied this method to the measure changes in soil structure during centrifugation; however, this method has the potential to quantify the detailed mechanical deformation of soil and other materials exposed to any other type of external forcing.

Acknowledgments

This research was supported by the German Federal Ministry of Food and Agriculture (BMEL), award T343D123. We thank two anonymous reviewers for helpful comments that helped to improve them anuscript considerably. The article processing charges for this open-access publication were covered by a Research Centre of the Helmholtz Association.

2.3. Analysis of Soil Structure Turnover with Garnet Particles and X-Ray Microtomography (Schlüter & Vogel 2016. PLoS ONE, 11(7), e0159948, doi: 10.1371/journal.pone.0159948)

Abstract

Matter turnover in soil is tightly linked to soil structure which governs the heterogeneous distribution of habitats, reaction sites and pathways in soil. Thereby, the temporal dynamics of soil structure alteration is deemed to be important for essential ecosystem functions of soil but very little is known about it. A major reason for this knowledge gap is the lack of methods to study soil structure turnover directly at microscopic scales. Here we devise a conceptual approach and an image processing workflow to study soil structure turnover by labeling some initial state of soil structure with small garnet particles and tracking their fate with X-ray microtomography. The particles adhere to aggregate boundaries at the beginning of the experiment but gradually change their position relative to the nearest pore as structure formation progresses and pores are destructed or newly formed. A new metric based on the contact distances between particles and pores is proposed that allows for a direct quantification of soil structure turnover rates. The methodology is tested for a case study about soil compaction of a silty loam soil during stepwise increase of bulk density (ρ = [1.1, 1.3, 1.5] g/cm3). We demonstrate that the analysis of mean contact distances provides genuinely new insights about changing diffusion pathways that cannot be inferred neither from conventional pore space attributes (porosity, mean pore size, pore connectivity) nor from deformation analysis with digital image correlation. This structure labeling approach to quantify soil structure turnover provides a direct analogy to stable isotope labeling for the analysis of matter turnover and can be readily combined with each other.

Introduction

Soil structure provides the pathways for matter fluxes, entails a high diversity of microhabitats and causes a heterogeneous distribution of reaction sites in soil. Through these regulatory traits it acts as a major driver for important soil functions like stabilization of soil organic matter, maintenance of biodiversity or water and nutrient cycling (Bronick and Lal, 2005; Schmidt et al., 2011). Soil structure is not static, but continuously evolving through abiotic (e.g. tillage, moisture changes) and biotic agents (e.g. bioturbation, root growth) (Six et al., 2004). These soil structure dynamics are also sometimes referred as aggregate turnover, i.e. the continuous formation and destruction of aggregates especially in soils under agricultural use (Plante and McGill, 2002; Six et al., 1998).

Aggregate turnover rates are hard to quantify directly. However, the lifetime of organic matter (OM) in aggregates is strongly correlated with turnover of aggregates themselves (von Lützow et al., 2006). Therefore stable isotope methods are frequently applied to study soil structure dynamics indirectly.
Labeled organic matter enriched in 13C or 15N (Angers et al., 1997; McMahon et al., 2005; Moran et al., 2005) or a change in cultivation from C3 to C4 plants with natural differences in C isotope ratios (Puget et al., 2000; Six et al., 1998) are used to study the fate of OM in soil (for comprehensive reviews see (Amelung et al., 2008; Bernoux et al., 1998; Six et al., 2004)). After a certain incubation time the soil is discerned into different aggregate size classes through wet sieving and OM turnover rates are derived from the proportion of labeled OM in each aggregate size class. This approach to linking OM turnover to structure turnover is often motivated by the aggregate hierarchy concept first proposed by Tisdall and Oades (1982). In this conceptual framework, soil structure is organized in different levels ranging from organo-mineral complexes, to microaggregates (<250μm) and macroaggregates (> 250μm). The predominant binding agents at each level differ in lifetime from very stable to transient. Macroaggregates are deemed to be formed and destructed relatively fast, whereas microaggregates are formed slowly within macroaggregates and are the main driver for OM stabilization in soil. An indirect inference about structure turnover from fractions of labeled OM in different aggregate size pools can be made under the assumption that macroaggregate formation and microaggregate formation rates are the ultimate cause for

the observed fractionation of labeled OM. However, the validity of this aggregate hierarchy concept and therewith the congruency of OM turnover and aggregate turnover seems to be limited to soils rich in clay and silt and rather high OM concentrations (Christensen, 2001). Moreover, labeled OM might be stabilized by other mechanisms than physical protection in microaggregates, such as inherent recalcitrance, association with minerals, or a shortage in readily available organic compounds required as an energy source for microbial decomposition of labeled OM (Kuzyakov et al., 2000; Mikutta et al., 2006).

A similar approach to estimation of aggregate turnover rates is provided by studying the fate of microparticles, e.g. ceramic dysprosium oxide tracer spheres (d: 0.4 mm) that can be detected through neutron emission (Plante and McGill, 2002). These spheres were added to a field soil with a rototiller and from their recovery in different aggregate size classes after wet sieving a macroaggregation rate was derived. This derivation of aggregate turnover rates from aggregate stability during wet sieving has obvious flaws. Aggregation or more precisely the disintegration of aggregates strongly depends on the energy input and forces that act on them during wet sieving (Beare and Bruce, 1993). Comparability among different studies therefore requires highly standardized laboratory protocols. It does, however, not imply the existence of clearly separable aggregates within undisturbed soil (Young et al., 2001). Instead, soil structure manifests itself through a complex network of pores at all scales and their heterogeneous distribution in space evokes preferential failure zones during mechanical disturbance. This complex patterns of pores ultimately governs the distribution of water, nutrient supply and oxygen levels and should therefore be studied in its original context. In summary, indirect methods to quantify structure turnover rates are flawed because measures based on OM turnover and aggregate stability are not necessarily correlated with the formation and destruction of pores at microscopic scales.

Imaging techniques like X-ray microtomography (µCT) provide a detailed view into the physical structure of undisturbed soil at a spatial resolution of a few microns. The three-dimensional images do not only enable a visual inspection of the internal structure of opaque soil but are also amenable to quantitative image analysis. The spatial attributes which can be derived from µCT images are numerous and range from pore size distribution and pore connectivity (Vogel et al., 2010), to spatial correlation of pores (Nunan et al., 2006) and distances between pores and occluded particulate OM (Kravchenko et al., 2014; Negassa et al., 2015), just to name a few. Repeated sampling of field soils during a growing season facilitates the detection of statistical changes in pore space attributes, e.g. during a growing season (Jégou et al., 2002; Schlüter et al., 2011). Incubation experiments in the laboratory allow for a more detailed look on soil structure dynamics, since the same samples can be scanned repeatedly under controlled conditions (Crawford et al., 2012; Feeney et al., 2006; Helliwell et al., 2014). This allows for a direct analysis of changing of pore size distributions or pore connectivities as a function of different C input, microbial activity and so on. Yet, this is still a statistical evaluation of pore space changes and therefore only provides indirect clues on aggregate turnover. A rather new method to directly study the movement of soil constituents during soil structure development is called digital image correlation (or digital volume correlation) (Hall, 2010; Peth et al., 2010; Schlüter et al., 2016). The rationale of this method to recover the deformation field in soil by image registration. That is, the image of a deformed soil is aligned to an image of the original soil and the transformation matrix that resulted in an optimal spatial alignment is used to calculate the deformation field. This yields detailed patterns of how much soil has been displaced how far in which direction. Digital image correlation and related methods like particle image velocimetry have mainly been used to study soil deformation through mechanical stresses and its great potential to investigate aggregate turnover is not yet explored. One major hurdle for a direct assessment of aggregate turnover is that the displacement of soil constituents need to be studied in its spatial context. For instance, organic matter on an aggregate surfaces with direct contact to a macropore may end up in the center of a newly formed aggregate, if the macropore is closed due to compression, even though the active displacement of this organic matter may have been negligible. Likewise, crack formation due to drying

may expose formerly occluded organic matter and create a completely new microenvironment in spite of its constant position in space.

In this paper we present a new image processing protocol that allows for a direct quantification of aggregate turnover by tracking strategically positioned microparticles. Since these garnet particles contain iron oxide with high X-ray attenuation, they can be easily detected in spite of their small diameter of a few voxels (d: 0.045 - 0.1mm). Beds of aggregates are prepared from sieved aggregates covered with microparticles. In this way, the position of garnet particles marks the delineation of initial macroaggregates. In this study, soil structure changes are induced by controlled soil compaction. The position of individual particles is evaluated with respect to distances to the nearest pore. These new metrics are underpinned with conventional pore space attributes and metrics derived from digital image correlation to provide a sound picture of soil structure changes at a spatial scale of a few microns. Finally, the findings for structure dynamics during compaction are used to conceptualize an approach to quantify soil structure turnover rates.

Materials and Methods

Soil was collected from the upper 5 cm of a Haplic Chernozem (WRB classification) developed from loess and managed as bare fallow at the Experimental station (51.3943N, 11.8777E) of the Helmholtz-Centre for Environmental Research—UFZ in Bad Lauchstädt, Germany. The owner of the land gave permission to conduct the study on this site. Soil texture was composed of 11% sand, 68% silt and 21% clay (Sedimat 4–12, UGT GmbH, Müncheberg, Germany). The organic carbon and total nitrogen content of the soil were C_{org} = 2.05% and N_{t} = 0.19%, respectively (Elementar Analysator Vario EL cube, Elemantar Analysensysteme GmbH, Hanau Germany). The fresh soil was sieved under moist conditions close to field capacity. Aggregates in the size range of 0.5–2 mm were collected and stored in the fridge at 4°C.Weeks later the aggregates were carefully moistened by putting them on a moist paper towel for 30 min, so that the gravimetric water content in the aggregates adapted to 10.5±1.3%. Subsequently, the aggregates were fully covered with garnet fine sand (Garnit #240, Kuhmichel Abrasiv GmbH, Ballenstedt, Germany) with a grain size of 45–100 µm. This garnet fine sand, from here on denoted as particles, consists of the mineral Almandine, which is composed of 33% FE_2O_3. This iron content leads to a better contrast against the surrounding soil than conventional quartz sand (Ketcham and Carlson, 2001), but does not lead to a drastic attenuation of X-ray photons like similar sized particles of metallic iron so that shading artifacts are avoided. The aggregates were gently shaken on a 0.2 mm sieve for 1 min to remove excess particles. 5 g of these moist aggregates were filled into 5 ml plastic syringes with an inner diameter of 12.5 mm (5 replicates). Occasionally some coarse garnet grains (Garnit #12-20, Kuhmichel Abrasiv GmbH, Ballenstedt, Germany) with a grain size of 0.5–1.2 mm were added to the aggregate packing. These coarse garnet grains, from here on denoted as grains, are easily detected in the CT images and serve as additional position markers for subsequent image analysis. The dry weight of this packing of moist aggregates was determined from equally prepared samples (3 replicates) after oven drying at 105°C for 24 h. Bulk density was then adjusted in steps (1.1 g/cm³, 1.3 g/cm³, 1.5 g/cm³) by compressing the soil with the piston of the syringe to a specific volume. This uni-axial, static compression is likely to cause qualitatively different compaction than elastic soil displacement through dynamic loading during wheel traffic. Nevertheless it fulfills the purpose to evoke some easily reproducible changes to the soil structure on which our new conceptual approach can be tested.
After each compression step the samples were scanned with X-ray microtomography (X-TEk XCT 225, Nikon Metrology). The energy settings (80 keV, 120 µA, no filter) resulted in good contrast without overexposure at the lateral margins of the detector panel. An entire scan comprised 2300 projections with an exposure time of 1 s (one frame per projection). The syringes were scanned in two-heights to cover 60% of the total height of the uncompressed aggregate packing. The reconstruction of three-dimensional

images via filtered back projection was done with the CT Pro 3D software package (version 3.1) at a spatial resolution of 8µm and 8-bit gray scale resolution.

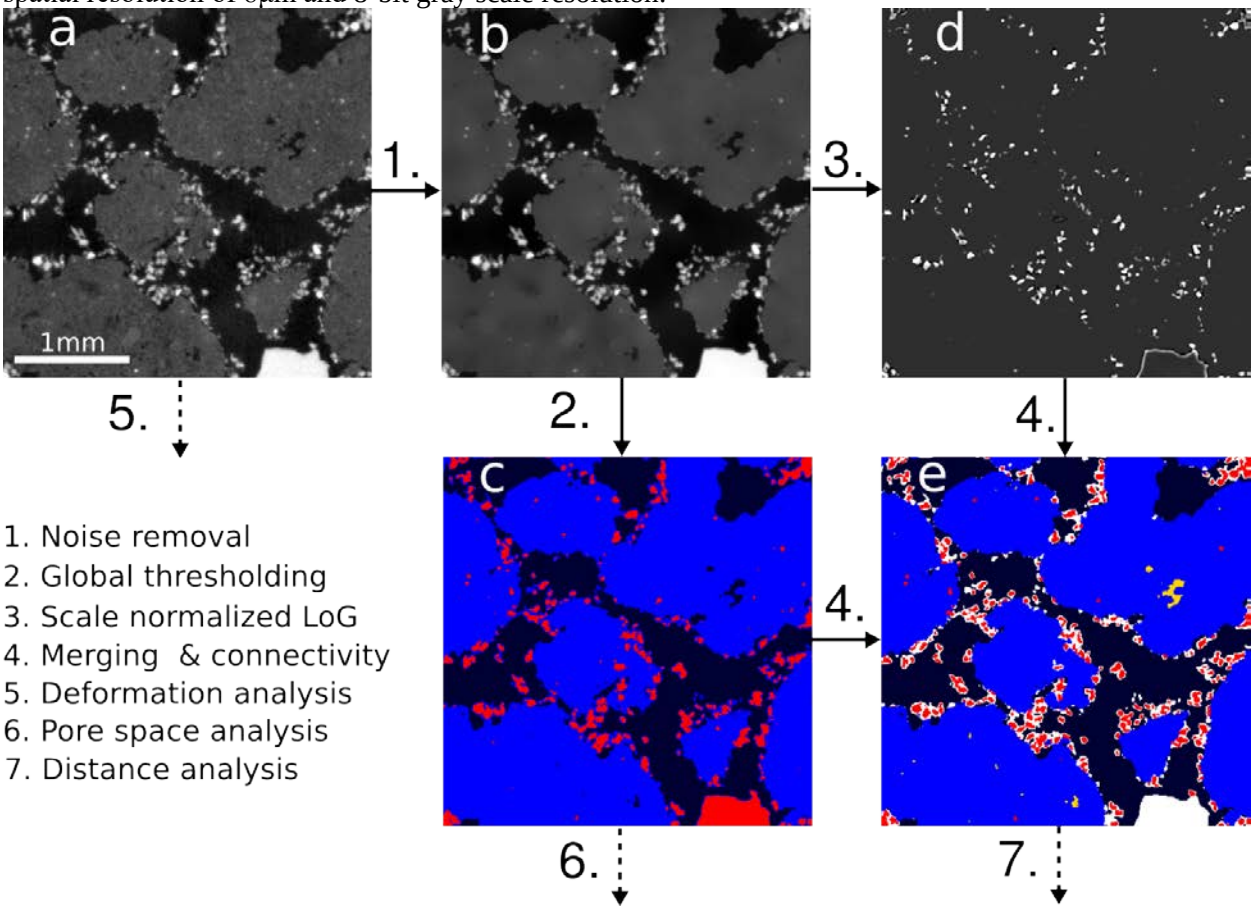

Figure 23: Image processing workflow for this study depicted for a small two-dimensional subset (a). Noise is removed with a non-local means filter (b). Image segmentation is performed in several steps. First, gray values are tentatively segmented into pores (black), aggregates (blue) and garnet (red) via simple thresholding (c). Then particles are detected with a Laplacian of Gaussian Filter (LoG) (c) and subsequent hysteresis thresholding of the LoG Image. Note that the edges of large grains are masked out during particle detection (not shown). For the final segmentation (e) partial volume voxels tentatively assigned to the aggregate class are set to unassigned (white) with a morphological opening of the aggregate class by a small structuring element (d_{SE} = 5 voxels). The tentative garnet class is set to unassigned (white) and overwritten by the thresholded LoG image (red). Pores are further differentiated with respect to whether they are fully enclosed in soil aggregates (yellow) or not (black) (f). These images are subjected to different types of analysis (5.-7.).

The raw images are subjected to an image processing workflow that was especially tailored for this study (Figure 20). The entire workflow is described in detail in the supporting information 6.1 (**S1**) by means of the small subset within the yellow frame in Figure 20(a) and only briefly summarized in the following. Noise in the raw images was removed with a non-local means denoising filter (Figure 20b) (Buades et al., 2005). Thresholds for three classes are detected automatically according to Schlüter et al. (2014). Global thresholding leads to a tentative segmentation into pores (black), aggregates (blue) and garnet (red) (Figure 20c). Partial volume effects due to limited image resolution cause false aggregate voxels around particles. These thin films of aggregate voxels around particles are removed by a combination of erosion, removal of small objects and dilation. The identification of particles is improved with a Laplacian of Gaussian (LoG) filter (Gonzalez and Woods, 2002) for blob detection (Figure 20d). The garnet particles are segmented with hysteresis thresholding of the scale normalized LoG result (Schlüter et al., 2014; Schlüter et al., 2010). The combination of blob detection and partial volume voxel treatment leads to an improved segmentation result (Figure 20e). The tentative pore class is labeled differently depending on

whether pores are fully enclosed by aggregates (yellow) or connected to the interaggregate pore space (black). All removed aggregate and garnet voxels are gathered in an unassigned class (white). Quantitative analysis of the CT images is directed towards different ends (step 5.-7. in Figure 20):

• The deformation analysis via digital volume correlation is performed on the raw images. The workflow for digital image correlation is described in (Schlüter et al., 2016) and implemented in elastix(Klein et al., 2010). As preprocessing steps the image dimensions are rescaled by a factor of four in each direction to reduce computational costs and the grayscale is rescaled such that all pores and aggregates are black and garnet grains are depicted with optimal contrast. It has been shown previously that this improves the image registration of the deformed grain matrix onto the original grain matrix (Schlüter et al., 2016).

• The pore space analysis is done for both the interaggregate pore space and isolated pores together. Depth-dependent changes in pore volume are detected with porosity profiles, i.e. the area fraction of pores in each xy-plane. Pore size distributions are computed with the maximum inscribed sphere method as implemented in the BoneJ plugin for ImageJ (Doube et al., 2010). Pore connectivity Γ is computed from the size distribution of individual pore clusters (Renard and Allard, 2013):

$$\Gamma = \frac{1}{N_v^2} \sum_{i=1}^{N_c} n_i^2 \qquad (19)$$

where N_v is the number of pore voxels, N_c is the number of individual pore clusters and n_i is the number of voxels in cluster i. This second moment of the cluster size distribution equals one if all pores are connected in one percolating cluster and converges to zero if porosity is fragmented into many clusters of similar size.

• Distance analysis: A Euclidean distance transform as implemented in the 3D Image suite for ImageJ (Ollion et al., 2013) determines the minimum distance of each voxel (including aggregates, garnet and occluded pores) to the interaggregate pore space. This is also referred to as the contact distribution (Ohser and Mücklich, 2000). The average of this contact distribution is an estimate for the mean diffusion lengths of air into the soil matrix assuming that small unresolved pores remain water-filled. On top of that the Euclidean distances between garnet particles and air-filled pores can be determined and compared to that of any point within the soil matrix.

Results

Porosity changes due to compaction

The changes in soil structure due to compaction are depicted in (Figure 21). The uncompacted soil at a bulk density of ρ = 1.1 g/cm³ exhibits a loose aggregate packing. The coverage of aggregates with garnet particles is not perfectly homogeneous (Figure 21a, green circles). Some aggregates, probably wetter than others during sieving, are covered with a thick layer of particles (green #1), while other aggregates are only sparsely covered with particles (green #2). Upon drying and/or unintentional shaking some particles detach from the aggregates and gather at pore constrictions (green #3). Bigger garnet grains are randomly distributed across the sample. This grain matrix will be the basis for subsequent deformation analysis. The different X-ray adsorption of garnet (yellow #1) and grains of iron-free minerals like quartz (yellow #2) is clearly visible. The piston of the syringe enters the field of view from above during uni-axial compression of the soil to a bulk density of ρ = 1.3 g/cm³ and ρ = 1.5 g/cm³ (Fig 2b and 2c). Soil compaction does not occur uniformly. Pores in front of the piston are strongly compressed, whereas the pore space further away from the piston is less affected. The position of garnet particles in relation to macropores changes drastically through soil compaction (red boxes). In uncompacted soil almost all garnet particles are in direct contact with air due to the way the sample was prepared. At an intermediate bulk density a large fraction of particles is already occluded between aggregates. At the highest bulk density many pores

vanished completely so that the former aggregate boundaries can only be identified through linings of garnet particles.

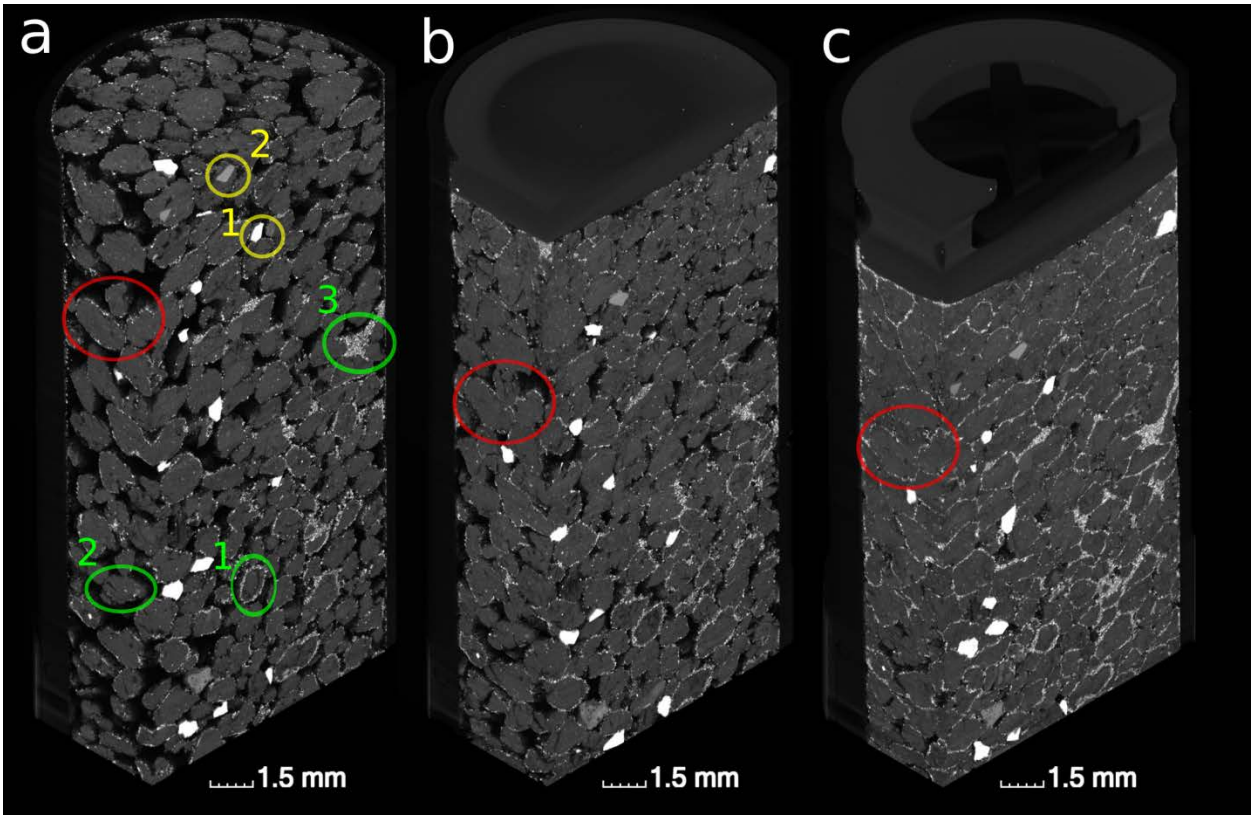

Figure 24: 3D rendering of a sample at a bulk density of (a) ρ = 1.1 g/cm³, (b) ρ = 1.3 g/cm³ and (c) ρ = 1.5 g/cm³. The green circles highlight aggregates which are strongly (#1) or weakly (#2) covered with particles or pores in which detached particles gather (#3). The yellow circles highlight that photon absorption in garnet (#1) is higher than in iron-free minerals like quartz (#2). The red circles highlight in the incorporation of particles into the soil matrix in the course of compaction.

In the following these visual observations will be confirmed by quantitative image analysis. First, the different bulk densities are compared with respect to height profiles of porosity (Figure 22a). Sample preparation at the lowest bulk density (ρ = 1.1 g/cm³) lead to a uniform porosity profile around an average porosity of ϕ = 0.30. The uni-axial compression to a bulk density of ρ = 1.3 g/cm³ caused a linear decrease in porosity from ϕ = 0.24 at the bottom of the field of view to ϕ = 0.12 at the top in close proximity to the piston (average ϕ = 0.18). The second compaction to a bulk density of ρ = 1.5 g/cm³ reduced average porosity further to an average of ϕ = 0.05, again showing a linear decrease in porosity from the bottom of the field of view to a height of about 15 mm. Above that height an irreducible porosity of ϕ = 0.03 is reached. Due to the porosity gradient in the sample all subsequent analysis will be presented separately for the top and bottom of the sample. The cumulative pore size distribution (Figure 22b) clearly shows a shift in the range of pore diameters with changing bulk density. An increase in bulk density leads to a shift in the pore size distribution towards smaller pore diameters. At the same time the curves become steeper, i.e. the range of prevalent pores diameters gets narrower as big pores get compacted more easily. Interestingly, the average pore diameter (Figure 22c) scales linearly with porosity. Note that this only refers to porosity above the resolution limit of 8 µm. Connectivity, in turn, exhibits a very non-linear relationship with porosity (Figure 22d). Above a critical porosity of 10–12% the pore space is well connected and only a small fraction of pores is not connected to the main,

percolating pore cluster. Close to the percolation threshold a small reduction in porosity entails a huge fragmentation of the pore network.

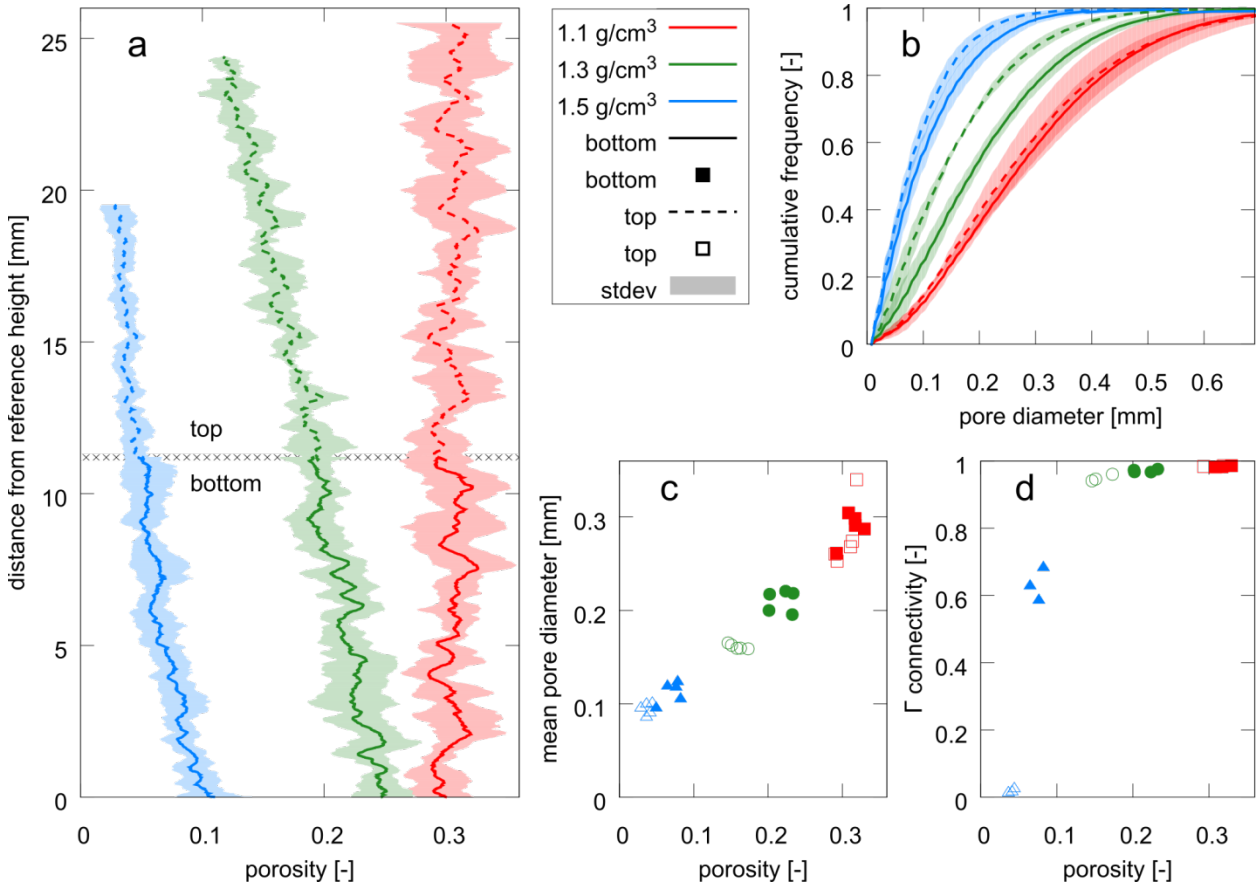

Figure 25: Pore space analysis for soil at three bulk density levels (ρ = 1.1, 1.3, 1.5 g/cm³) with five replicates: (a) porosity profiles, (b) cumulative pore size distribution, (c) mean pore size and (d) Γ connectivity as a function of pore diameter. Because of the depth gradient in porosity results are shown separately for the top and bottom of the samples.

Soil deformation

The deformation of soil during compaction is analyzed with digital image correlation. The displacement of individual garnet grains during compaction from ρ = 1.1 g/cm³ to ρ = 1.3 g/cm³ for one out of five replicates is depicted in Figure 23(a). Evidently the displacement is smaller at the bottom of the field of view and strongest close to the piston of the syringe. The exact displacement of garnet grains is computed with elastic registration of the deformed image onto the original image using a B-spline transform of a regular grid of control points. A successful registration is achieved for all grains and even for larger clusters of particles, as indicated with yellow color in Figure 23(b). The resulting deformation field shows a gradual increase in compaction with vertical position ranging from 1.5 mm at the bottom to 5.5 mm at the top of the field of view (Figure 23c). The compaction to ρ = 1.5 g/cm³ increases the vertical displacement to 2.5 mm at the bottom and 8.5 mm at the top (Figure 23(b)). There is only little lateral heterogeneity in the downward movement (z-components of the vectors) and hardly any horizontal movement of garnet grains (x-y components of the vectors).

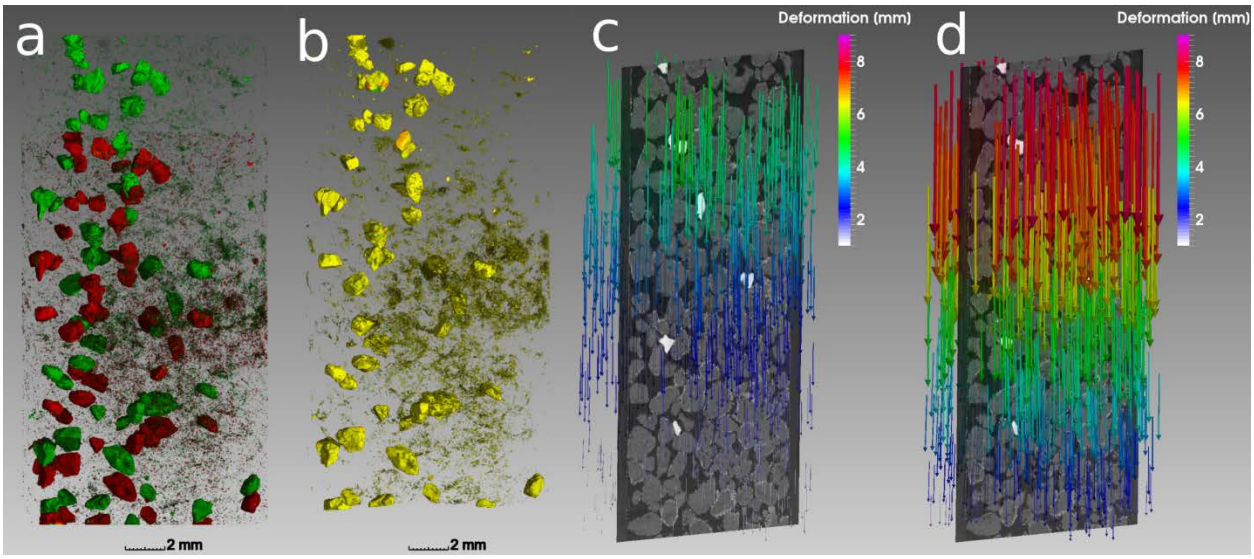

Figure 26: (a) Spatial distribution of big garnet grains and small garnet particles at a bulk density of 1.1 (green) and 1.3 g/cm³ (red). (b) Elastic image registration leads to a very good spatial alignment between the deformed and the original image. (c) The resulting displacement field shows a gradient in vertical displacement. (d) Compaction to 1.5 g/cm³ increases this gradient even further.

Particle distribution

Pores may disappear completely during soil compaction. As a consequence the minimum distance from any location within the soil matrix to the nearest pore undergoes characteristic changes. This is summarized in the histogram of contact distances for all non-pore voxels (Figure 24a, inset). The aggregate packing at ρ = 1.1 g/cm³ renders a lot of aggregate surfaces in direct vicinity to a well-connected pore network. The exponential decline in frequency with increasing contact distance is a consequence of the compact shape of aggregates, which are all of similar size. When only the garnet particles are considered (Figure 24a), the decline is much steeper. Evidently, all garnet particles have only small contact distances at the beginning of the experiment, because they adhere to aggregate surfaces. The natural fine sand fraction of the soil, which is also detected as particles during image processing, only evokes a minor tailing of the histogram for distances above 0.1 mm. When the soil is compacted to ρ = 1.3 g/cm³ the frequency distribution of contact distances does not change, neither for garnet particles nor for all non-pore voxels in general. Only at a bulk density of ρ = 1.5 g/cm³ there is a considerable shift towards greater contact distances because a large fraction of garnet particles is not in direct contact with the pores anymore. The comparison between average pore distance of soil and garnet particles (Figure 24b) exhibits the following features: (1) There is a linear relationship between average contact distance for particles and average contact distance for soil during soil compaction. (2). All data points are below the 1:1 line, i.e. on average the particles remain closer to pores as compared to bulk soil. (3) Differences in the pore space attributes of the top and bottom parts do not entail different contact distances.

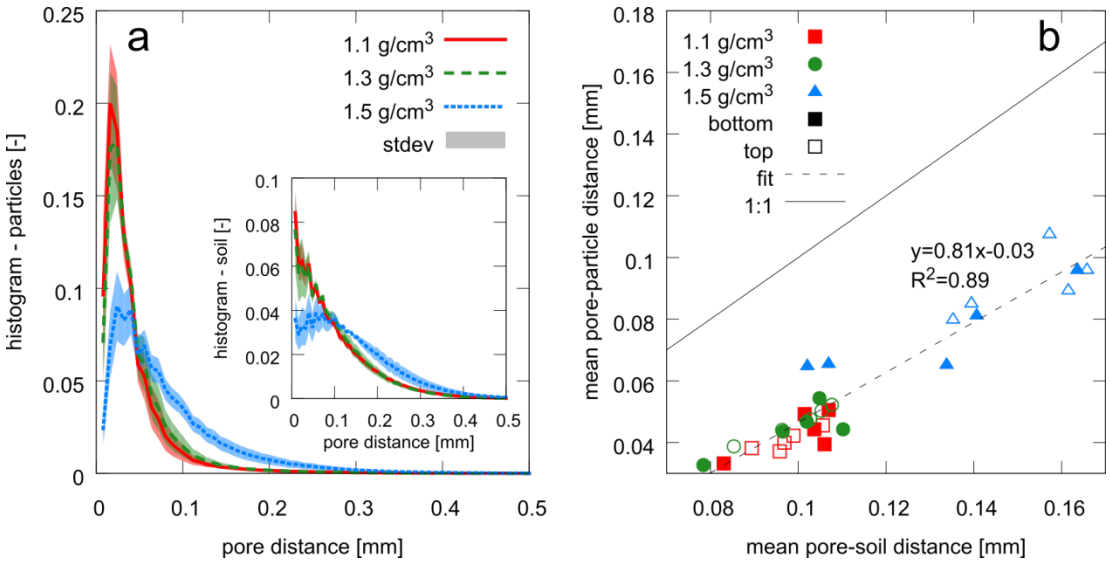

Figure 27: (a) Frequency distribution of contact distances between particles and pores with average and standard deviation of five replicates. The inset shows the contact distance distribution between bulk soil and pores with is generally much larger. (b) The mean contact distance of particles and bulk soil is shown for each replicate and further separated into top and bottom part of the sample. The mean contact distance for particles scales linearly with the mean contact distance for bulk soil during compaction.

Discussion

Relationship between contact distances and porosity

Bulk density changes due to soil compaction affect soil structure in many ways. Some pore space attributes like porosity and mean pore diameter scale linearly with bulk density. Pore connectivity, in turn, exhibits a very non-linear behavior. At first, compaction only leads to a reduction of pore sizes without a disruption of the pore network. Only when a critical porosity threshold of 10–12% is reached, the well-connected pore network breaks into many evenly sized, isolated pores. The sharp transition in pore connectivity in a narrow porosity range is due to the regular packing of similar-sized aggregates. The transition is likely to be more gradual in natural soil with a more irregular network to start with. Looking at soil structure changes from the perspective of the pore space seems to be the natural choice, since many important soil functions like aeration, water storage or solute transport depend on the size distribution and continuity of pores. However, soil functions which relate structure-mediated accessibility of soil constituents calls for a shift of focus towards soil matrix attributes. For instance, the physical protection of particulate organic matter against microbial decomposition within soil aggregates is mainly governed by diffusion-limited supply of nutrients, oxygen and exoenzymes through predominantly water-filled intra-aggregate pores, which cannot be captured by the image resolution of 8µm. For oxygen, this information on accessibility is best described by the diffusion length from the substrate through the soil matrix to the next air-filled pore (Ebrahimi and Or, 2015; Negassa et al., 2015). Evidently, this diffusion length is a transient property that depends on soil matric potential ψ_m. At the image resolution of 8µm used in this study we cover the pore space which is air-filled at a matric potential of ψ_m= −375 cm (derived from Young-Laplace law assuming perfect wettability). If ψ_m was controlled during the experiment and air and water was segmented separately in the µCT images or if the distribution of air and water was modelled e.g. with maximum inscribed sphere analysis of the pore space (Hazlett, 1995; Kumahor et al., 2015), then the contact distances to air-filled pores, could be examined for any matric potential higher (i.e. moister) than ψ_m = −375 hPa. Hence, based on the contact distances, it is possible to evaluate diffusion lengths into water-filled regions for a wide moisture range as typical for many soils.

This average contact distance undergoes non-linear changes with decreasing porosity caused by compaction (Figure 25). At ρ = 1.3 g/cm³, the reduction in porosity does not lead to increased contact distances, because most pores shrink in size, but not beyond the resolution limit. Only at a critical porosity of 10–12% there is a substantial occlusion of pores within the dense soil matrix or even a complete removal of resolved porosity. Note that this porosity threshold coincides with the steep decline in pore connectivity (Figure 22d). The black curve fitted to the data in Figure 25 suggests an exponential decline in mean contact distance with increasing porosity. In the supporting information 6.1 (**S2**) we show that this exponential trend is in line with contact distances for overlapping spheres of different packing geometry and a diameter comparable to the maximum inscribed sphere of the irregular-shaped aggregates used in this study. This indicates that the exponential trend is caused by changes in interaggregate porosity, i.e. by a change in void space between aggregates.

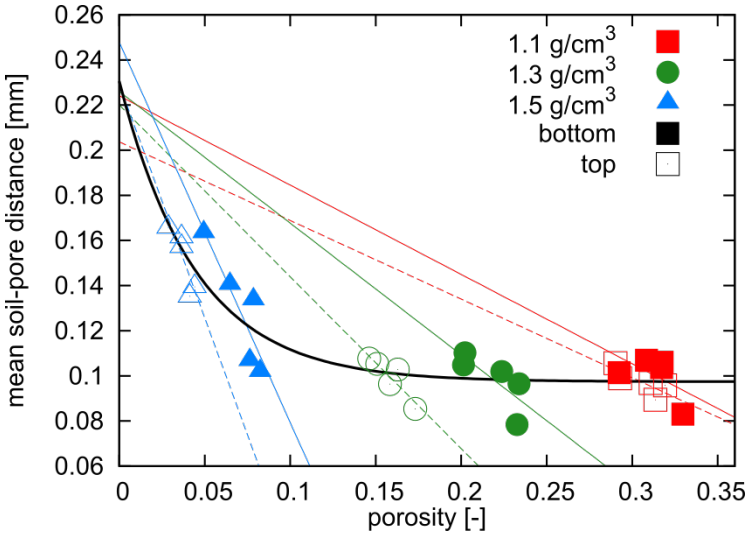

Figure 28: The mean contact distance between bulk soil and pores scales exponentially with decreasing porosity during soil compaction. This exponential trend follows from the non-linear increase of contact distances as pores start to vanish completely at higher bulk density. The scatter with subgroups of similar bulk density is caused by different degree of intra-aggregate porosity mostly due to crack-formation. This variability in intra-aggregate porosity causes a linear scaling relationship between contact distances and porosity. All fitted curve converge to a similar contact distance at vanishing porosity which is mainly determined by the average size of aggregates.

Interestingly, the scatter within the different compaction levels is quite high. However, this scatter is not random, but shows a negative linear trend between porosity and mean contact distance for each bulk density sub-group. At constant bulk density, an increased porosity is mainly due to additional intra-aggregate pores, which mainly results from micro-crack formation that reduces the mean contact distance to pores. All fitted curves converge towards the same mean contact distance for vanishing porosity, which we show in the supporting information 6.1 (**S2**) File to mainly depend on the average size of aggregates.
In summary, this assessment of soil structural dynamics via changes in contact distances is a valuable information based on the spatial arrangement of the soil, which cannot be inferred from a statistical analysis of pore space attributes alone. By analyzing the distribution of water and air in the pore space, changing diffusion pathways due to water dynamics or soil structure dynamics could potentially be treated separately.

Measuring soil structure turnover

In the following, we will therefore use contact distances to outline a direct approach to measuring soil structure turnover. To do so, we make use of a close analogy to stable isotope methods as a standard

method to quantify turnover rates of different carbon pools in soil. By labeling of a certain pool or substrate its fate in the carbon cycle can be monitored over time and net fluxes can be derived even under steady-state conditions. Likewise, soil structure can be distinguished in two pools according to their spatial context: (i) regions in direct contact with oxygen, e.g. aggregate surfaces and the soil around macropores, and (ii) the interior of aggregates where OM is potentially protected from mineralization. Pulse labeling of the soil structure is then achieved by covering aggregate surfaces with inert particles and the fate of these particles can be studied over time.

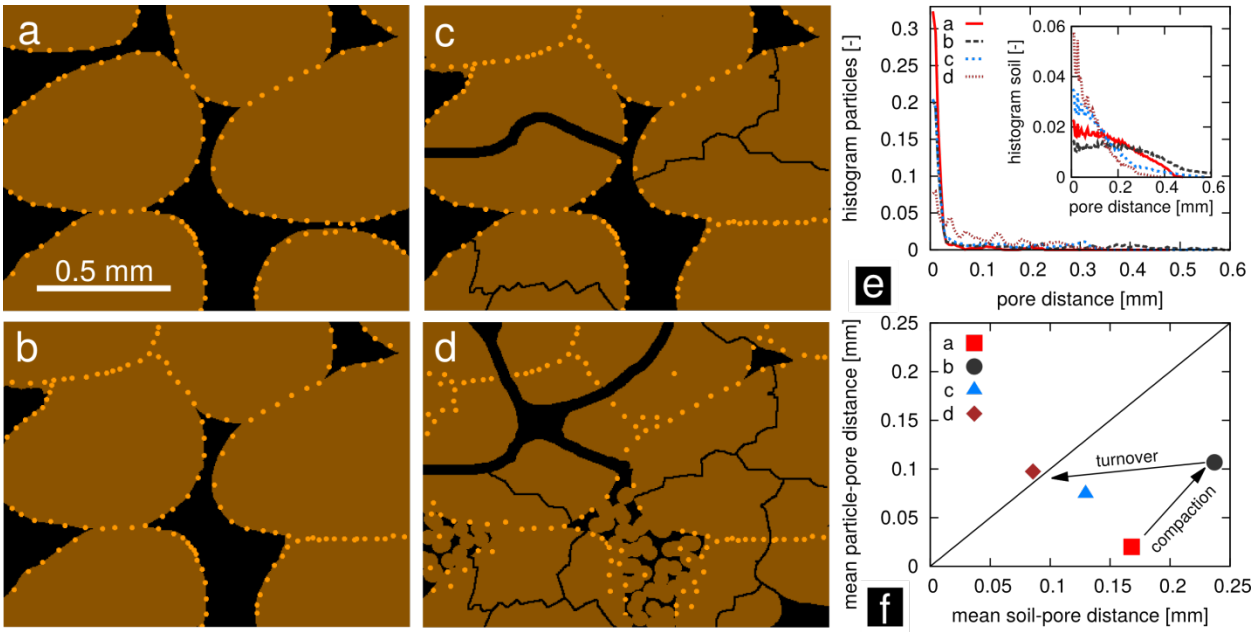

Figure 29: Conceptual scheme for the quantification of soil structure turnover rates. (a) A two-dimensional packing of aggregates is covered with garnet particles. (b) The aggregates are first compressed by soil compaction. Subsequently, soil structure turnover is initiated through new root channel formation, micro-crack formation and the partial refilling of pores with earthworm casts, where (c) and (d) represent two consecutive moments in time. (e) The distribution of contact distances between pores and particles or between pores and bulk soil (inset). (f) The mean contact distance of particles is initially much smaller than the mean contact distance for bulk soil. Soil compaction does not lead to a trajectory towards the 1:1 line (randomized position of particles), whereas structure turnover does.

This is illustrated in the conceptual scheme in Figure 26. If particles were distributed randomly across soil, then the mean contact distance between particles and pores should equal the mean contact distance between all soil voxels and pores. Evidently, the distribution of particles at the beginning of the structure labeling experiment is far from being random, as all particles adhere to the surface of aggregates (Figure 26a). That is to say, the pool of small contact distances is strongly enriched with particles. We have shown in our experiment, that soil compaction has only a small effect on the ratio between particle contact distances and soil contact distances (Figure 24) in spite of large physical displacement of soil constituents during compaction (Figure 23). Many particles become occluded within bigger aggregates so that their minimum distance to the next pore increases, but so does the pore distance for bulk soil in general (Figure 26b). As a consequence, the trajectory in Figure 26(f) proceeds in parallel to the 1:1 line. Actual soil structure turnover, i.e. the formation and destruction of pores through rearrangement of soil constituents by abiotic and biotic agents, will likely cause a different trajectory. This soil structure turnover is illustrated with different degrees of bioturbation (root channels, refilling of pores with earthworm casts) and micro-crack formation Fig Figure 26 (c) and Figure 26 (d). As a result, the mean contact distance of particles approaches that of bulk soil. The spatial distribution of particles may not be random and still demarcate former aggregate boundaries. However, it becomes statistically similar to the

distance distribution of bulk soil as the trajectory approaches the 1:1 line in Figure 26(f). Soil structure has reached a dynamic equilibrium then, because continued turnover will only randomize the spatial distribution of particles even further without diverging from the 1:1 line. The rate at which this dynamic equilibrium is reached can be interpreted as the turnover rate of soil structure. Evidently this turnover rate will depend on the activity of biotic and abiotic agents, but also on whether old pores are continuously reused or newly formed and destructed. This effect of natural processes of structure formation on contact distances will be investigated in a future structure labeling study.

Practical considerations

From a practical point of view, a structure labeling experiment will always entail some degree of initial disturbance to bring the garnet particles into contact with the soil matrix. We coated the surfaces of sieved aggregates with fine sand particles that are indistinguishable from the fine sand fraction of soil. Our study represents an extreme case of pulse labeling, since the soil matrix was almost devoid of fine sand and many garnet particles were used. Such a structure labeling approach would still be feasible with soils naturally containing a considerable fine sand fraction or lower coverage of aggregate surfaces with garnet particles, as long as the pool of short contact distances is significantly enriched after structure labeling. Moreover, packings of sieved aggregates represent a rather artificial soil structure to begin a structure dynamics experiment with. In a more natural setting garnet particles could be added to a field soil during plowing or harrowing similar to (Plante and McGill, 2002) under the tacit assumption that particles are preferably located at short contact distances due to the way they are added during tillage. Evidently the total abundance of garnet particles would be much lower in this case and the imbalances of initial contact distances are less strong. In analogy to stable isotope methods this is more similar to a natural abundance study than a pulse labeling study and consequently has a different set of requirements in terms of measurement precision and level of background noise. For instance, the soil matrix should be free of fine sand in this case, or chemical microscopy methods like SEM-EDX (Hapca et al., 2015) are required to distinguish garnet particles from the natural fine sand fraction.
Other limitations are posed by the sample size and image resolution. Macropores in natural soil which are induced by desiccation cracks and bioturbation are too big to be captured adequately in 5 ml samples (d:12.5 mm). Our focus is on the small scale dynamics of the inter- and intraaggregate pore space which we believe is highly relevant especially for the turnover of organic matter. This requires a sample size that is small enough to detect the garnet fine sand fraction. A simultaneous investigation of the pore architecture at both scales calls for a hierarchical sampling scheme (Vogel et al., 2010) in which bigger soil cores are scanned first to analyze the macropore network and smaller subsamples are extracted subsequently based on the location in the first scan. The image resolution of 8 μm which was used in this study resulted in a good compromise between visible details and a sufficiently big volume to representatively capture interaggregate pores and garnet particles. Micropores in which soil organic matter is protected against decay are not visible in μCT images. However, we think that micropores are present everywhere all the time. What turns them into oxygen depleted regions is the distance to air-filled mesopores. This distance between garnet powder and mesopores is in fact what we address with our conceptual idea of soil structure turnover.
Finally, garnet particles can be considered as chemically stable for typical timescales of incubation experiments or field experiments. Almandine is a nesosilicate with dissolution rates mainly depending on soil pH, grain size and the existence of protective oxide layers. For instance, for a garnet powder of slightly smaller grain size (d:30±8.3 μm) the reported almandine dissolution rate (weight loss per mineral surface area after 90 days) at pH 3.6 (9.8 mg/m²) was two orders of magnitude higher than at pH 8 (0.16 mg/m²) (Nickel, 1973). Moreover, the field dissolution of garnet minerals usually amounts to 0.1–10% of dissolution of pure powders, because a high percentage of moisture is stagnant, i.e. ions in solution reach equilibrium which slows down dissolution (Velbel, 1993). Using these values we may assume a

dissolution rate of 5×10^{-7} mg/(mm² a) for an agricultural soil like that in Bad Lauchstädt with pH 7.3 (Altermann et al., 2005). A rough calculation shows that the dissolution of a spherical garnet grain from a diameter of d = 50 µm (lower end of the range used in this study) to d = 25 µm (minimum size of detectable objects at 8µm image resolution) takes 10000 years in this case.

Conclusion

Microscopic changes of soil structure during soil compaction were analyzed with µCT. The increase in bulk density due to compression of soil leads to consistent changes in porosity and mean pore diameter. Pore connectivity in turn remains high initially and breaks down suddenly within a narrow porosity range. We demonstrated that these pore space attributes provide limited insights into structural properties associated with matter turnover. This knowledge gap is closed by analyzing the contact distances between soil and pores and therewith the diffusion lengths for oxygen and nutrients. For the first time we have delineated the conceptual framework and the image processing workflow to study the evolution of contact distances for small garnet particles. Similar to stable isotope labeling of carbon pools, a structure labeling experiment can be devised by bringing garnet particles into contact with aggregate boundaries. In this way, the "pool" of small contact distances to inter-aggregate pores is highly enriched and the dilution into all distance "pools" can be studied over time. In this framework, soil structure turnover manifests itself as an evolution of mean particle contact distances towards the mean contact distance of bulk soil. We have shown that soil compaction entails a large physical displacement of particles due to strong deformation of soil. However, this movement of particles is embedded in the collective movement of all soil constituents. The mean contact distance for particles increases, but not stronger than the contact distance of bulk soil. Yet, particles have not randomized their position relative to pores. This randomization does not depend on the physical extent of particle movement as analyzed with digital image correlation, but on a changing spatial context of particles through formation and destruction of nearby pores. With this conceptual approach the effect of soil compaction on soil structure can be clearly separated from other processes which are expected to occur during soil structure turnover. Finally, the structure labeling approach to quantify soil structure turnover rates can be readily combined with stable isotope labeling of organic compounds to quantify matter turnover.

Supporting Information (chapter 6.1)
SI 1: Image processing workflow (*with 1 figure*)
SI 2: Contact distances for regular sphere packings (*with 1 figure*)

Acknowledgments
This study was partially funded by the Deutsche Forschungsgemeinschaft through the research unit DFG-FOR 2337: Denitrification in Agricultural Soils: Integrated Control and Modelling at Various Scales (DASIM). We thank two anonymous reviewers for the valuable comments. We are grateful to Robert Mikutta, Klaus Kaiser, Thimo Klotzbücher and Uwe Franko for illuminating discussions during the preparation of this manuscript.

2.4. Correlative imaging reveals holistic view of soil microenvironments (Schlüter et al. 2019, Environmental Science & Technology, 53(2), 829-837, doi: 10.1021/acs.est.8b05245)

Abstract

The micro-environmental conditions in soil exert a major control on many ecosystem functions of soil. Their investigation in intact soil samples is impaired by methodological challenges in the joint investigation of structural heterogeneity that defines pathways for matter fluxes and biogeochemical heterogeneity that governs reaction patterns and microhabitats. Here we demonstrate how these challenges can be overcome with a novel protocol for correlative imaging based on image registration to combine three-dimensional microstructure analysis of X-ray tomography data with biogeochemical microscopic data of various modalities and scales (light microscopy, fluorescence microscopy, electron microscopy, secondary ion mass spectrometry). Correlative imaging of a microcosm study shows that the majority (75%) of bacteria are located in mesopores (<10µm). Furthermore they have a preference to forage near macropore surfaces and near fresh particulate organic matter. Ignoring the structural complexity coming from the third dimension is justified for metrics based on size and distances but leads to a substantial bias for metrics based on continuity. This versatile combination of imaging modalities with freely available software and protocols may open up completely new avenues for the investigation of many important biogeochemical and physical processes in structured soils.

Introduction

Small-scale heterogeneity of environmental conditions in soil exerts a major control on carbon and nutrient cycling. Physical accessibility at the pore scale plays an important role for long-term carbon stabilization (Dungait et al., 2012; Lehmann and Kleber, 2015) and for microbial diversity in soil through spatial separation in diverse ecological niches (Schimel and Schaeffer, 2012; Tecon and Or, 2017; Vos et al., 2013). Many microbial processes like respiration, nitrification and denitrification are known to occur in hotspots of microbial activity which are imprints of the patchy distribution of microhabitats in soil (Kuzyakov and Blagodatskaya, 2015). These patterns form as a result of a complex interplay between biotic and abiotic agents, so their formation cannot be understood, if individual processes are studied in isolation. This calls for a joint characterization of (i) the physical soil structure providing the pathways for matter fluxes, (ii) the chemical properties that drive local reactions in soil and (iii) the distribution of soil biota that is both resulting from and actively changing the former (Baveye et al., 2018; Young and Crawford, 2004).

While the three-dimensional (3D) characterization of the physical structure of intact soil has advanced tremendously with the advent of non-invasive imaging techniques like X-ray micro-tomography (Cnudde and Boone, 2013; Helliwell et al., 2013; Wildenschild and Sheppard, 2013) (µCT), 3D imaging of biogeochemical heterogeneity in opaque soil is still not achievable. Thus, it is still common practice to cut the soil into pieces, with or without prior resin impregnation, in order to apply two-dimensional (2D) microscopic and micro-spectroscopic imaging techniques on exposed surfaces. The combination of various biogeochemical imaging methods is an emerging field in life sciences called correlative imaging or correlative microscopy (Caplan et al., 2011; Handschuh et al., 2013). In contrast to the fast growing number of applications of 3D chemical imaging using fluorescence microscopy approaches, such a straightforward approach is not at hand for intact natural geological materials including opaque soil and plant-soil systems. Consequently applications in soil science are few, in particular the combination of two-dimensional biogeochemical imaging modalities with 3D non-invasive imaging. When using soil sections for 2D biogeochemical imaging, a major hurdle is to find the exact plane of the exposed surface

within a bigger 3D volume. Depending on the scale gap this can turn into a search for a two-dimensional needle in the 3D haystack. One pragmatic solution is to cut or grind down the exposed surface strictly along a principle axis of the 3D image to reduce the degrees of freedom with which the 2D plane can potentially be oriented. In this way, the spatial distribution of *P. fluorescens* in fluorescence microscopy (FM) images of soil microcosms was directly related to pore space attributes measured with X-ray microtomography (Juyal et al., 2019). The more flexible approach is to pose this 2D-3D image registration as an optimization problem. In a pioneering study by Hapca et al. (2011), stacks of elemental maps obtained with scanning electron microscopy coupled to energy-dispersive X-ray spectroscopy (SEM-EDX) were registered to a µCT image of resin-embedded soil. This was done by a search algorithm with three degrees of freedom (one vertical translation, two rotations) that optimized the correlation coefficient between the elemental map and the aligned µCT plane. The search was guided by reducing the 3D volume in vertical direction to the most probable region and by reducing the range of allowed rotation angles in both directions.

In this paper we present a new protocol for correlative imaging based on elastix(Klein et al., 2010; Shamonin et al., 2014), a free image registration software popular in biomedical imaging. The main methodological objective is to outline best practices for successful 2D-3D image registration along the lines of Hapca et al. (2011) but extended and improved in different ways. Correlative microscopy is demonstrated for various image modalities including µCT, FM, SEM-EDX, light microscopy (LM), and nano-scale secondary ion mass spectroscopy (NanoSIMS). They cover a large range of scales from a lateral resolution of 0.1 µm in nanoSIMS images to continuity of air-filled pores in a sample 2 cm in size. The LM of the entire sample cross section serves as a reference plane to which all other imaging modalities including µCT are registered. The main scientific objective of the paper is to link microhabitats with the physical structure of soil by exploring the spatial distribution of bacteria and relating it to pore architecture and substrate availability in the detritusphere around a decaying leaf. For the first time we systematically analyze the bias in habitat metrics that is introduced by ignoring structural information from the third dimension. The versatility of the image registration approach is further demonstrated by spatial alignment of SEM-EDX and NanoSIMS data.

Material and methods

Sample preparation

The repacked sample was composed of fine textured-soil (silt loam, derived from a subsoil horizon of a Stagnosol). Sand grains (coarse sand, 5% v/v) were amended for structural support. A poplar leaf fragment was placed in the center while the sample was repacked to a bulk density of 1.3 g cm^{-3} in a PTFE cylinder (10 mm inner diameter, 20 mm height). The soil was incubated at field capacity and room temperature for 7 days. The water used for saturation was amended with five bacterial strains (Vitabac, Bactivia GmbH, Germany) to enrich the subsoil material with soil bacteria.

After incubation the sample was chemically fixated with 2% formaldehyde solution to keep the structure of the cells and microbial nucleic acids intact. After fixation the intact cores were initially dehydrated with acetone (graded series from 70 to 100% (v/v)) and then impregnated with a series of Araldite 502:acetone mixtures (1:3, 1:1 (vl:vl)) and finally with 100% Araldite 502 (Araldite kit 502, electron microscope sciences, Hatfield, USA). The blocks were cured at 60°C for 48 h (Mueller et al., 2017). Prior to sectioning of the cylinders the samples were measured using X-ray microtomography. The cylindrical sample was cut vertically with a diamond saw (Struers Discoplan TS) to achieve a large cross-sectional area. The cut sample was subsequently polished and glued onto a round glass disc of 25.4 mm diameter. The remaining sample was cut to a thickness of approx. 0.5 mm using a diamond saw (see above, sample fixed on a vacuum holder). Finally the vertical cross section was ground down and polished to obtain a thin section with a surface of low topography (Mueller et al., 2013).

X-ray microtomography

After resin impregnation the intact sample was scanned with X-ray microtomography (X-tek XMT 225, Nikon Metrology, Herts UK). 2800 Projections (110 kV, 140 µA, no filter, 700ms, 2 frames per projection) were acquired and reconstructed into a 3D tomogram with a voxel length of 7µm using the X-tek Pro software. The image was filtered and segmented into pores and solid with protocols explained in Schlüter et al. (2014) using Fiji/ImageJ (Schindelin et al., 2012) and QuantIm (Vogel et al., 2010). The leaf was segmented with the region growing tool in VG Studio Max 2.1 (Volume Graphics). Occasional over-segmentation due to low contrast between leaf and resin had to be removed manually in VG Studio Max 2.1.

Light microscopy

The entire cross sectional area was mapped with reflected light microscopy (Zeiss AxioImager 2) using polarized light and the extended depth of focus mode. Individual images (z-stacks and mosaic images) were stitched together using the Zeiss software (Zeiss AxioVision). The 50x magnification resulted in a pixel length of 1.1 µm. Some regions of interest were scanned again at higher magnification (200 x) to map the sample surface for easier location of subsequent NanoSIMS measurements.

Fluorescence microscopy

A large area of the exposed surface partially covering the leaf was scanned with fluorescence microscopy (Zeiss Axiospkop 2 equipped with an HBO 103 W/2 Hg vapour lamp and Plan-Neofluar objectives 20× and 40×). The polished thin section was stained using DAPI (Vectashield H-1200), which selectively binds to DNA. Fluorescence filter sets were used to visualize DAPI-stained cells (F46-000, AHF) and organic soil compounds (double excitation, #24, Zeiss). Imaging was done with a CCD camera (Colorview II, Soft Imaging) connected to an imaging software (AnalySIS, Soft Imaging). Several images were stitched together automatically with the multiple image alignment module of the AnalySIS software and Adobe PhotoShop CS6.

NanoSIMS microspectroscopy

A 0.2 mm transect from the leaf into the surrounding soil was mapped using nano-scale secondary ion mass spectrometry (NanoSIMS). The NanoSIMS images were recorded with a Cameca NanoSIMS 50 L (Gennevilliers, France). Prior to the NanoSIMS measurements, an Au/Pd layer (~30 nm) was sputter coated to avoid charging during the measurements. The Cs+ primary ion beam was used with a primary ion impact energy of 16 keV. Prior to final analysis, any contaminants and the Au/Pd coating layer were sputtered away at 50 by 50 µm using a high primary beam current (pre-sputtering). During this pre-sputtering, the reactive Cs+ ions were implanted into the sample to enhance the secondary ion yields. The primary beam (ca. 1.2 pA) was focused at a lateral resolution ca. 100 nm and was scanned over the sample, with 12C-, 12C14N-, 16O-, and 56Fe16O- secondary ions collected on electron multipliers with an electronic dead time fixed at 44 ns. The estimated depth resolution with 16 keV Cs+ ions was 10 nm. The electron flood gun was used to compensate for any charging effects due to the non-conductive mineral particles (e.g. larger quartz grains). All measurements were done in imaging mode. For ion images with a field of view of 30 by 30 µm, 40 planes were acquired using a dwell time of 1 ms/pixel, with 256 pixels by 256 pixels. Images were corrected for electron multiplier dead time and the measurements stacks were accumulated using the Look@NanoSIMS software (Polerecky et al., 2012).

SEM-EDX microspectroscopy

The larger area around the NanoSIMS transect across the leaf-soil interface was scanned again with SEM-EDX (JEOL-JSM7200F). The area was scanned using the backscatter electron detector to obtain high resolution images of the detritusphere, using the material contrast to differentiate between minerals and organic tissues and resin. Additionally a mosaic at the detritus interface was analyzed using EDX at 15 keV to show the elemental distribution at a larger field of view. The resulting images were stacked using the MosaicJ plugin in Fiji/ImageJ (Schindelin et al., 2012).

Image Analysis

The 3D physical structure can be analyzed in various ways. In this study we are interested in microhabitats which are likely to be modulated by the presence of the leaf and by the distribution of water and air in the pore space. The water distribution during incubation is unknown, since the intact sample was only scanned after resin impregnation. However, the distribution can be modelled with a morphological approach using the maximum inscribed sphere method in combination with a connectivity rule (Hazlett, 1995). That is, pores are assigned to air, if they can entirely fit a sphere of a certain radius and have a continuous path to the headspace of the sample from where the air invades. All smaller or disconnected pores are assigned to water. The radius is directly linked to the curvature of the air-water interface and hence related to capillary pressure through Young-Laplace's law. Thus, a step-wise decrease in radius resembles a drainage process. For any drainage step, the Euclidean distance of all non-air voxels to the closest air voxel can be computed, which gives a rough estimate of diffusion lengths of dissolved oxygen in soil that can be limiting for microbial respiration. In the same vein, Euclidean distances can be computed from the leaf into the soil, or from the soil-pore interface into the soil or into the pore space. The pore size distribution and Euclidean distance transforms were computed with Fiji/ImageJ (Schindelin et al., 2012) and air continuity were evaluated with the MorpholibJ plugin (Legland et al., 2016). The algorithm to model drainage based on pore size distribution and air continuity is explained in detail in the supporting information (chapter 6.2 **S1**).

The exact micro-environmental conditions during incubation cannot be recovered through image analysis. However, the spatial distribution of bacteria visualized via epifluorescence microscopy (FM images) may indicate favorable microenvironments. Even though there are dedicated protocols for automatic cell counting (Schmidt et al., 2018), we resorted to manual cell counting using the ROI manager in Fiji, which is still feasible for such a proof-of-concept study. The distribution of bacteria is analyzed with respect to site preference, e.g the tendency to proliferate near the leaf surface. To do so, the average Euclidean distance from a cell to the closest leaf surface is determined for a fixed number of cells (n=50) randomly chosen from the population of all manually detected cells (n=536). A normalized bacteria-leaf distance ratio is calculated by dividing the bacteria-leaf distance with the average Euclidean distance of an equal amount of randomly chosen soil voxels to the closest leaf surface. This ratio is computed repeatedly for a number of realizations (n=50) to get a robust estimate of the ratio that may either indicate preference (<1), avoidance (>1) or indifference (=1). Same is done for the distance of bacteria to pore surfaces. In addition, the relative bacteria abundance in three different pore size classes (mesopores, narrow macropores, macropores) was determined. Cells in voxel locations which were assigned to soil during µCT image segmentation are all assigned to unresolved mesopores, i.e. smaller 1-2 voxels (≈ 10µm), assuming that cells are too big to fit into unresolved micropores (<0.2µm). Cells within visible pores are further differentiated by a pore diameter threshold of 7 voxels (7 x 7µm ≈ 50µm) into narrow macropores that drain at a capillary pressure range of 60-300hPa and macropores (>50µm) that are drained at field capacity (60hPa).

Image Registration

The objective of image registration is to find a transformation matrix that aligns a moving image with a target image such that an objective function is optimized. The target image is always the light microscopy

(LM) image of the entire polished surface. The moving images to be transformed are either the 3D X-ray CT image of the physical structure or various biogeochemical, spectromicroscopic images of smaller sub-sections. The objective function consists of two terms: a) the sum of Euclidean distances between corresponding landmark points set manually at easily identifiable objects in the microscopy plane and b) the mutual information criterion (Mattes et al., 2001) that quantifies the entropy in a two-dimensional histogram composed of the corresponding gray values at random locations of the aligned image pairs. This mutual information criterion is more suitable to verify the alignment of images from different modalities than simple correlation coefficients since different material classes may not always have proportional intensities in both images. Image registration was carried out with the elastix software (Klein et al., 2010; Shamonin et al., 2014) by employing a similarity transform with seven degrees of freedom in 3D (three rotations, three translations and one scaling parameter) and four degrees of freedom in 2D (one rotation, two translations and one scaling parameter). Convergence was accelerated by imposing a pyramid schedule, i.e. quick registration was achieved with coarse, rescaled copies and alignments was sequentially refined at the next finer scale. Note that image registration with different dimensionality (2D vs. 3D) is not implemented in elastix so that the LM image had to be converted into a 3D image with a thickness of one slice first. A minimum example including images, landmark and parameter files and execution commands are provided as supporting information.

The transformation matrix can not only be employed on the moving image for which it was optimized, but also on any other spatial data resulting from image analysis, such as point patterns of bacteria distribution in FM images or pore size maps and distance maps obtained from segmented X-ray CT images. This is done with transformix, a sub-routine of elastix, for which an example is also added as supporting information (chapter 6.2 **S3**).

Results and Discussion

3D Physical Structure

The 3D tomogram is cut virtually at three principle planes in Figure 30(a) to reveal to position of the embedded leaf (green). The outcome of 2D-3D image registration is a plane through the moving µCT image (Figure 30b) that is perfectly aligned with the target LM image (Figure 30c). The exact position of the LM plane is somewhat arbitrary and a result of cutting and polishing during sample preparation. However, the µCT image could in fact be used to identify points of interest and guide the positioning of microscopy planes. The eleven landmarks that helped find the plane are also depicted. The final, average distance of corresponding landmarks was 9.5µm, which corresponds to 1.4 voxels in the X-ray CT image and 8.6 pixels in the LM image. Note that even though most landmarks are deliberately set in the vicinity of the leaf, the spatial alignment of objects further away from the leaf is also excellent.

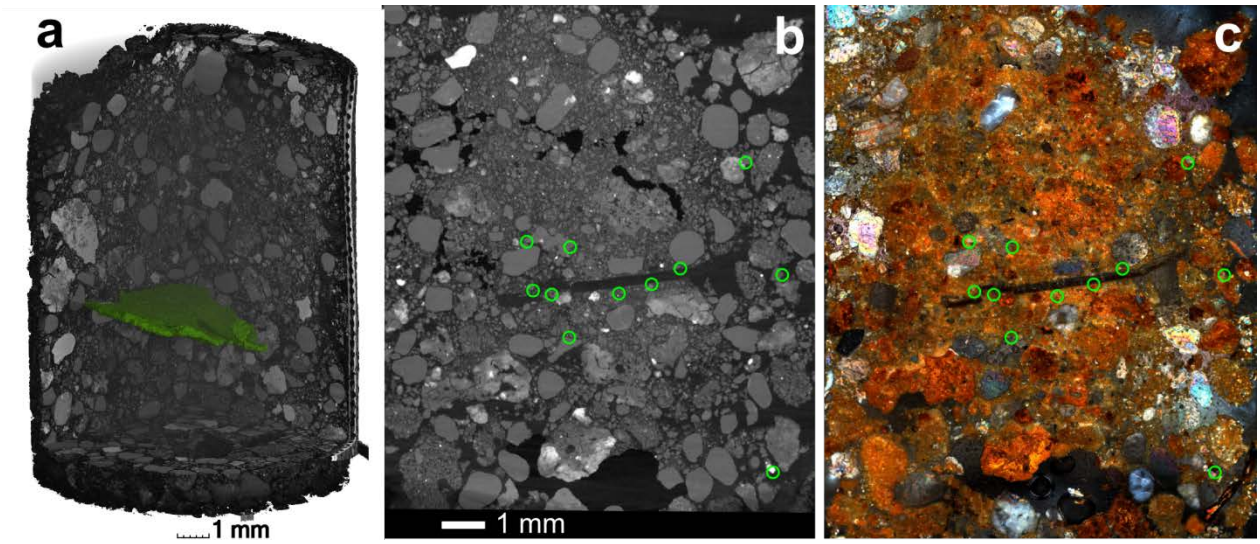

Figure 30: (a) X-ray CT scan with the embedded leaf in green. (b) 2D-3D registration and (c) the reference microscopy image that was used as a target for image registration. Eleven landmarks (green circles) were used for image registration.

After an adequate transformation matrix for the µCT gray scale data had been found, it was used to project the 3D pore size map into the LM plane (Figure 31a). Likewise, the results of a 3D drainage model based on local pore size and global air continuity were also co-registered with the LM plane (Figure 31b), just like the 3D Euclidean distance from any non-air voxel to the closest air-filled pore at a certain capillary pressure (25hPa in Figure 31c). Averaging over all soil voxels in the registered plane results in the mean air distance at this capillary pressure (Figure 31d). This decreases from 0.39mm to 0.12mm when the sample is drained from 18hPa to roughly field capacity (71hPa). The mean air distance in the leaf is a bit higher (0.43mm) at 18hPa because it is occluded in the wet soil matrix. The distance drops to 0.13mm in a narrow range around 25hPa because the small gap that formed above the leaf is invaded by air at that capillary pressure.

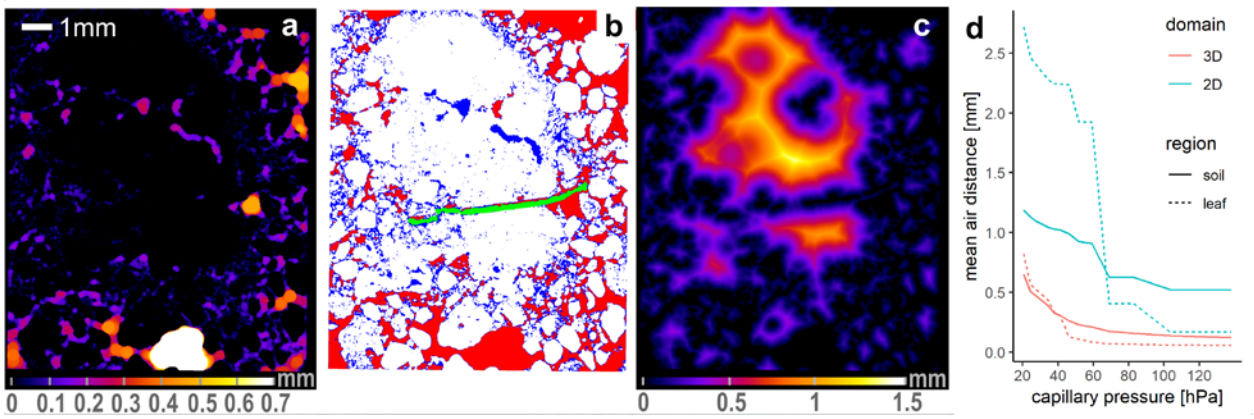

Figure 31: Pore size distribution and modeled air distances: (a) 3D pore size distribution depicted in the 2D reference plane. (b) Modeled distribution of water (blue) and air (red) at a capillary pressure of 50 hPa. Soil and leaf are shown in white and green. (c) 3D Euclidean distance towards air-filled pores at a capillary pressure of 50 hPa. (d) Mean air distance as a function of capillary pressure for the entire soil or the leaf only. Air distribution is either modelled in 3D and 3D distances registered into the LM plane or modelled in 2D on the registered, segmented image.

Such modelled air distances in the LM plane would be vastly overestimated if 3D structural information is not available. The main reasons are that (1) air continuity through the third dimension is lost and that (2)

air-filled pores in close vicinity are ignored, when they are outside of the plane. Even if the connectivity rule is relaxed from the top boundary to all four boundaries, the mean 2D air distances in soil still range from 1.19 mm to 0.52 mm in the investigated capillary pressure range, a three to four fold increase (Figure 31d). Also the critical value to overcome the air-entry pressure of the gap in the vicinity of the leaf is only reached at 70hPa. The reduction in dimensionality always leads to an overestimation of diffusion distances through the water-filled soil matrix. However, the magnitude depends on water saturation and bulk density. Expanding the modelled capillary range to higher capillary pressure could only be achieved with higher image resolution (<7µm) which comes at the expense of smaller sample size. However, it can also be extended by evaluating the pore space in SEM images (Latham et al., 2008) (see below).

Measuring the actual air-water distribution with X-ray CT should always be favored over 3D modelling, since it has become a routine operation even without contrast agents (Geistlinger et al., 2014; Kumahor et al., 2015). If possible, CT scans could be carried out twice, once at the water content of interest and once more after resin impregnation to recover any internal deformation that may occur during fluid displacement and resin curing. Methods for deformation analysis are elastic registration or digital volume correlation (Peth et al., 2010; Schlüter et al., 2016). Finally, there are also resin impregnation protocols that maintain the location of fluid interfaces by sequential application of two differently dyed resins(Seth et al., 2007). However this approach has not been adopted in soil science yet.

Microhabitats

All 2D biogeochemical microscopy results only need to be registered to the LM plane to project co-registered 3D structural information onto them. This is shown for the double excitation fluorescence microscopy results in the supporting information (chapter 6.2 **S2**), which map the auto-fluorescence intensity as a result of local concentrations in plant tissue and other organic compounds. Furthermore, this is shown for blue-excitation fluorescence microscopy (FM) including the cell count results (Figure 32a). Cells counted in 2D thin sections (n=536) corresponded to cell numbers of 1×10^{7} cells g^{-1} soil. This is estimated from the area of the FM scene (19.91 mm^2), the representative observation depth (1 µm) and bulk density (1.3 g/cm^3). Individual bacteria are visible in the enlarged region (Figure 32b), that was subsequently chosen for chemical microscopy. The spatial analysis reveals that bacteria tend to be located near the leaf, which is indicated by a distance ratio of 0.75. That is, a randomly chosen cell has only 75% of the 3D Euclidean distance to the nearest leaf surface as compared to the average leaf distance in the FM image. For this metric the bias caused by only considering 2D leaf distances vanished completely, since the LM plane is oriented roughly normal to the leaf and there is no additional leaf fragment located out of plane. Bacteria also have a preference to reside near pore surfaces with a distance ratio of 0.78. This supports previous findings(Nunan et al., 2003) showing that pore surface preference was strongly developed in subsoil samples of a sandy silt loam, but less evident in the topsoil. One reason for this preference is that bacteria are directly attached to surfaces of air-filled macropores (Flemming et al., 2016; Or et al., 2007), be it in biofilms or open, water-filled capillaries along rough surfaces. Furthermore, cells in bigger pores are moved towards the pore surface when fluids are replaced during sample preparation (Juyal et al., 2019). Another explanation is that bacteria in the water-filled soil matrix are more abundant at oxic sites near air-filled pores than at anoxic sites with longer diffusion distances of dissolved oxygen (Horn et al., 1994). Note that the site preference to visible macropores is also evident if only cells within invisible mesopores are considered (data not shown) which rules out a simple sample preparation artifact. The difference between 3D and 2D distances ratios is again negligible for pore surfaces, this time because the plane is densely populated with many pore surfaces of presumably isotropic shape, so the 2D plane is representative for its proximal 3D vicinity. The absolute distances are larger in 2D than in 3D, but the ratios are comparable.

The spatial distribution of bacteria can also be characterized with respect to the size of pores in which they are located. Roughly 75% of all detected bacteria were found in unresolved mesopores, which are known for their favorable micro-environmental conditions for bacteria (Akbari and Ghoshal, 2015; Crawford et al., 2012; Negassa et al., 2015). Switching from co-registered 3D pore sizes in the LM plane to maximum inscribed circles computed in the 2D plane has hardly any effect on unresolved mesopores, but increases the area fraction of macropores on the expense of narrow macropores. This is a general trend, because obstacles within bigger pores, which are outside of the plane, are ignored with the maximum inscribed circle method in 2D.

In summary, the combination of 3D structural information with 2D fluorescence microscopy opens up completely new avenues for the characterization of soil microbial habitats. The spatial distribution of bacteria are not only analyzed with respect to each other (Raynaud and Nunan, 2014), but with respect to their environment (Juyal et al., 2019; Nunan et al., 2003). Note that segmentation into pores and background could have also been done on the FM image directly (Nunan et al., 2003), as the difference between distance ratios in 3D and 2D were tolerable. However, pore segmentation is much easier with X-ray CT as it directly reflects the local electron density without out-of-focus and illumination artifacts. Comparable results between 3D and 2D pore space attributes like porosity and pore surface area in microbial habitats were also reported in Juyal et al. (2019). We have demonstrated that large differences between 2D and 3D may arise in pore space attributes that rely on pore continuity like drainage processes. In that case a correlative imaging approach with X-ray microtomography is superior to microhabitat characterization with FM only. We showed that bacteria were more abundant in the detritusphere hot spot of a decaying plant leaf, most abundant in mesopores and had a higher site preference for pore surfaces.

The selected DAPI stain, which binds to all accessible DNA, was applied directly on the polished surface after resin impregnation in order to be readily integrated in our imaging pipeline. Combinations with dyes that selectively bind to active or dead cells are feasible (Blagodatskaya and Kuzyakov, 2013; Emerson et al., 2017), but those need to be applied during incubation to interact with the cells. Moreover, phyla-specific cell detection via fluorescence in situ hybridization (FISH) with different probes may reveal differences in microhabitats (e.g. bacteria vs. archaea) (Eickhorst and Tippkötter, 2008), which can also be combined with information of microbial activity using isotopic tracing (Eichorst et al., 2015; Musat et al., 2012; Pett-Ridge and Weber, 2012; Tominski et al., 2018). Finally, microbiological techniques and isotope enrichment can be used to track metabolic activity of individual cells in their microenvironments via mapping with secondary ion mass spectrometry as described below.

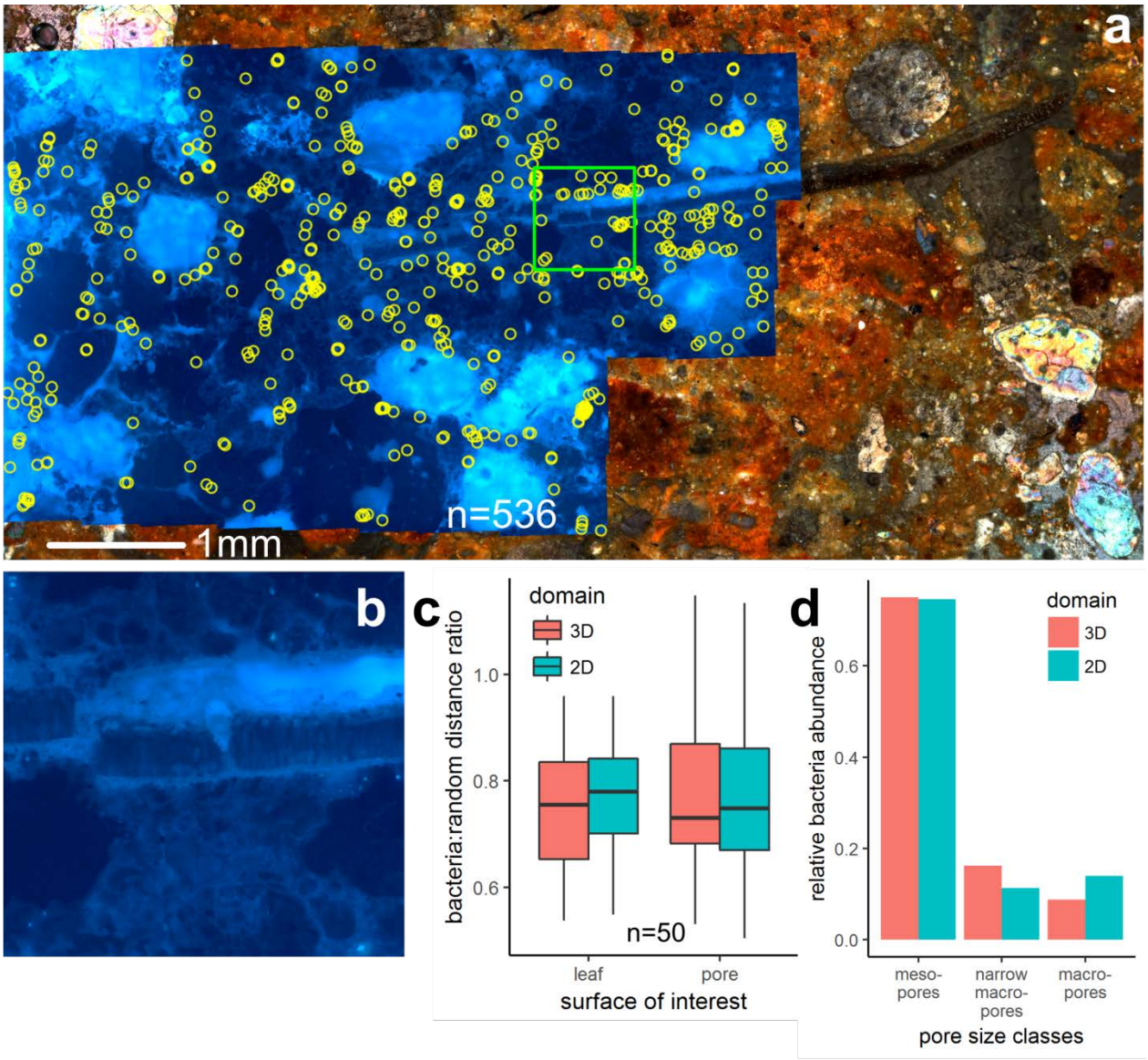

Figure 32: Image registration of fluorescence microscopy data: (a) 2D-2D image registration with fluorescence microscopy (FM) and light microscopy (LM). Yellow circles indicate the spatial distribution of bacteria. The green frame indicates the region enlarged in (b) that was chosen for chemical microscopy in Figure 4. (c) Bacteria distances to the leaf surface or pore surfaces are normalized by distances of randomly chosen points to these surfaces. The data represents 30 samples comprising 30 locations each. *Chemical microscopy*

The backscattered electron microscopy image provides a very good material contrast between mineral particles and the resin to differentiate between pores and soil material. Also the leaf is clearly visible due to distinct small-scale structures of the tissue (plant cells) within an otherwise homogeneous resin (Figure 33a). The dark stripes in the center were caused by prior NanoSIMS imaging due to the sputtering process which removes the Au/Pd layer and thus slightly changes the material contrast of the sample surface, which is a useful effect to relocate NanoSIMS measurements using SEM. Both transects were analyzed using NanoSIMS (Figure 33d), whereas the left transect was a test measurement. SEM provides a good alternative as a bridging technique for image registration, the more so since direct attempts to register

NanoSIMS images into the LM plane failed (data not shown) due to the scale gap between the LM images and the small field of view of the NanoSIMS measurements. It was only successful by means of an additional light microscopy image with only one depth of focus directly targeted at the surface roughness of the resin so that crevices in the resin could be used for corresponding landmarks (Figure 33d). This auxiliary LM image can then be used to align the NanoSIMS transect to the LM image of the entire plane in a second image registration step.

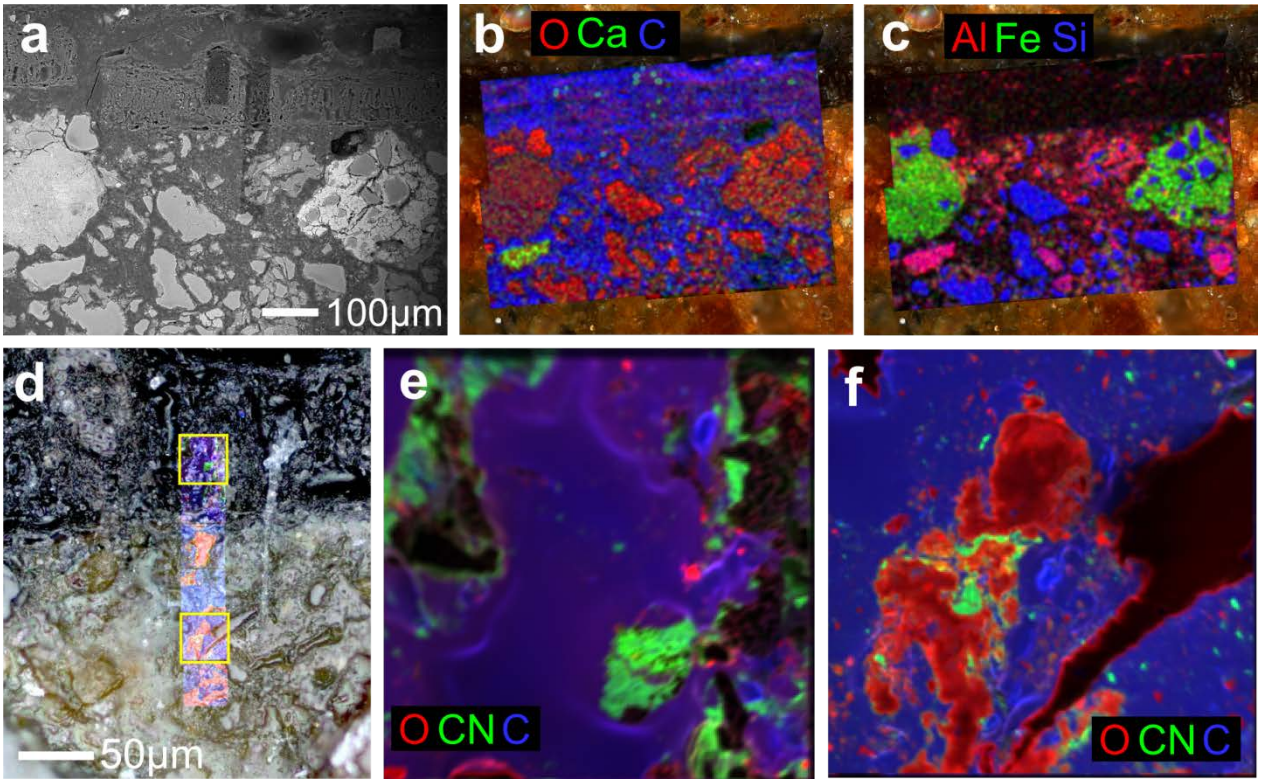

Figure 33: Image registration of chemical microscopy data: (a) unregistered SEM image in back-scattered mode. (b-c) Registered SEM-EDX image showing six elemental distributions in different colors. (d) NanoSIMS transect registered to an auxiliary LM image with depth focus on resin surface. (e-f) Overlay of three ion channels for two scenes in the transect highlighted with a yellow frame in (d).

The SEM-EDX elemental maps are easily registered into the LM plane by using the O- or C-channel with good contrast between mineral particles and the resin (Figure 33b). The resulting transformation matrix can then be employed on other elemental maps that do not contain sufficient structural information like the Ca-channel (Figure 33b). The elemental inventory obtained through SEM-EDX shows a heterogeneous distribution of element concentrations at a small scale (Figure 33b-c). Two iron-rich micro-aggregates contain several smaller, sharply delineated Si-rich minerals, presumably quartz grains encrusted in iron oxide concretions, a feature reported before for Quartz grains within macro-aggregates (Steffens et al., 2017). The soil matrix is composed of a mix between Si-rich (quartz) and Al-rich particles (feldspars, clay minerals). High concentrations of Ca are highly localized, either in the leaf or in individual particles. First attempts have been made to use the correlation between µCT attenuation values and co-located element intensities to extrapolate elemental maps into 3D space via co-kriging (Hapca et al., 2015). This is an elegant approach to fully exploit the potential of correlative imaging.

It was conjectured that the O:C ratio obtained from SEM-EDX could be used to distinguish particulate organic matter from the resin (Hapca et al., 2015). However, our attempts failed (data not shown).

NanoSIMS imaging is a viable alternative in this regard due to the high sensitivity for the detection of organic matter specific $^{12}C^{14}N$ and ^{12}C secondary ion species. In contrast to SEM-EDX, this technique can visualize nitrogen distributions and thus map organic matter (OM) through the detection of cyanide secondary ions ($^{12}C^{14}N$) (Schweizer et al., 2018), which is at very low concentrations in the used epoxy resin. In this transect OM mainly occurs as leaf tissue (Figure 33e) or is occluded in microaggregates (Figure 33f). The high $^{12}C^{14}N$ ion counts at the leaf or particulate organic matter surface and within the microaggregate clearly point to a distinct amount of microbial derived OM (Hatton et al., 2012) . Thus the leaf detritusphere providing easily available substrates supports microbial activity and fosters microaggregate formation by microbial residues as gluing agents (Mueller et al., 2017). This finding correlates well with the higher bacterial cell numbers in the vicinity of the particulate organic matter (Figure 32). Such NanoSIMS transects along a gradient of microenviromental conditions are a formidable tool to detect rhizodeposits through ^{13}C labeling (Clode et al., 2009; Vidal et al., 2018), map zones of different redox conditions across the rhizosphere in paddy soils (Kölbl et al., 2017) or identify different functional domains with soil aggregates with respect to carbon sequestration and nutrient cycling (Steffens et al., 2017).

Acknowledgments

This study was funded by the Deutsche Forschungsgemeinschaft through the research unit DFG-FOR 2337: Denitrification in Agricultural Soils: Integrated Control and Modelling at Various Scales (DASIM). We thank Gertraut Harrington for sample preparation, Max Koehne for CT scanning and Philippe Baveye for inspiring discussions during the preparation of the paper. We are grateful to three anonymous reviewers for the valuable comments.

Supporting information (chapter 6.2)

S1 - Detailed Description of Drainage Model

S2 - Mapping organic compounds with double-excitation fluorescence microscopy

S3 – File link and description of minimum example for 2D-3D registration with Elastix

3. Results and Discussion

3.1. Long-term effects of conventional and reduced tillage on soil structure, soil ecological and soil hydraulic properties (Schlüter et al. Geoderma 2018, 332, 10-19, doi:10.1016/j.geoderma.2018.07.001)

Abstract

There is a long-lasting debate about the effects of tillage practices on soil structure and structure-mediated ecosystem properties like hydraulic conductivity and crop productivity. This is investigated in a long-term field experiment on tillage practices at the Westerfeld trial in Bernburg, Germany (25 years of different management). Here we combine soil structure information obtained by X-ray microtomography with bulk properties like bulk density, air capacity and saturated hydraulic conductivity, as well as integrative, ecological properties like earthworm abundance and crop yield. This study goes beyond previous studies in that the soil microstructure is investigated in two different depths, within (13-23cm) and underneath (28-38cm) the plow horizon. Furthermore the microstructure is investigated at two different resolutions (60µm and 20µm) by employing a nested sampling design.

The plowed horizon in the conventional tillage plots differs from the undisturbed soil underneath the cultivator depth (13-23cm) in the reduced tillage plot by lower bulk density, higher air capacity, higher saturated hydraulic conductivity, higher macroporosity and pore connectivity. After 25 years of reduced tillage saturated hydraulic conductivity only marginally recovered in the abandoned plow pan (28-38 cm). Macropore density and connectivity did not change significantly as compared to the current plow pan under conventional tillage. The topsoil underneath the cultivator depth in the reduced tillage plot developed a “no-till pan”, as porosity and pore connectivity where smaller than in greater soil depths. Image-based macroporosity and laboratory-based air capacity showed good agreement.

Overall, the combination of hydraulic measurements and X-ray CT imaging of soil microstructure at different resolutions provides a comprehensive view on soil structure modification by tillage practices. The change from conventional to reduced tillage led to a compaction of soil that was not compensated by higher bioturbation as reported for other sites. This is explained by unfavorable conditions for anecic earthworms (frequent dry periods with severely impaired penetrability of the loess substrate) as well as the absence of very deep rooting, perennial crops in crop rotation.

Introduction

Conservation agriculture has a profound impact on soil structure and consequently on structure-mediated ecosystem functions like carbon sequestration, greenhouse gas emissions and soil water storage. The benefits of reduced tillage practices as compared to conventional plowing may be lower costs, higher carbon storage, higher energy input/output ratio, reduced erosion, more stability against compaction and lower herbicide loss (Palm et al., 2014; Tebrügge and Düring, 1999). Drawbacks associated with reduced tillage can be a risk of topsoil compaction, reduced aeration and lower soil temperature (Soane et al., 2012). With reduced tillage the absence of plowing typically leads to a loss in air capacity and an increase in bulk density and penetration resistance in the topsoil beneath the tillage depth of disc harrows or other cultivators (Abdollahi et al., 2017; Abdollahi and Munkholm, 2017; Deubel et al., 2011; Pagliai et al., 2004; Rasmussen, 1999; Rücknagel et al., 2017). Saturated hydraulic conductivity (K_s) and infiltration capacity are typically lower under reduced tillage (Abdollahi et al., 2014; Lipiec et al., 2006; Pagliai et al., 2004) but can also exceed values for conventional tillage (Kahlon et al., 2013; Vogeler et al., 2009) depending on whether intact, elongated macropores resulting from root growth and earthworm burrowing activity can compensate for the overall reduction in macroporosity. Rücknagel et al. (2017) compared K_s

values under conventional and reduced tillage in seven field trials in Germany and found comparable (five) or significantly lower (two) K_s values under reduced tillage. A comprehensive literature review about tillage effects on hydraulic properties (Strudley et al., 2008) indicated inconsistent results across soil textures, climate and specific managements with respect to trends in saturated hydraulic conductivity and infiltration capacity. Often temporal and spatial variability mask these long-term treatment effects.

The inconsistent trends between tillage practices and hydraulic properties can be better understood by investigating tillage effects on soil microstructure. In recent years traditional approaches to measuring tillage-induced changes in soil physical properties have been increasingly complemented by the characterization of undisturbed soil structure via non-invasive imaging techniques like X-ray computed tomography (X-ray CT). Attributes of the macropore network measured with X-ray CT and image analysis have been used to explain a range of bulk soil properties like water and solute transport (Larsbo et al., 2014; Paradelo et al., 2016) , soil friability (Munkholm et al., 2012) and soil structure turnover (Schlüter and Vogel, 2016). Studies on management induced changes in pore space attributes mainly comprise fertilization effects (Dal Ferro et al., 2013; Naveed et al., 2014; Schlüter et al., 2011) and tillage effects (Dal Ferro et al., 2014; Garbout et al., 2013; Kravchenko et al., 2011; Pöhlitz et al., 2018). A typical outcome of these studies is that visible porosity above the image resolution is highly correlated with bulk density, since unresolved micro- and mesoporosity is less affected by management practices. Plow horizons with loose soil structure typically have an isotropic, well connected pore network, whereas macropores in unplowed soil tend to be less connected and more vertical and anisotropic, since they mainly evolve from bioturbation and are less susceptible to concomitant compaction (Hartge and Bohne, 1983).

One major shortcoming of soil structure analysis with X-ray CT is the trade-off between image resolution and sample size, with a fixed factor of 1000-2000 depending on the X-ray detector hardware (Rabot et al., 2018). Information on mesopores (<10µm or <50µm depending on definition) can only be achieved with small soil cores or individual aggregates (Crawford et al., 2012; Kravchenko et al., 2011; Schlüter and Vogel, 2016), whereas representative samples for preferential flow in large macropores require big samples up to 20cm in diameter with image resolutions of 100µm and larger (Luo et al., 2008; Paradelo et al., 2016). Nested sampling strategies are a viable strategy to extend the scale window towards mesopores (Dal Ferro et al., 2013; Schlüter et al., 2011; Vogel et al., 2010). First a soil column is scanned at coarse resolution and then subsamples are extracted and scanned at a higher resolution, so that eventually the pore size distribution from both scales can be merged. A second shortcoming of X-ray tomography is the time and labor for taking undisturbed soil columns at large soil depths as well as the time-consuming image analysis of large datasets. While soil physical properties like penetration resistance, air capacity or bulk density are easily measured at high spatial resolution for entire soil profiles (Abdollahi et al., 2017; Deubel et al., 2011), X-ray CT studies on tillage practices are often restricted to soil samples from one depth within the first 30cm.

This paper addresses both shortcomings by employing a nested sampling design in two soil depths, the plow horizon and the deeper soil partially covering the plow pan. The objective of the paper is (1) study changes in pore space attributes after 25years of reduced tillage in a long-term field trial on tillage effects and (2) to relate these changes in pore morphology to soil physical properties like bulk density, air capacity and saturated hydraulic conductivity as well as ecological properties like earthworm abundance and crop yield.

Materials and Methods

Field site

The long-term tillage trial at the Westerfeld site in Bernburg, Germany, was established in 1992 (Deubel et al., 2011). The Chernozem soil (WRB) is developed on loess over limestone and has a texture of 8% sand, 79% silt and 13% clay (0-30cm). The average annual temperature is 9.7°C with a rather low average annual precipitation of 511mm (1981-2010). The crop rotation on five experimental blocks (1.2ha each) is grain maize (*Zea maize*), winter wheat (*Triticum aestivum*), winter barley (*Hordeum vulgare*), winter rape (*Brassica napus ssp. napus*) and again winter wheat. N-fertilization is site-specific and pest management as required. An experimental block consists of four non-randomized plots, each split into two subplots with different tillage practices, resulting in a total of 40 subplots. Reduced tillage (RT), is carried out as stubble processing and soil loosening with a cultivator (down to 12-15cm), whereas conventional tillage (CT) comprises stubble control and soil turning with a moldboard plow (down to 20-30cm, varying depth to reduce plow pan). All residues remain on the field after harvest.

Yields [dt ha^{-1}] were measured every year as triplicates per subplot (total of twelve harvest plots per crop and tillage treatment, each 18 m^2, threshed with a parcel harvester). Grain yields are reported here as averages for the period 2012-2016 with 14% and 9% moisture for cereals and oilseed rape, respectively. Earthworm abundance was determined with hand sampling of the topsoil down to a depth of 30cm in combination with subsoil extraction by 0.2% formaldehyde solution on eight replicated areas (0,125m^2), i.e. two per sub-plot (DIN ISO 23611-1, 2007). Sampling was carried out in 2016 on the maize block, which was also used for undisturbed soil sampling in the following year (see section 2.2. below). Values are reported as numbers of individuals [m^{-2}] and biomass [g m^{-2}] and aggregated into anecic and endogeic species as well as adults and juveniles, whereas epigeic species where absent. Older time series (2010-2013/14) for rape and wheat on rotating blocks are also reported here.

Sampling

Soil sampling took place in April 2017 on the winter wheat block (after maize in 2016), six months after last tillage. Undisturbed soil cores for X-ray tomography analysis were taken by pushing down polycarbonate cylinders (94mm inner diameter, 100m height, 694cm^3) with a rotating sampling device (sample ring extraction device, UGT GmbH, Germany) (Kuka et al., 2013) in two different depths. The first depth (13-23cm) corresponds to the plow horizon in the conventional tillage plots (CT) or the lower topsoil beneath the tillage depth of the cultivator in the conservation tillage plots (RT). Previous studies at this site demonstrated large differences in penetration resistance (CT: 0.6MPa, RT: 1.4MPa), bulk density (CT: 1.25g/cm^3, RT:1.52g/cm^3) and air capacity (CT: 17%, RT: 6%) in that depth (Deubel et al., 2011). The second depth (28-38cm) corresponds to deeper soil within and underneath the compacted plow pan in CT plots and the former plow pan in the RT treatment. Reported soil physical properties (Deubel et al., 2011) in that depth indicate higher compaction in the conventional tillage plots (penetration resistance – CT: 1.4MPa, RT: 1MPa, bulk density - CT: 1.42g/cm^3, RT:1.35g/cm^3, air capacity - CT: 9%, RT: 11%). Two samples per tillage sub-plot and depth were taken from each of the four plots in the winter wheat block, constituting a total of 32 undisturbed samples. For soil physical laboratory analysis 32 smaller, undisturbed soil samples (250cm^3) were taken in the same pits. All results will be presented as averages out of two samples per sub-plot, i.e. n=4 for each tillage practice and depth. Samples were stored at 4°C until X-ray CT scanning and soil physical analysis.

Soil physical analysis

Samples were fully saturated and then the volumetric water loss after drainage to a matric potential of h_m=-60hPa on a sand box (DIN ISO 11274-1, 2001) was measured to derive air capacity, i.e. the volume fraction of air-filled pores at field capacity. Subsequently, samples were fully saturated again and placed into a constant-head percolation apparatus (Klute and Dirksen, 1986) for 4h to measure saturated hydraulic conductivity. Finally, bulk density was determined after drying the samples at 105°C for 24h.

X-ray tomography analysis

Samples were scanned with an X-ray CT scanner (X-tek XMT 225, Nikon Metrology) at an energy of 195kV and a beam current of 280-300µA using a 1.5mm Cu filter for beam hardening reduction. 2800 projections were acquired with an exposure time of 700mS and two frames per projection. The projections were reconstructed into a 3D tomogram with a voxel resolution of 60µm using the filtered back projection method implemented in the X-tex CT Pro software. Another 36 smaller subsamples (26mm inner diameter, 30mm height, volume 16cm³) were taken from within the bigger cores with a smaller sampling device (soil sample minimizer, UGT GmbH, Germany). These were scanned at an energy of 130kV and a beam current of 150µA using a 0.1mm Cu filter and reconstructed into 3D tomogram with a voxel resolution of 20µm.

Image Processing and analysis was done with the Fiji software (Schindelin et al., 2012). The raw images were filtered with a non-local means filter (Buades et al., 2005) for noise removal and an unsharp mask (Schlüter et al., 2014) for edge enhancement. Vertical intensity drifts were corrected by normalizing the gray values with the average soil matrix gray value in each horizontal slice (Schlüter et al., 2016). Objective image segmentation into pores and soil matrix was carried out by combining gray scale and edge information (Schlüter et al., 2010). First, thresholds were automatically determined as the average gray value within gradient masks that focus only on the partial volume effects on pore boundaries. Then, hysteresis thresholding implemented in the 3D ImageJ Suite (Ollion et al., 2013) is applied with these thresholds, which efficiently removes segmentation noise while preserving the intact pore network. The segmented images were analyzed with respect to pore size distributions (PSD) by employing the maximum inscribed sphere method implemented in BoneJ (Doube et al., 2010). A joint pore size distribution was constructed by merging the information from the whole column X-ray CT scans and the high-resolution subsample scans (Schlüter et al., 2011). The visible porosity is derived from this joint PSD. The pore connectivity is estimated for both scales independently from the 2nd moment of the cluster size distribution, the so-called Γ indicator or connection probability (Renard and Allard, 2013; Schlüter et al., 2014), where $\Gamma = 1$ for a perfectly connected pore network and $\Gamma \to 0$ for many equal-sized, isolated pores. The connection probability corresponds to the volume fraction of the largest pore cluster squared. The cluster size distribution is computed by labeling connected components in the MorphoLibJ plugin (Legland et al., 2016) in Fiji. The whole image processing workflow is summarized in Figure 1.

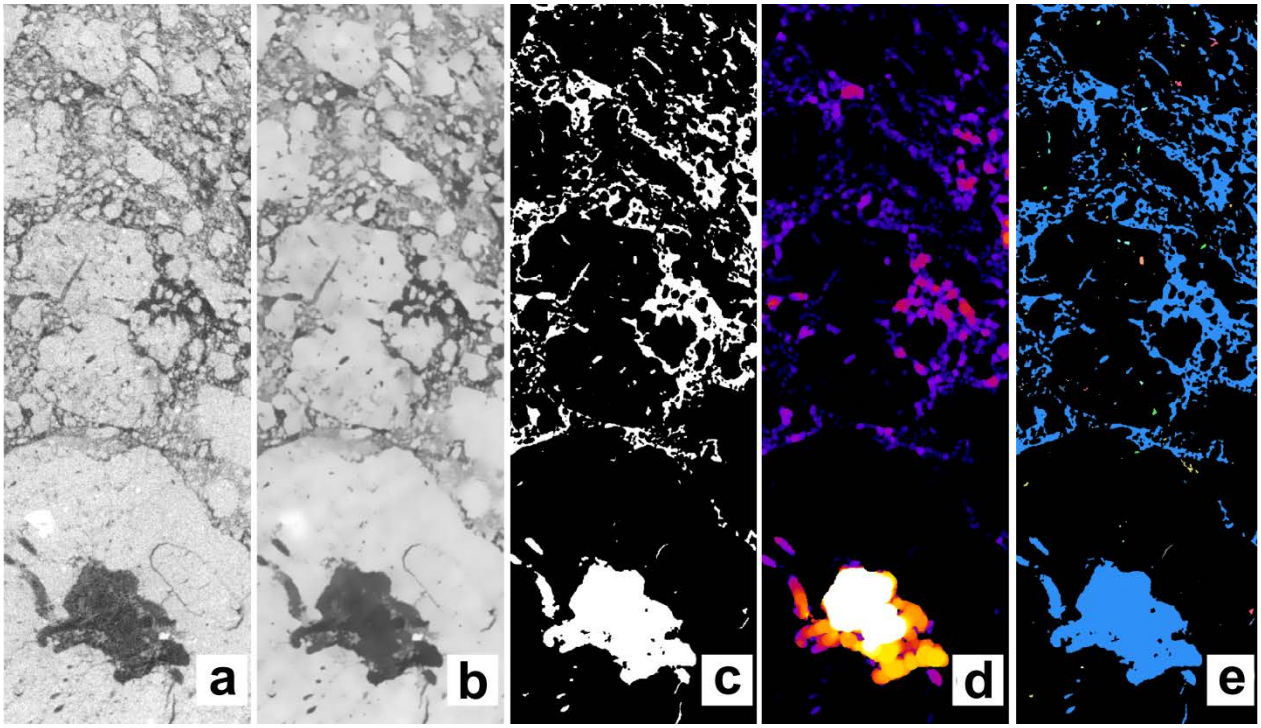

Figure 34: Demonstration of the image workflow with a2D slice of an X-ray CT scan: (a) raw image, (b) noise removal with a non-local means filter, (c) segmentation with hysteresis thresholding, (d) pore size distribution according to maximum inscribed sphere method, (e) connected components labelling to derive the connectivity indicator Γ.

Statistics

All statistical analyses were conducted in R (R Core Team, 2017). Saturated hydraulic conductivity was log-transformed ($\log_{10}(K_s)$) prior to statistical analysis. The effect of tillage and depth on various response variables is explored with two-way ANOVA tests allowing synergistic effects due to interaction between the two factors. Normality in the residuals was confirmed visually and with Shapiro-Wilk tests. The multiple pair-wise comparisons between tillage treatments in one depth and between depths for one tillage treatment are conducted with Tukey Honest Significant Differences and tested at a probability value of p=0.05. Linear models were employed for linear regression between an individual factor and a dependent variable. The joint effect of various pore space attributes on hydraulic conductivity was explored with partial least squares regression implemented in the *pls* package (Mevik, 2016).

Results

Soil physical properties

Results for bulk density (BD), air capacity (AC) and log-transformed saturated hydraulic conductivity ($\log_{10}(K_s)$) for both tillages practices and both depths are depicted in Figure 2. The plow horizon in the CT subplot has by far the lowest bulk density. Bulk densities in greater depths (28-38 cm) are similar for both tillage practices. The lower topsoil in the RT plot exhibits a minor trend towards higher bulk densities than the soil underneath (p=0.21). These differences in bulk density are mainly caused by differences in big structural pores, as the differences are reflected in air capacity (Figure 2b). The plow horizon in the CT plots has the highest AC, the lower topsoil in the RT plots exhibit and trend towards lower AC than the deeper soil (p=0.09), and means do not differ significantly between CT and RT in deeper soil. The general trends are similar for saturated hydraulic conductivity, yet differences in are not

significant due to high standard deviations, except for the difference between the plow horizon and the plow pan in the CT plots. The $\log_{10}(K_s)$ values in the abandoned plow pan (RT - 28-38 cm) are larger than in current the plow pan in the conventional tillage plot (CT - 28-38 cm), but this recovery is not significant (p=0.25) due to large spatial variability.

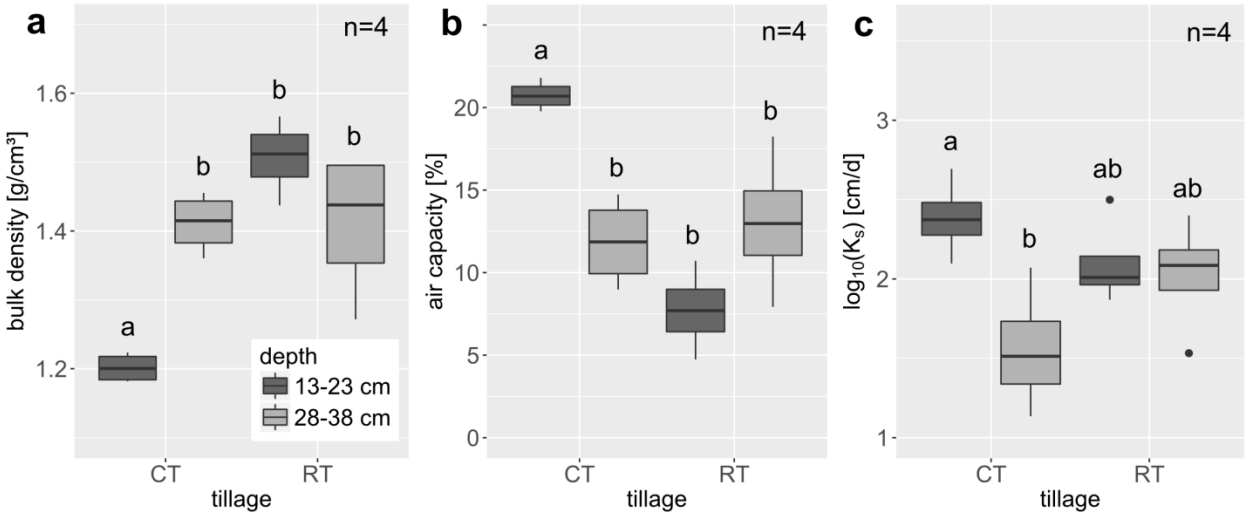

Figure 35: Soil physical properties including (a) bulk density, (b) air capacity and (c) saturated hydraulic conductivity at two depths in both tillage treatments (CT - conventional tillage, RT - reduced tillage). Different letters represent significant differences between treatments (p<0.05).

Visual assessment

These quantitative results of soil physical properties are reflected in the morphology of the microstructure depicted for selected topsoil samples (13-23cm depth) of the CT and RT plot in Figure 3. Plowing results in clearly distinguishable aggregates in the CT plots from the microscale up to clods >1cm embedded in a loose soil matrix with high macroporosity. Plant residues of maize grown in the previous growing season can be found in a depth of 13-23cm. The lower topsoil of the RT plots has a more compact, coherent structure, in which clearly separated aggregates are not visible anymore and the loose matrix around them is still faintly visible in patches. Root channels and earthworm burrows, partly refilled, stand out against the coherent soil matrix.

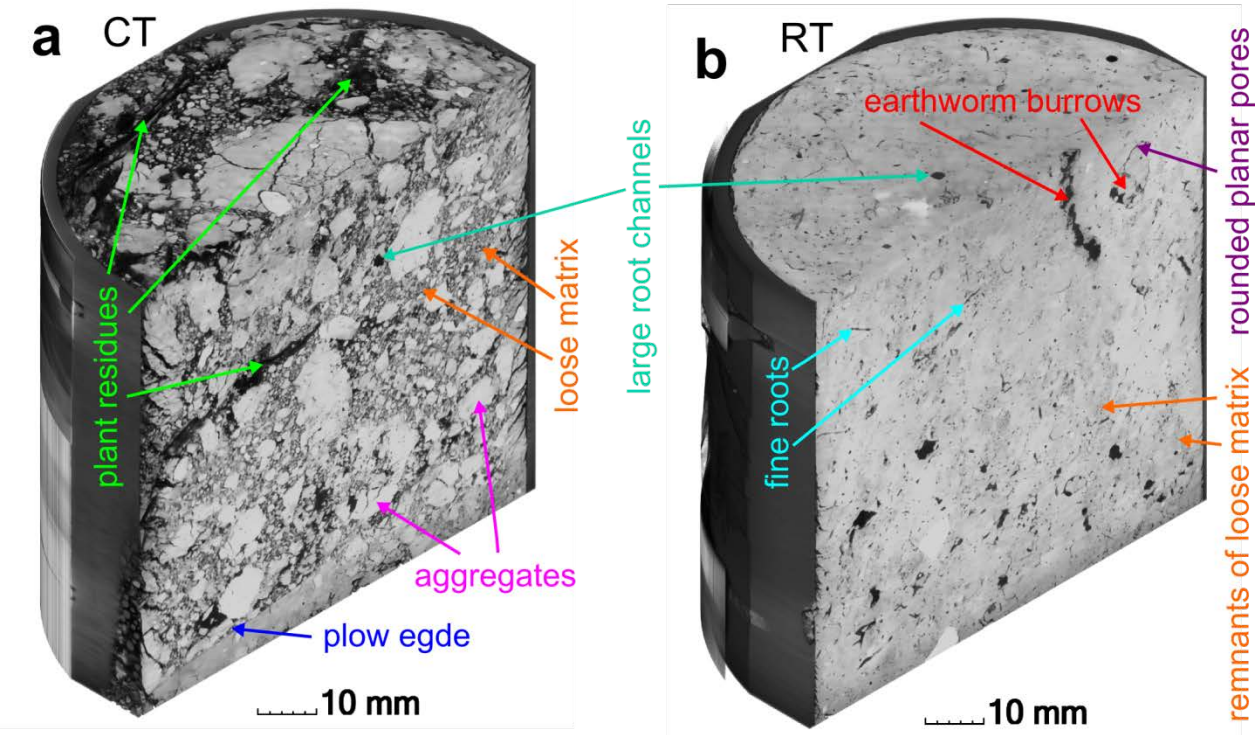

Figure 36: Typical examples of a plowed topsoil in the CT plot (a) and unplowed topsoil in the RT plot (b) at a depth of 13-23cm scanned with X-ray CT. Salient features are marked with arrows.

The microstructure in deeper soil (28-38cm depth) of the CT and RT plot is shown in Figure 4. Bioturbation dominates as the main structure forming agent in both plots. The top part (28-30cm) of the CT sample (Figure 4a) has the lowest abundance of root channels (marked in yellow) and seems to originate from the plow pan. Underneath this plow pan there seems to be a homogeneous macropore density, i.e. no further vertical trends in visible porosity. The former plow pan in the RT plot (Figure 4b) is pervaded with rounded planar pores, also denoted as planar packing poroids (Hubert et al., 2007) probably forming along former earthworm burrows as shown in Figure 3(b).

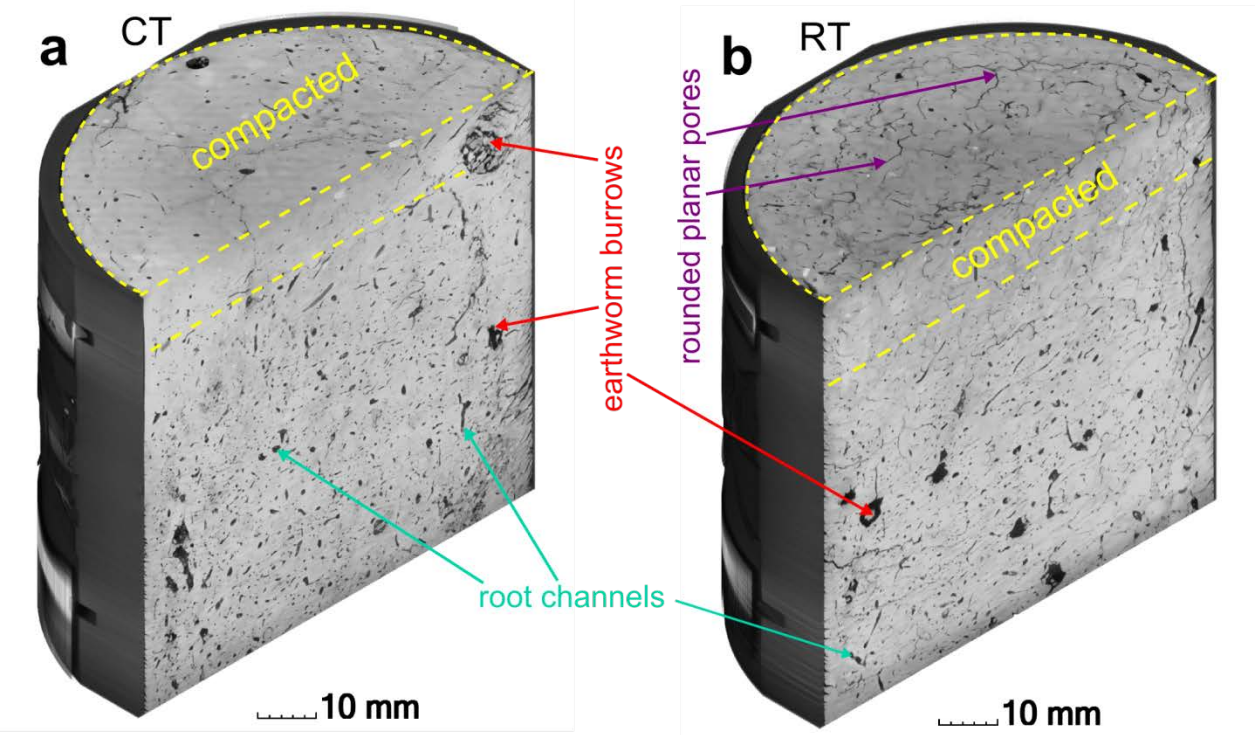

Figure 37: Typical examples of a compacted plow pan in the CT plot (a) and an abandoned plow pan in the RT plot (b) at a depth of 28-38cm scanned with X-ray CT. Salient features are marked with arrows.

Pore structure properties

The volume fraction of visible pores depends on the image resolution and the total volume of the scanned samples. This is demonstrated for the plow horizon of the CT plots (Figure 5a). The frequency distribution of pore diameters derived by class width (unit: mm^{-1}) allows for comparison of pore size distributions from different sample sizes with different step sizes in pore diameters. Pore diameters <0.15mm are ignored for the whole column scans (10cm samples) with an image resolution of 0.06mm. Moreover, pore diameters < 0.25mm are also underrepresented as compared to the high-resolution scans, because small pores in the same size range like image noise are removed during image processing. Pore diameters >0.25mm, in turn, are underrepresented in high-resolution scans (3cm sample, 0.02m image resolution) for two reasons: First, the chance to capture big pores in a small soil volume is lower. Secondly, individual particles attached to bigger pores are well-resolved, so that pores > 0.25mm fall apart into several smaller pores when employing the maximum inscribed sphere method. A joint frequency distributions is constructed by taking the maximum of both frequencies values at each pore diameter (Schlüter et al., 2011). The individual and joint, cumulative pore size distribution is obtained by integrating over all pore diameters (starting at the largest pore) and multiplying with respective porosities (Figure 5a, inset). They represent the volume fraction of pores larger than a certain pore diameter, where final points indicate total, visible porosity. The pore size distribution for the other tillage treatment and soil depth are presented as supplementary information, both as class derivatives (SI 6.3 Figure S 5) and cumulative pore size distributions (SI 6.3 Figure S 6). Total visible porosity from individual sample sizes and joint curves show a consistent trend towards higher visible porosity in the high-resolution scans among all treatments (Figure 5b) as small macropores typical for silt-rich textures is captured better at an image resolution of 0.02mm. In line with air capacity results (Figure 2b), the plow horizon (CT, 13-23cm) has by far the highest visible porosity. The untilled topsoil (RT, 13-23cm) has a lower visible porosity than greater soil depths (CT & RT, 28-38cm) at each scale, but the differences are not significant. The

unresolved porosity (micro- and mesopores) is fairly similar with 28-32% for both depths and tillage treatments, when the visible porosity in the 3cm samples is subtracted from the total porosity (data not shown).

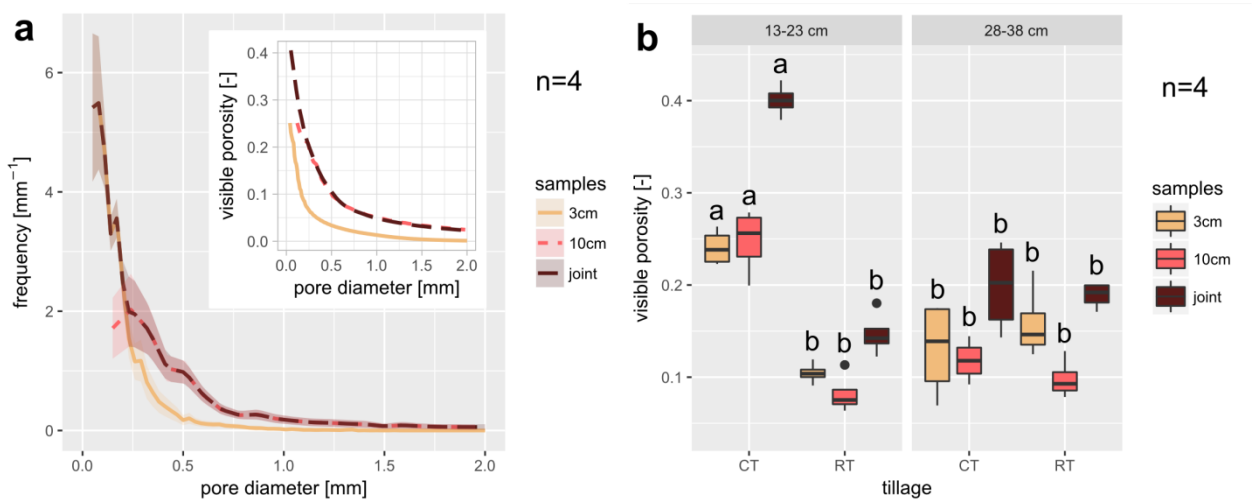

Figure 38:(a) Frequency of pore diameters derived by class width (unit: mm^{-1}) allows for comparison of pore size distributions from different sample sizes (different diameter steps). Data is shown for the plow horizon (CT, 13-23cm). A joint frequency distribution and a joint, cumulative pore size distribution (inset) is obtained according to Figure S1,S2. (b) Visible porosity at individual or joint scales for both depths and tillage treatments (CT - conventional tillage, RT - reduced tillage). Different letters represent significant differences in visible porosity at a given scale.

The pore connectivity represented by the Γ indicator is shown only for the individual sample sizes as it is not straightforward to combine information from both scales into a joint connection probability (Figure 6a). Again, pore connectivity is higher in the small samples, most likely because small pore throats are resolved better at higher image resolution. In line with visible porosity (Figure 5b), the pore connectivity is highest in the plow horizon (CT, 13-23cm). With $\Gamma > 0.95$ almost the entire pore network is comprised of one connected pore cluster with only few isolated pores (e.g. Figure 1e).The Γ indicator in the untilled topsoil (RT, 13-23cm) has a significantly lower connection probability than greater soil depths, whereas the difference in Γ between both tillage treatments in deeper soil is not significant (CT & RT, 28-38cm). In general, the connection probabilities are rather high with $\Gamma > 0.6$ for all depths, i.e. one connected pore cluster always dominates. There is a non-linear relationship between visible porosity and pore connectivity for both resolutions (Figure 6b). The general shape is similar to a previous study (Schlüter and Vogel, 2016) in which complete connection probability ($\Gamma > 0.95$) was also achieved around a visible porosity of 20% and Γ quickly diverged from zero beyond the critical value around 3-5%. Interestingly, a smaller sample diameter induces a small right-shift in the scatter plot, but only for the untilled topsoil (RT, 13-23cm). Apparently, the gain in porosity due to a higher resolution is higher than the gain in connection probability, whereas in the other treatments both gains are more balanced.

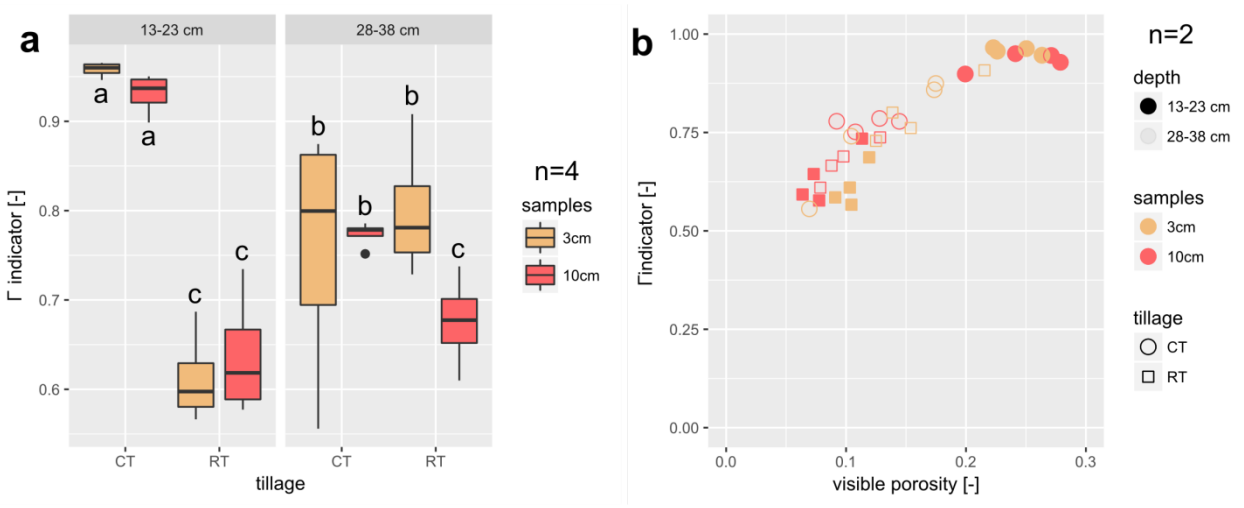

Figure 39: (a) Connectivity indicator Γ for both depths and tillage treatments (CT - conventional tillage, RT - reduced tillage). Data is shown for two different sample diameters. Different letters represent significant differences ($p<0.05$) at a given scale. (b) Non-linear relationship between visible porosity and connectivity indicator Γ lumped over all data points shows slight differences between the two sample sizes.

Average pore diameters, i.e. the first central moment of the pore size distribution, are shown for individual sample diameters and joint data in each depth and tillage treatment (Figure 7a). Obviously, they are quite different for different sample sizes, with average pore diameters derived from the joint pore size distribution in between the averages for whole-columns scans (10cm sample) and 3cm subsamples. More importantly, there are no significant differences between RT and CT in both depths. This indicates that the increase in porosity in the plow horizon is equally distributed among all pore diameters (Fig. S2) so that the average pore size does not change much. The relationship between porosity and average pore diameter is stronger when plotted individually for both tillage treatments and depths, so that characteristic differences in pore morphologies are accounted for (Figure 7b). There is a clear linear trend ($R^2=0.995$) for the plow horizon with a high proportion of packing pores between soil clods. The drift in porosity and pore size may be caused by a spatial gradient in soil structure stability along the four plots, in particular in the stability of big, abiotic packing pores, as the trend is absent in the small samples. Presumably this trend is caused by a known gradient in lime content due to a spatial gradient in the shallowness of the loess layer above limestone. In the other tillage treatment and soil depth there are less packing pores due to absent plowing and bioturbation pores dominates, for which soil structure stability seems to be less relevant.

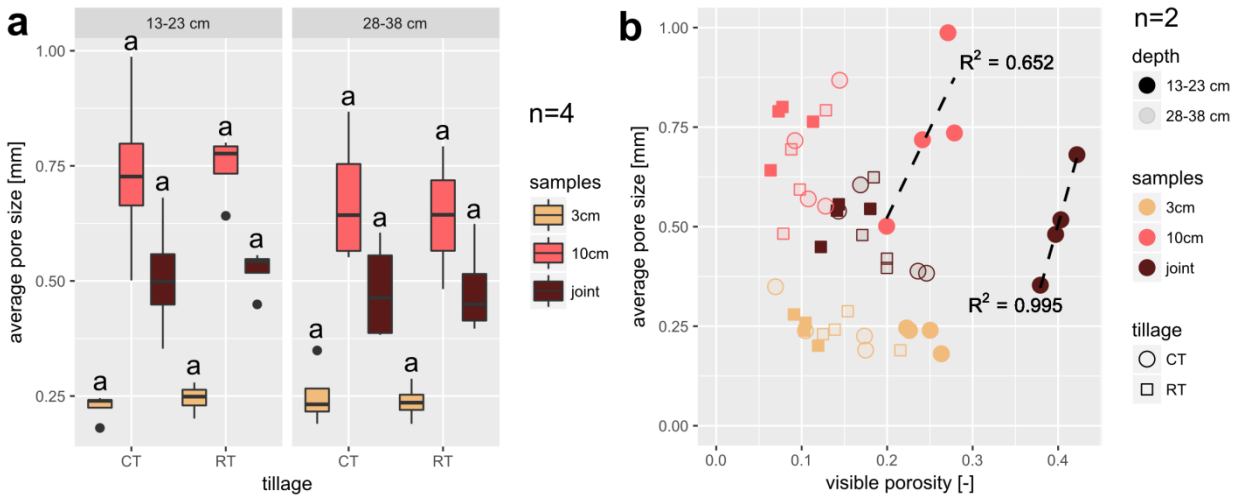

Figure 40: (a) Average pore size at individual or joint scales for both depths and tillage treatments (CT - conventional tillage, RT - reduced tillage). Different letters represent significant differences in visible porosity at a given scale. (b) No clear trends between visible porosity and average pore size except for macroporosity in the plow horizon (CT - 13-23 cm).

Comparison between soil physical and structural properties

A direct comparison between air capacity and visible porosity arises from the capillary rise equation recast in the simplified form $h_m[-hPa] \approx \frac{3}{d}\ [mm]$. In a simplified capillary bundle model of soil all pores with a diameter d>0.05mm will be air-filled at field capacity (matric potential $h_m = -60$ hPa). Hence, this air capacity should be in line with visible porosity in the whole-column scans (10cm sample), where the image resolution (0.06mm) is similar to this critical pore diameter. In fact, pores<0.15mm are underrepresented in the 10cm samples and visible porosity in the 3cm samples should be a better estimate for small air-filled pores. However, the support volume in 10cm samples is much bigger so that macropores are captured more representatively. Indeed, air capacity can be predicted from visible porosity fairly well (R^2=0.711) despite being measured at different samples (Figure 8a). The regression line is close to the 1:1 line. The slope is slightly smaller as the aforementioned underestimation seems to be more important when macroporosity is high.

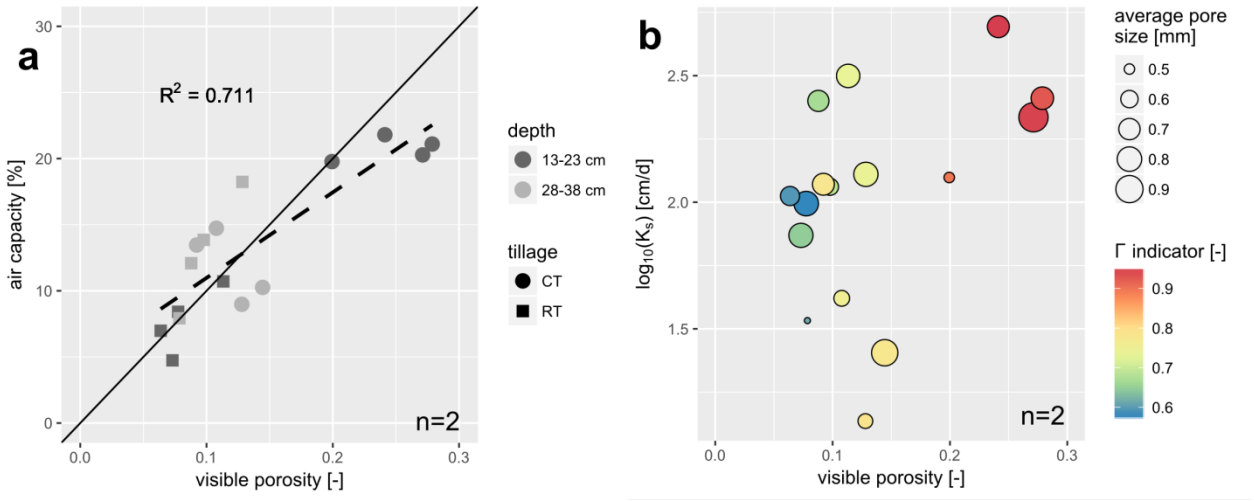

Figure 41: (a) Regression between visible porosity in 10cm samples and air capacity at the subplot level. (b) Relationship between image-derived soil structure properties (visible porosity, connectivity indicator Γ, average pore size) and saturated hydraulic conductivity $\log_{10}(K_s)$ at the subplot level.

The saturated hydraulic conductivity $\log_{10}(K_s)$ is governed by the hydraulic radius of macropores and the overall abundance and continuity of macropores. These pore space attributes should be reflected in measured average pore diameter, visible porosity and the pore connectivity Γ. Yet, visible porosity only explains 18.0% of the observed variability in $\log_{10}(K_s)$ at the subplot level, a value that is only increased to 23.7% if all three properties are jointly taken into account by employing partial least square analysis. This low predictive power is not surprising as $\log_{10}(K_s)$ and soil structure properties were measured at different samples. $K_s$has a notoriously high spatial variability and only two samples were averaged per subplot and depth. Pore connectivity is highly correlated with porosity and therefore does not contribute additional predictive power (Figure 6b). Average pore size provides complementary information as it reflects the presence of large macropores, which again exhibits large spatial variability that might be poorly represented by 1.4L of soil per subplot and depth (n=2).

Soil ecological properties

Tillage had no consistent effect on grain yield across the crop rotation. Differences in the 'wheat after maize' block used for soil sampling are negligible (Figure 9a). The earthworm abundance in the sampled block one year prior to undisturbed soil sampling showed clear differences between the tillage treatments (Figure 9b). The numbers per m² in the conventional tillage plot (54) is less than half the number in the reduced tillage plot (133). Endogeic juveniles with small mass contribute the highest fraction of all ecophysiological categories. The total earthworm biomass in the CT treatment therefore amounts to a smaller gap of only 78% of the RT treatment. Results from additional earthworm abundance sampling campaigns in previous years (2010-14) for other crops (oilseed rape, winter wheat after rape) on the same long-term trial paint a fairly consistent picture of lower earthworm abundance in the conventional tillage plots (SI 6.3 Figure S 5). The numbers and biomass per m² in the CT plots only amount to 68 and 75% of values in the RT plots, respectively. In eight out of ten comparisons earthworm abundance was higher in RT plots. However, weather-dependent differences between the years and even differences between investigated crops were as high as or higher than tillage-induced differences.

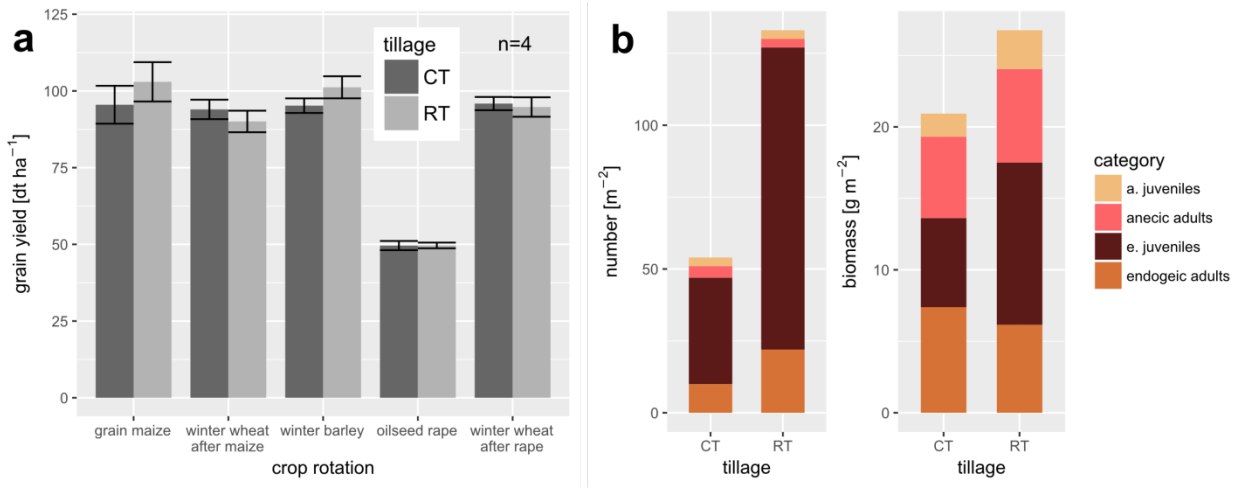

Figure 42: (a) Crop yields for the period 2012-2016 across all five crops for both tillage treatments (CT – conventional tillage, RT – reduced tillage). There are no significant differences (p<0.05) between tillage treatment for any crop. (b) Earthworm abundance in terms of numbers and biomass in the two tillage treatments on the grain maize block in 2016.

Discussion

Tillage effect on structural properties after 25 years

In the RT plots a very compact soil structure has evolved in the lower topsoil (13-23cm) that has not been plowed for 25 years. Bulk density (1.50g/cm³) even exceeded and air capacity (7.7%) fell below values observed in deeper soil horizons covering the recent (CT, 28-38cm: 1.41 g/cm³, 11.9 %) or former plow pan (RT, 28-38cm: 1.41 g/cm³, 13.0 %). This confirms previous results from the RT plots in the same long-term trail (Deubel et al., 2011) that indicate a higher bulk density (1.52 g/cm³), lower air capacity (6 %) and higher penetration resistance (1.4 MPa) in the lower topsoil (15-30cm) as compared to the former plow pan below (1.35 g/cm³, 11%, 1.0 MPa). These vertical differences in soil physical properties within the soil profile of RT plots are confirmed by a decrease in image-derived macroporosity and macropore connectivity in the lower topsoil. Similar results, including the existence of a so-called "no-till pan" after many years of deep-reduced conservation tillage have already been reported by Reichert et al. (2009) and Rücknagel et al. (2017). This can be explained by the stresses exerted to the soil by agricultural machinery. The mechanical load induces a primarily vertical normal stress in the center of the load axis, which decreases with increasing distance from the wheel-to-ground contact surface (Rücknagel et al., 2015; Soehne, 1953). Hence the vertical stresses exerted by the majority of tillage operations are higher in 13-23cm depth within RT subplots than in 28-38cm depth within RT or CT subplots, which may have caused the observed compaction in the upper RT layer. Only in areas where the tractor wheel drives directly in the furrow during ploughing, larger vertical stresses are directly exerted to the subsoil (Weisskopf et al., 2000). In the investigated Bernburg tillage trial, however, this operation is carried out only once a year on the CT subplots with a proportion between the overrun area by the wheels and the total furrow area of only about 40 %. This is relatively small in comparison to overrun area fractions of more than 80% reported by Kroulik et al. (2012).

The old and recent plow pan was clearly visible in the top part of X-ray CT scans of soil samples taken at a depth of 28-38cm (Figure 4) but in fact stretches across a much larger depth range of 25-55cm as shown by penetrometer measurements (Deubel et al., 2011). Despite 25 years without plowing, the functional recovery of the old plow pan by conservation tillage as shown visually in Figure 4(b) has not yet resulted in quantitative differences in terms of BD, AC, macropore density and connectivity although the abundance of earthworms is higher. The $\log_{10}(K_s)$ values only show a small, non-significant recovery.

This finding is consistent with the results of other long-term tillage trials in Central Germany (Hofmann et al., 1993; Rücknagel et al., 2004). Tests on the persistence of soil compaction in the subsoil have also repeatedly shown that it can exist over a long period of time (Alakukku, 1996; Berisso et al., 2012). The most important drivers of natural regeneration for compacted soils are swelling and shrinking processes as a result of wetting and drying (Dexter, 1988), the activity of earthworms and the cultivation of perennial, deep-rooting arable crops. In particular, earth worm and deep roots promote the formation of biogenic macropores and the infiltration of water (Kautz et al., 2010; Meek et al., 1989). However, perennial crops are not integrated in the crop rotation of this long-term trial, so that microstructural processes are limited to swelling and shrinkage as well as earthworm activity. For reasons discussed below the higher earthworm abundance in the RT plots has only induced a minor trend towards higher saturated hydraulic conductivity ($p=0.23$), but no recovery in terms of average structural properties.

Interplay between tillage effects and ecological properties

The the compacted lower topsoil of the RT subplots (13-23 cm) essentially meets the minimum requirements for an intact soil structure of 8 % air capacity and a saturated hydraulic conductivity of 10 cm/d (Werner and Paul, 1999).The optimum dry density for the given texture of approx. 1.40 g/cm³ is only exceeded moderately (Kaufmann et al., 2010). As a consequence, soil structure is not limiting for plant growth and has no unfavorable effect on crop yield.

The earthworm population at the Bernburg site is comparable to similar sites (Koblenz et al., 2015; Ulrich et al., 2010; van Capelle et al., 2012) which are also subject to annual fluctuations in earthworm abundance. Absolute values in another long-term tillage trial in Seehausen, Central Germany, with similar soil texture and climatic conditions differed between 120 m^{-2} (30 g/m²) for CT and 220/m² (65 g/m²) for RT (Ulrich et al., 2010), which is at the higher end of values reported here (Figure 9b, Figure S3). Although other studies highlighted the importance of earthworms for the regeneration of compacted soils, internal soil relocation by burrowing activity can create additional macropores without reducing the bulk density of the entire soil (Capowiez et al., 2012). The increased earthworm abundance in the RT plots did not lead to a sufficient gain in macropore density to compensate the reduction in saturated hydraulic conductivity caused by the absence of plowing. One reason may be the low number of adult individuals of anecic species like *Lumbricus terrestris*. Deep burrowing earthworms were only slightly more abundant in RT plots during all sampling campaigns (Figure 9b, Figure S3). The greatest effect can be seen on endogeic species which rapidly proliferate near the soil surface (high percentage of juveniles), where residues of preceding crops are enriched in RT plots. In addition, topsoil compaction reduced the positive effects of RT, especially in dry periods because it complicates the penetration by earthworms. Ulrich et al. (2010) for instance, found no anecic species in no-till treatments. In general, the relatively dry conditions on site should reduce earthworm effects compared to other studies. A recent meta-analysis (Briones and Schmidt, 2017) reported advantages of reduced tillage treatments on earthworm abundance, but lowest effects in loamy soils, soils with >1.2% soil organic carbon and soils with pH >7.2. In addition, frequent dry periods and a limited soil depth by lime stone at the study site are less favorable for deep-burrowing varieties.

Conclusions

The differences in soil structure between conventional tillage and reduced tillage only manifested themselves in a shallow depth of 13-23cm. Plowing leads to a periodic loosening of soil which not only increases macroporosity and macropore connectivity but also saturated hydraulic conductivity. The absence of plowing, in turn, causes compaction and the onset of a no-till pan beneath the tillage depth of the cultivator and a reduction in K_s that is not compensated by the observed increase in earthworm abundance due to the scarcity of anecic species. Soil structure at greater depths (28-38cm) is

indistinguishable despite 25 years of different tillage and K_s is only mildly increased as deep roots or burrowing activity hardly exert any soil structure modification beneath the plow horizon. The differences in structural, physical and ecological properties between the tillage treatments have no effect on crop yield, since it is not limited by structural but by climatic constraints at this site.

Image-derived macroporosity and directly measured air capacity show good agreement, whereas predictability of saturated hydraulic conductivity from image-derived, microstructural properties is limited by the vast spatial variability of K_s. The nested sampling in combination with X-ray CT analysis at different resolutions is a suitable approach to extend the range of scales amenable to microstructural analysis from a voxel size of $(20\mu m)^3$ to a sample size of 700 cm^3.

Acknowledgments

We thank two anonymous reviewers for their valuable comments. The study was organized in cooperation with the DiControl project within the initiative Soil as sustainable resource for bioeconomy (Bonares), funded by the German Federal Ministry of Education and Research (BMBF).

Supporting information (chapter 6.3)

three figures

3.2. Denitrification in soil aggregate analogues - effect of aggregate size and oxygen diffusion (Schlüter et al. Frontiers in Environmental Science, 6(17),1-10, doi: 10.3389/fenvs.2018.00017)

Abstract

Soil-borne nitrous oxide (N_2O) emissions have a high spatial and temporal variability which is commonly attributed to the occurrence of hotspots and hot moments for microbial activity in aggregated soil. Yet there is only limited information about the biophysical processes that regulate the production and consumption of N_2O on microscopic scales in undisturbed soil. In this study, we introduce an experimental framework relying on simplified porous media that circumvents some of the complexities occuring in natural soils while fully accounting for physical constraints believed to control microbial activity in general and denitrification in particular.

We used this framework to explore the impact of aggregate size and external oxygen concentration on the kinetics of O_2 consumption, as well as CO_2 and N_2O production. Model aggregates of different sizes (3.5 vs. 7 mm diameter) composed of porous, sintered glass were saturated with a defined growth medium containing roughly 10^9 cells ml^{-1} of the facultative anaerobic, *nosZ*-deficient denitrifier *Agrobacterium tumefaciens* with N_2O as final denitrification product and incubated at five different oxygen levels (0-13 vol-%). We demonstrate that the onset of denitrification depends on the amount of external oxygen and the size of aggregates. Smaller aggregates were better supplied with oxygen due to a larger surface-to-volume ratio, which resulted in faster growth and an earlier onset of denitrification. In larger aggregates, the onset of denitrification was more gradual, but with comparably higher N_2O production rates once the anoxic aggregate centers were fully developed.

The normalized electron flow from the reduced carbon substrate to N-oxyanions ($e^-_{\text{denit}}/e^-_{\text{total}}$ ratio) could be solely described as a function of initial oxygen concentration in the headspace with a simple, hyperbolic model, for which the two empirical parameters changed with aggregate size in a consistent way. These findings confirm the important role of soil structure on N_2O emissions from denitrification by shaping the spatial patterns of microbial activity and anoxia in aggregated soil. Our dataset may serve as a

benchmark for constraining or validating spatially explicit, biophysical models of denitrification in aggregated soil.

Introduction

Emission and uptake of greenhouse gases (CO_2, CH_4, N_2O) by soil are subject to pronounced spatial and temporal fluctuations. Emission patterns in space and time appear to be controlled by the spatial and temporal distribution of labile organic matter (e.g., roots, crop residues, animal manure, particulate organic matter) and the occurrence of physicochemical conditions (e.g., temperature, soil moisture, anoxic volumes) favorable for specific microbial processes (e.g., nitrification, denitrification). This has led to the notion that the bulk of microbially driven greenhouse gas (GHG) turnover occurs in "hotspots" and during "hot moments" (Groffman et al., 2009; Kuzyakov and Blagodatskaya, 2015; Tecon and Or, 2017; Vos et al., 2013). While the emission of carbon dioxide (CO_2) through soil respiration exhibits a fairly low spatio-temporal variability, nitrous oxide emissions (N_2O) are a notorious example for extreme variability. Sampling campaigns with undisturbed soil often exhibit a log-normal distribution of denitrification activity in aerated soil with numerous "coldspots" without emissions and some samples with very high emissions (Mathieu et al., 2006; Röver et al., 1999). In a seminal study Parkin (1987) demonstrated that 25-85% of denitrification activity was associated with particulate organic matter that comprised less than 1% of the soil volume. Thus, a better understanding of denitrification activity on microscopic scales is required to improve predictions of N_2O emissions at relevant spatial scales.

Denitrifiers are facultative aerobes that start to denitrify when oxygen becomes limiting. The reduction of nitrate (NO_3^-) to dinitrogen (N_2) occurs via a series of enzymatic steps and intermediates (NO_2^-, NO, N_2O)(Philippot et al., 2007). The basic requirements for heterotrophic denitrification in soil are (1) the presence of decomposable carbon supplying electrons for anaerobic respiration, (2) a shortage of O_2 as electron acceptor, (3) the availability of NO_3^- as an alternative electron acceptor and (4) a microbial community that has the capacity to express the enzymes for some or all reduction steps in denitrification. Key soil environmental factors that govern denitrification are well understood and can be roughly grouped into biochemical constraints and physical constraints, but it is the interaction of all factors that causes the seemingly erratic nature of denitrification activity in soils. Firstly, denitrification is constrained biochemically by the availability and quality of carbon substrates in soil such as root exsudates, plant litter and soil organic matter. Besides sustaining denitrification, organic substrates fuel aerobic respiration, thus enhancing local anoxia in micro-sites. Secondly, the denitrifier community is composed of species exhibiting different regulatory phenotypes (Bergaust et al., 2011) that differ in completeness and timing of denitrification gene transcription. This causes the onset of denitrification as well as the accumulation of intermediates to be different for different denitrifying communities (Dörsch et al., 2012). Notably, a significant fraction of the denitrifiers does not have the genetic capacity to reduce N_2O (Jones and Hallin, 2010) and it is debated whether functional redundancy enabling complete denitrification is always warranted in soil microbial consortia at a micro-scale (Philippot et al., 2011; Philippot et al., 2013). Simplistic estimates of spatially explicit bacterial diversity in soil suggest that moderately active soil (10^9 cells g^{-1} soil) harbors around 100 bacterial species within interaction distance (<20μm) and this number remains below 400 in hotspots (10^{10} cells g^{-1} soil) (Raynaud and Nunan, 2014). Thirdly, microbial activity as well as post-transcriptional regulation are controlled by environmental factors such as the presence of N-oxides (NO_2^-, NO, N_2O), temperature and pH. It is well known, for instance, that a low pH suppresses the N_2O reductase enzyme post-transcriptionally so that the molar ratio between N_2O and N_2 is shifted towards N_2O (Bakken et al., 2012; Liu et al., 2010; SImek and Cooper, 2002). On the other hand, diffusion of reactants and products to and from the sites of microbial denitrification are constrained physically in the soil matrix. The diffusion pathways for gaseous fluxes are mainly governed

by the water content, because the diffusion coefficients are many orders of magnitudes smaller in water than in air. This leads to the well-known phenomenon that N_2O emissions exhibit a threshold behavior around a water saturation of 70% and peaks around 90% (Linn and Doran, 1984a; Ruser et al., 2006) at which the air becomes discontinuous. With lost air continuity the average distance for dissolved oxygen to reach a microbial hotspot starts to diverge from the size of the hotspot itself to typical aggregate sizes. If aggregation is poorly developed, then the mean diffusion length amounts to the average half distances between air-filled macropores. At higher saturation, the N_2O/N_2 ratio shifts towards N_2, because large fractions of the soil become anoxic so that dissolved N_2O is consumed where it is produced or during its extended diffusion path towards the atmosphere. Even the role of wet soils as a sink for atmospheric N_2O is debated but poorly investigated (Chapuis-Lardy et al., 2007; Kolb and Horn, 2012). Finally, denitrification activity in hotspots can also be constrained by nitrate diffusion to sites of active denitrification (Smith, 1990). The well-known observation that nitrate amendment leads to increased denitrification activity is often interpreted from a biochemical standpoint as the effect of a high half-saturation constant of dissimilatory NO_3^- reductase(Firestone, 1982). Yet, by employing Fick's law it can be shown that the diffusion flux into a hotspot also scales linearly with the concentration gradient between the NO_3^- depleted hotspot and the external NO_3^- concentration regulated by the nitrate amendment (Myrold and Tiedje, 1985). Hence, the high half-saturation constant can simply be a consequence of a NO_3^- diffusion constraint.

Microscale denitrification models that combine the aforementioned biochemical and physical controls based on a set of reaction-diffusion equations typically employ individual soil aggregates as a model domain (Arah and Smith, 1989; Leffelaar and Wessel, 1988). Assuming a steady-state situation and uniform initial substrate concentration, the denitrification activity typically scales with the volume fraction of the anoxic aggregate center which, in turn, is mainly controlled by the aggregate size. The resulting oxygen profiles as a function of distance to the aggregate boundary typically exhibit an exponential decline at a rate that scales with microbial activity. This has been confirmed experimentally with micro-sensors (Højberg et al., 1994; Sexstone et al., 1985; Zausig et al., 1993). Currently, new models are underway that allow for numerical experiments on the role of substrate location for denitrification activity through spatial self-organization of aerobic and anaerobic species along oxygen gradients (Ebrahimi and Or, 2015). A major outcome is that an internal carbon source such as sequestered particulate organic matter is more efficient in invoking denitrification activity in an anoxic micro-site than an external carbon source like dissolved organic matter.

Such new insights into spatially explicit, micro-scale denitrification models call for new, systematic laboratory experiments on denitrification in soil aggregates. The objective of this study was to explore the impact of aggregate size and external oxygen concentration on aerobic and anaerobic respiration in model soil aggregates. For this, we inoculated the aggregates with a single bacterial strain (*Agrobacterium tumefaciens*), which is able to switch from aerobic respiration to denitrification. In this way, the physical constraints on denitrification kinetics could be studied without the added complexity of spatial or temporal patterns in denitrification activity through interactions within bacterial consortia. Furthermore, the delicate balance between N_2O and the difficult to quantify N_2 production could be neglected as *A. tumefaciens* lacks the *nosZ* gene encoding N_2O reductase and hence has N_2O as its final denitrification product. This still leaves a wealth of diffusion and reaction processes co-occurring within an aggregate as depicted in Figure?. Denitrification activity was assessed by incubating differently sized aggregates loosely placed in closed bottles and monitoring O_2 depletion and N_2O accumulation in the headspace of the bottles at high resolution until the added carbon source (succinate) or the electron acceptor (NO_3^-) were depleted. We did not measure dissolved oxygen directly, but inferred the spatial extent of the anoxic

volume from denitrification kinetics. The data can be used to predict the critical aggregate size for denitrification in *A. tumefaciens* to occur at different external O_2 concentrations.

Materials & Methods

Bacterial strain and growth medium

We used a pure culture of the bacterial strain *Agrobacterium tumefaciens* C58 (ATCC 33970), a facultative anaerobic α-proteobacterium, which lacks the genes encoding nitrous oxide reductase (Baek and Shapleigh, 2005; Bergaust et al., 2008). Therefore N_2O was the final denitrification product. Sistrom's medium (Sistrom, 1960) with an initial pH of 7 was used as growth medium. The medium contained (l^{-1}): K_2HPO_4 3.48 g, NH_4Cl 0.195 g, succinic acid 4 g, L-glutamic acid 0.1 g, L-aspartic acid 0.04 g, NaCl 0.5 g, nitrolotriacetic acid 0.2 g, $MgSO_4{*}7H_2O$ 0.3 g, $CaCl_2{*}7H_2O$ 15 mg and $FeSO_2{*}7H_2O$ 7 mg. In addition, trace elements and vitamins were added (l^{-1}): EDTA (triplex 3) 1.765 mg, $ZnSO_4{*}7H_2O$ 10.95 mg, $FeSO_4{*}7H_2O$ 5 mg, $MnSO_4{*}7H_2O$ 1.54 mg, $CuSO_4{*}5H_2O$ 0.392 mg, $Co(NO3)_7{*}6H_2O$ 0.248 mg, H_3BO_3 0.114 mg, nicotinic acid 1 mg, thiamine HCl 0.5 mg, biotin 0.01 mg. pH was brought to 7.0 with 10 M KOH and the medium was sterilized by autoclaving. KNO_3 was added to the medium to a concentration of 5mM as a substrate for denitrification. A stirred culture was grown aerobically at 25˚C. Cells were harvested during exponential growth by centrifugation (10000 rpm for 7 min). The resulting cell pellets were immediately resuspended in fresh growth medium to a density of $\approx 3\times10^9$ cells ml^{-1} which is typical for hotspots in real soil (Raynaud and Nunan, 2014). The cultures were kept on ice to inhibit growth until the start of the experiment.

Aggregate inoculation

Porous borosilicate glass beads (VitraPOR P100, ROBU Glasfilter Geräte GmbH, Hattert Germany) served as a simplified analogue for soil aggregates. The sintered glass beads had a porosity of 32 % and an internal pore size in the range of 45-100 µm. Two different bead sizes were used with a diameter of 3.5 mm and 7 mm and an internal pore volume of 8.3±0.2 µl and 64.0±0.6 µl, respectively. In the following these will be referred to as small and large aggregates. The shape and internal pore structure as obtained via X-ray microtomography are depicted in Figure 40. After submersion of the aggregates in the growth cultures, roughly 3% of the pore space was filled with entrapped air (data not shown). These bubbles were removed completely from the submersed aggregates through vacuum application in a gas-tight bottle for 1-2 min.

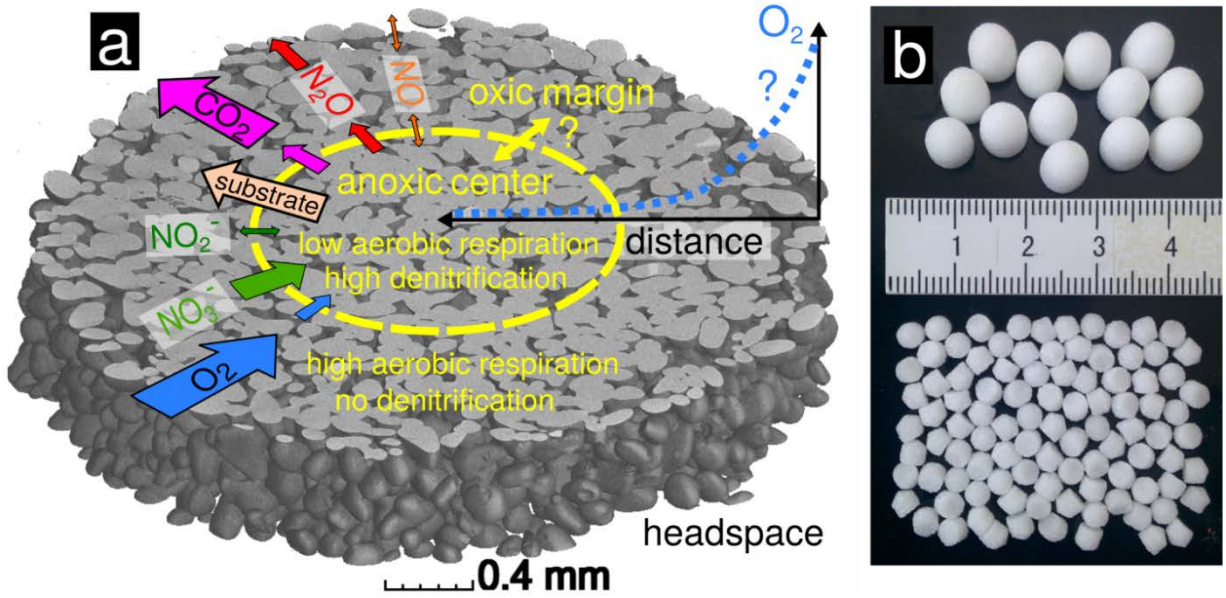

Figure 43: (a) An anoxic aggregate center of variable extent is expected to form during incubation. Here it is depicted within a sub-volume of a 3.5 mm aggregate scanned with X-ray micro-tomography, showing the grains in gray while the liquid-filled pore space is transparent. Arrows are drawn proportionally to the expected fluxes between the headspace, aggregate margin and center. Precursor substances of aerobic respiration and denitrification (substrate, O2, NO_3^-) as well as final products (CO_2, N_2O) are drawn as one-sided arrows, whereas intermediate substances may diffuse in any direction depending on concentration gradients. (b) Two different aggregate sizes (3.5 mm, and 7 mm diameter) were used for incubation. Identical fluid volumes (0.83 ml) were used during incubation by adjusting the number of inoculated aggregates per bottle (100 and 13).

Either 100 small or 13 large aggregates were placed into empty 120 ml glass bottles so that in both cases the pore volume inside of the aggregates filled with cell culture was about 830 µl per bottle, with some 10-20% additional liquid adhering to aggregate surfaces by weak capillary forces. After closing the bottles with an air-tight butyl rubber septum, the bottles were purged with helium by applying five cycles of vacuum and He filling. The bottles were immediately spiked with oxygen, to adjust final concentrations (v/v) of 13%, 7%, 3.5%, 2% and 0% O2 in the head space. Hence, the pre-incubation of the cell cultures was aerobic during the entire sample preparation, except for the short intervals of degassing and He purging. Two replicates were prepared for each aggregate size and initial oxygen concentration, resulting in a total of ten treatments and twenty bottles. Finally, the bottles were moved from the ice bath to a water bath kept at 20∘C to initiate microbial activity and the overpressure that built up due to spiking with O2 and warming of the bottles was released, before the gas chromatography (GC) measurements started.

Incubation

The incubations were carried out with a robotized incubation system consisting of an autosampler (GC-PAL, CTC Analytics, Zwingen, Switzerland) connected to a GC (Agilent Model 7890A, Santa Clara, CA, USA) and an NO analyzer (Teledyne T200, San Diego, CA, USA), allowing for repeated headspace analysis of oxygen (O_2) and carbon dioxide (CO_2) as well as the denitrification products nitric oxide (NO), nitrous oxide (N_2O) and dinitrogen (N_2) via a peristaltic pump (Molstad et al., 2007). The gas volume (≈1ml) lost with each sampling was automatically replaced by He, so that the pressure in the bottles was kept at ≈1 atm. The bottles were sampled every three hours for 45 hours. The nitrate (NO_3^-) and nitrite (NO_2^-) concentrations that remained in the aggregates at the end of the experiment were

measured with a colorimetric assay. To do so, all bottles were kept on ice after the experiment and aggregates from each treatment were thoroughly crushed in a mortar and taken up with 0.9% NaCl solution. The turbid fluid containing medium, cells and bead fragments was collected in Eppendorf tubes and centrifuged (10000 rpm, 5 min) to obtain a clear solution. The protocols for nitrite and nitrite + nitrate quantification were adapted from Keeney and Nelson (1982) and Doane and Horwáth (2003). Nitrate concentrations were obtained through subtraction using two technical replicates per assay. The spectrophotometric measurement was carried out at 540 nm (Tecan infinite F50, Tecan, Männedorf, Switzerland) and converted into concentrations through calibration curves.

Results

Aggregate size effects

Aerobic microbial respiration as determined by decrease in O_2 and increase in CO_2 over time in Figure 41(a,b) was clearly limited by the carbon substrate in the aerobic cultures. Depletion of succinate was indicated by a slow-down of O_2 consumption, which occurred in the small aggregates, depending on initial O_2 level, between 15 and 30 h into the incubation. O_2 consumption after this period was reduced substantially. The slow-down in O_2 consumption and CO_2 accumulation occurred synchronously. The added succinate in the fresh growth medium amounted to 68µmol C/bottle, of which 27-35µmol/bottle were converted to CO_2, which suggests a yield factor between assimilation and total carbon consumption of 0.4-0.5 depending on treatment. However, the absolute accumulation of CO_2 in the headspace might have been reduced by an increase in CO_2 solubility due to a pH increase caused by the reduction of NO_3^- to NO_2^-. Respiration kinetics in Figure 41(a,b) show that microbial activity was clearly delayed in the large aggregates as compared to the small aggregates. Irrespective of aggregate size, the onset of substrate depletion as well as the total amount of produced CO_2 at the end of the experiment scaled positively with the O_2 concentration in the headspace. The higher the amount of external O2, the steeper the gradient between dissolved O_2 at the aggregate boundary and in the aggregate center, which in turn results in a larger diffusive flux, a better supply with O_2 and eventually a smaller extent of anoxic centers.

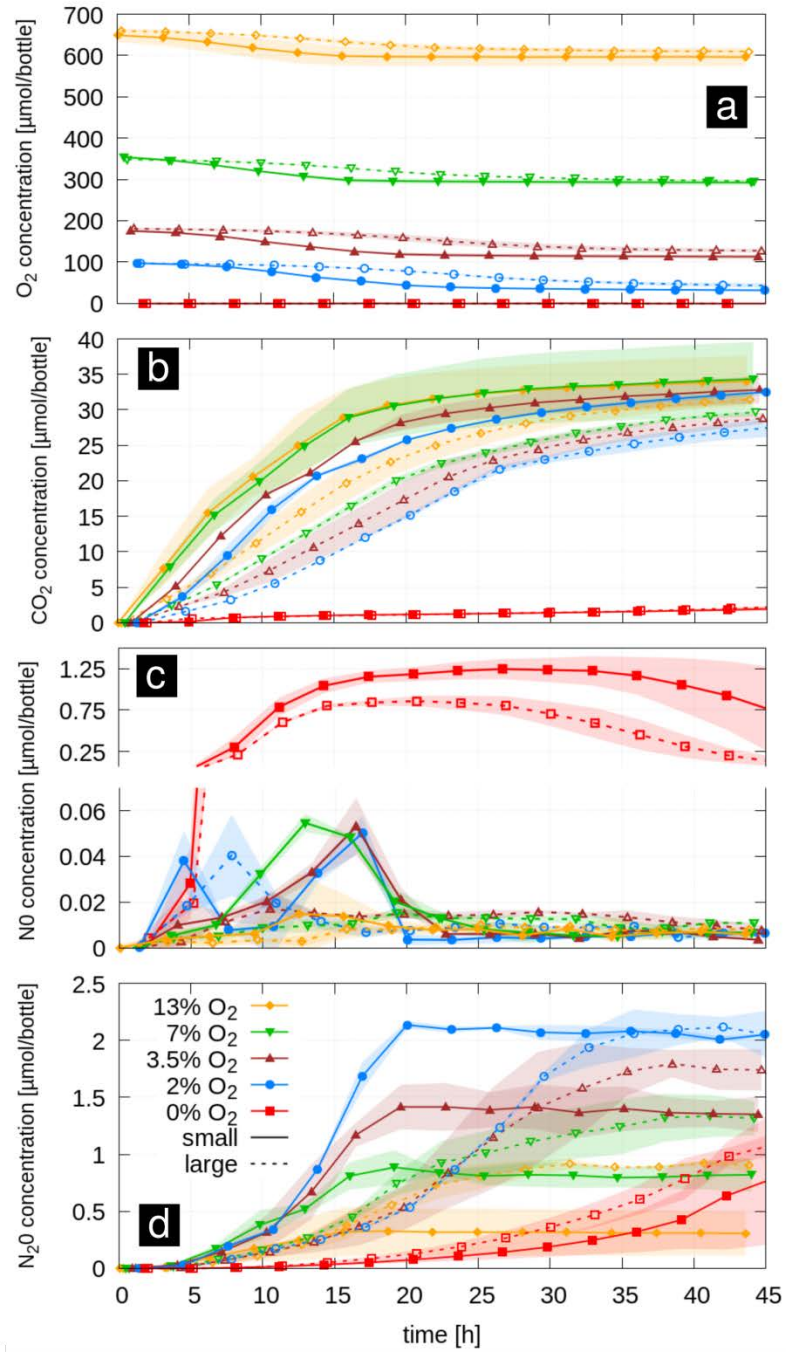

Figure 44: Respiration kinetics of *A. tumefaciens* in small and large aggregates at five initial oxygen concentrations shown as average headspace concentrations (n=2) of (a) O_2, (b) CO_2, (c) NO and (d) the final denitrification product N_2O. Shaded areas represent standard deviations.

Note that microbial respiration in the completely anoxic treatments (0% O_2) was exceptionally small, irrespective of aggregate size. This effect can be explained by unbalanced kinetics of denitrification associated enzyme induction in *A. tumefaciens*. Sudden anoxia in growing cultures resulted in pronounced NO release, accumulating NO to more than 1µmol/bottle, which corresponds to more than 0.5µM in the liquid medium (Figure 41 (c)). Dissolved NO concentrations >0.3µM have been shown to repress

metabolic activity in *A. tumefaciens* (Bergaust et al., 2008). In all oxic treatments the NO concentrations were 1-2 orders of magnitude smaller. In the small aggregates the NO peak coincided with the depletion of the primary carbon substrate, after which NO was quickly consumed by the microbes inside the aggregates. The oxic treatment with the lowest oxygen concentration (2% O_2) showed an interesting double peak in NO, one at a very early stage in the logarithmic growth phase and another shortly before succinate was depleted. Except for the 2% O_2 treatment, large aggregates did not show a clear NO peak but higher steady-state NO concentrations than small aggregates towards the end of the incubation, suggesting different denitrification kinetics in small and large aggregates.

N_2O accumulation in the headspace followed a characteristic pattern with respect to initial O_2 concentration (Figure 41(d)). The lower the initial O_2 concentration in the headspace, and the less oxygen was available for aerobic growth, the more N_2O accumulated as the final denitrification product. In the small aggregates denitrification abruptly stopped after ca. 18 h. At this point all succinate was consumed (as judged from the O_2 and CO_2 kinetics, Figure 41(a,b)).

Microbial respiration beyond the point of succinate depletion was small and likely fell below the rate of O_2 diffusion into the aggregate so that the anoxic centers vanished. Larger aggregates released N_2O more gradually because slower aerobic growth led to less anoxia initially. The point in time when the N_2O accumulation in the large aggregates exceeded the value from small aggregates decreased with increasing oxygen concentration in the headspace from 36 h (2% O_2) to 28 h (3.5% O_2), 21 h (7% O_2) and 16 h (13% O_2). The total N_2O production by large aggregates was either as large (2% O_2) or 25% (3.5% O_2), 50% (7% O_2) and 100% (13% O_2) larger than in the small aggregates with comparable oxygen concentrations. Here as well, N_2O accumulation leveled off when O_2 consumption decreased due to C-limitation. Aggregates incubated without O_2 (0 vol-%) exhibited a delayed accumulation of N_2O. Only after approximately 24 h did NO start to be net consumed and N_2O production rates increased.

The recovery of the initially added NO_3^--N (4.15 µmol per bottle) ranged between 88-102% in the oxic treatments with large aggregates (Figure 42). Less N was recovered in the treatments with small aggregates (51-100%) and the mismatch increased with increasing oxygen levels. Presumably, with higher oxygen availability, cell growth exceeded the supply of ammonia contained in the medium so that some nitrate was assimilated. In both anoxic treatments more N was recovered than supplied with the added nitrate when estimated from the internal porosity of the aggregates, but was still within a range that could be explained with surplus of medium by liquid adhering to aggregate surfaces (118-122%). In general, the N-mass balances indicate that negligible amounts of denitrification intermediates (NO_2^-, NO) accumulated, while the partitioning into N still present as nitrate after 45 h incubation and N denitrified to N_2O followed a similar pattern over O_2 availability for both aggregate sizes.

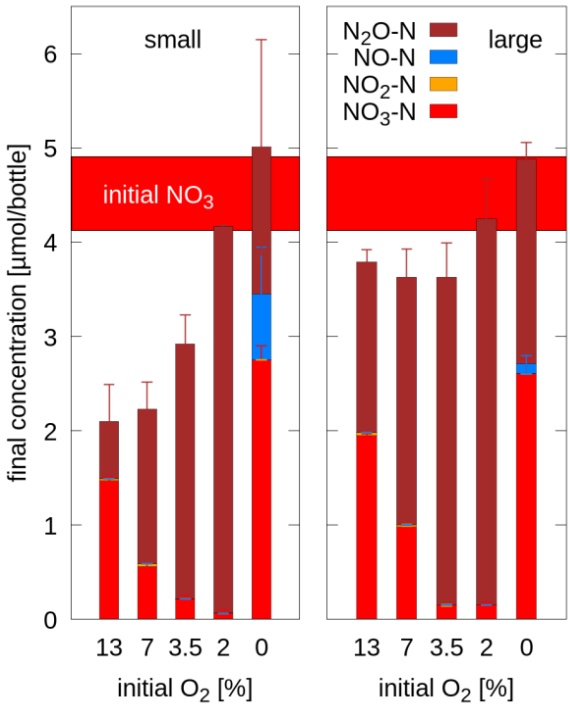

Figure 45: Nitrogen mass balance in small aggregates (left panel) and large aggregates (right panel) after 45 h of incubation at different initial O2 concentrations depicted as the sum of NO_3^--N (supplied with the medium), accumulated denitrification intermediates (NO_2^--N, NO-N) and the final product (N_2O-N). The estimated amount of initial NO_3^--N is depicted as a horizontal bar.

Discussion

Denitrification kinetics

Denitrifying bacteria fall into different categories denoted as denitrification regulatory phenotypes (Bergaust et al., 2011), depending on how they manage the transition from oxic to anoxic conditions. The optimal switch between respiration strategies is important for two reasons: (1) The ATP yield by aerobic respiration is higher than by denitrification, thus, electrons should be directed towards oxygen when possible. (2) The enzymes for denitrification activity have to be expressed before oxygen is completely depleted, so that cells do not get caught in a situation of metabolic arrest. Batch incubation experiments with stirred cultures with nitrate amendment and the same growth medium have shown that Agrobacterium tumefaciens belongs to a common denitrification regulatory phenotype with a sequential production of denitrification intermediates (Bergaust et al., 2011; Bergaust et al., 2008). Nitrate reduction is induced while oxygen is still present, whereas nitrite and NO reduction commence after oxygen depletion. In cultures where oxygen depletion was too rapid, NO accumulated to toxic concentrations, resulting in respiratory arrest (Bergaust et al., 2008). This general pattern was confirmed by our study. Indeed, NO production was maximal and growth delayed when the aerobic inoculum was suddenly subjected to 0% oxygen conditions. In the oxic treatments NO and N_2O accumulation in the headspace commenced simultaneously. In larger aggregates, the NO peak was widened into a broad plateau at lower levels. Presumably, the oxic aggregate margins were thicker in larger aggregates with more gradual growth, so that a quick NO release was buffered by longer diffusion distances between the production sites in the anoxic aggregate center and the headspace, causing longer residence times which increased the chance for NO reduction along the way.

5.2 Anoxic aggregate centers

The purpose of our experiment was to study denitrification kinetics under dynamic growth conditions, in contrast to steady-state conditions which are typically invoked as a simplifying assumption in physically-based denitrification models (Arah and Smith, 1989; Leffelaar and Wessel, 1988). Hence, we needed to account for the different growth rates when comparing the denitrification kinetics in both aggregate sizes, since the cells grew faster in small aggregates due to a better oxygen supply caused by a larger surface-to-volume ratio. A correction for growth effects can be achieved by analyzing N_2O/CO_2 ratios as depicted in Figure 43(a), i.e. the amount of N_2O as the final product of denitrification is normalized against CO_2 as the final production of respiration. There was hardly any difference in normalized denitrification between the two aggregate sizes at the same initial oxygen level during the first 12h. Only after the anoxic centers were fully established in the aggregates two consistent trends evolved. First, denitrification was always larger in the large aggregates, irrespective of external O_2 concentration, implying that the volume fraction of anoxic centers is smaller in small aggregates. Second, denitrification increased with decreasing external O_2 concentration, as the diffusive flux of O_2 was driven by the gradient between the oxygen depleted aggregate centers and the dissolved O_2 at the aggregate boundary, which is in equilibrium with the concentration of gaseous O_2 in the headspace of the bottle. Interestingly, doubling of the aggregate size had roughly the same effect on the final N_2O/CO_2 ratio as a reduction of external O_2 concentration by 50%. The absolute values of the N_2O/CO_2 ratio, however, should not be taken for granted due to the expected pH increase caused by nitrate reduction that changes CO_2 solubility.

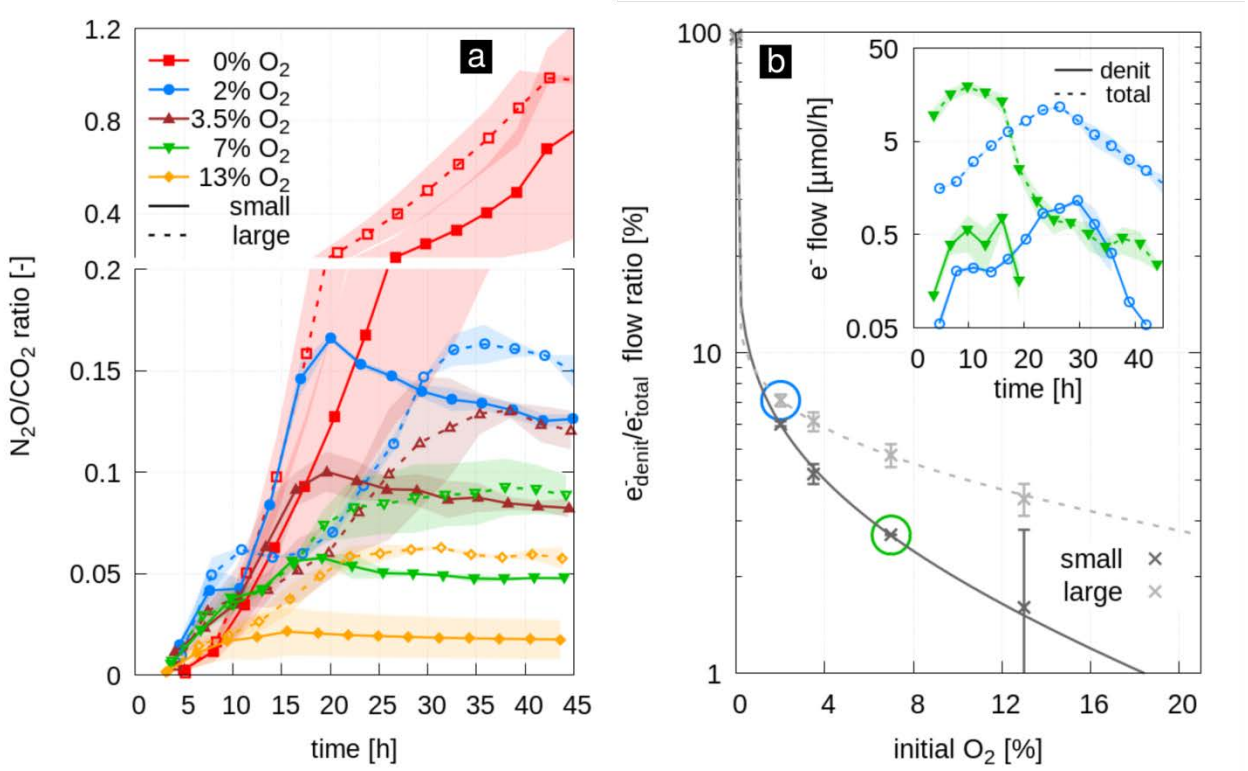

Figure 46: (a) Time series of the N_2O/CO_2 ratio shown as average (lines) and standard deviation (shaded area) for two replicates of small aggregates (solid) and large aggregates (dashed) at five different initial O_2 concentrations. (b) Ratio of electron flow diverted in denitrification and total electron flow both measured and modeled with eq. (20). The inset shows the time series of electron flows for two selected treatments (large aggregates at 2% O_2, blue, and small aggregates at 7% O_2, green).

A more direct approach to assess denitrification activity is to compute the fraction of electron flow diverted to electron acceptors for anaerobic respiration (e^-_{denit}, including NO_3^-, NO_2^-,NO) and total respiration (e^-_{total}, including NO_3^-, NO_2^-,NO and O_2)(Bergaust et al., 2008). Time series of these electron flows are shown for selected treatments in Figure 43(b,inset). The ratio of cumulative electron flows at the end of incubation exhibited a systematic trend (Figure 43b) that is described by a hyperbolic relationship between the e−denit/e−total ratio [%] and the initial oxygen concentration CO2 [%]:

$$\frac{e^-_{\text{denit}}}{e^-_{\text{total}}} = 100\left(1-\left(\frac{C_{O_2}}{100}\right)^a\right)^b \qquad (20)$$

where a and b are dimensionless fitting parameters. The values of the fitting parameters are shown in Table 4. The fit across all investigated oxygen levels was excellent for both aggregate sizes. Note that a similar model of the form $[a/(a-C_{O_2})]^b$ was also capable to reproduce the sharp decline in the electron flow ratio with only slightly larger errors, whereas an exponential model resulted in a too smooth decline

(data not shown). The good model fit across a wide oxygen range may allow for extrapolation towards higher O_2 concentrations. At ambient conditions (21% O_2), small aggregates are likely to be devoid of anoxia, whereas large aggregates may still have roughly 2% of electron flow diverted to denitrification. The outer exponent b was roughly increased by a factor of two, as the aggregate diameter was doubled. This consistent scaling of the exponent suggests that predictions for larger aggregates are feasible, but this cannot be validated on a set of two different aggregate diameters. Further experiments would be necessary.

Table 4: Fitting parameters (a, b) for the hyperbolic relationship between initial oxygen concentration and the ratio of electron flows (eq. 20) for large and small aggregates. Fitting is done by minimizing the weighted errors between the measurements and model using the standard deviation between two technical replicates as weighting factor. The root mean square error (RMSE) is also reported.

size	a	b	weighted error	RMSE
large	0.0955	2.4189	0.0016	0.0414
small	0.0240	1.0935	0.0016	0.0712

Consequences for greenhouse gas emissions from "hotspots" in soil

The delicate balance between growth rates and the transient formation of anoxic centers led to a rich variety of denitrification dynamics which resulted from the interplay of a number of diffusive fluxes summarized in Figure 40(a). The diffusive flux of oxygen into the aggregates and the diffusive flux of the final respiration products (CO_2 and N_2O) out of the aggregates can be considered as uni-directional processes that solely depend on concentration gradients, since the diffusion coefficient does not change at constant (complete) saturation. Likewise, the diffusive flux of the dissolved carbon substrate (succinate) from the less active, anoxic aggregate center into the more substrate-depleted, oxic aggregate margin as well as the diffusive flux of nitrate from the well O_2-supplied aggregate margin into the actively denitrifying aggregate center are uni-directional, yet without any exchange with the headspace. Finally, the diffusion of intermediates (NO_2^-, NO) is bi-directional and changing during incubation. Therefore, it might look surprising that a rather simple model with two empirical parameters is able to capture the denitrification behavior for a large range of oxygen concentrations and different aggregate sizes. However, this can be ascribed to the fact that (1) all oxic treatments were equally constrained by electron-donor and not electron-acceptor limitation and (2) that the model describes cumulative electron fluxes and not denitrification kinetics.

There are several reasons why our findings cannot be directly transferred to natural conditions. Natural consortia and a more complex composition of reduced carbon in soil would lead to coexistence and spatially separated niches causing spatial and temporal variability of aerobic respiration and denitrification activity (Kuzyakov and Blagodatskaya, 2015; Vos et al., 2013) as well as other N_2O forming processes (e.g., nitrification) to occur simultaneously (Philippot et al., 2007; Stange et al., 2013). While the sudden removal of oxygen that was induced in the anoxic treatments could certainly occur under natural conditions, e.g., after a heavy rainfall, the toxic NO accumulation would not happen in natural consortia with a certain amount of functional redundancy (Schimel and Schaeffer, 2012). Moreover, a mobile carbon substrate like dissolved organic matter is likely to evoke a different spatio-temporal pattern in aerobic respiration and denitrification than a stationary carbon substrate like particulate organic matter (Ebrahimi and Or, 2015). An exponentially growing culture foraging on a low-molecular carbon substrate like in our experiments may also occur under natural conditions, when easily decomposable organic matter is added to the soil (e.g., animal manure, plant residues after harvest or plowing). But this scenario is rather an exception, whereas a steady-state or gradual change in microbial activity typically prevails in soil. Nevertheless, dynamic growth also poses an interesting case for

modeling. Even though hotspots of microbial activity are believed to be the dominating sites of denitrification in soil, they cannot readily be investigated in isolation from the surrounding soil matrix, as the varying water content in the soil matrix acts as a major control on the micro-environmental conditions in the hotspots. Changing the external O_2 concentration as a substitute for changing water contents is only an indirect analogue as it does not account for dilution of nitrate and carbon substrate as well as the osmotic effects induced by a rewetting event (Fierer and Schimel, 2003; Groffman et al., 2009). Moreover, undisturbed soil structure does typically not manifest itself as isolated, well-sorted aggregates but a coherent soil matrix pervaded with a complex pore network (Rabot et al., 2018). Hence, the aggregate size should rather be interpreted as the typical distance to the closest air-filled pore (Schlüter and Vogel, 2016) and the varying oxygen levels for instance as a depth gradient in the partial pressure of O2 within a soil profile. Finally, experiments in closed systems affect the residence time of gaseous intermediates which increases the chances of soil to act as a sink for NO and N_2O (Chapuis-Lardy et al., 2007).

Despite those limitations our simplified incubation experiment may serve as an interesting case for studying the dynamics of soil denitrification as an important source of N_2O. Thus, the experiments with artificial aggregates may provide a useful benchmark data set for physically-based diffusion-reaction models of microbial activity in model soil aggregates. The pioneering studies of Leffelaar and Wessel (1988) and Arah and Smith (1989), which assumed simplified one-dimensional, radial domains, are gradually superseded by spatially explicit, three-dimensional models of the pore space (Ebrahimi and Or, 2015; Ebrahimi and Or, 2014; Falconer et al., 2015) that can be directly derived from X-ray CT scans like shown in Figure 40(a). These models can inherently take into account the fragmentation of microbial niches under normal hydraulic conditions due to a discontinuous water phase as well as increased microbial dispersal after a rewetting event (Tecon and Or, 2017). They have the potential to explore microscopic biochemical processes, which are impossible to measure directly, in order to inform or improve macroscopic models of greenhouse gas emission, which operate with emergent properties on much larger scales like transient, anoxic soil volumes (Ebrahimi and Or, 2016; Li et al., 2000). The development of a new spatially-explicit, physically-based model of denitrification kinetics based on the modeling framework of (Hron et al., 2015) is currently underway, but beyond the scope of the study.

Conclusions

This incubation experiment clearly demonstrates how denitrification in fully saturated aggregates is governed by physical constraints that give rise to a transient formation of anoxic aggregate centers. The spatial gradients in dissolved oxygen which drive the diffusive flux are controlled by the aggregate size and the external oxygen concentration in very predictable ways. The better supply with oxygen in small aggregates leads to faster growth and an earlier onset of N_2O emission, whereas larger aggregates have a larger N_2O accumulation and larger N_2O/CO_2 production ratio on the long run. The main conclusions for physically-based modeling is that under dynamic growth conditions denitrification activity can only be predicted if both the aggregate size and the oxygen concentration at the aggregate surface are known.

The reduction of external oxygen concentration consistently leads to a reduction in aerobic respiration as well as to an increase in the denitrification activity and the N_2O/CO_2 production ratio. The cumulative diversion of electrons from reduced carbon to N-oxyanions is perfectly described by a simple, empirical model across a large oxygen concentration range, which confirms the dominant role of physical constraints on N_2O emissions from these simplified model aggregates inoculated with a single bacterial strain and a simple growth medium.

Incubation studies with these simplified soil aggregates can be extended towards more realistic soil conditions in several ways. We are currently working with experimental setups, in which aggregates are inoculated with different bacterial strains and embedded in explicit geometries in a sandy soil matrix

adjusted to different water contents to account for interactions between hotspots and to explore the role of spatial distribution of hotspots on greenhouse gas emissions.

Author Contributions

SS, HV, MH, OI and PD conceived the experiment. LB provided the bacterial strain. SS, SH, LB and PD conducted the experiments. SS, SH, JZ and PD analyzed the data. All authors contributed to writing the manuscript.

Funding

This study was funded by the Deutsche Forschungsgemeinschaft through the research unit DFG-FOR 2337: Denitrification in Agricultural Soils: Integrated Control and Modelling at Various Scales (DASIM).

3.3. Physical constraints for respiration in microbial hotspots in soil and their importance for denitrification (Schlüter et al. Biogeosciences Discussions, 2019, 1-31, doi:10.5194/bg-2019-2)

Abstract

Soil denitrification is the most important terrestrial process returning reactive nitrogen to the atmosphere, but remains poorly understood. In upland soils, denitrification occurs in hotspots of enhanced microbial activity, even under well-aerated conditions, and causes harmful emissions of nitric (NO) and nitrous oxide (N_2O). Timing and magnitude of such emissions are difficult to predict due to the delicate balance of oxygen (O_2) consumption and diffusion in soil. To study how spatial distribution of hotspots affects O_2 exchange and denitrification, we embedded porous glass beads inoculated with either *Agrobacterium tumefaciens* (a denitrifier lacking N_2O reductase) or *Paracoccus denitrificans* (a "complete" denitrifier) in different architectures (random vs. layered) in sterile sand adjusted to different water saturations (30%, 60%, 90%) and measured gas kinetics (O_2, CO_2, NO, N_2O and N_2) at high temporal resolution. Air connectivity, air distance and air tortuosity were determined by X-ray tomography after the experiment. The hotspot architecture exerted strong control on microbial growth and timing of denitrification at low and intermediate saturations, because the separation distance between the microbial hotspots governed local oxygen supply. Electron flow diverted to denitrification in anoxic hotspot centers was low (2-7%) but increased markedly (17-27%) at high water saturation. X-ray analysis revealed that the air phase around most of the hotspots remained connected to the headspace even at 90% saturation, suggesting that the threshold response of denitrification to soil moisture could be ascribed solely to increasing tortuosity of air-filled pores. Our findings suggest that denitrification and its gaseous product stoichiometry do not only depend on the amount of microbial hotspots in aerated soil, but also on their spatial distribution. We demonstrate that combining measurements of microbial activity with quantitative analysis of diffusion lengths using X-ray tomography provides unprecedented insights into physical constraints regulating soil microbial respiration in general and denitrification in particular. This opens new avenues to use observable soil structural attributes to predict denitrification and to parameterize models. Further experiments with natural soil structure, carbon substrates and microbial communities are required to demonstrate this under realistic conditions.

Introduction

Soil carbon and nitrogen turnover is governed by soil heterogeneity at the microscale. Much of the turnover is concentrated in microsites, providing favorable conditions (pO_2, temperature, pH) and substrates (carbon, nutrients) for soil microbial activity. The partitioning of aerobic and anaerobic respiration in microsites is largely controlled by the water content in the soil matrix which defines the scale across which O_2 diffuses towards microsites of high O_2-consuming activity. Aqueous diffusion lengths range from distances across thin water films in well-aerated soils, to individual soil aggregates of different radii at field capacity, up to the distance to the soil surface when the soil is saturated (Ball, 2013; Elberling et al., 2011; Parkin, 1987; Smith et al., 2003). Aerobic respiration is less affected by soil moisture than anaerobic respiration and typically peaks around water saturations of 20-60% in forest, grass and cropland soils (Moyano et al., 2012; Ruser et al., 2006; Schaufler et al., 2010). Bulk soil respiration starts to decline at higher saturations due to the development of anoxic microsites with lower redox potential, supporting carbon mineralization at typically only a tenth of the rates observed under oxic conditions (Keiluweit et al., 2017). Denitrification, i.e. the dissimilatory respiration of N oxyanions instead of oxygen, is commonly observed at water saturations above 60-70% and peaks beyond 90% (Linn and Doran, 1984a; Ruser et al., 2006). The occurrence of anaerobic microsites is governed by the balance between saturation-dependent diffusion and microbial consumption of O_2, which in turn depends

on the quantity, quality and distribution of soil organic matter in the soil matrix terms and environmental factors like temperature and pH, which control microbial activity (Nunan, 2017; Smith et al., 2003; Tecon and Or, 2017). In fact, water films around decaying plant material may suffice to induce anaerobic respiration, if microbial respiration exceeds O_2 diffusion through that minute barrier (Kravchenko et al., 2017; Parkin, 1987).

The interplay between physical constraints and biological activity in soil controls microbial respiration at microscopic scales and complicates the prediction of denitrification and N-gas fluxes at larger scales. For instance, nitrous oxide (N_2O) emissions show notoriously large spatial variability, which has been attributed to heterogeneous distribution of anoxic microsites in the soil (Mathieu et al., 2006; Parkin, 1987; Parry et al., 1999; Röver et al., 1999). Together with the often observed high temporal variability of microbial respiration and its fluctuations under transient conditions, this has led to the notion of "hotspots" and "hot moments" for microbial activity and emissions (Groffman et al., 2009; Kuzyakov and Blagodatskaya, 2015). "Hotspots" of denitrification have traditionally been linked to diffusion constraints in soil aggregates. Cell numbers and O_2 concentration have been shown to decline exponentially towards aggregate centers (Højberg et al., 1994; Horn et al., 1994; Sexstone et al., 1985; Zausig et al., 1993) and the critical aggregate radius for the development of anoxic centers and is typically >1 mm (Højberg et al., 1994; Schlüter et al., 2018b; Sierra and Renault, 1996), However, anoxic microsites have also been reported for smaller aggregates (equivalent diameter of 0.03-0.13 mm) in well-aerated, repacked soils (Keiluweit et al., 2018).

An important, but often neglected aspect of physical diffusion constraints on microbial respiration is the spatial distribution of microbial hotspots within the soil matrix. Incubation experiments were either designed to control the aggregate size in repacked soil (Mangalassery et al., 2013; Miller et al., 2009) or the volume fraction of sieved soil mixed evenly into sterile quartz sand (Keiluweit et al., 2018). Some incubation studies were carried out with undisturbed soil and investigated diffusion constraints within the pore network (Rabot et al., 2015). However, these studies did not address the location of hotspots nor the diffusion lengths towards air-filled pores. The vast majority of incubations studies merely reports bulk soil properties like carbon and nitrogen content, bulk density and water saturation. Notable exceptions are Kravchenko et al. (2017) who controlled the position of microbial hotspots by placing decaying plant leaf material into repacked soils with different aggregate sizes and water saturations and Ebrahimi and Or (2018), who placed several layers of remolded aggregates as artificial hotspots into a sand matrix and controlled the volume fraction of anaerobic and aerobic respiration by adjusting the water table in the sand column. Such systematic studies with simplified soil analogues, yet fully accounting for transport processes from and towards hotspots, including interactions between hotspots, are needed to improve our understanding about how physical constraints on microbial respiration control the anaerobic soil volume and transient denitrification activity.

The objective of the present study was to study the interplay between microbial activity and physical diffusion in controlling aerobic and anaerobic respiration for different spatial distributions of hotspots. We embedded uniform artificial hotspots inoculated with denitrifying pure cultures (Schlüter et al., 2018b) in sterile sand, which was adjusted to different water saturations. We hypothesized that the competition for oxygen would depend on the separation distance between the hotspots, which in turn would control microbial cell growth and O_2 consumption and thus affect the timing of the aerobe-anaerobe transition in respiration, i.e. the onset of denitrification. Further, by placing hotspots inoculated with complete (*P. denitrificans*) and truncated (*A. tumefaciens*) denitrifiers in distinct horizontal layers, we expected to see interactions with respect to overall N_2O turnover. To capture the highly dynamic respiration kinetics, we monitored O_2, CO_2, NO, N_2O and N_2 exchange between the headspace and the sand-hotspot matrix at high temporal resolution. The morphology of the air-filled pore space in terms of

air connectivity, air tortuosity and air distance was determined by X-ray computed tomography after the experiment.

Material and methods

Microbial hotspots

Two facultative anaerobic bacteria were used in this study. *Paracoccus denitrificans* expresses all denitrification enzymes necessary to reduce NO_3^- to N_2, whereas *Agrobacterium tumefaciens* lacks the gene *nos*Z encoding nitrous oxide reductase (N_2OR), which makes N_2O the final denitrification product. Moreover, the two strains differ in their regulatory phenotypes with respect to inducing denitrification in response to oxygen depletion, which leads to characteristic patterns of product accumulation (Bergaust et al., 2011). *P. denitrificans* induces NO and N_2O reductase early during O_2 depletion (Bergaust et al., 2010), thus releasing little N_2O. By contrast, *A. tumefaciens* is known to be less stringent in controlling intermediates which may result in the release of large amounts of NO, up to cell-toxic, milli-molar concentrations (Bergaust et al., 2008). Both strains were grown in Sistrom's medium (Sistrom, 1960) as described in a previous study (Schlüter et al., 2018b), but at double strength to provide enough substrate for depleting O_2 during aerobic growth. The medium was amended with 10 mM NH_4NO_3 and 5 mM KNO_3 for anaerobic growth. To produce microbial hotspots, porous borosilicate glass beads (VitraPOR P100, ROBU Glasfilter Geräte GmbH) with a diameter of 7 mm, a porosity of 32% and a medium pore diameter of 60 µm were saturated with freshly inoculated growth medium ($\approx 10^8$ cells ml^{-1}) by submersion into one of the two cultures. In the following, the inoculated porous glass beads are referred to as *At-* (*A. tumefaciens*) and *Pd-* (*P. denitrificans*) hotspots. Detailed information about the culture conditions and the inoculation procedure can be found in Schlüter et al. (2018b).

Repacked sand

Fifty *At* and *Pd* hotspots each were placed into 120 ml of washed, sterile quartz sand (0.2-0.5 mm grain size) yielding a volume fraction of 14% (20 ml; Fig. **S8a**). The sand was packed into 240 ml glass jars (Ball Corporation, Bloomfield, CA) in portions of 10 ml layers and adjusted to target saturation by adding sterile water with a spray can. The packing procedure resulted in some minor changes in porosity between layers and some larger gaps around the hotspots (Fig. **S10**) which affected air distribution in the sand (Fig. **S9a**). Three saturations were used, corresponding to water-filled pore spaces (WFPS) of 30, 60 and 90%. The fully saturated hotspots were placed into the sand at three different architectures (**Fig. 1**). For the "random" distribution, the hotspots were placed in five equidistant (~9.8 mm, center to center) horizontal layers with a random distribution of ten *At* and ten *Pd* hotspots per layer. For the "layered *At/Pd*" and "layered *Pd/At"* distributions, all fifty hotspots of each strain were placed into one of two horizontal layers spaced 21 mm from each other (center to center) at an average headspace distance of 18.2 and 39.2 mm, respectively, where the order represents *top/bottom*. Care was taken to keep the hotspots cool (on crushed ice) during the packing procedure. The pore size distribution of the porous hotspots and the sand in the bulk soil and in hotspot vicinity are reported in Fig. **S10**.

Incubation

To establish aerobic and anaerobic growth patterns and denitrification kinetics for both bacterial strains when growing inside the glass beads, a pre-experiment was conducted without sand. Fifty *Pd* or *At* hotspots were placed in empty 120 ml serum bottles (Fig. **S6b**) and incubated at 15°C under either oxic (He/O_2 80/20%) or anoxic (He 100%) conditions in two replicates per treatment. Headspace concentrations of O_2, CO_2, NO, N_2O and N_2 were measured every 4 h by piercing the septum with a hypodermic needle mounted to the robotic arm of an autosampler (GC-PAL, CTC Analytics, Switzerland). The autosampler was connected to a gas chromatograph (Agilent Model 7890A, Santa

Clara, CA, USA) and a NO analyzer (Teledyne 200. San Diego, CA, USA) via a peristaltic pump. Detailed information about the robotized incubation system and the experimental setup can be retrieved elsewhere (Molstad et al., 2007; Schlüter et al., 2018b).

In the main experiment, freshly inoculated glass beads were packed into incubation vessels as described above, three replicates for each of the nine combinations of saturation and hotspot distribution. Jars with 30% and 60% WFPS were flushed with He/O_2 for 40 min, using ten cycles of vacuum (3 min) and purging (1 min). Jars with 90% WFPS were flushed using 180 cycles of mild vacuum (~ 600 mbar) and O_2/He purging to avoid structural changes of the packed columns due to bubbling of trapped gas. The jars were then placed into a water bath kept at 15°C and after temperature equilibration O_2/He overpressure was released. Gas concentrations in the headspace were analyzed as described above. Gas production and consumption kinetics were used to calculate the fraction of electrons diverted to O_2 or N oxyanions and thus to estimate the contribution of denitrification to total respiration (e^-_{denit}/e^-_{total}) (Bergaust et al., 2011; Schlüter et al., 2018b). The NO/(NO+ N_2O + N_2) and N_2O/(NO+ N_2O + N_2) product ratios were estimated from the cumulative release of gaseous denitrification products (NO, N_2O, N_2), after subtracting precursors from products (NO from N_2O + N_2 and NO + N_2O from N_2). The rationale behind the latter was to mimic an open system, in which N-gases released to the atmosphere are not available any longer as electron acceptors for denitrification. Details about the calculation of denitrification product ratios can be found in the Supporting Information (chapter 6.4, SI **1.2 Methods: Product ratios**).

X-ray tomography and image analysis

After the incubation experiment, the glass jars were scanned with X-ray micro-tomography (X-tek XCT 225, Nikon Metrology) with a beam energy of 145 kV, a beam current of 280 µA, an exposure time of 708 ms per frame, a 0.5 mm copper filter for reducing beam hardening artefacts and a total of 3000 projection for a full scan. Individual hotspots were also scanned (100 kV, 90µA, 1000ms per frame, no filter) to analyze the internal pore morphology. The 2D projections were reconstructed into a 3D image with a resolution of 35 µm using a filtered-back projection algorithm in the X-tek CT Pro 3D software. Image processing from raw gray-scale data (**Fig. 1a**) to segmented data including sand grains, air and water (**Fig. 1b-c**) was carried out according to well-established protocols for multi-phase segmentation (Schlüter et al., 2014). The porous glass beads were assigned to *At* or *Pd* hotspots according to the orientation of the flat end in the random architecture or by the vertical position in the layered architecture (**Fig. 1b-c**). The segmented images were analyzed with respect to three different spatial attributes of the air-filled pore spaces deemed important for oxygen supply. 1. Air connectivity by distinguishing isolated air-filled pores and air-filled pores with a continuous path to the headspace (yellow and red in **Fig. 1d**). Air connectivity is then defined as the ratio of connected air-filled pore space and total air-filled pore space 2. Air tortuosity as derived from the geodesic length of connected air-filled pores. The geodesic length is the distance of any connected air voxel to the headspace along curved paths around obstacles like solid particles and water-blocked pores **(Fig. 1e**). Air tortuosity is the ratio between geodesic and vertical Euclidean distance to the headspace averaged over all connected, air-filled voxels. It is a proxy for the diffusive transport of gaseous oxygen in air-filled pores 3. Air distances of water-filled pores as defined by the average geodesic distance from any water voxel to the closest air-filled pore with headspace connection (white in **Fig. 1f**). Air distance is a proxy for the slow diffusive transport of dissolved oxygen. All image processing steps were carried out with Fiji/ImageJ (Schindelin et al., 2012) and associated plugins (Doube et al., 2010; Legland et al., 2016) or with VG Studio Max 2.1 (Volume Graphics). Each image processing and analysis step is explained in detail in the supporting information (chapter 6.4, SI **1.3 Methods: Image processing and analysis**).

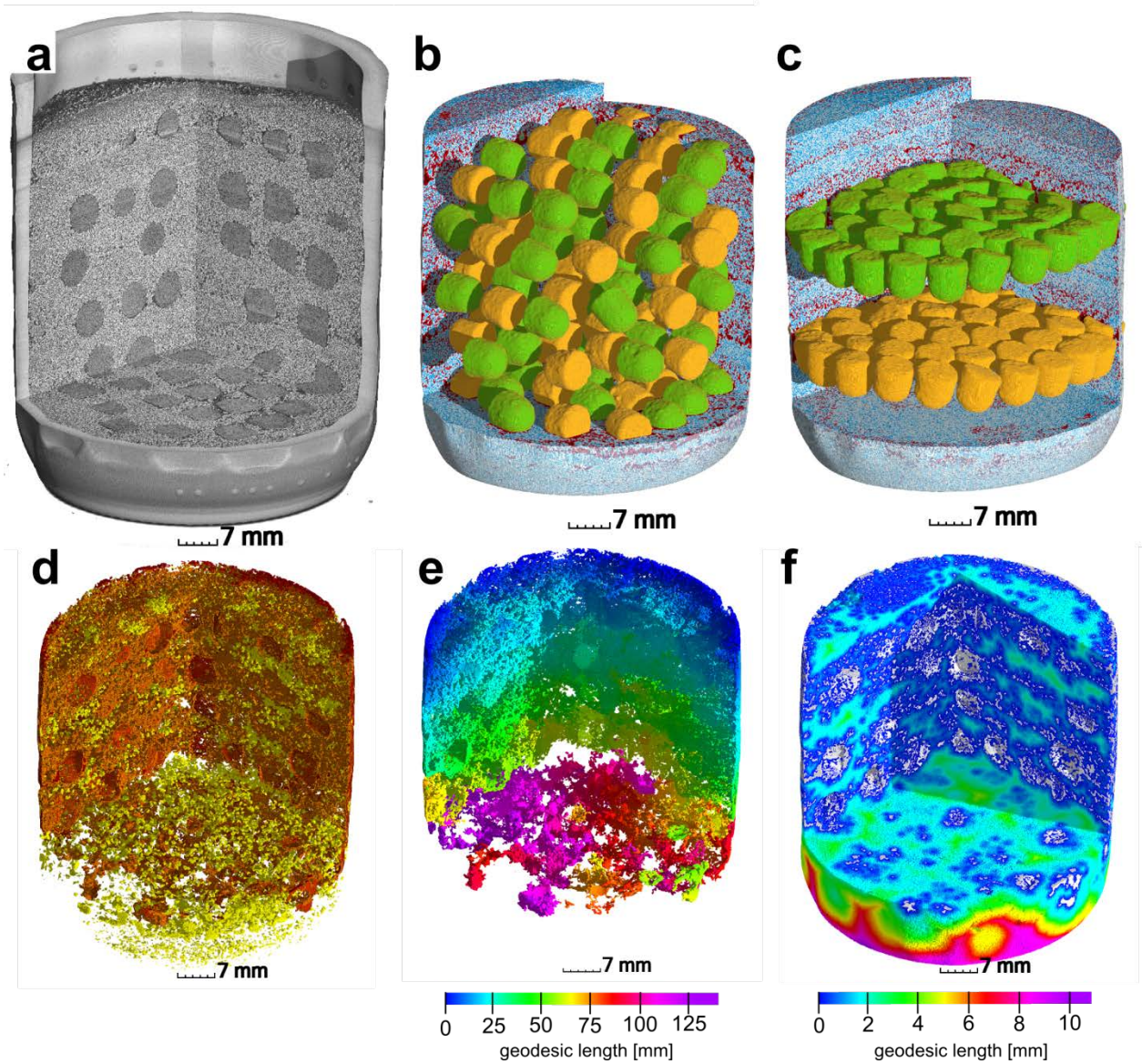

Figure 47. Spatial distribution of hotspots and spatial attributes of air-filled pore space in incubation jars. Upper panel: (a) X-ray CT scan of an incubation jar with random hotspot architecture and medium saturation (60% WFPS). (b) Image segmentation of the same jar into air (red), water (blue), sand (transparent), *A. tumefaciens* hotspots (orange) and *P. denitrificans* hotspots (green). (c) A different jar at medium saturation (60% WFPS) with layered *Pd/At* hotspot architecture. Lower panel: a jar with random distribution at high saturation (90% WFPS). (d) Air connectivity, determined as the volume fraction of air connected to the headspace (red, disconnected air shown in yellow). (e) Air tortuosity as derived from the geodesic length to the headspace within the connected air cluster. (f) Diffusion lengths determined as the geodesic length to the closest connected air cluster (white) within water-filled pores.

Results

Aerobic respiration and denitrification without sand

At grew faster than *Pd* at 15°C in the experiment with loosely placed porous glass beads as indicated by faster O_2 consumption and CO_2 accumulation in the oxic treatment (**Figure 2a,b**). Also under fully anoxic conditions, *At* accumulated CO_2 faster than *Pd* (Figure 2b). N-gas kinetics clearly reflected the distinct

regulatory phenotypes of the two bacterial denitrifiers. Anoxic *At* instantly accumulated a large amounts of NO (**Figure 2c**) which persisted until all NO_3^- was reduced to N_2O (as judged from the stable plateau in N_2O, **Figure 2d**). Due to slower growth and O_2 consumption, *Pd* induced denitrification much later than *At*, but accumulated less intermediates (NO, N_2O) than *At*. Oxically incubated *Pd* accumulated no detectable NO, indicating efficient regulation of denitrification when switched slowly to anaerobic conditions in hotspots. Also, NO may have been reduced to N_2O when diffusing from the anoxic center to the boundary of the hotspot. In the initially oxic treatments, denitrification contributed 7% to the total electron flow in *At* hotspots and 13% in *Pd* hotspots, reflecting the fact that (i) *Pd* has one more reduction step in the denitrification sequence and that (ii) *At* used less nitrate for anaerobic respiration in anoxic hotspots centers and more oxygen for aerobic respiration in oxic hotspots margins than *Pd*.

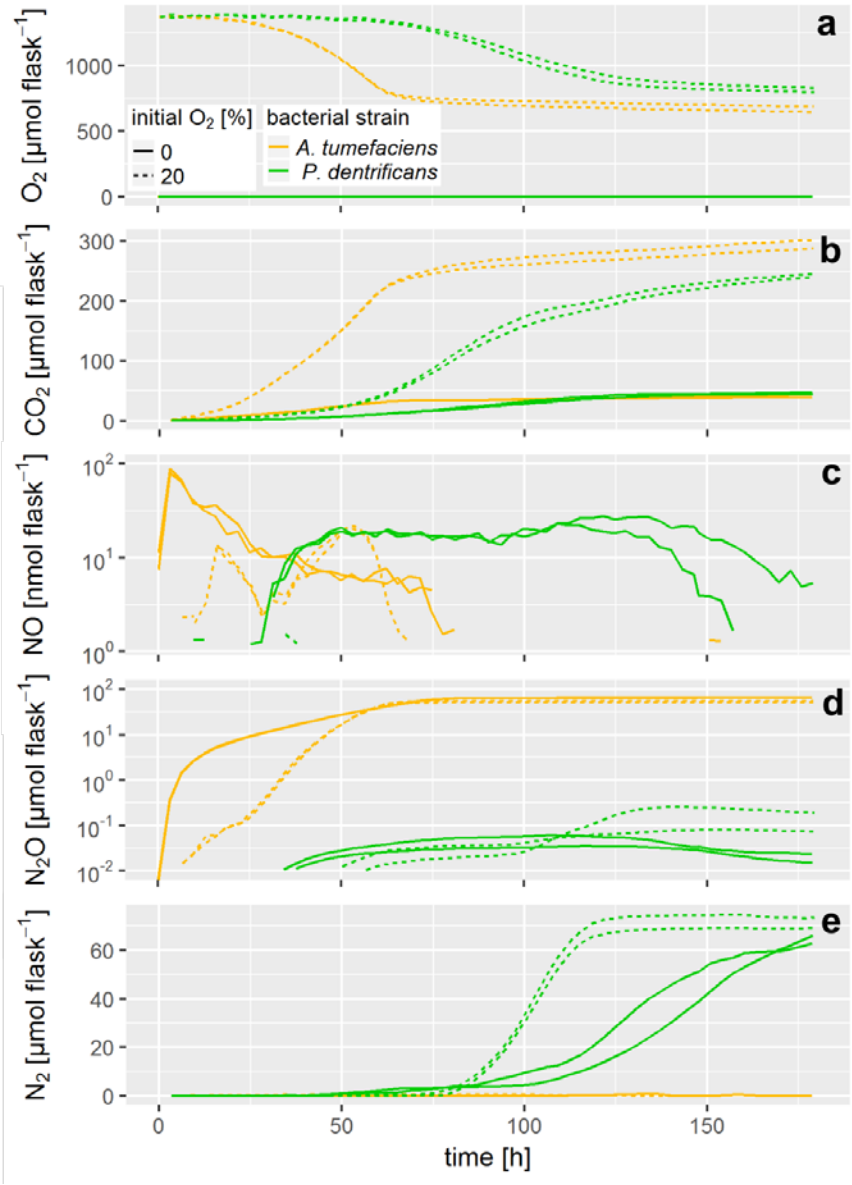

Figure 48: Gas kinetics of individual sets of hotspots inoculated with two different bacterial strains, under oxic and anoxic conditions: (a) O_2, (b) CO_2, (c) NO, (d) N_2O, (e) N_2. Note the logarithmic ordinate in (c) and (d).

Effects of hotspot distribution in sand

The distribution of microbial hotspots within the sand strongly impacted bulk respiration. This is evident for treatments with medium saturation (60% WFPS) for the first 210 h of incubation (**Figure 3)** and with other saturations for the entire incubation period (300 h; **Fig. S11-13**). The random distribution of hotspots allowed for much faster aerobic growth than the layered architectures, leading to complete consumption of O_2 from the jars after 70 h (**Figure 3a**). Given the slow growth of *Pd* (**Figure 2a**), initial O_2 consumption was dominated by the activity of *At* hotspots turning them partly anoxic. Hence, the pronounced NO peak in the random treatment, coinciding with complete O_2 exhaustion from the headspace (**Figure 3c**), was due to *At* activity, similar to what was seen in the unconstrained *At* hotspots under anoxic conditions (**Figure 2c**). N_2O production was observed long before O_2 was depleted from the

headspace (**Figure 3d**) and is attributed entirely to *At* denitrification. *Pd* denitrification did not start before all O_2 was depleted and manifested itself in a transient increase in N_2O production at ~70 h together with an exponential increase in N_2 production (**Figure 3e**) which was also observed with unconstrained *Pd* hotspots (**Figure 2e**). Note that the apparent net consumption of CO_2 (**Figure 3b**) upon O_2 depletion was due to internal alkalization driven by accelerating denitrification, once all hotspots turned anoxic.

In the layered architectures, O_2 consumption was slower and complete anoxia was not reached before 120 h into the incubation. In contrast to the random architecture, less O_2 was available for each individual hotspot in the densely packed hotspot layers, allowing for less aerobic growth per unit time. As a consequence, there was more time for fully denitrifying *At* hotspots to interact with *Pd* hotspots which induced denitrification gradually between 80 and 120 h. Indeed, less N_2O accumulated in the headspace than in the random treatment (**Figure 3d**, **Fig. S13d**) and the onset of N_2 accumulation appeared long before complete O_2 depletion from the headspace (**Figure 3a,e**). In other words, *Pd* hotspots consumed N_2O produced in *At* hotspots. Upon O_2 depletion in the headspace, a burst of NO production occurred (**Figure 3c**) as seen previously with *At* hotspots (**Figure 2c**). However, since *Pd* denitrification was now fully developed, the NO peak was much more short-lived than with the random distribution, because *Pd* hotspots reduced NO produced by *At* hotspots all the way to N_2.

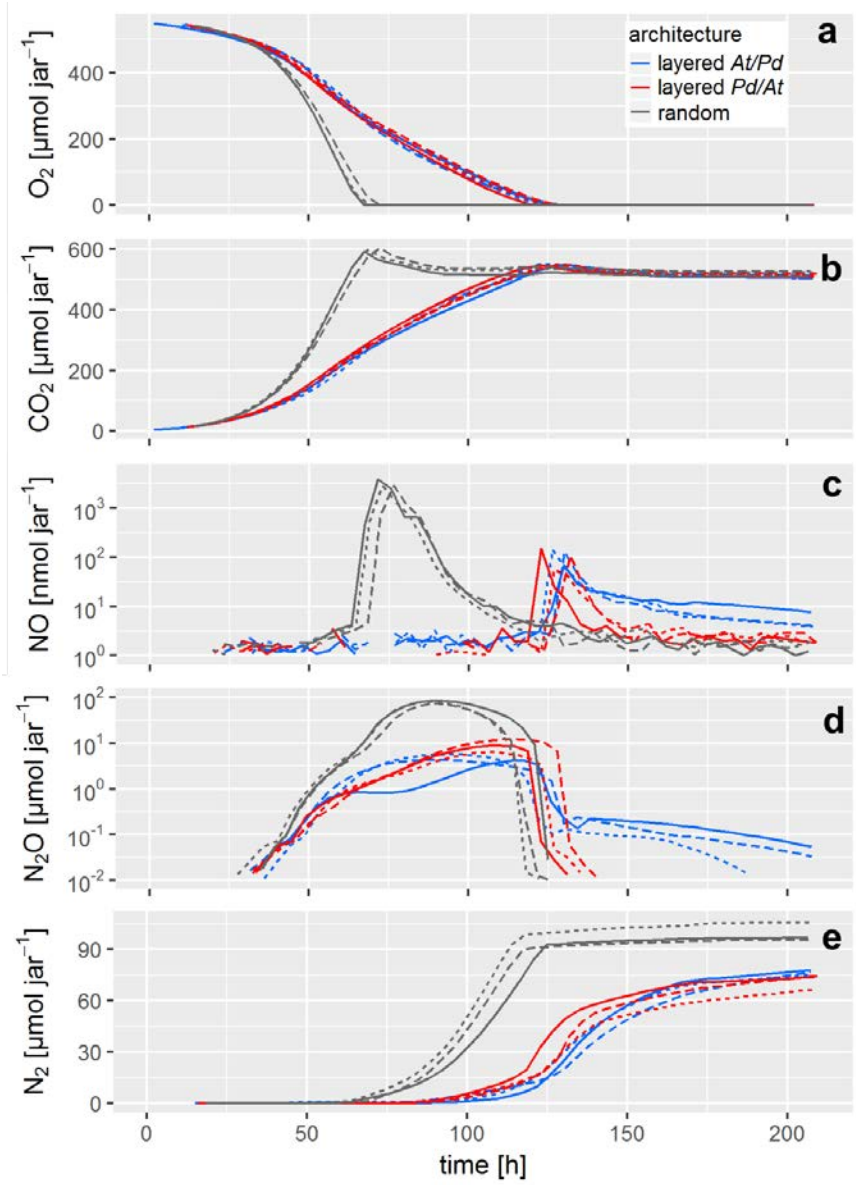

Figure 49: Gas kinetics in all treatments at medium saturation (60% WFPS) for three different hotspot architectures : (a) O_2, (b) CO_2, (c) NO, (d) N_2O, (e) N_2. Note the logarithmic ordinate in (c) and (d).

Effects of water saturation in sand

Differences in water saturation resulted in different absolute amounts of oxygen initially present in the jars (**Figure 4a**) but did not affect the O_2 concentration in the sand matrix. Oxygen was depleted slightly faster at 60% than at 90% saturation even though there was absolutely more O_2 initially present at 60% WFPS. This illustrates the paramount role of oxic growth for the oxic-anoxic transition in the hotspots: the more O_2 available initially, the stronger the aerobic growth and the faster the oxic-anoxic transition.

Increasing saturation from 60 to 90% in the randomly distributed hotspots had a strong effect on the timing and accumulation of denitrification products. The expected NO burst upon O_2 depletion was damped by two orders of magnitude (**Figure 4c**), because the oxic-anoxic transition proceeded more

smoothly in the 90% treatment and NO was reduced further to N_2O before it could escape to the headspace. On the other hand, N_2O and N_2 production commenced earlier in the 90% than in the 60% treatment (**Figure 4d-e**), indicating that O_2 availability was *a priori* smaller irrespective of metabolic activity (which was larger in the 60% treatment). The switch from net N_2O production to net N_2O consumption indicates the moment when microbial activity in *Pd* hotspots caught up with *At* hotspots.

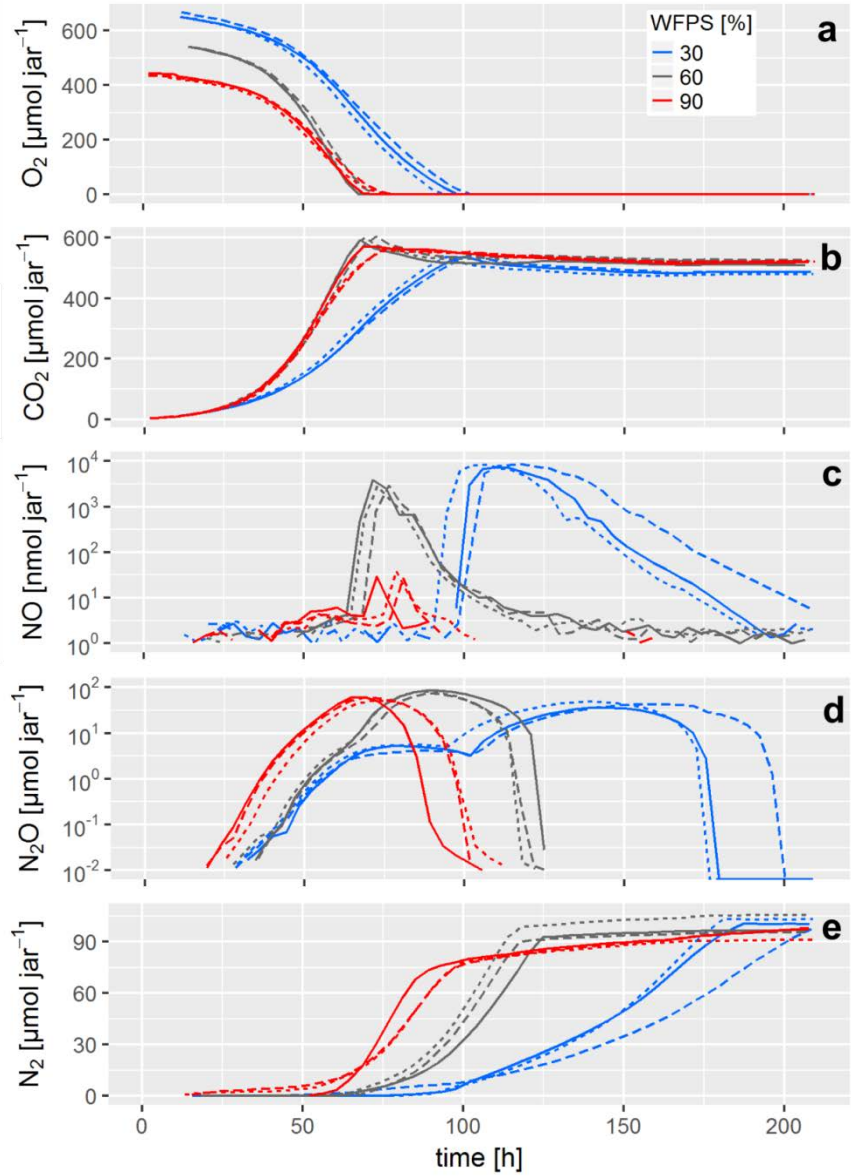

Figure 50: Gas kinetics of randomly placed hotspots at three different saturations: (a) O_2, (b) CO_2, (c) NO, (d) N_2O, (e) N_2. Note the logarithmic ordinate in (c) and (d).

Surprisingly, O_2 consumption in the 30% treatments was slow despite having the largest amount of O_2 in the jar. This was caused by unintended substrate limitation. Due to overlapping pore size distribution between porous hotspots and sand (**Fig. S10c**), medium was sucked by capillary force from the hotspot into the surrounding sand, as could be seen in a parallel experiment with brilliant blue dye (**Fig. S14**). This separated cells, which were likely immobilized in the pore space of the hotspots, temporarily from a

considerable fraction of the carbon and NO_3^- supplied with the medium, before the dissolved substrate would diffuse back into the hotspots due to the evolving gradient induced by consumption in the hotspots. Decreasing the saturation from 60% to 30% also resulted in different timing and accumulation of denitrification products. The slow oxic growth of both *At* and *Pd* hotspots due to the substrate diffusion limitation at 30% WFPS provided more time for *Pd* hotspots to interact with *At* hotspots than in the 60% WFPS treatment. Indeed, the NO burst from *At* hotspots after complete O_2 exhaustion in the random architecture was 50% higher at 30% WFPS indicating higher *At* cell numbers due to prolonged oxic growth (**Figure 4c, Figure 5c**), whereas the N_2O peak was 50% lower, due to concomitant N_2O reduction in *Pt* hotspots (**Figure 4d , Figure 5d**).

Mass balances

By the end of the incubation, oxygen was exhausted in all treatments. Likewise, NO_3^- was consumed by all treatments, except for the layered hotspots at 30% and 60% WFPS. This means that respiration was electron acceptor limited and that the cumulated recovery of denitrification products can be compared with the amount of NO_3^- initially present (**Fig. S15**). The balance between aerobic and anaerobic respiration, e^-_{denit}/e^-_{total} (Bergaust et al., 2011), is given by the electron flow to nitrogenous electron acceptors relative to the total electron flow, including O_2 respiration (**Figure 5**). When seen over all three water saturations, early stage denitrification under oxic headspace conditions (**Figure 5a**) showed a threshold response to increasing moisture with disproportionally higher e^-_{denit}/e^-_{total} ratios at 90% WFPS (17-27%) than at 60% or 30%. The proportions of electrons diverted to denitrification at low and medium saturations were small (2-7%) and even smaller than those observed in unconstrained hotspots (7-13%). Differences between saturations were less pronounced when the entire incubation period is considered (**Figure 5b**), since fully anoxic conditions during late stage incubation overrode saturation effects. Overall, the effect of hotspot architecture on e^-_{denit}/e^-_{total} ratios was smaller than the effect of saturation.

This stands in stark contrast to the pronounced effect of hotspot architecture on denitrification product ratios (**Figure 5c, d**). Hotspot architecture governed growth rates through local competition for O_2 and therewith the number of active cells involved in net production sites (*At* hotspots) and net consumption sites (*Pd* hotspots) of NO once O_2 was exhausted. In layered hotspot architectures there was hardly any net-release of NO to the headspace irrespective of saturation (**Figure 5c**). With random hotspot architecture, there was substantial NO release, the magnitude of which, however, decreased linearly with saturation. This pattern in NO stoichiometry clearly reflects the number of *At* cells at the moment of complete O_2 depletion, as affected by oxic growth which lasted longer with lower saturation. The N_2O product ratio (**Figure 5d**) was influenced by both saturation and hotspot architecture. In layered architectures, the N_2O ratio increased exponentially with increasing saturation similar to what was observed for relative electron flow to denitrification (**Figure 5a**). In random architectures, the N_2O product ratio was consistently higher than in layered architectures irrespective of saturation, yet the highest ratio was reached at 60% WFPS, due to the most vigorous growth, and hence fastest oxic-anoxic transition at intermediate saturation.

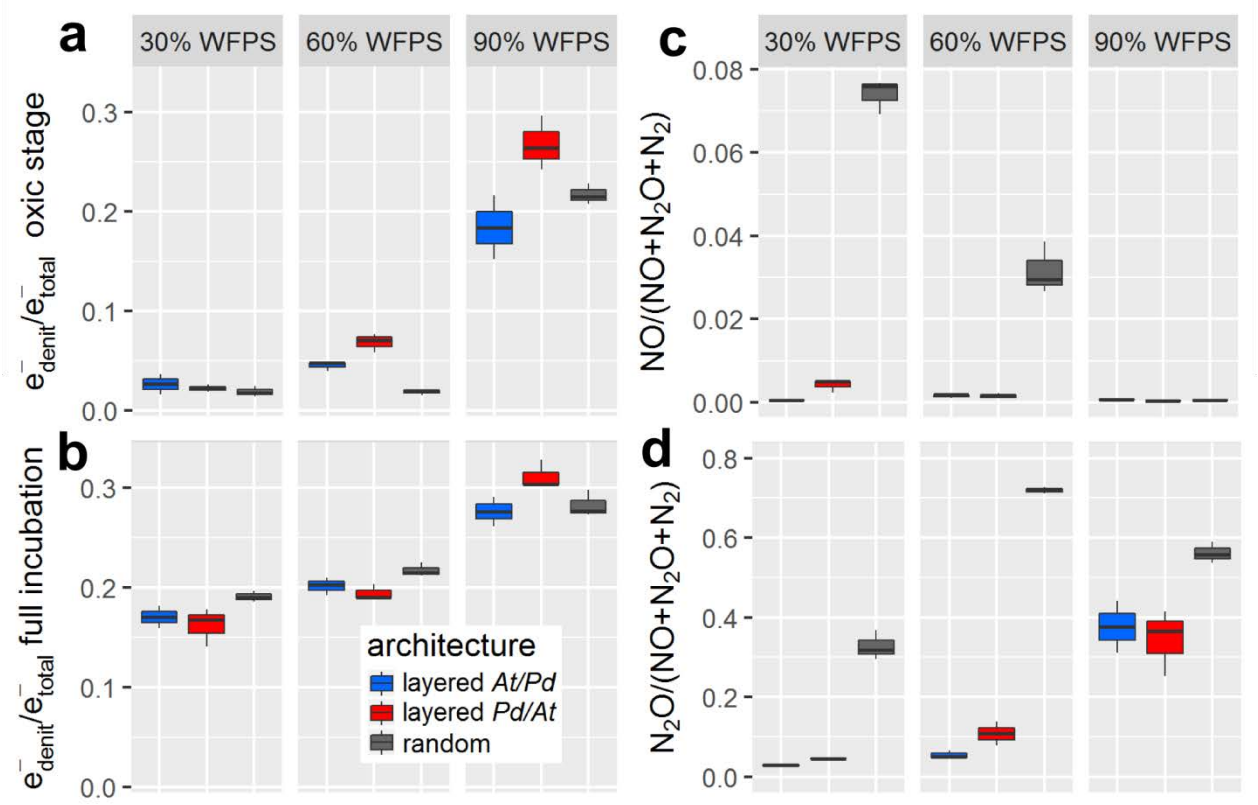

Figure 51: The proportion of denitrification in total respiration expressed as relative electron flow for all architectures and saturations. Values are reported for (a) the initial, oxic to hypoxic stage (O_2 present in headspace) and (b) for the full incubation period of 300 h. The product ratios for NO (c) and N_2O (d) consider the full incubation period and are corrected for the release of precursor gases.

Pore space properties

At the lowest saturation (30% WFPS), the entire air-filled pore space was connected to the headspace (**Figure 6a**) and tortuosity was close to unity, i.e. the diffusion lengths in air only depended on the vertical distance to the headspace (**Figure 6b**). The diffusion distances in water-filled pores (**Figure 6c**) corresponded to the size of small, evenly distributed water clusters. At medium saturation (60% WFPS), the amount of disconnected air was still negligible and tortuosity only slightly increased. The increase in air distance was due to a few large water pockets, which were caused by the step-wise addition of water to the repacked sand. Only at 90% saturation a considerable air volume of 5-20% became disconnected from the headspace. The path along which the remaining air was connected to the headspace became more tortuous with increasing saturation and average diffusion distances in water to the connected air cluster increased to 1 mm. This is still surprisingly short as compared to the size of the hotspots (7 mm). Independent tests showed that the high air connectivity at this low air content was facilitated by vacuum application during He/O_2-purging prior to the incubation. Directly after packing, the continuous air cluster only reached 10-15 mm into the sand (data not shown), whereas bubbling due to vacuum application formed continuous air channels that reached deep into the sand matrix connecting even the deepest hotspots with the headspace. Moreover, some larger gaps remained around hotspots during packing which tended to be air-filled after wetting. This is reflected in the consistently higher air-connectivity, lower air tortuosity and lower air distance, when only pores in the direct vicinity of hotspots are analyzed (**Figure 6a-c**). More than 90% of hotspot surfaces still had a direct air-filled connection with the headspace at 90% WFPS (**Figure 6a**). Depth profiles of these pore space attributes are reported in **Fig. S9**.

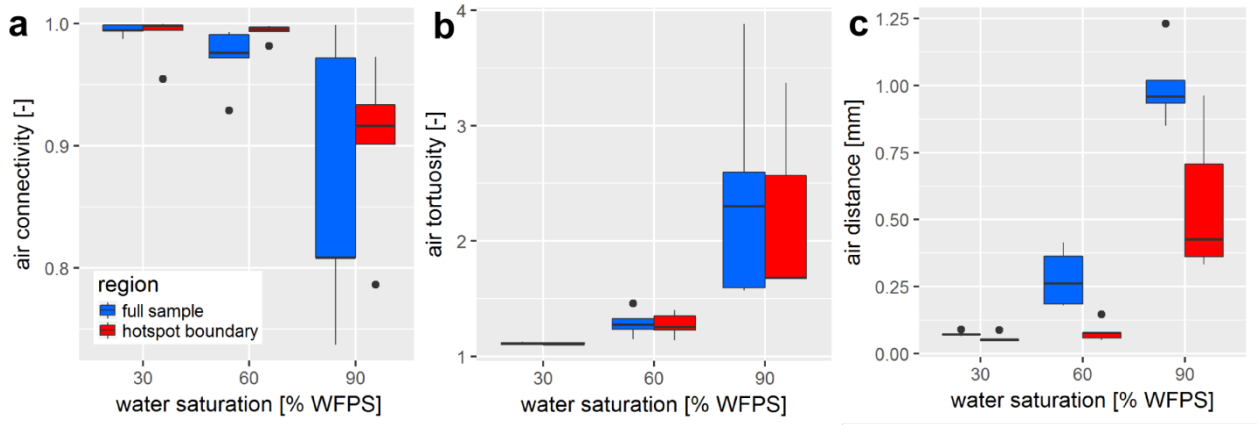

Figure 52: Morphological properties of air-filled pores at different saturations averaged over different hotspots architectures (n=5). These properties are reported separately for the entire pore space within the region of interest (full sample) and for the pore space in direct vicinity to the porous glass beads (hotspot boundary): (a) air connectivity represents the volume fraction of air with direct connection to the headspace. (b) Air tortuosity represents the ratio between geodesic length to the headspace and Euclidean distance for any voxel within the connected air-cluster. (c) Air distance represents the geodesic distance to the connected air cluster within the water-filled pores.

Discussion

Physical constraints on denitrification kinetics

The experimental setup in this incubation study was designed to investigate physical constraints on microbial respiration in hotspots as affected by the interplay between gaseous diffusion through a sterile matrix and local competition for oxygen. For this, we compared different combinations of water saturation in the matrix and spatial distributions of hotspots. The setup is a coarse simplification of soil in which metabolic activity in hotspots not only depends on oxygen supply, but also on diffusion of substrates from the matrix to the hotspots. As such, our experiment does not allow to draw direct conclusions about the functioning of hotspots in real soils with respect to denitrification and its product stoichiometry. However, by placing denitrifiers and their substrates into hotspots, we considerably reduced the level of complexity and created a system that is amenable to studying the dynamic interrelations between denitrifier growth, oxygen consumption and induction of denitrification by gas kinetics. Soil N_2O emissions are known to be highly variable in time and a unifying concept incorporating dynamic changes in denitrification activity and product stoichiometry in response to changing environmental conditions is still missing. Our model system provides a first data set for validating mathematical process models that are explicit for structural distribution of hotspots and dynamic changes in boundary conditions (here mimicked by different hotspot architectures and declining oxygen concentrations in the headspace of batch incubations, respectively). The development of such models is a core activity of the DASIM project (http://www.dasim.net/). By combining metabolic measurements with advanced structural imaging and computation, we also provide a link to parameterizing such models with real soil data in future research.

Inoculating growing denitrifiers into porous glass beads and embedding them in sterile sand resulted in a highly dynamic system with respect to oxygen consumption and induction of denitrification. This was intended for the sake of experimental depth, but it must be noted that oxic-anoxic transitions are likely slower, i.e. less dynamic in real-soil hotspots. In real soils, even highly organic hotspots contain a fair amount of recalcitrant organic C that limits microbial growth and oxygen consumption. Also with respect to denitrification stoichiometry, real soils may be expected to be less dynamic as multiple denitrifying phenotypes contained in the natural soil microbiome (Roco et al., 2017) utilize denitrification

intermediates mutually. Notwithstanding, soil NO and N_2O emissions are known to be episodic in nature. Large, denitrification driven emission pulses occur upon abrupt changes in O_2 availability, caused by external factors like heavy rainfalls or soil freezing (Flessa et al., 1995), O_2 consumption by nitrification after ammoniacal fertilization (Huang et al., 2014) or incorporation of easily degradable organic matter (Flessa et al., 1995) which cannot be captured satisfactorily by common steady-state models for soil respiration and N_2O emission (Li et al., 1992; Parton et al., 2001). Even though the concept of hotspots is central in the understanding of denitrification dynamics in upland soils, common soil denitrification models do not account for the dynamics of spatially explicit hotspots in the soil matrix but rather scale bulk denitrification with a generic anoxic volume fraction (Blagodatsky et al., 2011; Li et al., 2000). To advance soil denitrification models, it is obvious that microbial respiration dynamics in hotspots have to be targeted, both conceptually (Wang et al., 2019) and experimentally (Ebrahimi and Or, 2018; Kravchenko et al., 2017). Our study is a first step in this direction.

One of the main findings of this study is that soil microbial respiration and the propensity to develop denitrifying anoxic hotspots does depend on their distribution in space. The onset of denitrification and its kinetics was linked to the spatial and temporal extent of anoxia developing in hotspot centers, which was governed by the interplay between denitrifier growth and diffusion constraints and hotspot architecture had a strong impact on this interplay. When distributed randomly, microbial activity was most disperse relative to available oxygen, resulting in more growth, faster O_2 draw down and earlier anoxia than when packed densely in layers (**Figure 3**). Rapid oxic-anoxic transition led to higher release rates of denitrification intermediates increasing the product ratios of NO and N_2O (**Figure 5c-d**). This effect was most pronounced at low and intermediate saturations but was dampened at 90%WPFS because oxygen supply was impeded by bulk diffusion irrespective of hotspot placement. Thus, our results highlight the significance of hotspot distribution at low soil moistures and exemplifies why N_2O emissions are notoriously difficult to predict under these conditions.

Even though we failed to fully synchronize *At* and *Pd* growth in time, our experiment demonstrates that contrasting denitrification phenotypes may interact in modulating N_2O flux to the atmosphere. *Pd* hotspots reduced N_2O released from *At* hotspots irrespective of the layers' orientation (**Figure 3d**), which can be attributed to the high degree of air connectivity in the sand column (**Figure 1d**). We had expected more N_2O reduction with *Pd* on top (layered *Pd/At*), but since *At* grew faster than *Pd*, partial anoxia and NO and N_2O formation was induced in *At*, long before N_2O consuming activity was induced in *Pd* hotspots. Future experiments with artificial hotspots should therefore carefully consider potential growth rates and air connectivity in packed soil.

Physical constraints on cumulative denitrification

The cumulative release of gaseous denitrification products, as described by electron flow ratios, depended less on hotspot architecture than on soil moisture. Electron flows to denitrification ranged from <5% of total respiratory flow at low to medium saturations (30, 60% WFPS) to almost 23% at 90% WFPS (**Figure 5a**). We attribute this low denitrification electron flow to the small active volume relative to the sterile sand matrix (the total volume fraction of hotspots was 14%, less of which was actually anoxic) and the large amount of oxygen initially present in the incubation jars. Yet, we found a typical, non-linear denitrification response to soil moisture (**Figure 5a**). This threshold behavior is well known (Weier et al., 1993) and has been attributed to a disproportional contribution of small pores to the anoxic volume at higher saturation (Schurgers et al., 2006). In our system, consisting of coarse sand with a relatively homogenous pore size distribution, we attribute the non-linear response to an increase in tortuosity of air-filled pores that was pronounced enough to impair the supply of hotspots with oxygen. Air connectivity and distance to the next continuous, air-filled pore also increased non-linearly, but did not reach a critical value (**Figure 6**), ruling out that differences in NO and N_2O release at different saturations were due to

gas entrapment but rather due to elongated diffusion pathways in air-filled pore networks, leading to longer residence times of denitrification intermediates and stronger reduction of intermediates in hotspots along the way to the headspace. Saturation-dependent threshold behavior for denitrification is a well-studied phenomenon in soils (Linn and Doran, 1984a; Paul et al., 2003; Ruser et al., 2006), but for a lack of pore scale measurements often attributed to reduced bulk soil diffusivity. In undisturbed soil, the relative importance of air connectivity and distances between air-filled and water-filled pores might be more relevant for impairing oxygen supply and inducing denitrification. Air connectivity to the headspace was shown to affect N_2O emissions in terms of intensity and speed in repeated wetting/drying cycles in an intact soil column (Rabot et al., 2015). In agricultural soil with different crop rotations, N_2O emissions were shown to correlate positively with the volume fraction of soil with macropore distances larger than 180 µm, used as an *ad-hoc* definition for poorly aerated soil (Kravchenko et al., 2018). In a mesocosm study on microstructural drivers for local redox conditions, none of the investigated soil pore metrics derived from X-ray CT data (excluding those examined here) correlated with redox kinetics during a wetting/drying cycle (Wanzek et al., 2018). Hence, combining metabolic monitoring by high-resolution gas kinetics with direct assessment of diffusion lengths of gaseous and dissolved oxygen and denitrification products via X-ray microtomography emerges as a promising tool to study physical constraints for aerobic and anaerobic respiration in soil. However, meaningful metrics derived from X-ray data relevant for denitrification are yet to be developed and will require additional experiments with both artificial and real soils. Improved understanding of factors and mechanisms controlling denitrification and N gas emission on a three-dimensional micro-scale may help to design and test soil management strategies that mediate the return of excess nitrogen to the atmosphere in a controlled way, i.e. with as little as possible NO and N_2O release, be it by crop residue (Kravchenko et al., 2017), pH (Russenes et al., 2016) or irrigation (Bergstermann et al., 2011) management. At the same time, our experiments call for the implementation of spatially explicit reaction-diffusion algorithms (Ebrahimi and Or, 2016; Hron et al., 2015) in soil process models. For instance, diffusion lengths between hotspots and air-filled pores connected to the headspace may serve as useful measure to parametrize model concepts like the anaerobic soil volume fraction in larger-scale continuum models (Blagodatsky et al., 2011; Li et al., 2000; Schurgers et al., 2006).

Conclusions

Using a highly simplified model system, we demonstrate that the factorial combination of water saturation and hotspot architecture creates a wealth of denitrification kinetics in response to declining oxygen concentrations with highly variable NO and N_2O release rates. Even though our experiment was conducted in a closed system, with growing denitrifier strains and a limited amount of substrate, the results are relevant for real soils in that they give a worst-case scenario of population dynamics and metabolic activity in hotspots. Hotspot architecture played a more pronounced role for denitrification kinetics at lower soil moisture (30 and 60% WFPS). Hence, denitrification and its gaseous product stoichiometry do not only depend on the amount of microbial hotspots in aerated soil, but also on their spatial distribution. The total amount of denitrification measured as cumulative electron flow, in turn, depended more on water saturation which is in line with the well-known saturation-dependent threshold behavior in denitrification also found in natural soil. For the case of artificial soil used in our study, we found that this threshold behavior was best explained by increased air tortuosity at high saturations. Future experiments with artificial and natural soils are needed to fully capture the regulation of denitrification at the micro-scale.

Acknowledgments

This study was funded by the Deutsche Forschungsgemeinschaft through the research unit DFG-FOR 2337: Denitrification in Agricultural Soils: Integrated Control and Modelling at Various Scales (DASIM).

PD received funding from the FACCE-ERA-GAS project MAGGE-pH under the Grant Agreement No. 696356. We thank Linda Bergaust for providing the bacterial strains, Jing Zhu for laboratory support and Olaf Ippisch and Marcus Horn for helpful discussions during the planning of the experiment.

Supporting Information (chapter 6.4)

SI 1 Methods (*with three figures*): 1.1 Incubation, 1.2 Product ratios, 1.3 Image processing and analysis

SI 2 Results (*with five figures*): 2.1 Incubation at 90% saturation, 2.2 Incubation at 60% saturation, 2.3 Incubation at 20% saturation, 2.4. Nitrogen balance

4. Conclusions and Outlook

4.1. Appraisal of soil structure as an indicator of soil functions

This cumulative thesis gathered the findings of seven papers that all dealt with various aspects of soil structure characterization, the quantification of its dynamics as well as the impact of soil structure on several soil function like water filter and storage, soil aeration and gas exchange with the atmosphere, carbon sequestration, maintenance of microbial habitats and plant production.

In the introduction the dichotomy of soil structure characterization from two different viewpoints was stressed - the aggregate perspective vs. the pore perspective. The aggregate perspective was adopted in this thesis when aggregates with predefined size and internal structure were used and incubated in isolation (chapter 3.1). For all other studies the pore perspective was adopted as it is the pore space that provides pathways for water and matter fluxes, the habitat for soil biota and the locations for chemical reactions. The main purpose of the four method papers in chapter 2 was to advance and extend our image processing methods in order to take full advantage of the change in perspective. Common to all papers was the limited range of pore sizes that can be captured with X-ray CT. The ratio between sample diameter and image resolution is roughly 1500-2000 for the X-ray CT scanner used in all studies. Hence, for the samples with a diameter of 10cm an image resolution of 60µm can be achieved (chapter 2.2, 3.1), so that only large macropores are captured. The range of pore sizes can be extended towards smaller pores by scanning smaller subsamples and merging the pore size distributions, which was originally proposed in (Vogel et al., 2010) and applied in chapter 3.1. The range of pore sizes can even be extended beyond the technical limits of X-ray CT by taking electron microscopy or secondary ion mass spectrometry into account through correlative imaging (chapter 2.4). Eventually, the adequate scale to study soil structure depends on the process or function of interest. The distribution of bacteria within soil is captured representatively in less than a cm^2 (chapter 2.4), whereas $700cm^3$ of soil was not enough to capture saturated hydraulic conductivity of a field soil representatively, indicated by the large variability among replicates from the same treatment (chapter 3.1).

On several occasions it was shown that soil structure is a formidable indicator for the soil ecological status sometimes also referred to as soil health (Kibblewhite et al., 2008; Rabot et al., 2018). This is because soil structure governs many processes in soils but at the same time is also actively shaped by them. For instance, the habitat function of soils was shown to be regulated by soil structure in terms of spatial distribution of bacteria (chapter 2.4) and differentiation into aerobic and anaerobic respiration (chapter 3.2,3.3). In turn, soil biota, in that case earthworms, actively modified soil structure through bioturbation (chapter 3.1).

A frequent observation in all studies was the non-linear relationship between structural properties as well as between structural properties and functional behavior. Two examples for the former were the steep change in macropore connectivity in a rather small macroporosity range in repacked soil (chapter 2.3) and a somewhat smoother transition in intact soil (chapter 3.1) and the non-linear increase in distances towards air-filled pores as well as tortuosity of air-filled pores with increasing water saturation (chapter 2.4,3.3). Examples for the non-linear relationship between structural properties and functional behavior were manifold. Saturated hydraulic conductivity increased by several orders of magnitude within a rather small macroporosity range (chapter 3.1). Grain yield was not affected at all by a reduction in

macroporosity (air capacity), since root growth is only impaired when a critical threshold in aeration and mechanical impedance is reached (chapter 3.1). The magnitude in denitrification and hence the anaerobic soil volume fraction depended non-linearly on the external oxygen distribution at aggregate boundaries (chapter 3.2) and on the water saturation in the sand samples containing microbial hotspots (chapter 3.3).

4.2. The way forward

This thesis has introduced the foundations for characterization of soil structure and soil structure dynamics via 3D imaging and applied these tools to a selected number of experimental studies. The logical next step is to take advantage of these methods and apply them to additional laboratory experiments and field trials of similar or completely different scope. Most of the future work outlined in the following is already ongoing:

- Incubation experiments to study the relationship between soil structure and microbial respiration and denitrification need to be extended to real soils. In the next step of structural complexity real soils are sieved into different aggregate size fraction and repacked to the original bulk density. Tentative results show that CO_2 and N_2O emissions mainly depend on organic carbon content, water saturation, aggregate size and bulk density. Oxygen micro-sensor measurements highlight an enormous variability in oxygen supply at mm-cm scales depending on the local distance to the closest air-filled pore. The final step in structural complexity is reached when intact soils are incubated directly. Soil structure effects can be assessed by comparing the gas emissions with those of repacked soils, as organic carbon content, water saturation and bulk density are the same.
- The new approach of soil structure labeling to estimate soil structure turnover has only been tested on soil compaction as an abiotic process of soil structure modification. Meanwhile, another experiment with the same setup has been carried out to study soil structure turnover through repeated wetting and drying cycles. The magnitude of soil structure changes depended on clay mineralogy and organic carbon content. Yet soil structure turnover in terms of randomization of particle-pore distances is not induced by wetting/drying cycles, because the original crack pattern imprinted by the first drying event is reused in subsequent drying events. It is more likely that biotic agents like plant growth and earthworm activity are more capable of inducing soil structure turnover, but this remains to be tested.
- The long-term trial in chapter 3.1 only comprised two tillage treatments (conventional tillage and reduced tillage) and the observed trends under reduced tillage (topsoil compaction by traffic cannot be compensated by bioturbation) might only by representative for the given soil texture and the climatic conditions on site. Meanwhile, the analysis of another long-term tillage trial has been finalized in which conventional tillage and no-till are compared on a similar parent material like in chapter 3.1 but slightly moister climate (Lüttewitz, Saxony). In that trial no-till let to a higher bulk density in the top 15cm as compared to the plowed soil and yet the saturated hydraulic conductivity of the no-till soil is significantly higher due to the presence of large, vertically oriented earthworm burrows. More field trials need to be analyzed with the presented methodology to paint a clearer picture of the tillage-induced changes in soil structure and its implications for the soil ecological status.
- Several issues arise when a large number of X-ray CT data from various field trials around the world are to be compared with each other. First, there is no generally accepted protocol for image

segmentation and analysis so that the results might be different depending on the protocols established in each institute. Secondly, the large file sizes (currently up to 8GB) pose huge requirements in terms of computing power, internal memory and disk space. Such infrastructure can only be provided by a few institutes. A soil structure library was recently launched at the Department of Soil System Science of the UFZ as an effort to provide the computing facility, a fixed protocol for uniform image analysis as well as the long-term storage capacity to build up an open-access archive for soil structure data. In order to facilitate data mining of a large number of datasets, important meta-information is required during the upload of each segmented image. This enables a differentiated look on soil structure development under different parent material, climate and management.

- Plant-Soil interactions have not been addressed in this thesis even though it is well known that root growth is affected by soil structure and at the same time root growth modifies soil structure through radial displacement of particles, release of rhizodeposits and desiccation through root water uptake. New image analysis protocols have been developed to study root system architecture from the soil perspective instead of the traditional root perspective (Schlüter et al., 2018a). That is, root system architecture has typically been assessed by root length density and root hierarchy. The new perspective is achieved by analyzing the distances of soil locations to the nearest root segment which informs about root clustering and the efficiency of soil exploration by roots. Hence, the combination of both approaches gathers complementary information on root system architecture, which is useful when the effect of soil structure on root growth is to be analyzed. A suite of pot experiments is currently underway that determine the role of bulk density, soil texture and plant genotypes on root system architecture. In the future, this pot experiments will be combined with the structure labeling approach introduced in chapter 2.3 to determine the role of root growth for soil structure turnover through the formation of root channels, induction of desiccation cracks and radial compaction around roots.

5. References

Abdollahi, L., Getahun, G.T., Munkholm, L.J., 2017. Eleven Years' Effect of Conservation Practices for Temperate Sandy Loams: I. Soil Physical Properties and Topsoil Carbon Content. Soil Science Society of America Journal 81(2), 380-391.

Abdollahi, L., Munkholm, L.J., 2017. Eleven Years' Effect of Conservation Practices for Temperate Sandy Loams: II. Soil Pore Characteristics. Soil Science Society of America Journal 81(2), 392-403.

Abdollahi, L., Munkholm, L.J., Garbout, A., 2014. Tillage System and Cover Crop Effects on Soil Quality: II. Pore Characteristics. Soil Science Society of America Journal 78(1), 271-279.

Ad-hoc-AG Boden, 2005. Bodenkundliche Kartieranleitung (KA 5). Schweizerbart, Stuttgart.

Adrian, R.J., 1991. Particle-imaging techniques for experimental fluid mechanics. Annual review of fluid mechanics 23(1), 261-304.

Akbari, A., Ghoshal, S., 2015. Bioaccessible Porosity in Soil Aggregates and Implications for Biodegradation of High Molecular Weight Petroleum Compounds. Environmental Science & Technology 49(24), 14368-14375.

Alakukku, L., 1996. Persistence of soil compaction due to high axle load traffic. II. Long-term effects on the properties of fine-textured and organic soils. Soil and Tillage Research 37(4), 223-238.

Almajmaie, A., Hardie, M., Acuna, T., Birch, C., 2017. Evaluation of methods for determining soil aggregate stability. Soil and Tillage Research 167, 39-45.

Altermann, M., Rinklebe, J., Merbach, I., Körschens, M., Langer, U., Hofmann, B., 2005. Chernozem - Soil of the Year 2005. Journal of Plant Nutrition and Soil Science 168, 725-740.

Amelung, W., Brodowski, S., Sandhage-Hofmann, A., Bol, R., 2008. Chapter 6 Combining Biomarker with Stable Isotope Analyses for Assessing the Transformation and Turnover of Soil Organic Matter. Academic Press, pp. 155-250.

Anderson, S.H., Hopmans, J.W., 2013. Soil-water-root Processes: Advances in Tomography and Imaging. SSSA Spec. Publ., 61. Soil Sci. Soc. of Am., Madison, WI.

Angers, D.A., Recous, S., Aita, C., 1997. Fate of carbon and nitrogen in water-stable aggregates during decomposition of 13C15N-labelled wheat straw in situ. European Journal of Soil Science 48(2), 295-300.

Arah, J.R.M., Smith, K.A., 1989. Steady-state denitrification in aggregated soils: a mathematical model. Journal of Soil Science 40(1), 139-149.

Armstrong, R.T., Porter, M.L., Wildenschild, D., 2012. Linking Pore-Scale Interfacial Curvature to Column-Scale Capillary Pressure. Advances in Water Resources.

Assouline, S., 2006. Modeling the Relationship between Soil Bulk Density and the Water Retention Curve. Vadose Zone Journal 5(2), 554-563.

Baba, H.O., Peth, S., 2012. Large scale soil box test to investigate soil deformation and creep movement on slopes by Particle Image Velocimetry (PIV). Soil and Tillage Research 125, 38-43.

Baek, S.-H., Shapleigh, J.P., 2005. Expression of Nitrite and Nitric Oxide Reductases in Free-Living and Plant-Associated Agrobacterium tumefaciens C58 Cells. Applied and Environmental Microbiology 71(8), 4427-4436.
Bakken, L.R., Bergaust, L., Liu, B., Frostegård, Å., 2012. Regulation of denitrification at the cellular level: a clue to the understanding of N₂O emissions from soils. Philosophical Transactions of the Royal Society B: Biological Sciences 367(1593), 1226-1234.
Ball, B.C., 2013. Soil structure and greenhouse gas emissions: a synthesis of 20 years of experimentation. European Journal of Soil Science 64(3), 357-373.
Ball, B.C., Batey, T., Munkholm, L.J., 2007. Field assessment of soil structural quality – a development of the Peerlkamp test. Soil Use and Management 23(4), 329-337.
Barnett, C., Bengough, A., McKenzie, B., 2009. Quantitative image analysis of earthworm-mediated soil displacement. Biology and Fertility of Soils 45(8), 821-828.
Baveye, P., 2006. Comment on "Soil structure and management: A review" by CJ Bronick and R. Lal. Geoderma 134(1-2), 231-232.
Baveye, P.C., Laba, M., Otten, W., Bouckaert, L., Sterpaio, P.D., Goswami, R.R., Grinev, D., Houston, A., Hu, Y., Liu, J., Mooney, S., Pajor, R., Sleutel, S., Tarquis, A., Wang, W., Wei, Q., Sezgin, M., 2010. Observer-dependent variability of the thresholding step in the quantitative analysis of soil images and X-ray microtomography data. Geoderma 157(1-2), 51-63.
Baveye, P.C., Otten, W., Kravchenko, A., Balseiro-Romero, M., Beckers, É., Chalhoub, M., Darnault, C., Eickhorst, T., Garnier, P., Hapca, S., Kiranyaz, S., Monga, O., Mueller, C.W., Nunan, N., Pot, V., Schlüter, S., Schmidt, H., Vogel, H.-J., 2018. Emergent Properties of Microbial Activity in Heterogeneous Soil Microenvironments: Different Research Approaches Are Slowly Converging, Yet Major Challenges Remain. Frontiers in Microbiology 9(1929), 1-48.
Bay, B.K., Smith, T.S., Fyhrie, D.P., Saad, M., 1999. Digital volume correlation: Three-dimensional strain mapping using X-ray tomography. Experimental Mechanics 39(3), 217-226.
Beare, M.H., Bruce, R.R., 1993. A comparison of methods for measuring water-stable aggregates: implications for determining environmental effects on soil structure. Geoderma 56(1-4), 87-104.
Bengough, A.G., Hans, J., Bransby, M.F., Valentine, T.A., 2010. PIV as a method for quantifying root cell growth and particle displacement in confocal images. Microscopy Research and Technique 73(1), 27-36.
Bergaust, L., Bakken, Lars R., Frostegård, Å., 2011. Denitrification regulatory phenotype, a new term for the characterization of denitrifying bacteria. Biochemical Society Transactions 39(1), 207-212.
Bergaust, L., Mao, Y., Bakken, L., Frostegard, A., 2010. Denitrification response patterns during the transition to anoxic respiration and posttranscriptional effects of suboptimal pH on nitrogen oxide reductase in Paracoccus denitrificans Appl. Environ. Microbiol. 76(19), 6387-6396.
Bergaust, L., Shapleigh, J., Frostegård, Å., Bakken, L., 2008. Transcription and activities of NOx reductases in Agrobacterium tumefaciens: the influence of nitrate, nitrite and oxygen availability. Environmental Microbiology 10(11), 3070-3081.

Bergstermann, A., Cárdenas, L., Bol, R., Gilliam, L., Goulding, K., Meijide, A., Scholefield, D., Vallejo, A., Well, R., 2011. Effect of antecedent soil moisture conditions on emissions and isotopologue distribution of N2O during denitrification. Soil Biology and Biochemistry 43(2), 240-250.
Berisso, F.E., Schjønning, P., Keller, T., Lamandé, M., Etana, A., de Jonge, L.W., Iversen, B.V., Arvidsson, J., Forkman, J., 2012. Persistent effects of subsoil compaction on pore size distribution and gas transport in a loamy soil. Soil and Tillage Research 122(Supplement C), 42-51.
Bernoux, M., Cerri, C.C., Neill, C., de Moraes, J.F.L., 1998. The use of stable carbon isotopes for estimating soil organic matter turnover rates. Geoderma 82(1-3), 43-58.
Berthod, M., Kato, Z., Yu, S., Zerubia, J., 1996. Bayesian image classification using Markov random fields. Image and Vision Computing 14(4), 285-293.
Besag, J., 1986. On the statistical analysis of dirty pictures. Journal of the Royal Statistical Society. Series B (Methodological), 259-302.
Beucher, S., Lantuejoul, C., 1979. Use of watersheds in contour detection. Proc. Int. Workshop Image Processing, Real-time Edge and Motion Detection/Estimation.
Blagodatskaya, E., Kuzyakov, Y., 2013. Active microorganisms in soil: Critical review of estimation criteria and approaches. Soil Biology and Biochemistry 67, 192-211.
Blagodatsky, S., Grote, R., Kiese, R., Werner, C., Butterbach-Bahl, K., 2011. Modelling of microbial carbon and nitrogen turnover in soil with special emphasis on N-trace gases emission. Plant and Soil 346(1), 297.
Blunt, M.J., Bijeljic, B., Dong, H., Gharbi, O., Iglauer, S., Mostaghimi, P., Paluszny, A., Pentland, C., 2013. Pore-scale imaging and modelling. Advances in Water Resources 51, 197-216.
Briones, M.J.I., Schmidt, O., 2017. Conventional tillage decreases the abundance and biomass of earthworms and alters their community structure in a global meta-analysis. Global Change Biology 23(10), 4396-4419.
Bronick, C.J., Lal, R., 2005. Soil structure and management: a review. Geoderma 124, 3-22.
Brown, K., Schlüter, S., Sheppard, A., Wildenschild, D., 2014. On the challenges of measuring interfacial characteristics of three-phase fluid flow with x-ray microtomography. Journal of Microscopy 253(3), 171-182.
Buades, A., Coll, B., Morel, J.-M., 2005. A non-local algorithm for image denoising, Computer Vision and Pattern Recognition, 2005. CVPR 2005. IEEE Computer Society Conference on, San Diego, California, pp. 60-65 vol. 62.
Buades, A., Coll, B., Morel, J.-M., 2008. Nonlocal Image and Movie Denoising. International Journal of Computer Vision 76(2), 123-139.
Canny, J., 1986. A Computational Approach to Edge Detection. Pattern Analysis and Machine Intelligence, IEEE Transactions on PAMI-8(6), 679-698.
Caplan, J., Niethammer, M., Taylor, R.M., Czymmek, K.J., 2011. The power of correlative microscopy: multi-modal, multi-scale, multi-dimensional. Current Opinion in Structural Biology 21(5), 686-693.
Capowiez, Y., Samartino, S., Cadoux, S., Bouchant, P., Richard, G., Boizard, H., 2012. Role of earthworms in regenerating soil structure after compaction in reduced tillage systems. Soil Biology and Biochemistry 55(Supplement C), 93-103.

Catté, F., Lions, P., Morel, J., Coll, T., 1992. Image Selective Smoothing and Edge Detection by Nonlinear Diffusion. SIAM Journal on Numerical Analysis 29(1), 182-193.
Chapuis-Lardy, L., Wrage, N., Metay, A., Chotte, J.-L., Bernoux, M., 2007. Soils, a sink for N2O? A review. Global Change Biology 13(1), 1-17.
Cho, S., Haralick, R., Yi, S., 1989. Improvement of kittler and illingworth's minimum error thresholding. Pattern Recognition 22(5), 609-617.
Christensen, B.T., 2001. Physical fractionation of soil and structural and functional complexity in organic matter turnover. European Journal of Soil Science 52(3), 345-353.
Chung, D.H., Sapiro, G., 2000. Segmentation-free skeletonization of gray-scale images via PDEs, Image Processing, 2000. Proceedings. IEEE International Conference on, Vancouver, BC, Canada, pp. 927-930 vol.922.
Clode, P.L., Kilburn, M.R., Jones, D.L., Stockdale, E.A., Cliff, J.B., Herrmann, A.M., Murphy, D.V., 2009. In Situ Mapping of Nutrient Uptake in the Rhizosphere Using Nanoscale Secondary Ion Mass Spectrometry. Plant Physiology 151(4), 1751-1757.
Cnudde, V., Boone, M.N., 2013. High-resolution X-ray computed tomography in geosciences: A review of the current technology and applications. Earth-Science Reviews 123, 1-17.
Costanza-Robinson, M.S., Harrold, K.H., Lieb-Lappen, R.M., 2008. X-ray Microtomography Determination of Air−Water Interfacial Area−Water Saturation Relationships in Sandy Porous Media. Environmental Science & Technology 42(8), 2949-2956.
Crawford, J.W., Deacon, L., Grinev, D., Harris, J.A., Ritz, K., Singh, B.K., Young, I., 2012. Microbial diversity affects self-organization of the soil-microbe system with consequences for function. Journal of The Royal Society Interface 9(71), 1302-1310.
Culligan, K.A., Wildenschild, D., Christensen, B.S.B., Gray, W.G., Rivers, M.L., Tompson, A.F.B., 2004. Interfacial area measurements for unsaturated flow through a porous medium. Water Resources Research 40(12), W12413.
Dal Ferro, N., Charrier, P., Morari, F., 2013. Dual-scale micro-CT assessment of soil structure in a long-term fertilization experiment. Geoderma 204, 84-93.
Dal Ferro, N., Sartori, L., Simonetti, G., Berti, A., Morari, F., 2014. Soil macro-and microstructure as affected by different tillage systems and their effects on maize root growth. Soil and Tillage Research 140, 55-65.
de Albuquerque, M.P., Esquef, I.A., Mello, A.R.G., de Albuquerque, M.P., 2004. Image thresholding using Tsallis entropy. Pattern Recognition Letters 25(9), 1059-1065.
Deubel, A., Hofmann, B., Orzessek, D., 2011. Long-term effects of tillage on stratification and plant availability of phosphate and potassium in a loess chernozem. Soil and Tillage Research 117, 85-92.
Dexter, A.R., 1988. Advances in Characterization of Soil Structure. Soil & Tillage Research 11, 199-238.
Díaz-Zorita, M., Perfect, E., Grove, J.H., 2002. Disruptive methods for assessing soil structure. Soil and Tillage Research 64(1), 3-22.
DIN ISO 11274-1, 2001. Bodenbeschaffenheit–Bestimmung des Wasserrückhaltevermögens–Laborverfahren. Beuth-Verlag, Berlin.
DIN ISO 23611-1, 2007. Bodenbeschaffenheit–Probenahme von Wirbellosen im Boden–Teil 1: Handauslese und Formalinextraktion von Regenwürmern, Berlin: Beuth.
Doane, T.A., Horwáth, W.R., 2003. Spectrophotometric Determination of Nitrate with a Single Reagent. Analytical Letters 36(12), 2713-2722.

Dörsch, P., Braker, G., Bakken, L.R., 2012. Community-specific pH response of denitrification: experiments with cells extracted from organic soils. FEMS Microbiology Ecology 79(2), 530-541.
Doube, M., Kłosowski, M.M., Arganda-Carreras, I., Cordelières, F.P., Dougherty, R.P., Jackson, J.S., Schmid, B., Hutchinson, J.R., Shefelbine, S.J., 2010. BoneJ: Free and extensible bone image analysis in ImageJ. Bone 47(6), 1076-1079.
Dungait, J.A.J., Hopkins, D.W., Gregory, A.S., Whitmore, A.P., 2012. Soil organic matter turnover is governed by accessibility not recalcitrance. Global Change Biology 18(6), 1781-1796.
Ebrahimi, A., Or, D., 2015. Hydration and diffusion processes shape microbial community organization and function in model soil aggregates. Water Resources Research 51(12), 9804-9827.
Ebrahimi, A., Or, D., 2016. Microbial community dynamics in soil aggregates shape biogeochemical gas fluxes from soil profiles - upscaling an aggregate biophysical model. Global Change Biology 22(9), 3141-3156.
Ebrahimi, A., Or, D., 2018. Dynamics of soil biogeochemical gas emissions shaped by remolded aggregate sizes and carbon configurations under hydration cycles. Global Change Biology 24(1), e378-e392.
Ebrahimi, A.N., Or, D., 2014. Microbial dispersal in unsaturated porous media: Characteristics of motile bacterial cell motions in unsaturated angular pore networks. Water Resources Research, n/a-n/a.
Eichorst, S.A., Strasser, F., Woyke, T., Schintlmeister, A., Wagner, M., Woebken, D., 2015. Advancements in the application of NanoSIMS and Raman microspectroscopy to investigate the activity of microbial cells in soils. FEMS Microbiology Ecology 91(10), fiv106.
Eickhorst, T., Tippkötter, R., 2008. Improved detection of soil microorganisms using fluorescence in situ hybridization (FISH) and catalyzed reporter deposition (CARD-FISH). Soil Biology and Biochemistry 40(7), 1883-1891.
Elberling, B., Askaer, L., Jørgensen, C.J., Joensen, H.P., Kühl, M., Glud, R.N., Lauritsen, F.R., 2011. Linking Soil O2, CO2, and CH4 Concentrations in a Wetland Soil: Implications for CO2 and CH4 Fluxes. Environmental Science & Technology 45(8), 3393-3399.
Emerson, J.B., Adams, R.I., Román, C.M.B., Brooks, B., Coil, D.A., Dahlhausen, K., Ganz, H.H., Hartmann, E.M., Hsu, T., Justice, N.B., Paulino-Lima, I.G., Luongo, J.C., Lymperopoulou, D.S., Gomez-Silvan, C., Rothschild-Mancinelli, B., Balk, M., Huttenhower, C., Nocker, A., Vaishampayan, P., Rothschild, L.J., 2017. Schrödinger's microbes: Tools for distinguishing the living from the dead in microbial ecosystems. Microbiome 5(1), 86.
Falconer, R.E., Battaia, G., Schmidt, S., Baveye, P., Chenu, C., Otten, W., 2015. Microscale Heterogeneity Explains Experimental Variability and Non-Linearity in Soil Organic Matter Mineralisation. PLoS ONE 10(5), e0123774.
Feeney, D.S., Crawford, J.W., Daniell, T., Hallett, P.D., Nunan, N., Ritz, K., Rivers, M., Young, I.M., 2006. Three-dimensional Microorganization of the Soil-Root-Microbe System. Microbial Ecology 52(1), 151-158.
Ferreira, T., Rasband, W., 2012. ImageJ User Guide - IJ 1.46r. National Insitute of Health, Bethesda, MD.

Fierer, N., Schimel, J.P., 2003. A proposed mechanism for the pulse in carbon dioxide production commonly observed following the rapid rewetting of a dry soil. Soil Science Society of America Journal 67(3), 798-805.
Firestone, M., 1982. Biological denitrification. Nitrogen in agricultural soils (nitrogeninagrics), 289-326.
Flemming, H.-C., Wingender, J., Szewzyk, U., Steinberg, P., Rice, S.A., Kjelleberg, S., 2016. Biofilms: an emergent form of bacterial life. Nature Reviews Microbiology 14, 563.
Flessa, H., Dörsch, P., Beese, F., 1995. Seasonal variation of N2O and CH4 fluxes in differently managed arable soils in southern Germany. Journal of Geophysical Research: Atmospheres 100(D11), 23115-23124.
Freundlich, D.A., 1987. Ring artifact correction for computerized tomography. Google Patents.
Garbout, A., Munkholm, L.J., Hansen, S.B., 2013. Tillage effects on topsoil structural quality assessed using X-ray CT, soil cores and visual soil evaluation. Soil and Tillage Research 128, 104-109.
Gardner, R., 1937. A method of measuring the capillary tension of soil moisture over a wide moisture range. Soil Science 43(4).
Geistlinger, H., Mohammadian, S., Schlüter, S., Vogel, H.-J., 2014. Quantification of capillary trapping of gas clusters using X-ray microtomography. Water Resources Research, n/a-n/a.
Gommes, C.J., Bons, A.J., Blacher, S., Dunsmuir, J.H., Tsou, A.H., 2009. Practical Methods for Measuring the Tortuosity of Porous Materials from Binary or Gray-Tone Tomographic Reconstructions. AIChE Journal 55(8), 2000-2012.
Gonzalez, R.G., Woods, R.G., 2002. Digital Image Processing. Prentice Hall, Upper Saddle Creek.
Groffman, P.M., Butterbach-Bahl, K., Fulweiler, R.W., Gold, A.J., Morse, J.L., Stander, E.K., Tague, C., Tonitto, C., Vidon, P., 2009. Challenges to incorporating spatially and temporally explicit phenomena (hotspots and hot moments) in denitrification models. Biogeochemistry 93(1), 49-77.
Guimarães, R.M.L., Ball, B.C., Tormena, C.A., 2011. Improvements in the visual evaluation of soil structure. Soil Use and Management 27(3), 395-403.
Guimarães, R.M.L., Ball, B.C., Tormena, C.A., Giarola, N.F.B., da Silva, Á.P., 2013. Relating visual evaluation of soil structure to other physical properties in soils of contrasting texture and management. Soil and Tillage Research 127, 92-99.
Hall, S.A., 2010. Discrete and continuum analysis of localised deformation in sand using X-ray μCT and volumetric digital image correlation. Géotechnique 60, 315-322(317).
Handschuh, S., Baeumler, N., Schwaha, T., Ruthensteiner, B., 2013. A correlative approach for combining microCT, light and transmission electron microscopy in a single 3D scenario. Frontiers in Zoology 10(1), 44.
Hapca, S., Baveye, P.C., Wilson, C., Lark, R.M., Otten, W., 2015. Three-Dimensional Mapping of Soil Chemical Characteristics at Micrometric Scale by Combining 2D SEM-EDX Data and 3D X-Ray CT Images. PLoS ONE 10(9), e0137205.
Hapca, S.M., Wang, Z.X., Otten, W., Wilson, C., Baveye, P.C., 2011. Automated statistical method to align 2D chemical maps with 3D X-ray computed micro-tomographic images of soils. Geoderma 164(3-4), 146-154.

Hartge, K., Bohne, H., 1983. Einfluss der Gefugegeometrie auf Verdichtbarkeit des Bodens und auf Keimung von Roggen. Zeitschrift fur Kulturtechnik und Flurbereinigung= Journal of rural engineering and development.
Hatton, P.-J., Remusat, L., Zeller, B., Derrien, D., 2012. A multi-scale approach to determine accurate elemental and isotopic ratios by nano-scale secondary ion mass spectrometry imaging. Rapid Communications in Mass Spectrometry 26(11), 1363-1371.
Hazlett, R.D., 1995. Simulation of capillary-dominated displacements in microtomographic images of reservoir rocks. Transport in Porous Media 20(1-2), 21-35.
Helliwell, J.R., Miller, A.J., Whalley, W.R., Mooney, S.J., Sturrock, C.J., 2014. Quantifying the impact of microbes on soil structural development and behaviour in wet soils. Soil Biology and Biochemistry 74(0), 138-147.
Helliwell, J.R., Sturrock, C.J., Grayling, K.M., Tracy, S.R., Flavel, R.J., Young, I.M., Whalley, W.R., Mooney, S.J., 2013. Applications of X-ray computed tomography for examining biophysical interactions and structural development in soil systems: a review. European Journal of Soil Science 64(3), 279-297.
Hilpert, M., Miller, C.T., 2001. Pore-morphology-based simulation of drainage in totally wetting porous media. Advances in Water Resources 24(3-4), 243-255.
Hofmann, B., Raebiger, H., Dunkel, J., 1993. The influence of structure-supporting tillage methods on selected soil properties and yields of a loamy sand site in Central Germany. Kuehn-Archiv (Germany).
Højberg, O., Revsbech, N.P., Tiedje, J.M., 1994. Denitrification in soil aggregates analyzed with microsensors for nitrous oxide and oxygen. Soil Science Society of America Journal 58(6), 1691-1698.
Horn, R., Baumgartl, T., 2002. Dynamic properties of soils, Soil Physics Companion. CRC Press, Boca Raton, FL, Boca Raton, FL, pp. 17-40.
Horn, R., Stepniewski, W., Wlodarczyk, T., Walenzik, G., Eckhardt, F., 1994. Denitrification rate and microbial distribution within homogeneous model soil aggregates. Int. Agrophysics 8, 65-74.
Hoshen, J., Kopelman, R., 1976. Percolation and cluster distribution. I. Cluster multiple labeling technique and critical concentration algorithm. Physical Review B 14, 3438-3445.
Houston, A., Schmidt, S., Tarquis, A., Otten, W., Baveye, P., Hapca, S., 2013a. Effect of scanning and image reconstruction settings in X-ray computed microtomography on quality and segmentation of 3D soil images. Geoderma 207, 154-165.
Houston, A.N., Otten, W., Baveye, P.C., Hapca, S., 2013b. Adaptive-window indicator kriging: A thresholding method for computed tomography images of porous media. Computers & Geosciences 54(0), 239-248.
Hron, P., Jost, D., Bastian, P., Gallert, C., Winter, J., Ippisch, O., 2015. Application of Reactive Transport Modeling to Growth and Transport of Microorganisms in the Capillary Fringe. Vadose Zone Journal 14(5).
Huang, T., Gao, B., Hu, X.-K., Lu, X., Well, R., Christie, P., Bakken, L.R., Ju, X.-T., 2014. Ammonia-oxidation as an engine to generate nitrous oxide in an intensively managed calcareous Fluvo-aquic soil. Scientific Reports 4, 3950.
Huang, T., Yang, G., Tang, G., 1979. A fast two-dimensional median filtering algorithm. Acoustics, Speech and Signal Processing, IEEE Transactions on 27(1), 13-18.

Hubert, F., Hallaire, V., Sardini, P., Caner, L., Heddadj, D., 2007. Pore morphology changes under tillage and no-tillage practices. Geoderma 142(1), 226-236.
Iassonov, P., Gebrenegus, T., Tuller, M., 2009. Segmentation of X-Ray CT Images of Porous Materials: A Crucial Step for Characterization and Quantitative Analysis of Pore Structures. Water Resources Research 45, W09415.
Iassonov, P., Tuller, M., 2010. Application of segmentation for correction of intensity bias in X-ray computed tomography images. Vadose Zone Journal 9(1), 187-191.
Ibanez, L., Schroeder, W., Ng, L., Cates, J., 2005. The ITK software guide. KITWARE.
Jahn, R., Blume, H., Asio, V., Spaargaren, O., Schad, P., 2006. Guidelines for soil description. 4th ed. FAO, Rome, Italy.
Jang, J.-H., Hong, K.-S., 2001. A pseudo-distance map for the segmentation-free skeletonization of gray-scale images, Computer Vision, 2001. ICCV 2001. Proceedings. Eighth IEEE International Conference on, pp. 18-23 vol.12.
Jawahar, C.V., Biswas, P.K., Ray, A.K., 1997. Investigations on fuzzy thresholding based on fuzzy clustering. Pattern Recognition 30(10), 1605-1613.
Jégou, D., Brunotte, J., Rogasik, H., Capowiez, Y., Diestel, H., Schrader, S., Cluzeau, D., 2002. Impact of soil compaction on earthworm burrow systems using X-ray computed tomography: preliminary study. European Journal of Soil Biology 38(3-4), 329-336.
Jones, C.M., Hallin, S., 2010. Ecological and evolutionary factors underlying global and local assembly of denitrifier communities. The Isme Journal 4, 633.
Juyal, A., Otten, W., Falconer, R., Hapca, S., Schmidt, H., Baveye, P.C., Eickhorst, T., 2019. Combination of techniques to quantify the distribution of bacteria in their soil microhabitats at different spatial scales. Geoderma 334, 165-174.
Kaestner, A., Lehmann, E., Stampanoni, M., 2008. Imaging and image processing in porous media research. Advances in Water Resources 31(9), 1174-1187.
Kahlon, M.S., Lal, R., Ann-Varughese, M., 2013. Twenty two years of tillage and mulching impacts on soil physical characteristics and carbon sequestration in Central Ohio. Soil and Tillage Research 126, 151-158.
Kapur, J.N., Sahoo, P.K., Wong, A.K.C., 1985. A new method for gray-level picture thresholding using the entropy of the histogram. Computer Vision, Graphics, and Image Processing 29(3), 273-285.
Kaufmann, M., Tobias, S., Schulin, R., 2010. Comparison of critical limits for crop plant growth based on different indicators for the state of soil compaction. Journal of Plant Nutrition and Soil Science 173(4), 573-583.
Kautz, T., Stumm, C., Kösters, R., Köpke, U., 2010. Effects of perennial fodder crops on soil structure in agricultural headlands. Journal of Plant Nutrition and Soil Science 173(4), 490-501.
Keeney, D., Nelson, D.W., 1982. Nitrogen--inorganic forms. Methods of soil analysis. Part 2. Chemical and microbiological properties, 643-698.
Keiluweit, M., Gee, K., Denney, A., Fendorf, S., 2018. Anoxic microsites in upland soils dominantly controlled by clay content. Soil Biology and Biochemistry 118, 42-50.
Keiluweit, M., Nico, P.S., Kleber, M., Fendorf, S., 2016. Are oxygen limitations under recognized regulators of organic carbon turnover in upland soils? Biogeochemistry 127(2), 157-171.

Keiluweit, M., Wanzek, T., Kleber, M., Nico, P., Fendorf, S., 2017. Anaerobic microsites have an unaccounted role in soil carbon stabilization. Nature Communications 8(1), 1771.
Ketcham, R.A., 2005. Computational methods for quantitative analysis of three-dimensional features in geological specimens. Geosphere 1(1), 32-41.
Ketcham, R.A., 2006. New algorithms for ring artifact removal. Proc. SPIE 6318, 63180O-63180O-63187.
Ketcham, R.A., Carlson, W.D., 2001. Acquisition, optimization and interpretation of X-ray computed tomographic imagery: applications to the geosciences. Computers & Geosciences 27(4), 381-400.
Khanzode, R.M., Vanapalli, S.K., Fredlund, D.G., 2002. Measurement of soil-water characteristic curves for fine-grained soils using a small-scale centrifuge. Canadian Geotechnical Journal 39(5), 1209-1217.
Kibblewhite, M.G., Ritz, K., Swift, M.J., 2008. Soil health in agricultural systems. Philosophical Transactions of the Royal Society B: Biological Sciences 363(1492), 685-701.
Kittler, J., Illingworth, J., 1986. Minimum error thresholding. Pattern Recognition 19(1), 41-47.
Klein, S., Staring, M., Murphy, K., Viergever, M.A., Pluim, J.P.W., 2010. elastix: A Toolbox for Intensity-Based Medical Image Registration. Medical Imaging, IEEE Transactions on 29(1), 196-205.
Klute, A., Dirksen, C., 1986. Hydraulic conductivity and diffusivity: laboratory methods. Methods of soil analysis: part 1—physical and mineralogical methods (methodsofsoilan1), 687-734.
Knight, R., Chapman, A., Knoll, M., 1990. Numerical modeling of microscopic fluid distribution in porous media. Journal of Applied Physics 68(3), 994-1001.
Koblenz, B., Tischer, S., Rücknagel, J., Christen, O., 2015. Influence of biogas digestate on density, biomass and community composition of earthworms. Industrial Crops and Products 66(Supplement C), 206-209.
Kolb, S., Horn, M., 2012. Microbial CH4 and N2O Consumption in Acidic Wetlands. Frontiers in Microbiology 3(78).
Kölbl, A., Schweizer, S., Mueller, C., Höschen, C., Said-Pullicino, D., Romani, M., Lugmeier, J., Schlüter, S., Kögel-Knabner, I., 2017. Legacy of Rice Roots as Encoded in Distinctive Microsites of Oxides, Silicates, and Organic Matter. Soils 1(1), 2.
Kravchenko, A., Negassa, W., Guber, A., Schmidt, S., 2014. New approach to measure soil particulateorganic matter in intact samples using X-ray computed microtomography. Soil Science Society of America Journal 78(4), 1177-1185.
Kravchenko, A., Wang, A., Smucker, A., Rivers, M., 2011. Long-term differences in tillage and land use affect intra-aggregate pore heterogeneity. Soil Science Society of America Journal 75(5), 1658-1666.
Kravchenko, A.N., Guber, A.K., 2017. Soil pores and their contributions to soil carbon processes. Geoderma 287, 31-39.
Kravchenko, A.N., Guber, A.K., Quigley, M.Y., Koestel, J., Gandhi, H., Ostrom, N.E., 2018. X-ray computed tomography to predict soil N2O production via bacterial denitrification and N2O emission in contrasting bioenergy cropping systems. GCB Bioenergy 0(0).
Kravchenko, A.N., Toosi, E.R., Guber, A.K., Ostrom, N.E., Yu, J., Azeem, K., Rivers, M.L., Robertson, G.P., 2017. Hotspots of soil N2O emission enhanced through water absorption by plant residue. Nature Geoscience 10, 496.

Kroulik, M., Kviz, Z., Masek, J., Misiewicz, P., 2012. Benefits of GPS agricultural guidance for sustainable agriculture. Agrociencia 16(3), 107-116.
Kuka, K., Illerhaus, B., Fritsch, G., Joschko, M., Rogasik, H., Paschen, M., Schulz, H., Seyfarth, M., 2013. A new method for the extraction of undisturbed soil samples for X-ray computed tomography. J. Nondestr. Test. 2013(8).
Kulkarni, R., Tuller, M., Fink, W., Wildenschild, D., 2012. Three-dimensional multiphase segmentation of X-Ray CT data of porous materials using a Bayesian Markov random field framework. Vadose Zone Journal 11(1).
Kumahor, S., de Rooij, G., Schlüter, S., Vogel, H.-J., 2015. Water Flow and Solute Transport in Unsaturated Sand--A Comprehensive Experimental Approach. Vadose Zone Journal 14.
Kurita, T., Otsu, N., Abdelmalek, N., 1992. Maximum likelihood thresholding based on population mixture models. Pattern Recognition 25(10), 1231-1240.
Kuzyakov, Y., Blagodatskaya, E., 2015. Microbial hotspots and hot moments in soil: Concept & review. Soil Biology and Biochemistry 83, 184-199.
Kuzyakov, Y., Friedel, J.K., Stahr, K., 2000. Review of mechanisms and quantification of priming effects. Soil Biology and Biochemistry 32(11-12), 1485-1498.
Larsbo, M., Koestel, J., Jarvis, N., 2014. Relations between macropore network characteristics and the degree of preferential solute transport. Hydrol. Earth Syst. Sci. 18(12), 5255-5269.
Latham, S., Varslot, T., Sheppard, A., 2008. Image Registration: Enhancing and Calibrating X-ray Micro-CT Imaging, Proceedings of the Society of Core Analysis, Abu Dhabi, UAE, October 2008, Abu Dhabi, UAE.
Leffelaar, P., Wessel, W., 1988. Denitrification in a homogeneous, closed system: experiment and simulation. Soil Science 146(5), 335-349.
Legland, D., Arganda-Carreras, I., Andrey, P., 2016. MorphoLibJ: integrated library and plugins for mathematical morphology with ImageJ. Bioinformatics 32(22), 3532-3534.
Lehmann, J., Kleber, M., 2015. The contentious nature of soil organic matter. Nature 528, 60.
Lehmann, P., Wyss, P., Flisch, A., Lehmann, E., Vontobel, P., Krafczyk, M., Kaestner, A., Beckmann, F., Gygi, A., Flühler, H., 2006. Tomographical Imaging and Mathematical Description of Porous Media Used for the Prediction of Fluid Distribution. Vadose Zone Journal 5, 80-97.
Leij, F.J., Ghezzehei, T.A., Or, D., 2002. Analytical Models for Soil Pore-Size Distribution After Tillage. Soil Science Society of America Journal 66, 1104-1114.
Lenoir, N., Bornert, M., Desrues, J., Bésuelle, P., Viggiani, G., 2007. Volumetric Digital Image Correlation Applied to X-ray Microtomography Images from Triaxial Compression Tests on Argillaceous Rock. Strain 43(3), 193-205.
Letey, J., 1991. The study of soil structure - Science or art. Soil Research 29(6), 699-707.
Li, C., Aber, J., Stange, F., Butterbach-Bahl, K., Papen, H., 2000. A process-oriented model of N2O and NO emissions from forest soils: 1. Model development. Journal of Geophysical Research: Atmospheres 105(D4), 4369-4384.
Li, C., Frolking, S., Frolking, T.A., 1992. A model of nitrous oxide evolution from soil driven by rainfall events: 1. Model structure and sensitivity. Journal of Geophysical Research: Atmospheres 97(D9), 9759-9776.
Liao, P.-S., Chen, T.-S., Chung, P.-C., 2001. A fast algorithm for multilevel thresholding. Journal of information science and engineering 17(5), 713-728.

Linn, D., Doran, J., 1984a. Effect of water-filled pore space on carbon dioxide and nitrous oxide production in tilled and nontilled soils. Soil Science Society of America Journal 48(6), 1267-1272.
Linn, D.M., Doran, J.W., 1984b. Effect of Water-Filled Pore Space on Carbon Dioxide and Nitrous Oxide Production in Tilled and Nontilled Soils1. Soil Science Society of America Journal 48(6), 1267-1272.
Lipiec, J., Kuś, J., Słowińska-Jurkiewicz, A., Nosalewicz, A., 2006. Soil porosity and water infiltration as influenced by tillage methods. Soil and Tillage research 89(2), 210-220.
Liu, B., Mørkved, P.T., Frostegård, Å., Bakken, L.R., 2010. Denitrification gene pools, transcription and kinetics of NO, N2O and N2 production as affected by soil pH. FEMS Microbiology Ecology 72(3), 407-417.
Luo, L., Lin, H., Halleck, P., 2008. Quantifying soil structure and preferential flow in intact soil using X-ray computed tomography. Soil Science Society of America Journal 72(4), 1058-1069.
Mangalassery, S., Sjögersten, S., Sparkes, D.L., Sturrock, C.J., Mooney, S.J., 2013. The effect of soil aggregate size on pore structure and its consequence on emission of greenhouse gases. Soil and Tillage Research 132, 39-46.
Mangane, P.O., Gouze, P., Luquot, L., 2013. Permeability impairment of a limestone reservoir triggered by heterogeneous dissolution and particles migration during CO2-rich injection. Geophysical Research Letters 40(17), 4614-4619.
Manzoni, S., Katul, G., 2014. Invariant soil water potential at zero microbial respiration explained by hydrological discontinuity in dry soils. Geophysical Research Letters 41(20), 7151-7158.
Mathieu, O., Lévêque, J., Hénault, C., Milloux, M.-J., Bizouard, F., Andreux, F., 2006. Emissions and spatial variability of N2O, N2 and nitrous oxide mole fraction at the field scale, revealed with 15N isotopic techniques. Soil Biology and Biochemistry 38(5), 941-951.
Mattes, D., Haynor, D.R., Vesselle, H., Lewellyn, T.K., Eubank, W., 2001. Nonrigid multimodality image registration, Proc. SPIE, San Diego, CA, pp. 1609-1620.
McCartney, J.S., 2007. Determination of the hydraulic characteristics of unsaturated soils using a centrifuge permeameter, University of Texas in Austin, University of Texas in Austin.
McCartney, J.S., Zornberg, J.G., 2010. Centrifuge Permeameter for Unsaturated Soils. II: Measurement of the Hydraulic Characteristics of an Unsaturated Clay. Journal of Geotechnical and Geoenvironmental Engineering 136(8), 1064-1076.
McClure, J.E., Adalsteinsson, D., Pan, C., Gray, W.G., Miller, C.T., 2007. Approximation of interfacial properties in multiphase porous medium systems. Advances in Water Resources 30(3), 354-365.
McKenzie, D.C., 2001. Rapid assessment of soil compaction damage I. The SOILpak score, a semi-quantitative measure of soil structural form. Soil Research 39(1), 117-125.
McMahon, S.K., Williams, M.A., Bottomley, P.J., Myrold, D.D., 2005. Dynamics of microbial communities during decomposition of carbon-13 labeled ryegrass fractions in soil. Soil Science Society of America Journal 69(4), 1238-1247.
Meek, B.D., Rechel, E.A., Carter, L.M., DeTar, W.R., 1989. Changes in Infiltration Under Alfalfa as Influenced by Time and Wheel Traffic. Soil Science Society of America Journal 53(1), 238-241.

Mevik, B.-H.W., Ron; Liland, Kristian Hovde, 2016. pls: Partial Least Squares and Principal Component Regression.
Mikutta, R., Kleber, M., Torn, M., Jahn, R., 2006. Stabilization of Soil Organic Matter: Association with Minerals or Chemical Recalcitrance? Biogeochemistry 77(1), 25-56.
Miller, M.N., Zebarth, B.J., Dandie, C.E., Burton, D.L., Goyer, C., Trevors, J.T., 2009. Denitrifier Community Dynamics in Soil Aggregates under Permanent Grassland and Arable Cropping Systems. Soil Science Society of America Journal 73(6), 1843-1851.
Mohebi, A., Fieguth, P., Ioannidis, M.A., 2009. Statistical fusion of two-scale images of porous media. Advances in Water Resources 32, 1567-1579.
Molstad, L., Dörsch, P., Bakken, L.R., 2007. Robotized incubation system for monitoring gases (O2, NO, N2O, N2) in denitrifying cultures. Journal of Microbiological Methods 71(3), 202-211.
Moran, K.K., Six, J., Horwath, W.R., van Kessel, C., 2005. Role of mineral-nitrogen in residue decomposition and stable soil organic matter formation. Soil Science Society of America Journal 69(6), 1730-1736.
Moyano, F.E., Manzoni, S., Chenu, C., 2013. Responses of soil heterotrophic respiration to moisture availability: An exploration of processes and models. Soil Biology and Biochemistry 59, 72-85.
Moyano, F.E., Vasilyeva, N., Bouckaert, L., Cook, F., Craine, J., Curiel Yuste, J., Don, A., Epron, D., Formanek, P., Franzluebbers, A., Ilstedt, U., Kätterer, T., Orchard, V., Reichstein, M., Rey, A., Ruamps, L., Subke, J.A., Thomsen, I.K., Chenu, C., 2012. The moisture response of soil heterotrophic respiration: interaction with soil properties. Biogeosciences 9(3), 1173-1182.
Mueller, C.W., Hoeschen, C., Steffens, M., Buddenbaum, H., Hinkel, K., Bockheim, J.G., Kao-Kniffin, J., 2017. Microscale soil structures foster organic matter stabilization in permafrost soils. Geoderma 293, 44-53.
Mueller, C.W., Weber, P.K., Kilburn, M.R., Hoeschen, C., Kleber, M., Pett-Ridge, J., 2013. Chapter One - Advances in the Analysis of Biogeochemical Interfaces: NanoSIMS to Investigate Soil Microenvironments. In: D.L. Sparks (Ed.), Advances in Agronomy. Academic Press, pp. 1-46.
Mueller, L., Kay, B.D., Hu, C., Li, Y., Schindler, U., Behrendt, A., Shepherd, T.G., Ball, B.C., 2009. Visual assessment of soil structure: Evaluation of methodologies on sites in Canada, China and Germany: Part I: Comparing visual methods and linking them with soil physical data and grain yield of cereals. Soil and Tillage Research 103(1), 178-187.
Münch, B., Trtik, P., Marone, F., Stampanoni, M., 2009. Stripe and ring artifact removal with combined wavelet--Fourier filtering. Opt. Express 17(10), 8567-8591.
Munkholm, L.J., Heck, R.J., Deen, B., 2012. Soil pore characteristics assessed from X-ray micro-CT derived images and correlations to soil friability. Geoderma 181, 22-29.
Musat, N., Foster, R., Vagner, T., Adam, B., Kuypers, M.M.M., 2012. Detecting metabolic activities in single cells, with emphasis on nanoSIMS. FEMS Microbiology Reviews 36(2), 486-511.
Myrold, D.D., Tiedje, J.M., 1985. Diffusional constraints on denitrification in soil. Soil Science Society of America Journal 49(3), 651-657.

Naveed, M., Moldrup, P., Vogel, H.-J., Lamandé, M., Wildenschild, D., Tuller, M., de Jonge, L.W., 2014. Impact of long-term fertilization practice on soil structure evolution. Geoderma 217, 181-189.
Negassa, W.C., Guber, A.K., Kravchenko, A.N., Marsh, T.L., Britton, H., Rivers, M.L., 2015. Properties of Soil Pore Space Regulate Pathways of Plant Residue Decomposition and Community Structure of Associated Bacteria. PLoS ONE 10(4), 1-22.
Newell-Price, J.P., Whittingham, M.J., Chambers, B.J., Peel, S., 2013. Visual soil evaluation in relation to measured soil physical properties in a survey of grassland soil compaction in England and Wales. Soil and Tillage Research 127, 65-73.
Nickel, E., 1973. Experimental dissolution of light and heavy minerals in comparison with weathering and intrastratal solution. Contributions to Sedimentology 1, 1-68.
Nunan, N., 2017. The microbial habitat in soil: Scale, heterogeneity and functional consequences. Journal of Plant Nutrition and Soil Science 180(4), 425-429.
Nunan, N., Ritz, K., Rivers, M., Feeney, D.S., Young, I.M., 2006. Investigating microbial micro-habitat structure using X-ray computed tomography. Geoderma 133(3-4), 398-407.
Nunan, N., Wu, K., Young, I.M., Crawford, J.W., Ritz, K., 2003. Spatial distribution of bacterial communities and their relationships with the micro-architecture of soil. FEMS Microbiology Ecology 44(2), 203-215.
Oden, S., 1975. An integral method for the determination of moisture retention curves by centrifugation. Grundfoerbaettring 27, 137-143.
Oh, W., Lindquist, B., 1999. Image Thresholding by Indicator Kriging. IEEE Transactions on Pattern Analysis and Machine Intelligence 21(7), 590-602.
Ohser, J., Mücklich, P., 2000. Statistical Analyisis of Microstructures in Material Science. Wiley & Sons, New York.
Ollion, J., Cochennec, J., Loll, F., Escudé, C., Boudier, T., 2013. TANGO: a generic tool for high-throughput 3D image analysis for studying nuclear organization. Bioinformatics 29(14), 1840-1841.
Or, D., Ghezzehei, T.A., 2002. Modeling post-tillage soil structural dynamics: a review. Soil & Tillage Research 64, 41-59.
Or, D., Smets, B.F., Wraith, J.M., Dechesne, A., Friedman, S.P., 2007. Physical constraints affecting bacterial habitats and activity in unsaturated porous media - a review. Advances in Water Resources 30(6-7), 1505-1527.
Otsu, N., 1975. A threshold selection method from gray-level histograms. Automatica 11(285-296), 23-27.
Page-Dumroese, D.S., Brown, R.E., Jurgensen, M.F., Mroz, G.D., 1999. Comparison of Methods for Determining Bulk Densities of Rocky Forest Soils. Soil Science Society of America Journal 63(2), 379-383.
Pagliai, M., Vignozzi, N., 2002. The soil pore system as an indicator of soil quality. Advances in Geoecology 34, 69-80.
Pagliai, M., Vignozzi, N., Pellegrini, S., 2004. Soil structure and the effect of management practices. Soil and Tillage Research 79(2), 131-143.
Pal, N.R., Bhandari, D., 1993. Image thresholding: Some new techniques. Signal Processing 33(2), 139-158.
Pal, N.R., Pal, S.K., 1993. A review on image segmentation techniques. Pattern Recognition 26(9), 1277-1294.

Palm, C., Blanco-Canqui, H., DeClerck, F., Gatere, L., Grace, P., 2014. Conservation agriculture and ecosystem services: An overview. Agriculture, Ecosystems & Environment 187, 87-105.
Panda, D.P., Rosenfeld, A., 1978. Image Segmentation by Pixel Classification in (Gray Level, Edge Value) Space. Computers, IEEE Transactions on C-27(9), 875-879.
Paradelo, M., Katuwal, S., Moldrup, P., Norgaard, T., Herath, L., de Jonge, L.W., 2016. X-ray CT-derived soil characteristics explain varying air, water, and solute transport properties across a loamy field. Vadose Zone Journal 15(4).
Parkin, T.B., 1987. Soil microsites as a source of denitrification variability. Soil Science Society of America Journal 51(5), 1194-1199.
Parry, S., Renault, P., Chenu, C., Lensi, R., 1999. Denitrification in pasture and cropped soil clods as affected by pore space structure. Soil Biology and Biochemistry 31(4), 493-501.
Parton, W.J., Holland, E.A., Del Grosso, S.J., Hartman, M.D., Martin, R.E., Mosier, A.R., Ojima, D.S., Schimel, D.S., 2001. Generalized model for NO x and N2O emissions from soils. Journal of Geophysical Research: Atmospheres 106(D15), 17403-17419.
Paul, K.I., Polglase, P.J., O'Connell, A.M., Carlyle, J.C., Smethurst, P.J., Khanna, P.K., 2003. Defining the relation between soil water content and net nitrogen mineralization. European Journal of Soil Science 54(1), 39-48.
Pérez, P., Gangnet, M., Blake, A., 2003. Poisson image editing. ACM Transactions on Graphics (TOG) 22(3), 313-318.
Perona, P., Malik, J., 1990. Scale-space and edge detection using anisotropic diffusion. IEEE Transactions on Pattern Analysis and Machine Intelligence 12(7), 629-639.
Peters, A., Durner, W., 2008. Simplified evaporation method for determining soil hydraulic properties. Journal of Hydrology 356(1-2), 147-162.
Peth, S., Nellesen, J., Fischer, G., Horn, R., 2010. Non-invasive 3D analysis of local soil deformation under mechanical and hydraulic stresses by μCT and digital image correlation. Soil and Tillage Research 111(1), 3-18.
Pett-Ridge, J., Weber, P.K., 2012. NanoSIP: NanoSIMS applications for microbial biology. Methods in molecular biology (Clifton, N.J.) 881, 375-408.
Philippot, L., Andert, J., Jones, C.M., Bru, D., Hallin, S., 2011. Importance of denitrifiers lacking the genes encoding the nitrous oxide reductase for N2O emissions from soil. Global Change Biology 17(3), 1497-1504.
Philippot, L., Hallin, S., Schloter, M., 2007. Ecology of Denitrifying Prokaryotes in Agricultural Soil, Advances in Agronomy. Academic Press, pp. 249-305.
Philippot, L., Spor, A., Henault, C., Bru, D., Bizouard, F., Jones, C.M., Sarr, A., Maron, P.-A., 2013. Loss in microbial diversity affects nitrogen cycling in soil. ISME J 7(8), 1609-1619.
Pizer, S.M., Amburn, E.P., Austin, J.D., Cromartie, R., Geselowitz, A., Greer, T., Romeny, B.t.H., Zimmerman, J.B., Zuiderveld, K., 1987. Adaptive histogram equalization and its variations. Computer Vision, Graphics, and Image Processing 39(3), 355-368.
Plante, A.F., McGill, W.B., 2002. Soil aggregate dynamics and the retention of organic matterin laboratory-incubated soil with differing simulated tillage frequencies. Soil & Tillage Research 66, 79-92.

Pöhlitz, J., Rücknagel, J., Koblenz, B., Schlüter, S., Vogel, H.-J., Christen, O., 2018. Computed tomography and soil physical measurements of compaction behaviour under strip tillage, mulch tillage and no tillage. Soil and Tillage Research 175, 205-216.
Polerecky, L., Adam, B., Milucka, J., Musat, N., Vagner, T., Kuypers, M.M.M., 2012. Look@NanoSIMS – a tool for the analysis of nanoSIMS data in environmental microbiology. Environmental Microbiology 14(4), 1009-1023.
Porter, M.L., Wildenschild, D., 2010. Image analysis algorithms for estimating porous media multiphase flow variables from computed microtomography data: a validation study. Computational Geosciences 14(1), 15-30.
Puget, P., Chenu, C., Balesdent, J., 2000. Dynamics of soil organic matter associated with particle-size fractions of water-stable aggregates. European Journal of Soil Science 51(4), 595-605.
Pulido Moncada, M., Gabriels, D., Lobo, D., Rey, J.C., Cornelis, W.M., 2014. Visual field assessment of soil structural quality in tropical soils. Soil and Tillage Research 139, 8-18.
R Core Team, 2017. R: A language and environment for statistical computing. Vienna, Austria: R Foundation for Statistical Computing; 2014. R Foundation for Statistical Computing, Vienna, Austria.
Rabot, E., Lacoste, M., Hénault, C., Cousin, I., 2015. Using X-ray Computed Tomography to Describe the Dynamics of Nitrous Oxide Emissions during Soil Drying. Vadose Zone Journal 14(8).
Rabot, E., Wiesmeier, M., Schlüter, S., Vogel, H.J., 2018. Soil structure as an indicator of soil functions: A review. Geoderma 314, 122-137.
Rasmussen, K., 1999. Impact of ploughless soil tillage on yield and soil quality: a Scandinavian review. Soil and Tillage Research 53(1), 3-14.
Raven, C., 1998. Numerical removal of ring artifacts in microtomography. Review of Scientific Instruments 69(8), 2978-2980.
Raynaud, X., Nunan, N., 2014. Spatial Ecology of Bacteria at the Microscale in Soil. PLOS ONE 9(1), e87217.
Reatto, A., Da Silva, E.M., Bruand, A., Martins, E.S., Lima, J.E.F.W., 2008. Validity of the centrifuge method for determining the water retention properties of tropical soils. Soil Science Society of America Journal 72(6), 1547-1553.
Reichert, J.M., Suzuki, L.E.A.S., Reinert, D.J., Horn, R., Håkansson, I., 2009. Reference bulk density and critical degree-of-compactness for no-till crop production in subtropical highly weathered soils. Soil and Tillage Research 102(2), 242-254.
Renard, P., Allard, D., 2013. Connectivity metrics for subsurface flow and transport. Advances in Water Resources 51(0), 168-196.
Ridler, T., Calvard, S., 1978. Picture Thresholding Using an Iterative Selection Method. Systems, Man and Cybernetics, IEEE Transactions on 8(8), 630-632.
Rillig, M.C., Mummey, D.L., 2006. Mycorrhizas and soil structure. New Phytologist 171(1), 41-53.
Ritz, K., Young, I.M., 2004. Interactions between soil structure and fungi. Mycologist 18, 52-59.
Roco, C.A., Bergaust, L.L., Bakken, L.R., Yavitt, J.B., Shapleigh, J.P., 2017. Modularity of nitrogen-oxide reducing soil bacteria: linking phenotype to genotype. Environmental Microbiology 19(6), 2507-2519.

Roerdink, J.B., Meijster, A., 2000. The watershed transform: Definitions, algorithms and parallelization strategies. Fundamenta Informaticae 41(1), 187-228.
Rogasik, H., Crawford, J.W., Wendroth, O., Young, I.M., Joschko, M., Ritz, K., 1999. Discrimination of Soil Phases by Dual Energy X-ray Tomography. Soil Science Society of America Journal 63, 741-751.
Rosin, P., 2001. Unimodal thresholding. Pattern Recognition 34(11), 2083-2096.
Röver, M., Heinemeyer, O., Munch, J.C., Kaiser, E.-A., 1999. Spatial heterogeneity within the plough layer: high variability of \N2O\ emission rates. Soil Biology and Biochemistry 31(2), 167-173.
Rücknagel, J., Hofman, B., Christen, O., 2004. Effect of soil tillage on soil physical properties, total organic carbon content and winter barley yield in a long term experiment in Germany, 4th International Crop Science Congress.
Rücknagel, J., Hofmann, B., Deumelandt, P., Reinicke, F., Bauhardt, J., Hülsbergen, K.-J., Christen, O., 2015. Indicator based assessment of the soil compaction risk at arable sites using the model REPRO. Ecological Indicators 52(Supplement C), 341-352.
Rücknagel, J., Rademacher, A., Götze, P., Hofmann, B., Christen, O., 2017. Uniaxial compression behaviour and soil physical quality of topsoils under conventional and conservation tillage. Geoderma 286, 1-7.
Rudin, L.I., Osher, S., Fatemi, E., 1992. Nonlinear total variation based noise removal algorithms. Physica D: Nonlinear Phenomena 60, 259-268.
Ruser, R., Flessa, H., Russow, R., Schmidt, G., Buegger, F., Munch, J.C., 2006. Emission of N2O, N2 and CO2 from soil fertilized with nitrate: effect of compaction, soil moisture and rewetting. Soil Biology and Biochemistry 38(2), 263-274.
Russ, J.C., 2006. The image processing handbook. CRC press, Boca Raton, FL.
Russell, M., Richards, L., 1939. The determination of soil moisture energy relations by centrifugation. Soil Science Society of America Journal 3(C), 65-69.
Russenes, A.L., Korsaeth, A., Bakken, L.R., Dörsch, P., 2016. Spatial variation in soil pH controls off-season N2O emission in an agricultural soil. Soil Biology and Biochemistry 99, 36-46.
Sahoo, P.K., Soltani, S., Wong, A.K.C., 1988. A Survey of Thresholding Techniques. Computer Vision, Graphics, and Image Processing 41(11), 233-260.
Schaufler, G., Kitzler, B., Schindlbacher, A., Skiba, U., Sutton, M.A., Zechmeister-Boltenstern, S., 2010. Greenhouse gas emissions from European soils under different land use: effects of soil moisture and temperature. European Journal of Soil Science 61(5), 683-696.
Schimel, J., Schaeffer, S., 2012. Microbial control over carbon cycling in soil. Frontiers in Microbiology 3(348), 1-11.
Schindelin, J., Arganda-Carreras, I., Frise, E., Kaynig, V., Longair, M., Pietzsch, T., Preibisch, S., Rueden, C., Saalfeld, S., Schmid, B., 2012. Fiji: an open-source platform for biological-image analysis. Nature methods 9(7), 676-682.
Schlüter, S., Blaser, S.R.G.A., Weber, M., Schmidt, V., Vetterlein, D., 2018a. Quantification of Root Growth Patterns From the Soil Perspective via Root Distance Models. Frontiers in Plant Science 9, 1084.
Schlüter, S., Henjes, S., Zawallich, J., Bergaust, L., Horn, M., Ippisch, O., Vogel, H.-J., Dörsch, P., 2018b. Denitrification in Soil Aggregate Analogues-Effect of Aggregate Size and Oxygen Diffusion. Frontiers in Environmental Science 6(17).

Schlüter, S., Leuther, F., Vogler, S., Vogel, H.-J., 2016. X-ray microtomography analysis of soil structure deformation caused by centrifugation. Solid Earth 7(1), 129-140.
Schlüter, S., Sheppard, A., Brown, K., Wildenschild, D., 2014. Image processing of multiphase images obtained via X-ray microtomography: A review. Water Resources Research 50(4), 3615-3639.
Schlüter, S., Vogel, H.-J., 2016. Analysis of Soil Structure Turnover with Garnet Particles and X-Ray Microtomography. PLoS ONE 11(7), e0159948.
Schlüter, S., Weller, U., Vogel, H.-J., 2010. Segmentation of X-ray microtomography images of soil using gradient masks. Computers & Geosciences 36(10), 1246-1251.
Schlüter, S., Weller, U., Vogel, H.-J., 2011. Soil-structure development including seasonal dynamics in a long-term fertilization experiment. Journal of Plant Nutrition and Soil Science 174(3), 395-403.
Schmidt, H., Nunan, N., Höck, A., Eickhorst, T., Kaiser, C., Woebken, D., Raynaud, X., 2018. Recognizing Patterns: Spatial Analysis of Observed Microbial Colonization on Root Surfaces. Frontiers in Environmental Science 6(61), 1-12.
Schmidt, M.W.I., Torn, M.S., Abiven, S., Dittmar, T., Guggenberger, G., Janssens, I.A., Kleber, M., Kögel-Knabner, I., Lehmann, J., Manning, D.A.C., Nannipieri, P., Rasse, D.P., Weiner, S., Trumbore, S.E., 2011. Persistence of soil organic matter as an ecosystem property. Nature 478(7367), 49-56.
Schurgers, G., Dorsch, P., Bakken, L., Leffelaar, P., Haugen, L.E., 2006. Modelling soil anaerobiosis from water retention characteristics and soil respiration. Soil Biology & Biochemistry 38(9), 2637-2644.
Schweizer, S., A., Hoeschen, C., Schlüter, S., Kögel-Knabner, I., Mueller, C., W., 2018. Rapid soil formation after glacial retreat shaped by spatial patterns of organic matter accrual in microaggregates. Global Change Biology 24(4), 1637-1650.
Serra, J., 1982. Mathematical Morphology and Image Analysis. Academic Press, San Diego.
Seth, S., Morrow, N.R., others, 2007. Efficiency of the conversion of work of drainage to surface energy for sandstone and carbonate. SPE Reservoir Evaluation & Engineering 10(04), 338-347.
Sexstone, A.J., Revsbech, N.P., Parkin, T.B., Tiedje, J.M., 1985. Direct measurement of oxygen profiles and denitrification rates in soil aggregates. Soil science society of America journal 49(3), 645-651.
Sezgin, M., Sankur, B., 2004. Survey over image thresholding techniques and quantitative performance evaluation. Journal of Electronic Imaging 13(1), 146-165.
Shamonin, D., Bron, E., Lelieveldt, B., Smits, M., Klein, S., Staring, M., 2014. Fast Parallel Image Registration on CPU and GPU for Diagnostic Classification of Alzheimer's Disease. Frontiers in Neuroinformatics 7(50), 1-15.
Shepherd, G., Stagnari, F., Pisante, M., Benites, J., 2008. Visual Soil Assessment–Field guide for annual crops. FAO, Rome, Italy.
Shepherd, T.G., 2003. Assessing soil quality using visual soil assessment. In: L.D. Currie, J.A. Hanly (Eds.), Tools for nutrient and pollutant management: : Applications to agriculture and environmental quality. Fertilizer and Lime Research Centre, Massey University, Palmerston North, pp. 153-166.

Sheppard, A.P., Sok, R.M., Averdunk, H., 2004. Techniques for image enhancement and segmentation of tomographic images of porous materials. Physica A: Statistical Mechanics and its Applications 339(1), 145-151.
Sierra, J., Renault, P., 1996. Respiratory Activity and Oxygen Distribution in Natural Aggregates in Relation to Anaerobiosis. Soil Science Society of America Journal 60(5), 1428-1438.
Sijbers, J., Postnov, A., 2004. Reduction of ring artefacts in high resolution micro-CT reconstructions. Physics in Medicine and Biology 49(14), N247.
Silverstein, D.L., Fort, T., 2000. Prediction of air-water interfacial area in wet unsaturated porous media. Langmuir 16(2), 829-834.
SImek, M., Cooper, J.E., 2002. The influence of soil pH on denitrification: progress towards the understanding of this interaction over the last 50 years. European Journal of Soil Science 53(3), 345-354.
Šimůnek, J., Nimmo, J.R., 2005. Estimating soil hydraulic parameters from transient flow experiments in a centrifuge using parameter optimization technique. Water Resources Research 41(4).
Simunek, J., van Genuchten, M.T., Wendroth, O., 1998. Parameter estimation analysis of the evaporation method for determining soil hydraulic properties. Soil Science Society of America Journal 62(4), 894-905.
Sistrom, W.R., 1960. A Requirement for Sodium in the Growth of Rhodopseudomonas spheroides. Microbiology 22(3), 778-785.
Six, J., Bossuyt, H., de Gryze, S., Denef, K., 2004. A history of research on the link between (micro)aggregates, soil biota, and soil organic matter dynamics. Soil & Tillage Research 79, 7-31.
Six, J., Elliott, E., Paustian, K., Doran, J., 1998. Aggregation and soil organic matter accumulation in cultivated and native grassland soils. Soil Science Society of America Journal 62(5), 1367-1377.
Skopp, J., Jawson, M.D., Doran, J.W., 1990. Steady-State Aerobic Microbial Activity as a Function of Soil Water Content. Soil Science Society of America Journal 54(6), 1619-1625.
Smith, K.A., 1990. Anaerobic Zones and Denitrification in Soil: Modelling and Measurement. In: N.P. Revsbech, J. Sørensen (Eds.), Denitrification in Soil and Sediment. Springer US, Boston, MA, pp. 229-244.
Smith, K.A., Ball, T., Conen, F., Dobbie, K.E., Massheder, J., Rey, A., 2003. Exchange of greenhouse gases between soil and atmosphere: interactions of soil physical factors and biological processes. European Journal of Soil Science 54(4), 779-791.
Soane, B.D., Ball, B.C., Arvidsson, J., Basch, G., Moreno, F., Roger-Estrade, J., 2012. No-till in northern, western and south-western Europe: A review of problems and opportunities for crop production and the environment. Soil and Tillage Research 118, 66-87.
Soehne, W., 1953. Druckverteilung im boden und bodenverformung unter schlepperreifen. Grundlagen der Landtechnik-Konstrukteurhefte (5).
Son, A., Medina-Cetina, Z., Rechenmacher, A., 2012. Local Deformation Analysis of a Sand Specimen Using 3D Digital Image Correlation for the Calibration of a Simple Elasto-Plastic Model, GeoCongress 2012-State of the Art and Practice in Geotechnical Engineering. ASCE, Reston, VA, USA, Geotechnical Special Publication, pp. 2292-2301.

Stange, C.F., Horn, R., 2005. Modeling the Soil Water Retention Curve for Conditions of Variable Porosity. Vadose Zone Journal 4(3), 602-613.
Stange, C.F., Spott, O., Arriaga, H., Menéndez, S., Estavillo, J.M., Merino, P., 2013. Use of the inverse abundance approach to identify the sources of NO and N2O release from Spanish forest soils under oxic and hypoxic conditions. Soil Biology and Biochemistry 57, 451-458.
Stark, J.A., 2000. Adaptive image contrast enhancement using generalizations of histogram equalization. Image Processing, IEEE Transactions on 9(5), 889-896.
Steffens, M., Rogge, D.M., Mueller, C.W., Höschen, C., Lugmeier, J., Kölbl, A., Kögel-Knabner, I., 2017. Identification of Distinct Functional Microstructural Domains Controlling C Storage in Soil. Environmental Science & Technology 51(21), 12182-12189.
Strudley, M.W., Green, T.R., Ascough, J.C., 2008. Tillage effects on soil hydraulic properties in space and time: State of the science. Soil and Tillage Research 99(1), 4-48.
Tebrügge, F., Düring, R.-A., 1999. Reducing tillage intensity—a review of results from a long-term study in Germany. Soil and tillage research 53(1), 15-28.
Tecon, R., Or, D., 2017. Biophysical processes supporting the diversity of microbial life in soil. FEMS Microbiology Reviews 41(5), 599-623.
Terzaghi, K., Peck, R.B., Mesri, G., 1996. Soil mechanics in engineering practice. John Wiley & Sons, New York, NY.
Tisdall, J.M., Oades, J.M., 1982. Organic matter and water-stable aggregates in soils. European Journal of Soil Science 33(2), 141-163.
Tominski, C., Lösekann-Behrens, T., Ruecker, A., Hagemann, N., Kleindienst, S., Mueller, C.W., Höschen, C., Kögel-Knabner, I., Kappler, A., Behrens, S., 2018. Insights into Carbon Metabolism Provided by Fluorescence In Situ Hybridization-Secondary Ion Mass Spectrometry Imaging of an Autotrophic, Nitrate-Reducing, Fe(II)-Oxidizing Enrichment Culture. Applied and Environmental Microbiology 84(9).
Trier, O.D., Jain, A.K., 1995. Goal-directed evaluation of binarization methods. Pattern Analysis and Machine Intelligence, IEEE Transactions on 17(12), 1191-1201.
Tristán-Vega, A., García-Pérez, V., Aja-Fernández, S., Westin, C.-F., 2012. Efficient and robust nonlocal means denoising of \MR\ data based on salient features matching. Computer Methods and Programs in Biomedicine 105(2), 131-144.
Tsai, D.-M., 1995. A fast thresholding selection procedure for multimodal and unimodal histograms. Pattern Recognition Letters 16(6), 653 - 666.
Tuller, M., Kulkarni, R., Fink, W., 2013. Segmentation of X-Ray CT Data of Porous Materials: A Review of Global and Locally Adaptive Algorithms, Soil-Water-Root Processes: Advances in Tomography and Imaging. The Soil Science Society of America, Inc., Madison, WI, USA, pp. 157-182.
Ulrich, S., Tischer, S., Hofmann, B., Christen, O., 2010. Biological soil properties in a long-term tillage trial in Germany. Journal of Plant Nutrition and Soil Science 173(4), 483-489.
van Capelle, C., Schrader, S., Brunotte, J., 2012. Tillage-induced changes in the functional diversity of soil biota – A review with a focus on German data. European Journal of Soil Biology 50(Supplement C), 165-181.

Van Dam, J., Stricker, J., Droogers, P., 1994. Inverse method to determine soil hydraulic functions from multistep outflow experiments. Soil Science Society of America Journal 58(3), 647-652.
Van den Berg, E., Perfect, E., Tu, C., Knappett, P., Leao, T., Donat, R., 2009. Unsaturated hydraulic conductivity measurements with centrifuges: a review. Vadose Zone Journal 8(3), 531-547.
Velbel, M.A., 1993. Constancy of silicate-mineral weathering-rate ratios between natural and experimental weathering: implications for hydrologic control of differences in absolute rates. Chemical Geology 105(1-3), 89-99.
Vidal, A., Hirte, J., Bender, S.F., Mayer, J., Gattinger, A., Höschen, C., Schädler, S., Iqbal, T.M., Mueller, C.W., 2018. Linking 3D Soil Structure and Plant-Microbe-Soil Carbon Transfer in the Rhizosphere. Frontiers in Environmental Science 6(9), 1-14.
Vincent, K.R., Chadwick, O.A., 1994. Synthesizing Bulk Density for Soils with Abundant Rock Fragments. Soil Science Society of America Journal 58(2), 455-464.
Vincent, L., Soille, P., 1991. Watersheds in digital spaces: an efficient algorithm based on immersion simulations. Pattern Analysis and Machine Intelligence, IEEE Transactions on 13(6), 583-598.
Vogel, H.-J., Kretzschmar, A., 1996. Topological characterization of pore space in soil sample preparation and digital image-processing. Geoderma 73(1), 23-38.
Vogel, H.-J., Weller, U., Schlüter, S., 2010. Quantification of soil structure based on Minkowski functions. Computers & Geosciences 36(10), 1236-1245.
Vogel, H.J., Samouëlian, A., Ippisch, O., 2008. Multi-step and two-step experiments in heterogeneous porous media to evaluate the relevance of dynamic effects. Advances in Water Resources 31(1), 181-188.
Vogeler, I., Rogasik, J., Funder, U., Panten, K., Schnug, E., 2009. Effect of tillage systems and P-fertilization on soil physical and chemical properties, crop yield and nutrient uptake. Soil and Tillage Research 103(1), 137-143.
von Lützow, M., Kögel-Knabner, I., Ekschmitt, K., Matzner, E., Guggenberger, G., Marschner, B., Flessa, H., 2006. Stabilization of organic matter in temperate soils: mechanisms and their relevance under different soil conditions - a review. European Journal of Soil Science 57(4), 426-445.
Vos, M., Wolf, A.B., Jennings, S.J., Kowalchuk, G.A., 2013. Micro-scale determinants of bacterial diversity in soil. FEMS Microbiology Reviews 37(6), 936-954.
Wang, B., Brewer, P.E., Shugart, H.H., Lerdau, M.T., Allison, S.D., 2019. Soil aggregates as biogeochemical reactors and implications for soil–atmosphere exchange of greenhouse gases—A concept. Global Change Biology 0(0).
Wang, W., Kravchenko, A.N., Smucker, A.J.M., Rivers, M.L., 2011. Comparison of image segmentation methods in simulated 2D and 3D microtomographic images of soil aggregates. Geoderma 162(3-4), 231-241.
Wanzek, T., Keiluweit, M., Varga, T., Lindsley, A., Nico, P.S., Fendorf, S., Kleber, M., 2018. The Ability of Soil Pore Network Metrics to Predict Redox Dynamics is Scale Dependent. Soil Systems 2(4), 66.
Wedler, W., Boguslawski, E., 1965. Zur Methodik der pF-Wert-Bestimmung mit der Zentrifuge. Zeitschrift für Pflanzenernährung, Düngung, Bodenkunde 109(3), 249-260.

Weier, K.L., Doran, J.W., Power, J.F., Walters, D.T., 1993. Denitrification and the Dinitrogen/Nitrous Oxide Ratio as Affected by Soil Water, Available Carbon, and Nitrate. Soil Science Society of America Journal 57(1), 66-72.
Weisskopf, P., Zihlmann, U., Wiermann, C., Horn, R., Anken, T., Diserens, E., 2000. Influences of conventional and onland ploughing on soil structure. Advances in Geoecology (32), 73-81.
Werner, D., Paul, R., 1999. Kennzeichnung der Verdichtungs-gefährdung landwirtschaftlich genutzter Böden. Wasser und Boden 51(12), 10-14.
White, D.J., 2003. Soil deformation measurement using particle image velocimetry (PIV) and photogrammetry. Géotechnique 53, 619-631(612).
Wildenschild, D., Hopmans, J.W., Rivers, M.L., Kent, A.J.R., 2005. Quantitative analysis of flow processes in a sand using synchrotron-based X-ray microtomography. Vadose Zone Journal 4(1), 112-126.
Wildenschild, D., Hopmans, J.W., Vaz, C.M.P., Rivers, M.L., Rikard, D., Christensen, B.S.B., 2002. Using X-ray computed tomography in hydrology: systems, resolutions, and limitations. Journal of Hydrology 267(3), 285-297.
Wildenschild, D., Sheppard, A.P., 2013. X-ray imaging and analysis techniques for quantifying pore-scale structure and processes in subsurface porous medium systems. Advances in Water Resources 51(0), 217-246.
Yanowitz, S.D., Bruckstein, A.M., 1989. A New Method for Image Segmentation. Computer Vision, Graphics, and Image Processing 46(1), 82-95.
Young, I.M., Crawford, J.W., 2004. Interactions and Self-Organization in the Soil-Microbe Complex. Science 304, 1634-1637.
Young, I.M., Crawford, J.W., Rappoldt, C., 2001. New methods and models for characterising structural heterogeneity of soil. Soil & Tillage Research 61, 33-45.
Zausig, J., Stepniewski, W., Horn, R., 1993. Oxygen Concentration and Redox Potential Gradients in Unsaturated Model Soil Aggregates. Soil Science Society of America Journal 57(4), 908-916.

6. Supporting Information

6.1. Supporting Information for "Analysis of Soil Structure Turnover with Garnet Particles and X-Ray Microtomography"

Supporting Information 1: Image processing workflow

All image processing steps are summarized in Fig 1 for a small subset of Fig 1 of the main paper. Noise in the raw images was removed with a non-local means denoising filter (Fig 1b) (Buades et al., 2005) as implemented in the ImageJ plugin by Thorsten Wagner. The non-local means filter is applied with an estimated noise level of five gray values. Thresholds for three classes are detected automatically according to Schlüter et al. (2014). That is, thresholds are detected according to five standard, histogram-based threshold detection methods, e.g. maximum variance, minimum error, maximum entropy, etc. The average after outlier removal is used to compute the final set of thresholds. This threshold detection is implemented in the Quantim image processing library (Vogel et al., 2010). Global thresholding leads to a tentative segmentation into pores (black), aggregates (blue) and garnet (red) (Fig 1c). Partial volume effects due to limited image resolution cause false aggregate voxels around particles (green regions in Fig 1d). These thin films of aggregate voxels around particles are removed by an ImageJ macro (Ferreira and Rasband, 2012) that (i) erodes the aggregate class by a spherical structuring element with a diameter d_{SE} of five voxels (=40µm), (ii) removes of all remaining clusters with a volume smaller than 10000 voxels (corresponds to volume of equivalent sphere with d=0.21mm) and (iii) dilates of the remaining bigger aggregates by a spherical structuring element with d_{SE} = 5 voxels. Subsequently, all holes in the aggregate class smaller than 100000 voxels (corresponds to volume of equivalent sphere with d=0.46mm) stemming from occluded pores and particles are closed (purple regions in Fig 1d). The identification of particles is improved with a Laplacian of Gaussian (LoG) filter (Gonzalez and Woods, 2002) for blob detection (Fig 1e) as implemented in the FeatureJ plugin for ImageJ by Erik Meijering. That is, spherical objects with a radius of σ, i.e. the standard deviation of the Gaussian kernel, evoke a strong signal in the second derivative of the smoothed image, whereas smaller objects have been removed. A scale-normalized LoG operator is constructed by taking the maximum of the various LoG operators at different spatial scales t each normalized (i.e. multiplied) with t = σ^2 (Lindeberg, 1993). In this study, $\sigma = (1,3,5)$ voxels was used, which corresponds to an optimally detected diameter of $\sigma = (24,56,88)$µm. Note that this range is slightly smaller than the true particle diameters (45 - 100 µm). The histogram mode (most frequent soil gray value) is subtracted from the image as a preprocessing step in order to remove edges between aggregates and pores from blob detection. Edges of larger grains are still enhanced and need to be masked out subsequently. This grain mask is achieved by applying a similar scheme of erosion, size-based removal and dilation as describe above but this time applied to the tentative garnet class. After these preparation steps the LoG image is segmented into particles and background with hysteresis thresholding (Schlüter et al., 2014; Schlüter et al., 2010)(Fig 1f) which is implemented in the 3D Image Suite plugin for ImageJ by Thomas Boudier (Ollion et al., 2013). An upper threshold $\hat{x} + a$ defines seed regions for a region growing process that detects all connected voxels above a lower threshold $\hat{x} + b$, where $\hat{x}$ is the average gray value and a, b are manually defined parameters tuned for an optimal result ($a = 40$, $b = 10$). The combination of blob detection and partial volume voxel treatment leads to an improved segmentation result (Fig 1g). The tentative pore class is labeled differently depending on whether pores

are fully enclosed by aggregates (yellow) or connected to the interaggregate pore space (black). All removed aggregate and garnet voxels are gathered in an unassigned class (white). Subsequently, different analysis are performed on different material classes, e.g. the pore size map is shown in (Fig 1h) and the distance map towards the interaggregate pores is shown in (Fig 1i). ImageJ macros, QuantIm code and elastix scripts are available from the authors upon request.

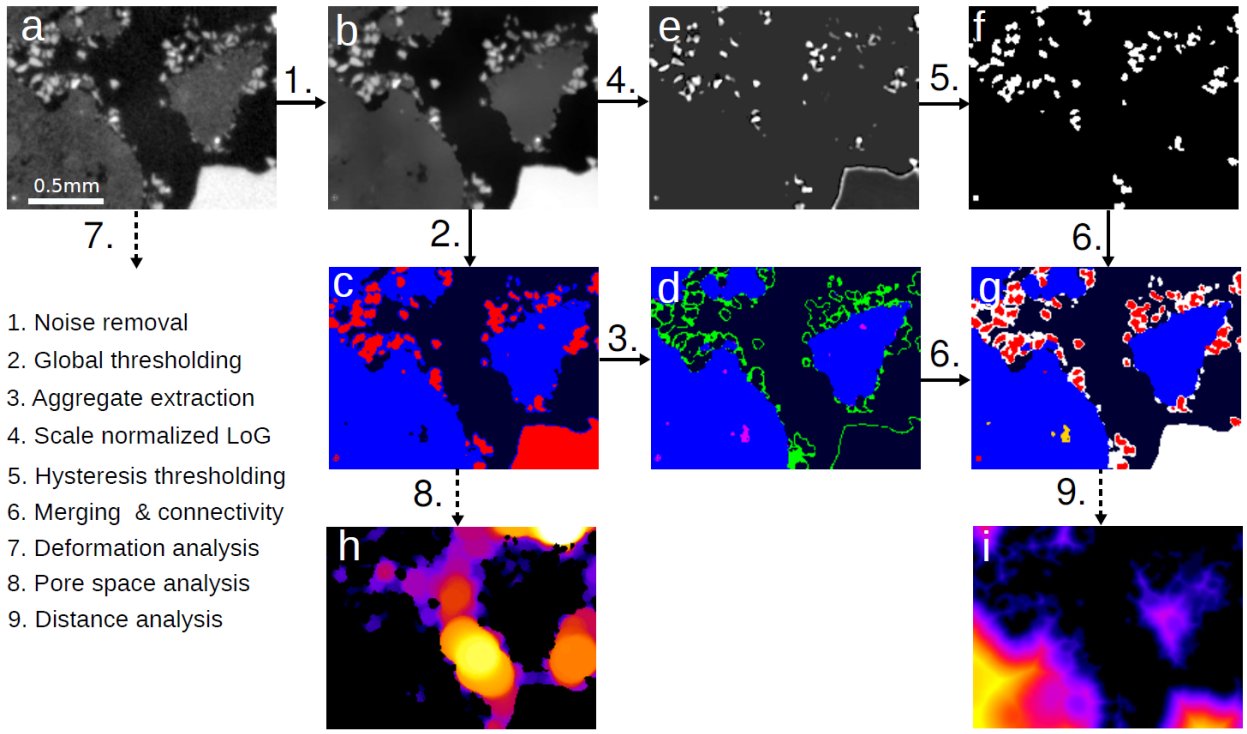

Figure S 1: Image processing workflow for this study depicted for a small two-dimensional subset (a). Noise is removed with a non-local means filter (b). Image segmentation is performed in several steps. First, gray values are tentatively segmented into pores (black), aggregates (blue) and garnet (red) via simple thresholding (c). The volume voxel are removed from the aggregate class and holes in the aggregates are closed (d). Particles are detected with a Laplacian of Gaussian Filter (LoG) (e) and subsequent hysteresis thresholding of the LoG Image (f). Note that the edges of large grains are masked out during particle detection. For the final segmentation (g) the aggregate class is combined with the tentative pore class. The tentative garnet class is set to unassigned (white) and overwritten by the thresholded LoG image (red). Pores are further differentiated with respect to whether they are fully enclosed in soil aggregates (yellow) or not (black) (f). These images are subjected to different types of analysis (7.-9.) of which the pore size map is shown in (h) and the distance map towards the interaggregate pores is shown in (i).

Supporting Information 2: Contact distances for regular sphere packings

Mean contact distances are determined for regular packings of equal-sized, solid overlapping spheres. Four different geometries are used: primitive cubic, body-centered cubic, face-centered cubic and hexagonal close packing. The separation distance between sphere centers is varied in steps for each geometry. The resulting porosities and mean contact distances are depicted in Figure S2 for a predefined sphere diameter of d=0.8 mm. Note that the sphere diameter only affects contact distances, but not porosity. For a fitted diameter of d=0.8mm the end members of each curve, i.e. contact distance at vanishing overlap and vanishing porosity, corresponds well to the experimental values (Figure 28 in the main paper). This diameter is at the lower end of aggregate sizes after sieving (d:0.5-2mm) and can be

thought of as the average diameter of maximum inscribed spheres within irregular-shaped aggregates. It can be easily shown analytically that for non-overlapping spheres the contact distance is independent of packing geometry and corresponds to $d/2^3$=0.125 d. The mean contact distance at vanishing porosity, in turn, depends on the packing geometry and may range between 0.2-0.28 d.

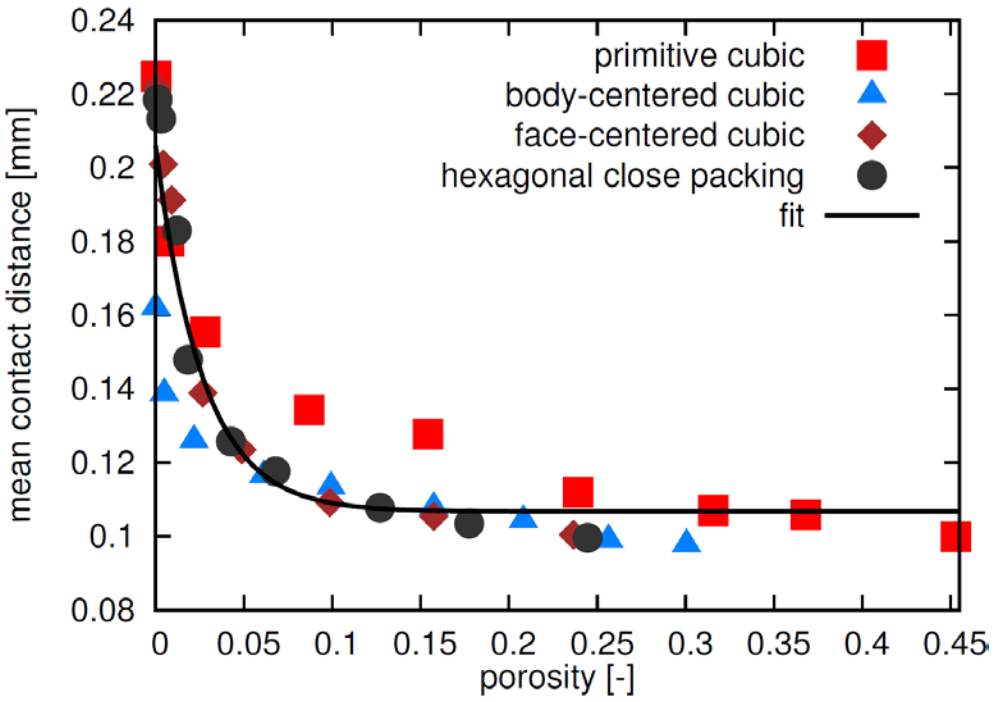

Figure S 2: Mean contact distance and porosity for overlapping spheres (d = 0.8mm) of different separation distance between sphere centers and arranged in different packing geometries. The exponential fit for all data points agrees well with the experimental data in Fig 6 in the main paper.

References

Buades, A., Coll, B., Morel, J.-M., 2005. A non-local algorithm for image denoising, Computer Vision and Pattern Recognition, 2005. CVPR 2005. IEEE Computer Society Conference on, San Diego, California, pp. 60-65 vol. 62.

Ferreira, T., Rasband, W., 2012. ImageJ User Guide - IJ 1.46r. National Insitute of Health, Bethesda, MD.

Gonzalez, R.G., Woods, R.G., 2002. Digital Image Processing. Prentice Hall, Upper Saddle Creek.

Lindeberg, T., 1993. Detecting salient blob-like image structures and their scales with a scale-space primal sketch: A method for focus-of-attention. International Journal of Computer Vision 11(3), 283-318.

Ollion, J., Cochennec, J., Loll, F., Escudé, C., Boudier, T., 2013. TANGO: a generic tool for high-throughput 3D image analysis for studying nuclear organization. Bioinformatics 29(14), 1840-1841.

Schlüter, S., Sheppard, A., Brown, K., Wildenschild, D., 2014. Image processing of multiphase images obtained via X-ray microtomography: A review. Water Resources Research 50(4), 3615-3639.

Schlüter, S., Weller, U., Vogel, H.-J., 2010. Segmentation of X-ray microtomography images of soil using gradient masks. Computers & Geosciences 36(10), 1246-1251.
Vogel, H.-J., Weller, U., Schlüter, S., 2010. Quantification of soil structure based on Minkowski functions. Computers & Geosciences 36(10), 1236-1245.

6.2. Supporting Information for "Correlative imaging reveals holistic view of soil microenvironments"

Supporting Information 1: Detailed Description of Drainage Model

The pore-morphology-based approach to modeling drainage is based on two criteria (Hazlett, 1995; Hilpert and Miller, 2001). The initial condition is a completely saturated pore space. A pore is drained when its air-entry pressure is overcome, i.e. when the capillary diameter D at a certain capillary pressure p_c derived from the Young-Laplace equation,

$$p_c = 4\gamma/D,$$

is smaller than the local pore diameter, where γ is interfacial tension between air and water. This equation holds for spherical interfaces at vanishing contact angle, which is a strong simplification of drainage processes in real soil. Implications and extensions are discussed in (Hilpert and Miller, 2001; Schulz et al., 2015). The pore diameter is probed with spherical structure elements, by testing whether they fit into the pore space at a certain location. A pore voxel is assign with the diameter of the largest sphere centered on this location that does not exceed the local pore boundaries, thus the term 'maximum inscribed sphere method'. The pore size map in Figure S55(a) shows local pore diameters in the segmented µCT image derived with the maximum inscribed sphere method, which is called 'Local thickness' in Fiji/ImageJ (Schindelin et al., 2012). The other criterion for drainage of a pore next to size is that air can invade the pore along a continuous pathway connected to the headspace. The headspace is delineated by a rough soil surface (Figure S55b) and determined with the region growing tool in VG Studio Max 2.1, which is initiated at the top image boundary.

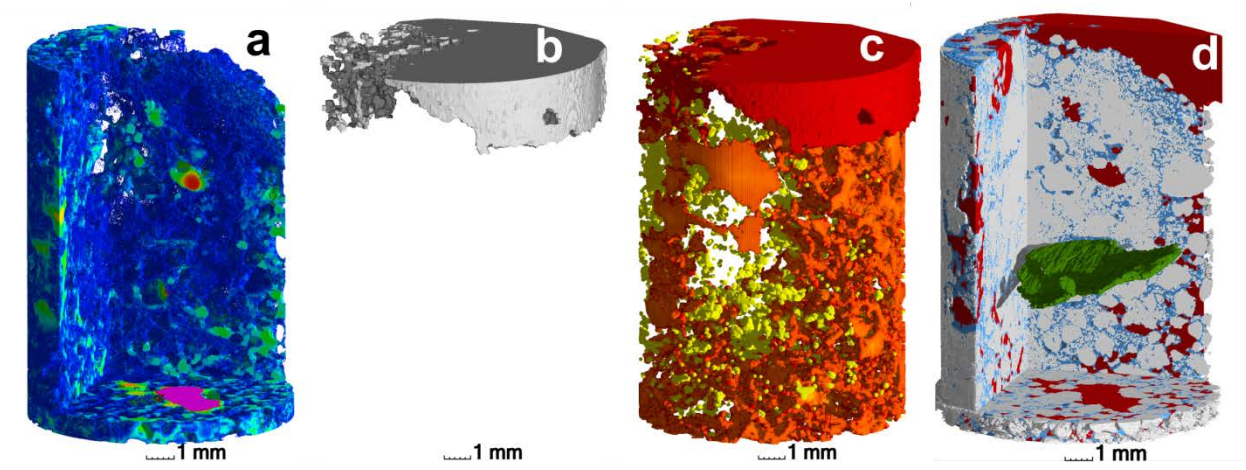

Figure S 3: (a) Local pore diameters in the segmented µCT image obtained with the maximum inscribed sphere method. (b) Headspace of the sample determined with region growing starting at the top boundary. (c) The drainage model results are depicted exemplarily for pore diameters > 119µm that drain at a capillary pressure of 25hPa. Only those pores > 119µm with connection to the headspace (red) get drained, while the disconnected pores > 119µm (yellow) cannot be invaded by air. (d) The modeled distribution of water and air at a capillary pressure of 25 hPa.

An example of this connectivity rule is shown in Figure S55(c). While all depicted pores are big enough (>119µm) to be drained at a capillary pressure of 25 hPa, only the red pores can be invaded by air,

whereas the yellow pores are isolated and remain water-filled. The modeled distribution of air (red) and water (blue) at this capillary pressure is shown in Figure S55(d). The 3D leaf fragment (green) is shown for orientation. A step-wise decrease in capillary pressure decreases the capillary diameter and iteratively desaturates the sample.

Supporting Information 2: Mapping organic compounds with fluorescence microscopy

Auto-fluorescence of plant tissue and organic compounds of the soil matrix are visualized by double-excitation (Figure S56). Double excitation fluorescence microscopy is achieved with a special filter set combining both blue and green excitation wavelengths. Thus auto-fluorescence of different compounds results in greenish and reddish emitted wavelengths respectively (Eickhorst and Tippkötter, 2008a). In combination with stains such as fluorescein the application of double excitation allows a discrete detection of a specific dye in front of the background fluorescence of the soil matrix (Eickhorst and Tippkötter, 2008b). In this example cell structures of the introduced leaf are highlighted and reveal details on its orientation and decomposition stage which could not be visualized by basic light microscopy, e.g. dark spots in the fluorescent image represent areas of less auto-fluorescing material such as minerals, iron oxides (black spots) or larger pores as characteristic features of the soil matrix (Bullock et al., 1985).

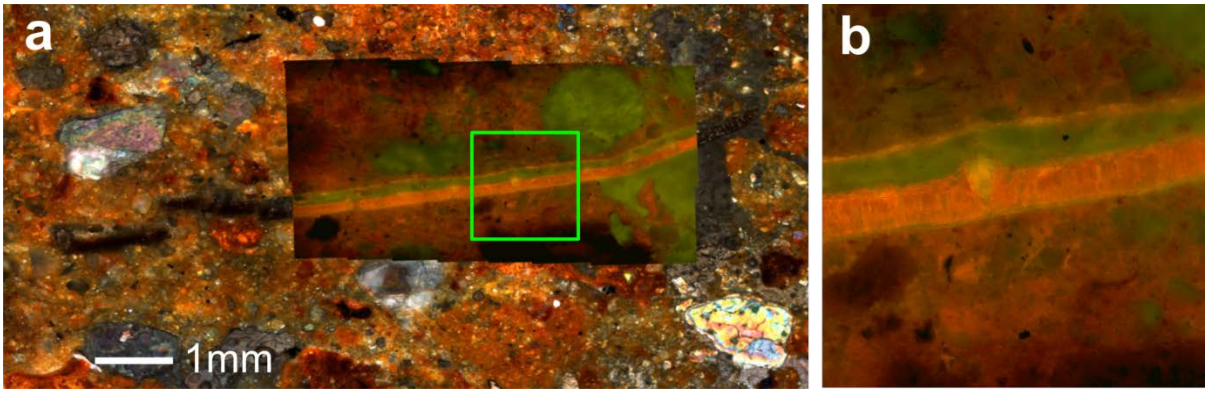

Figure S 4: (a) 2D-2D image registration with double-excitation fluorescence microscopy (FM) and light microscopy (LM). The green frame demarcates the zoomed are in (b).

Supporting Information 3: 2D-3D Image Registration example

All required files to run a 2D-3D image registration example are permanently stored under the following file link:

http://www.ufz.de/record/dmp/archive/6322

This compressed folder contains a minimum example to demonstrate the registration of a 3D computed tomography (CT) file into a 2D light microscopy (LM) image using Elastix (http://elastix.isi.uu.nl/). The demo was developed for a Linux OS (Ubuntu 16.04), tested with elastix version 4.700 and requires 3GB of RAM. The CT file is cropped and does not cover the full sample to save disk space and memory. Images are stored an ITK format which consists of the binary file containing the data (.raw) and a text file containing important meta information (.mhd). The registration is executed by running the shell script ./elastix.sh in a terminal. Open the shell script with a text editor to get more information about the required input for registration and to adapt folder locations, if necessary. Please consult the elastix homepage on how to download and install the software.

Contents of the compressed folder

Images:
CT.mhd – 3D X-ray CT image
LM.mhd – light microscopy image
CT_psd.mhd – pore size distribution derived from the segmented CT image (to demonstrate transformix)

Scripts:
elastix.sh – Shell script that executes elastix and transformix commands
Text files:

elastix_parameters.txt – contains all the parameters tun run the 2D-3D registration
CT_landmarks.txt – contains all corresponding landmark coordinates located in the CT image
LM_landmarks.txt – contains all corresponding landmark coordinates located in the LM image

References

Bullock, P., Fedoroff, N., Jongerius, A., Stoops, G., Tursina, T., 1985. Handbook for soil thin section description. Waine Research.

Eickhorst, T., Tippkötter, R., 2008a. Detection of FISH-stained microorganisms in soil microstructure by fluorescence microscopy. Microscopy and Microanalysis 14(S2), 754-755.

Eickhorst, T., Tippkötter, R., 2008b. Improved detection of soil microorganisms using fluorescence in situ hybridization (FISH) and catalyzed reporter deposition (CARD-FISH). Soil Biology and Biochemistry 40(7), 1883-1891.

Hazlett, R.D., 1995. Simulation of capillary-dominated displacements in microtomographic images of reservoir rocks. Transport in Porous Media 20(1-2), 21-35.

Hilpert, M., Miller, C.T., 2001. Pore-morphology-based simulation of drainage in totally wetting porous media. Advances in Water Resources 24(3-4), 243-255.

Schindelin, J., Arganda-Carreras, I., Frise, E., Kaynig, V., Longair, M., Pietzsch, T., Preibisch, S., Rueden, C., Saalfeld, S., Schmid, B., 2012. Fiji: an open-source platform for biological-image analysis. Nature methods 9(7), 676-682.

Schulz, V.P., Wargo, E.A., Kumbur, E.C., 2015. Pore-Morphology-Based Simulation of Drainage in Porous Media Featuring a Locally Variable Contact Angle. Transport in Porous Media 107(1), 13-25.

6.3. Supporting Information for “Long-term effects of conventional and reduced tillage on soil structure, soil ecological and soil hydraulic properties”

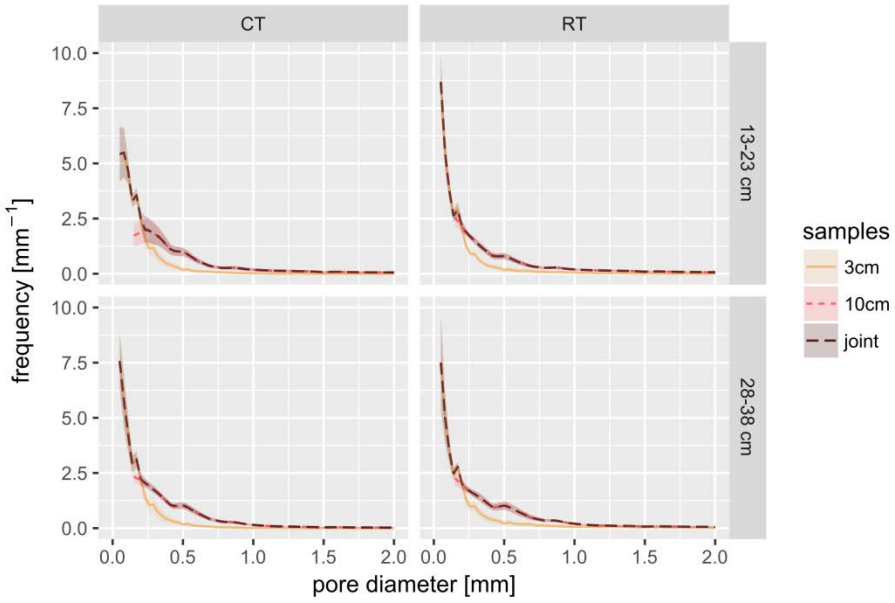

Figure S 5: Pore size distribution for both depths and tillage treatments (CT – conventional tillage, RT – reduced tillage). The frequency distribution of pore diameter is divided by diameter step size [mm-1] to obtain comparable results for different sample sizes with different steps in pore diameters. The joint curve represents the maximum of each curve at a pore diameters classes.

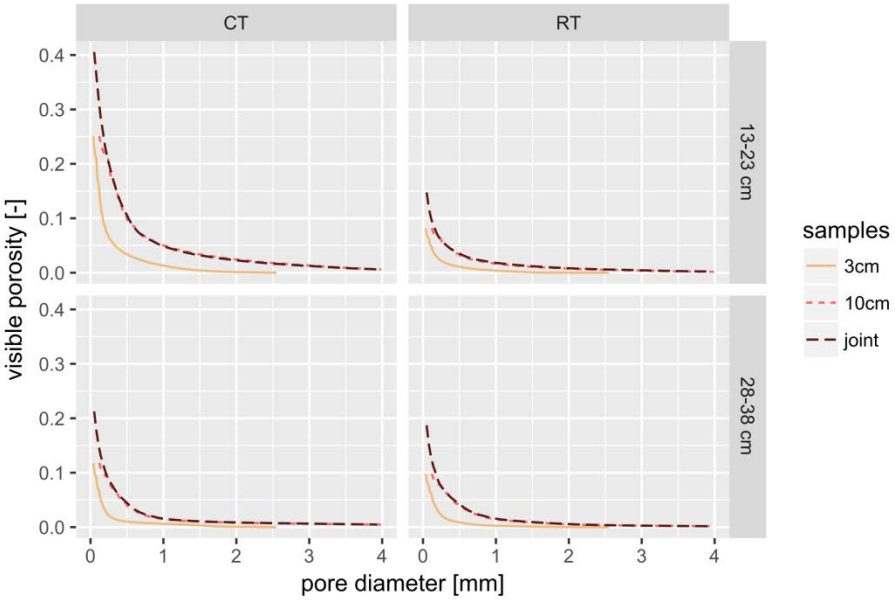

Figure S 6: Cumulative pore size distribution for both depths and tillage treatments (CT – conventional tillage, RT – reduced tillage). The curves are calculated by multiplying with diameter step size and integrating of all diameter classes. The curves start at total visible porosity and show volume fractions of pore larger than a certain diameter.

h

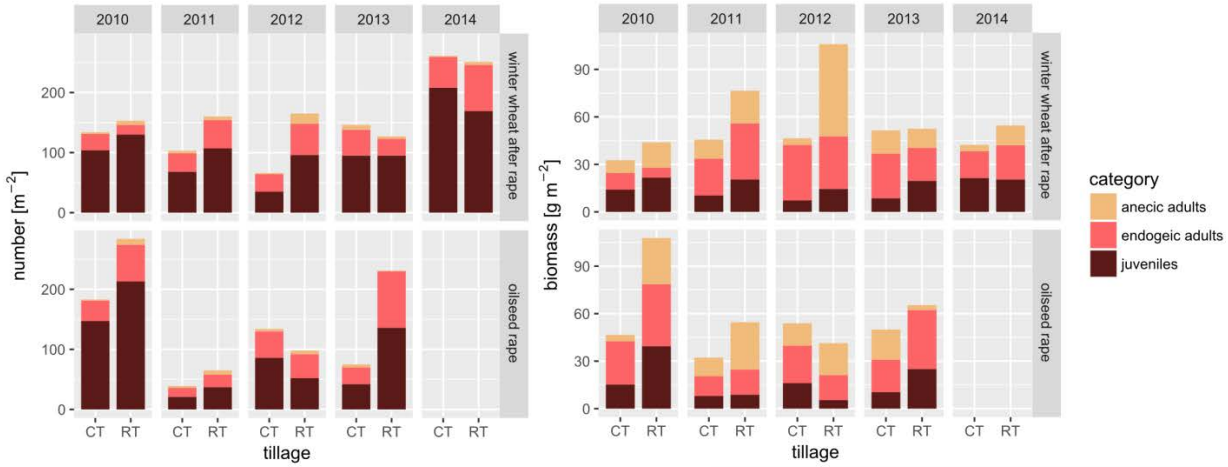

Figure S 7: Earthworm abundance in terms of numbers and biomass in several consecutive years for two crops (rape, wheat) and two tillage treatments (CT – conventional tillage, RT – reduced tillage)

6.4. Supporting Information for "Physical constraints for respiration in microbial hotspots in soil and their importance for denitrification"

Supporting Information 1 Methods

Supporting Information 1.1 Methods: Incubation

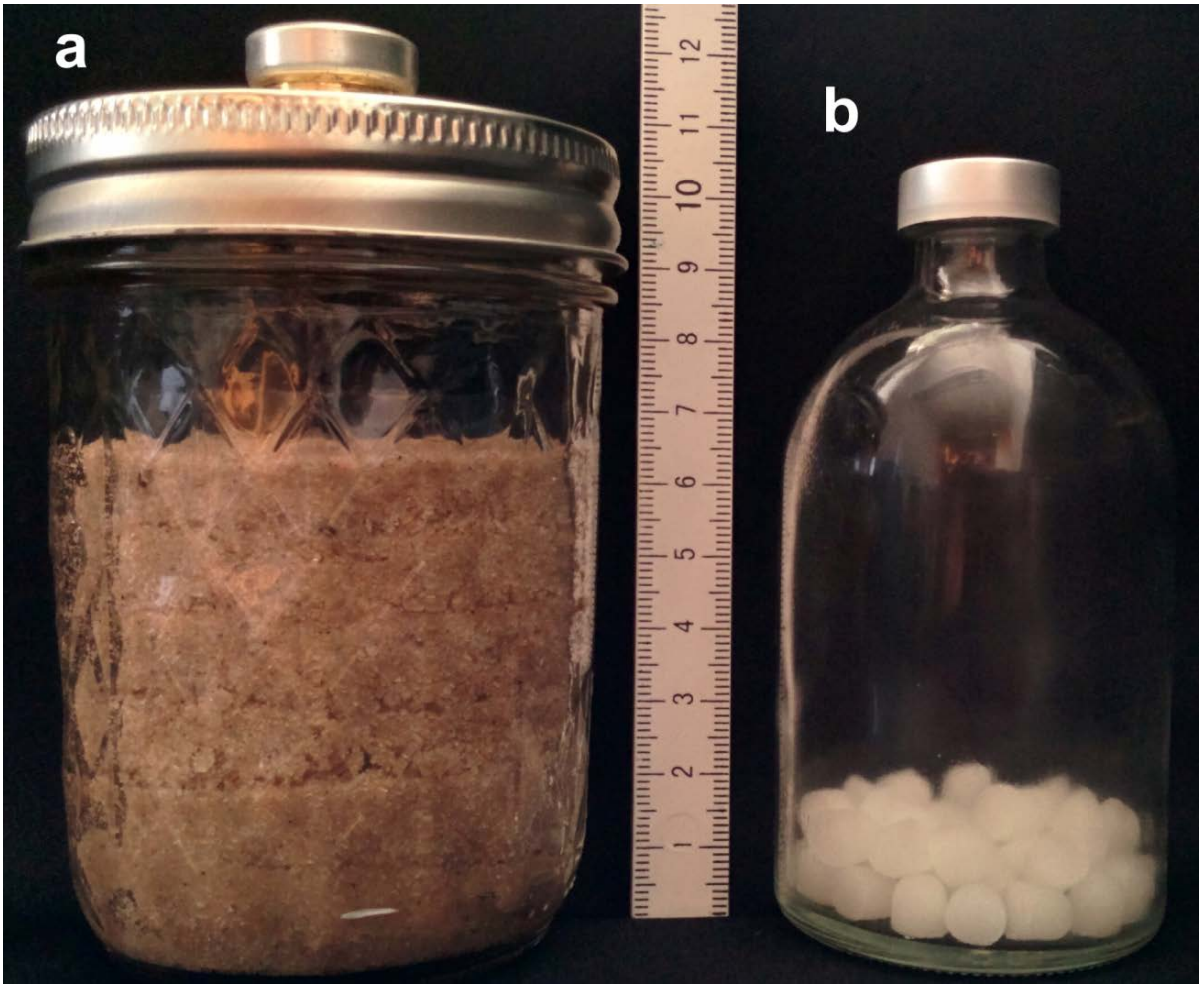

Figure S 8: (a) Half-pint incubation jar (230ml) filled with sand and porous glass beads that serve as microbial hotspots. (b) Respiration kinetics of different types of hotspots either inoculated with *Agrobacterium tumefaciens* or *Paracoccus denitrificans* are measured with 50 hotspots in an otherwise empty glass jar (120ml). Note that hotspots are packed densely with minimal distance, which might have affected aeration.

Supporting Information 1.2 Methods: Product ratios

Ratios of gaseous denitrification products may vary strongly depending on the incubation period for which they are computed. Moreover, in an experimental setup with a permanently close headspace, intermediates may temporarily accumulate in the headspace and still be available as an electron acceptor and diffuse back into the soil at a later incubation stage. This would not be the case in a continuous flow setup with a carrier gas that lack NO and N_2O and also to a much lesser extent under natural conditions were the NO and N_2O concentrations are immediately diluted down to atmospheric concentrations. Still,

apparent product ratios can still be computed by adding up the release of intermediates and subtracting this amount from subsequent denitrification product prior to computing ratios. To do so, we define

$$NO^* := \int_0^T \Theta\big(no'(t)\big)dt,\ N_2O^* := \int_0^T \Theta\big(n_2o'(t)\big)dt,\ {N_2}^* := \int_0^T \Theta\big({n_2}'(t)\big)dt$$

Where $F^*$is the cumulative release, T is the end of incubation, f' is the first time derivative of concentration f, and Θ is defined as

$$\Theta := \begin{cases} x & \text{if } x > 0 \\ 0 & \text{else.} \end{cases}$$

We then have

$NO = NO^*$, $N_2O = N_2O^* - NO^*$ and $N_2 = {N_2}^* - N_2O^*$.

We define the product ratios:

$\mathbf{NO} := \frac{NO}{NO+N_2O+N_2}$, $\mathbf{N_2O} := \frac{N_2O}{NO+N_2O+N_2}$ and $\mathbf{N_2} := \frac{N_2}{NO+N_2O+N_2}$.

Note that these estimated ratios disregard the actual effects that the presence of NO and N_2O may have on the regulation of enzymes for various denitrification steps. They should therefore only be considered as a rough approximation to product ratios in open systems. One benefit of this approach is that T is identical for all samples and does not have to be adjusted to individual denitrification kinetics.

Supporting Information 1.3 Methods: Image processing and analysis

The inner volume of the glass jars filled with quartz sand, water and air constitutes the region of interest (ROI) to be analyzed except for the porous hotspots which are considered as cavities in the ROI. The ROI was determined by semi-automatic region growing in VG StudioMax 2.1 (Volume Graphics) based on gradient images, i.e. the first derivative of the original gray scale image. The gradient was approximated by the Variance 3D filter in Fiji/ImageJ. Region growing was initiated on the homogeneous glass wall of the jar and in the homogeneous head space of the jar and stopped directly at the border of the repacked sand. The fully enclosed volume of both region growing processes is considered as ROI. Likewise, region growing in the relatively homogeneous hotspots stopped directly at the border between hotspots and repacked sand. This was used to demarcate the porous glass beads and subtract them from the ROI. The assignment to *At* and *Pd* hotspots was done according to the vertical position in the layered architecture and according to orientation of the flat and rounded end in the random architecture.

The raw image were filtered with a non-local means filter (Buades et al., 2005) for noise removal at an estimated noise level of $\sigma = 7$ gray values using the non-local denoising plugin for ImageJ. Edge enhancement was carried out with an unsharp mask filter (Schlüter et al., 2014; Sheppard et al., 2004). A vertical drift in gray values due to uneven illumination was detected and corrected for all voxels by subtracting the difference between the average gray values in sand grain voxels per slice with the average gray value of all sand grain voxels (Iassonov and Tuller, 2010; Schlüter et al., 2016). Thresholds were chosen manually and adjusted to the predefined water saturation within test regions. Simple thresholding

was carried out to segment the ROI voxels into air water and solid followed by a majority filter with a cubic 3^3 kernel to remove partial volume effects (Schlüter et al., 2014).

These segmented images were analyzed with respect to different morphological properties of the air-filled and water-filled pores space. All properties are reported separately for the complete ROI and the direct neighborhood of the hotspot boundaries to assess the local conditions experienced by the hotspots. The reduced ROI for the hotspot boundaries was created by dilation and subsequent subtraction of the hotspot ROI.

Dimensionless air connectivity was determined through the volume fraction of air-filled pores with a continuous path to the headspace. To do so, a connected components labelling was performed with the MorpholibJ plugin in Fiji/ImageJ (Legland et al., 2016) to mask out all air clusters without a connection to the headspace.

Air tortuosity was determined in the connected air cluster using the Geodesic Distance map 3D in the MorpholibJ plugin (Legland et al., 2016). This transform writes the shortest path lengths fully within the air cluster from the headspace to any location belong to the air cluster. The dimensionless tortuosity number is then determined for each voxel as the ratio between geodesic distance and depth-dependent, Euclidean distance.

Air distance is determined as the shortest, geodesic distance within the water-filled pore space from any water voxel to the closest air voxel belonging to the connected air cluster. This air distance cannot be normalized in a meaningful way and is therefore reported as a length in mm.

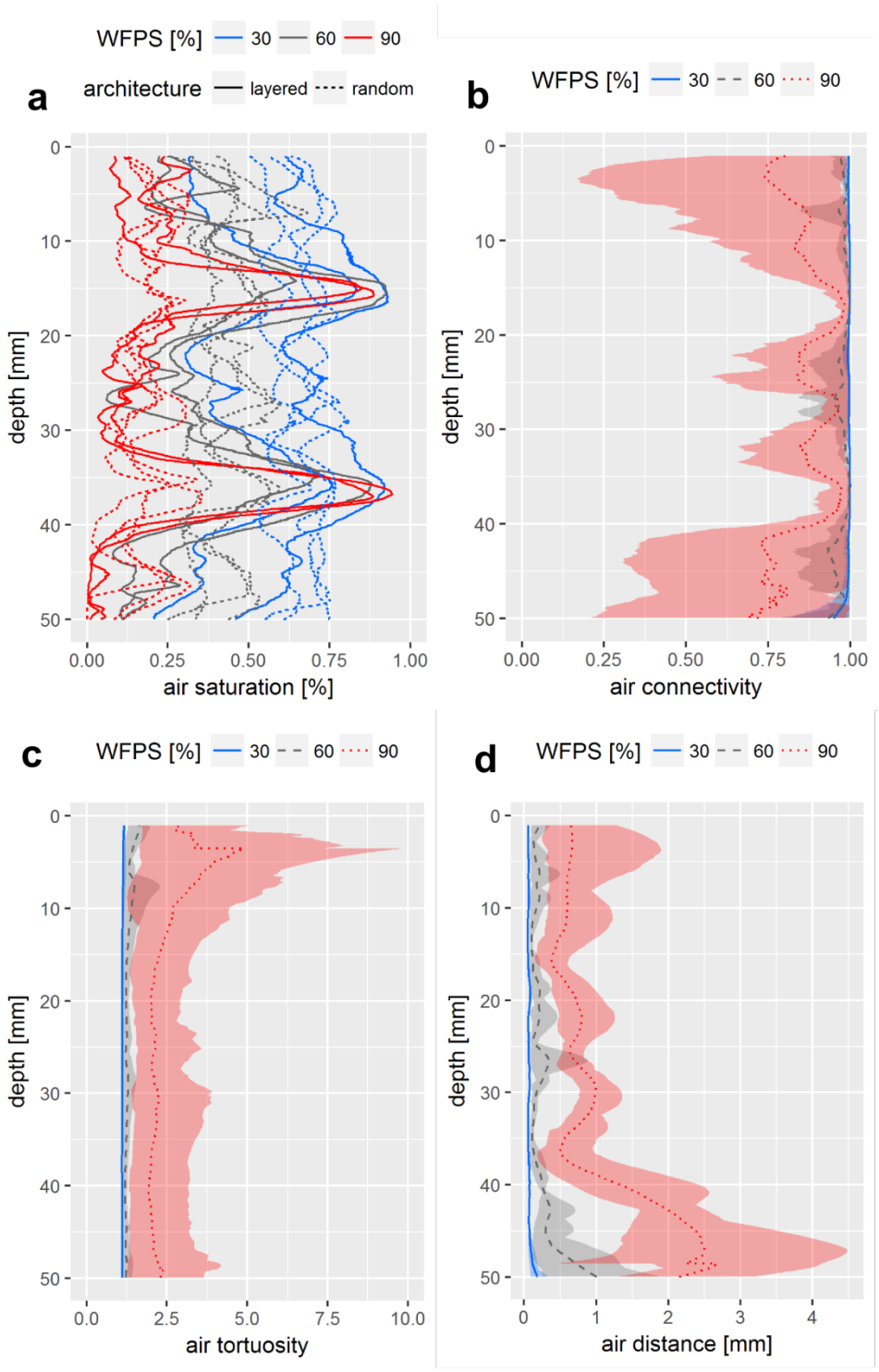

Figure S 9: Depth profiles (n=5) of (a) air saturation, (b) air connectivity, (c) air tortuosity and (d) air distance. Individual profiles are shown in (a) two highlight the differences between layered and random architectures that are caused by packing gaps around hotspots. All other profiles (b-d) are shown as averages (lines) with min-max bands (transparent areas).

m

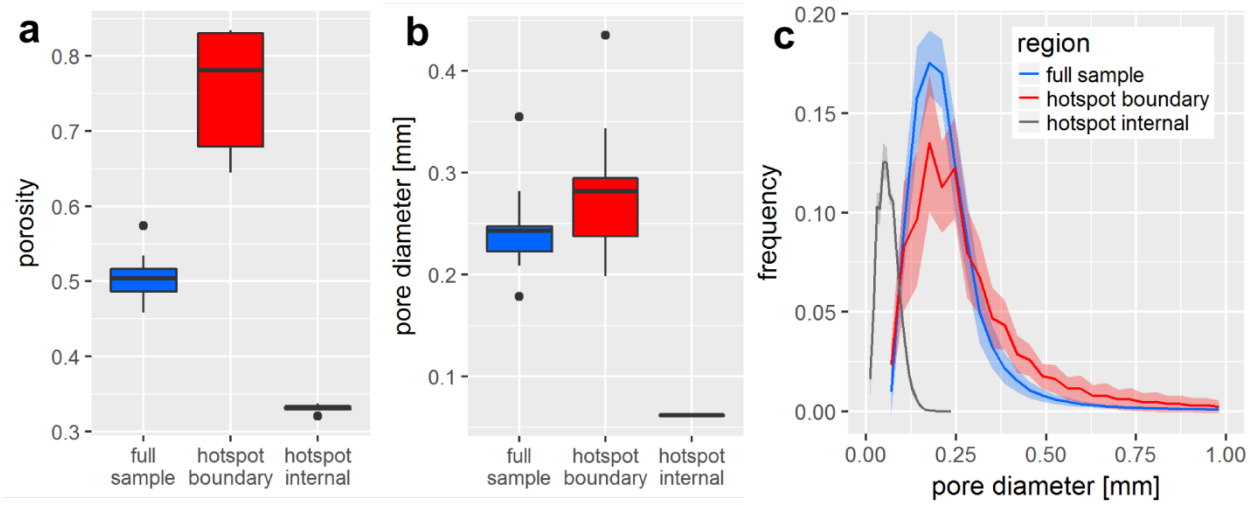

Figure S 10: (a) Visible porosity and (b) pore diameter of individual hotspots (n=4) and the incubated sand samples (n=9) reported separately for the full sample or the only the hotspot boundaries affected by packing gaps. (c) The pore size distributions have an overlap at a diameter range of 80-150µm, which explains why liquid is sucked out of the hotspots, when pores <150µm in the sand are air-filled. (a-b): Data shown as box-whisker plots: Whiskers- min-max, middle lines – median, dots: outliers. (c) Lines represent average and transparent bands the min-max range.

Supporting Information 2 Results

Supporting Information 2.1: Incubation at 90% saturation

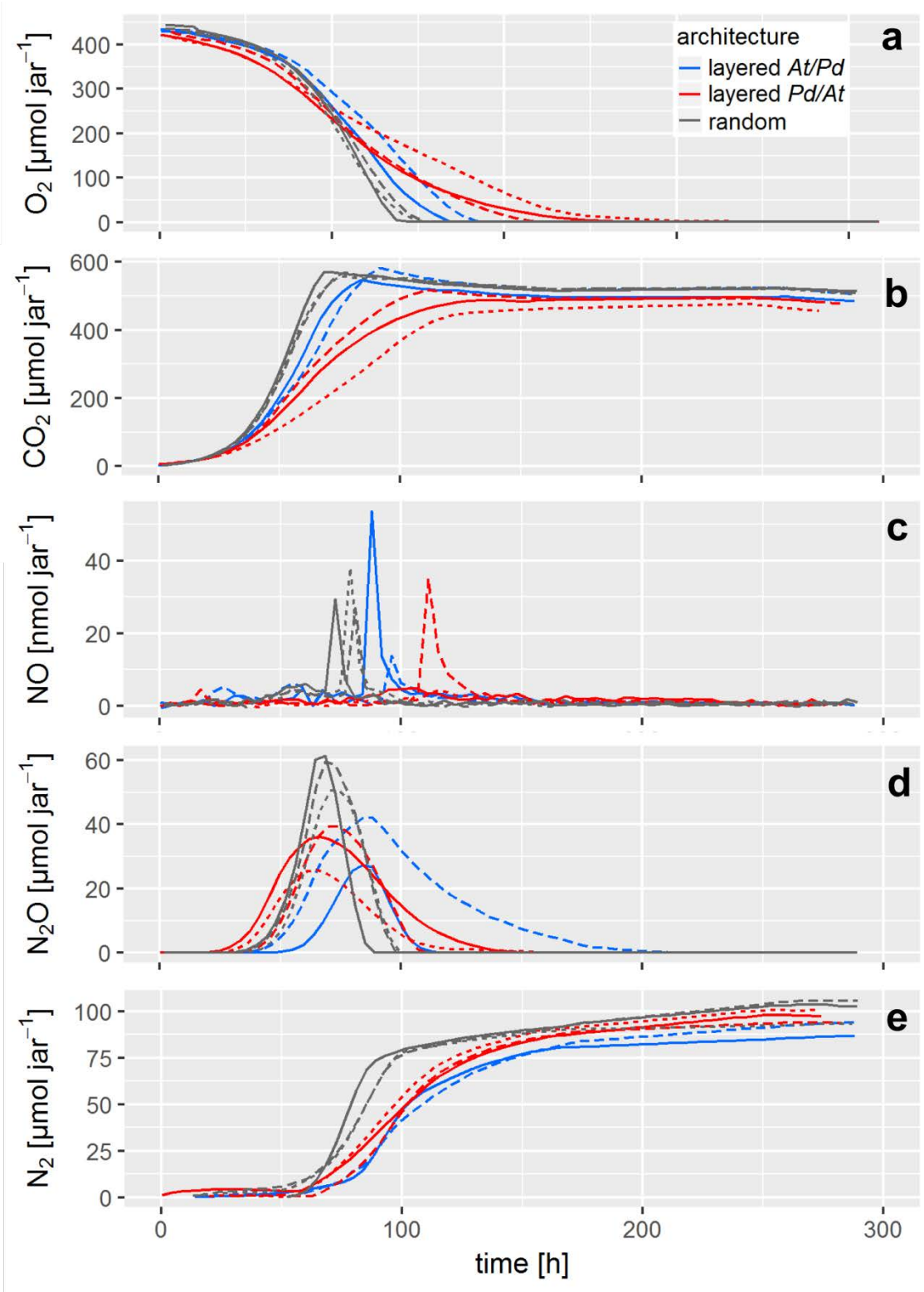

Figure S 11: Gas kinetics in all treatments at high saturation (90% WFPS) for three different hotspot architectures: (a) O2, (b) CO2, (c) NO, (d) N2O, (e) N2. Note the logarithmic ordinate in (c) and (d). Different lines styles represent replicates.

o

Supporting Information 2.2: Incubation at 60% saturation

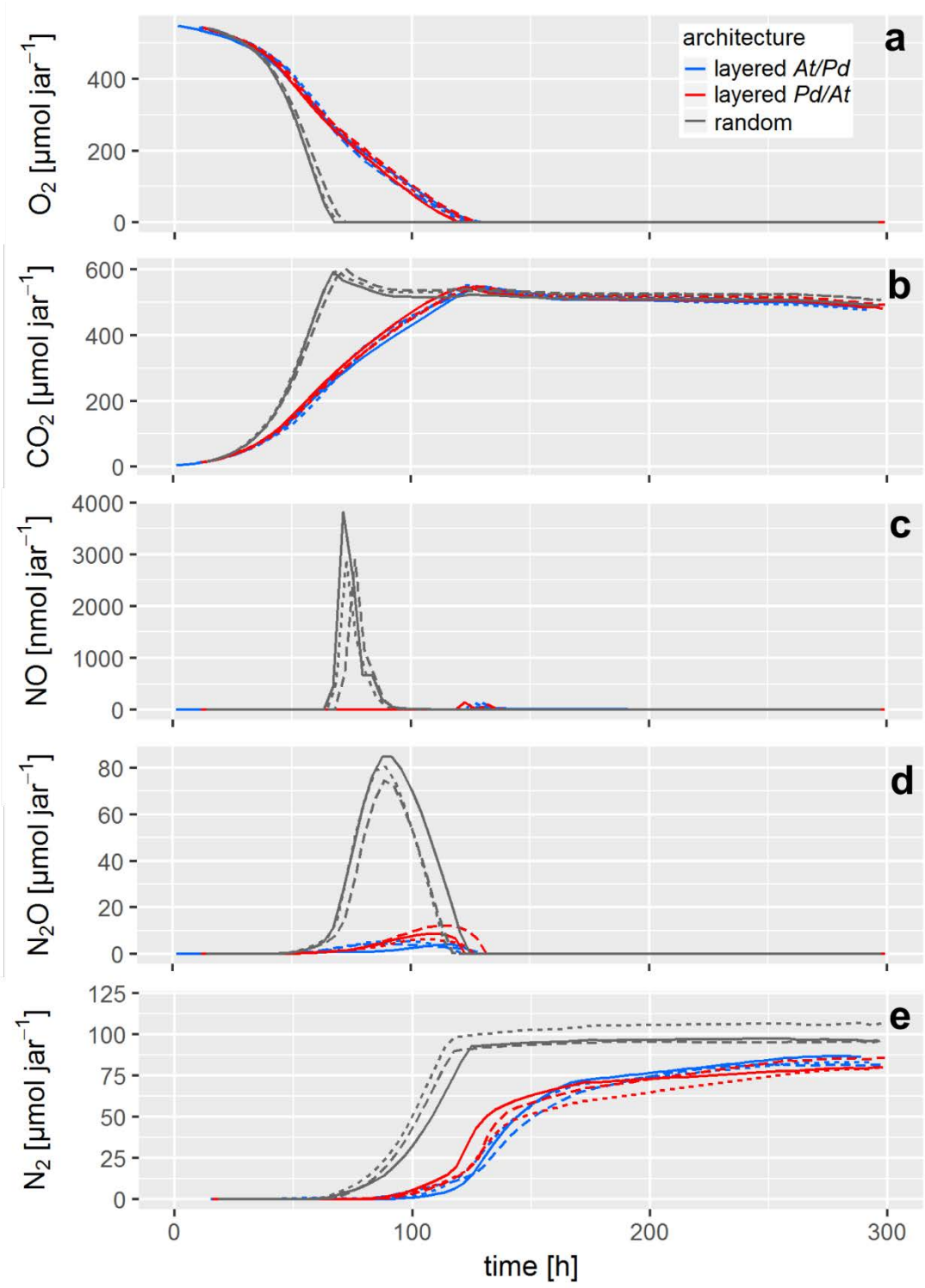

Figure S 12: Gas kinetics in all treatments at medium saturation (60% WFPS) for three different hotspot architectures: (a) O2, (b) CO2, (c) NO, (d) N2O, (e) N2. Note the logarithmic ordinate in (c) and (d). Different lines styles represent replicates.

p

Supporting Information 2.3: Incubation at 30% saturation

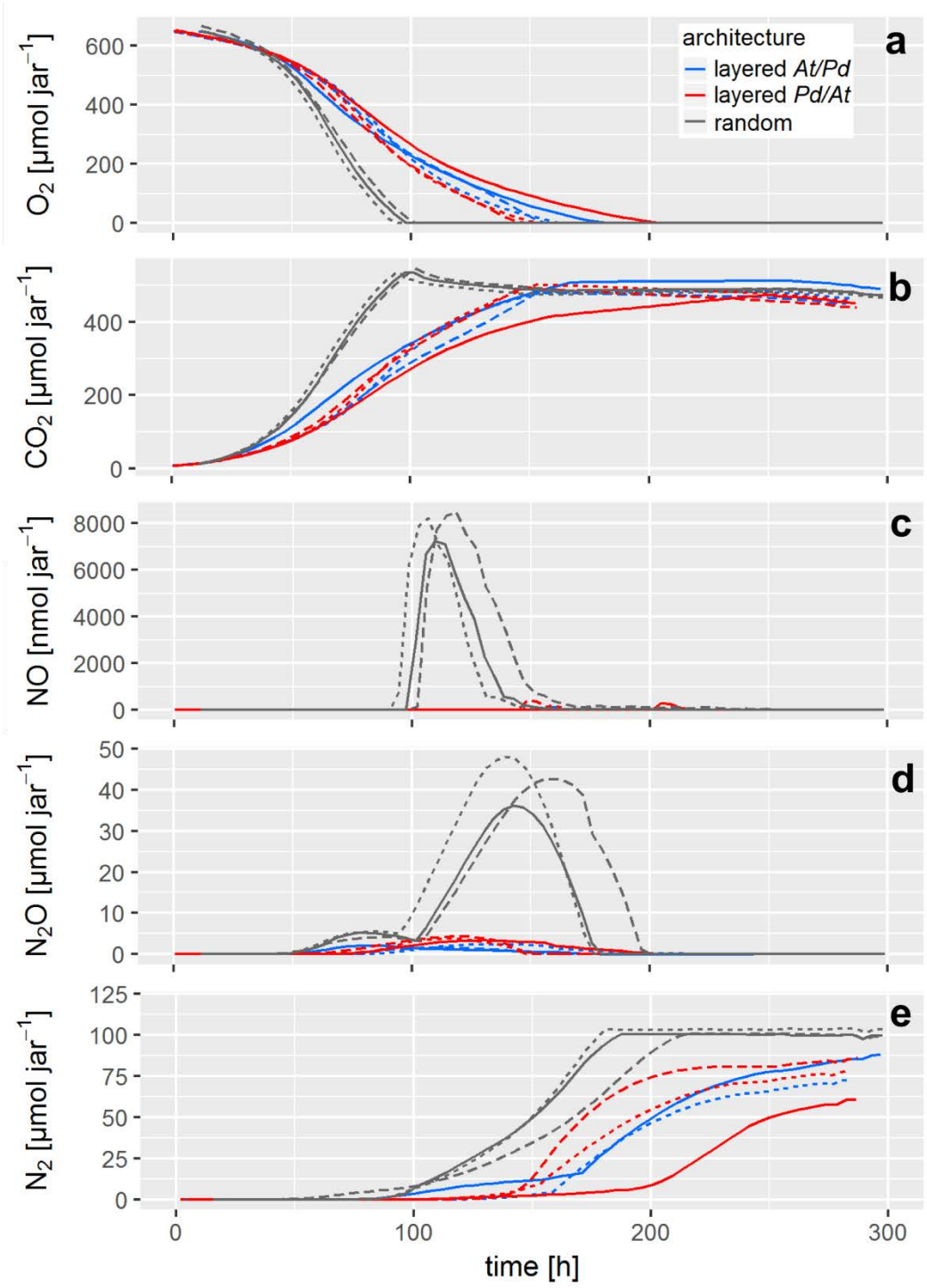

Figure S 13: Gas kinetics in all treatments at low saturation (30% WFPS) for three different hotspot architectures: (a) O2, (b) CO2, (c) NO, (d) N2O, (e) N2. Note the logarithmic ordinate in (c) and (d). Different lines styles represent replicates.

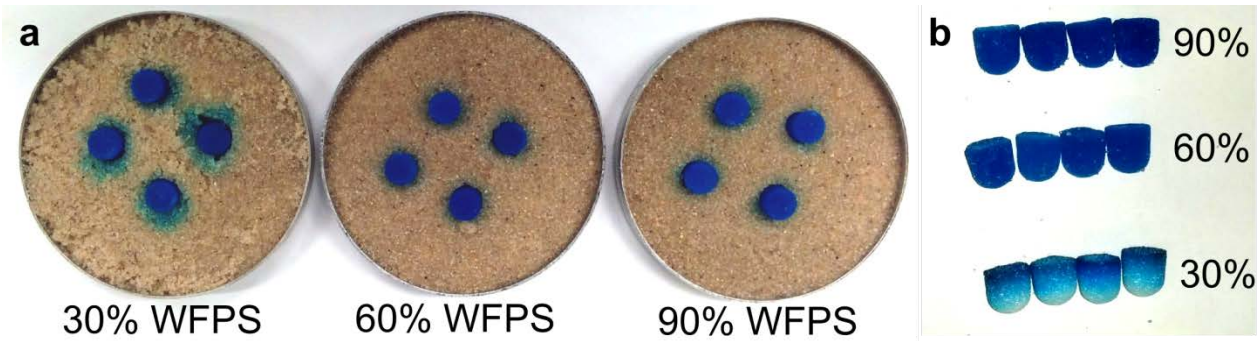

Figure S 14: (a) transport of brilliant blue dye from aggregates into sand at different saturations after≈10min. At 30% WFPS transport is dominated by convection, whereas at higher saturation only diffusion remains. (b) dye loss after one day

Supporting Information 2.4: Nitrogen balance

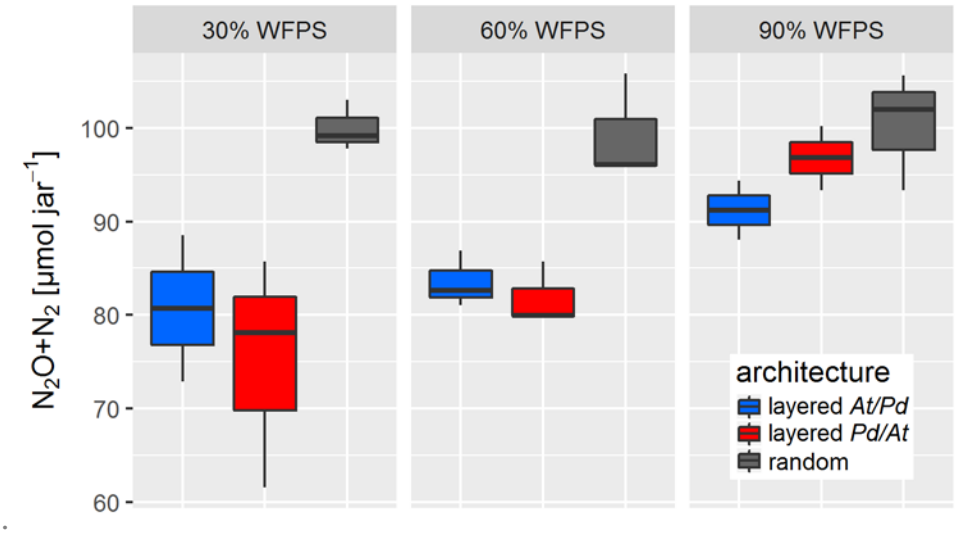

Figure S 15: Sum of denitrification products (N_2O, N_2) at the end of incubation (300h) for all architectures and saturations (n=3). The amount of initially present nitrate estimated from the internal porosity of hotspots was 96 µmol NO_3-N per jar, with some additional nitrate in growth medium adhering to the hotspot boundaries by week capillary forces during packing.

References

Buades, A., Coll, B., Morel, J.-M., 2005. A non-local algorithm for image denoising, Computer Vision and Pattern Recognition, 2005. CVPR 2005. IEEE Computer Society Conference on, San Diego, California, pp. 60-65 vol. 62.

Iassonov, P., Tuller, M., 2010. Application of segmentation for correction of intensity bias in X-ray computed tomography images. Vadose Zone Journal 9(1), 187-191.

Legland, D., Arganda-Carreras, I., Andrey, P., 2016. MorphoLibJ: integrated library and plugins for mathematical morphology with ImageJ. Bioinformatics 32(22), 3532-3534.

Schlüter, S., Leuther, F., Vogler, S., Vogel, H.-J., 2016. X-ray microtomography analysis of soil structure deformation caused by centrifugation. Solid Earth 7(1), 129-140.

Schlüter, S., Sheppard, A., Brown, K., Wildenschild, D., 2014. Image processing of multiphase images obtained via X-ray microtomography: A review. Water Resources Research 50(4), 3615-3639.
Sheppard, A.P., Sok, R.M., Averdunk, H., 2004. Techniques for image enhancement and segmentation of tomographic images of porous materials. Physica A: Statistical Mechanics and its Applications 339(1), 145-151.

Akademischer Lebenslauf

Name, Titel: Steffen Schlüter, Dr. rer nat

Ausbildung

2009-2012	Promotion in Geowissenschaften, Martin-Luther-Universität Halle-Wittenberg (Betreuer: Prof. Vogel), angestellt am UFZ, Abschluss: Dr. rer. nat. (summa cum laude) *Dissertation: Quantification of soil structural heterogeneity and its impact on flow and transport*
2002-2009	Geographie-Studium, TU Dresden, Abschluss: Diplom-Geograph, Gesamtnote 1,2 *Diplomarbeit: Röntgentomographische Analyse der Strukturdynamik in Ackerböden (Note 1,0)*
2001	Abitur, Johann-Gottfried-Herder Gymnasium, Schneeberg, Gesamtnote 1,3

Arbeitserfahrung

2018-	Arbeitsgruppenleiter am Helmholtz-Zentrum für Umweltforschung - UFZ
2015-2018	Postdoktorand am Helmholtz-Zentrum für Umweltforschung - UFZ
2014-2015	Feodor-Lynen-Rückkehrstipendium der A.-v.-Humboldtstiftung am Deutschen Zentrum für Neurodegenerative Erkrankungen – DZNE (Prof. Kempermann) und Helmholtz-Zentrum für Umweltforschung – UFZ (Prof. Vogel)
2013-2014	Feodor-Lynen-Stipendium der A.-v.-Humboldtstiftung an der Oregon State University (Prof. Wildenschild) und Australian National University (Dr. Sheppard)
2012-2013	Postdoktorand am Helmholtz-Zentrum für Umweltforschung - UFZ

Preise und Auszeichnungen

2018	Top Reviewer basierend auf der Statistik des Publons' Global Peer Review Awards – Top 1% in Agrarwissenschaften
2017	Outstanding Reviewer der Zeitschrift "Soil Science Society of America Journal"
2016	Bester Beitrag bei der Tagung der Society of Core Analysts in Snowmass, Colorado, für den Artikel SCA2016-009 „Flow Regimes During Immiscible Displacement" von Armstrong et al.
2015	Bestes Poster bei der Jahresversammlung der der Deutschen Bodenkundlichen Gesellschaft (DBG) für den Beitrag „Measuring changes of fluid configurations during two-phase flow with fast X-ray microtomography"
2014-2015	Feodor-Lynen Rückkehrstipendium der Alexander-von-Humboldt Stiftung
2013-2014	Feodor-Lynen Forschungsstipendium der Alexander-von-Humboldt Stiftung
2012	Luther Urkunde der Martin-Luther-Universität Halle-Wittenberg für die Dissertation "Quantification of soil structural heterogeneity and its impact on flow and transport"
2010	Best Paper Award in Computers & Geosciences für Vogel, H.-J., Weller, U., Schlüter, S. (2010): Quantification of soil structure based on Minkowski functions. Computers & Geosciences, 36(10),1239-1245. doi:10.1016/j.cageo.2010.03.007
2009	Enno-Heidebroek Urkunde der Technischen Universität Dresden für herausragende Studienleistungen

Selbständigkeitserklärung

Hiermit erkläre ich, dass die Habilitationsschrift selbständig und ohne fremde Hilfe verfasst, andere als die angegebenen Quellen und Hilfsmittel nicht benutzt und die den benutzten Werken wörtlich oder inhaltlich entnommenen Stellen als solche kenntlich gemacht wurden.

Steffen Schlüter

Titelseiten aller verwendeten Artikel

AGU PUBLICATIONS

Water Resources Research

REVIEW ARTICLE
10.1002/2014WR015256

Key Points:
- First survey of image processing methods for multiphase fluid images
- A novel protocol is suitable for various types of porous media
- Many routines come with a freely available open-source library

Correspondence to:
S. Schlüter,
schluets@onid.orst.edu

Citation:
Schlüter, S., A. Sheppard, K. Brown, and D. Wildenschild (2014), Image processing of multiphase images obtained via X-ray microtomography: A review, *Water Resour. Res.*, *50*, doi:10.1002/2014WR015256.

Received 4 JAN 2014
Accepted 2 APR 2014
Accepted article online 7 APR 2014

Image processing of multiphase images obtained via X-ray microtomography: A review

Steffen Schlüter[1,2,3], Adrian Sheppard[2], Kendra Brown[1], and Dorthe Wildenschild[1]

[1]School of Chemical, Biological and Environmental Engineering, Oregon State University, Corvallis, Oregon, USA, [2]Department of Applied Mathematics, Research School of Physics and Engineering, Australian National University, Canberra, Australian Capital Territory, Australia, [3]Department of Soil Physics, Helmholtz-Centre for Environmental Research—UFZ, Halle, Germany

Abstract Easier access to X-ray microtomography (μCT) facilities has provided much new insight from high-resolution imaging for various problems in porous media research. Pore space analysis with respect to functional properties usually requires segmentation of the intensity data into different classes. Image segmentation is a nontrivial problem that may have a profound impact on all subsequent image analyses. This review deals with two issues that are neglected in most of the recent studies on image segmentation: (i) focus on multiclass segmentation and (ii) detailed descriptions as to why a specific method may fail together with strategies for preventing the failure by applying suitable image enhancement prior to segmentation. In this way, the presented algorithms become very robust and are less prone to operator bias. Three different test images are examined: a synthetic image with ground-truth information, a synchrotron image of precision beads with three different fluids residing in the pore space, and a μCT image of a soil sample containing macropores, rocks, organic matter, and the soil matrix. Image blur is identified as the major cause for poor segmentation results. Other impairments of the raw data like noise, ring artifacts, and intensity variation can be removed with current image enhancement methods. Bayesian Markov random field segmentation, watershed segmentation, and converging active contours are well suited for multiclass segmentation, yet with different success to correct for partial volume effects and conserve small image features simultaneously.

1. Introduction

The last decade has seen a tremendous progress in X-ray tomography and imaging techniques providing new means to analyze a multitude of research problems in porous media research. In the scope of water resources research, applications range from soil-water-root interactions and mechanical and hydraulical properties of rocks to pore-scale modeling of multiphase flow and continue to appear in related fields of research (see reviews by *Blunt et al*. [2013], *Cnudde and Boone* [2013], *Wildenschild and Sheppard* [2013], and *Anderson and Hopmans* [2013]). Progress in image progressing has kept a comparable pace in terms of new developments in image enhancement, image analysis, and hardware architectures [e.g., *Ketcham and Carlson*, 2001; *Sheppard et al*., 2004; *Kaestner et al*., 2008; *Porter and Wildenschild*, 2010; *Tuller et al*., 2013]. Since X-ray tomography is becoming a standard technique available to an increasing number of research groups in water resources research, more and more scientists have a need for information on how to process their data. Not everyone new to the field has the resources to develop their own image processing toolbox, tailored for the research question at hand, or the budget to take advantage of powerful image processing software that often has a rather comprehensive scope. A relief in this regard are software toolboxes which are freely available to the scientific community like ImageJ [*Ferreira and Rasband*, 2012], ITK [*Ibanez et al*., 2005], Quantim [*Vogel et al*., 2010], Blob3D [*Ketcham*, 2005], or scikit-image [*van der Walt et al.,* 2014], just to name a few. Their multiphase segmentation capabilities are somewhat limited and may require substantial operator input. The software used in this study is described in the Appendix A.

However, comparing the performance of different image processing methods on the same set of test images often leads to very different results. A notorious example is image segmentation of a gray value image into objects and background [*Sezgin and Sankur*, 2004; *Iassonov et al*., 2009; *Baveye et al*., 2010]. Yet, these comparative studies often merely list the performance of several segmentation methods with respect

Solid Earth, 7, 129–140, 2016
www.solid-earth.net/7/129/2016/
doi:10.5194/se-7-129-2016

Solid Earth Open Access EGU

X-ray microtomography analysis of soil structure deformation caused by centrifugation

S. Schlüter[1,2], **F. Leuther**[1], **S. Vogler**[2], **and H.-J. Vogel**[1,3]

[1]Department of Soil Physics, Helmholtz-Centre for Environmental Research – UFZ, Halle (Saale), Germany
[2]German Center for Neurodegenerative Diseases (DZNE), Dresden, Germany
[3]Soil Science, Martin-Luther-University Halle-Witteberg, Haale (Saale), Germany

Correspondence to: S.Schlüter (steffen.schlueter@ufz.de)

Received: 2 September 2015 – Published in Solid Earth Discuss.: 6 October 2015
Revised: 4 January 2016 – Accepted: 5 January 2016 – Published: 26 January 2016

Abstract. Centrifugation provides a fast method to measure soil water retention curves over a wide moisture range. However, deformation of soil structure may occur at high angular velocities in the centrifuge. The objective of this study was to capture these changes in soil structure with X-ray microtomography and to measure local deformations via digital volume correlation. Two samples were investigated that differ in texture and rock content. A detailed analysis of the pore space reveals an interplay between shrinkage due to drying and soil compaction due to compression. Macroporosity increases at moderate angular velocity because of crack formation due to moisture release. At higher angular velocities, corresponding to capillary pressure of $\psi < -100$ kPa, macroporosity decreases again because of structure deformation due to compression. While volume changes due to swelling clay minerals are immanent in any drying process, the compaction of soil is a specific drawback of the centrifugation method. A new protocol for digital volume correlation was developed to analyze the spatial heterogeneity of deformation. In both samples the displacement of soil constituents is highest in the top part of the sample and exhibits high lateral variability explained by the spatial distribution of macropores in the sample. Centrifugation should therefore only be applied after the completion of all other hydraulic or thermal experiments, or any other analysis that depends on the integrity of soil structure.

1 Introduction

Soils, rocks and sediments are assumed to be rigid bodies in many modeling applications. Yet, the internal structure of these porous media is modified through a variety of technical and natural processes. The internal changes can either be gradual, e.g., through dissolution, biological activity or swelling/shrinking, or abrupt, e.g., landslides or tillage. Conventional laboratory methods can only provide a limited set of structural properties, such as bulk density and porosity, or provide indirect information through functional properties that are governed by the internal structure, such as gas diffusion, permeability or stress–strain relationships. Direct information on the deformation of the internal pore architecture is typically missing. X-ray microtomography has turned into a standard technique to fill this gap and measure the three-dimensional internal structure of porous media (Ketcham and Carlson, 2001; Cnudde and Boone, 2013; Wildenschild and Sheppard, 2013). There is a huge variety of image processing and image analysis methods that are all tailored for the ultimate goal to quantify the complex, structural heterogeneity based on a few meaningful parameters (Kaestner et al., 2008; Vogel et al., 2010; Schlüter et al., 2014). The changes in the internal structure can be assessed statistically, e.g., by comparing the pore size distribution or pore connectivity averaged over different samples at two points in time (Jégou et al., 2002; Schlüter et al., 2011). Evidently, spatially explicit information about the internal displacement of particles or aggregates is excluded from analysis in such an approach. However, this local deformation information is of particular interest, e.g., in soil mechanics (Terzaghi et al., 1996). So

PLOS ONE

RESEARCH ARTICLE

Analysis of Soil Structure Turnover with Garnet Particles and X-Ray Microtomography

Steffen Schlüter[1]*, **Hans-Jörg Vogel**[1,2]

1 Dept. Soil Physics, Helmholtz-Centre for Environmental Research - UFZ, Halle, Germany, **2** Institut für Agrar- und Ernährungswissenschaften, Martin-Luther-Universität Halle-Wittenberg, Halle, Germany

* steffen.schlueter@ufz.de

Abstract

Matter turnover in soil is tightly linked to soil structure which governs the heterogeneous distribution of habitats, reaction sites and pathways in soil. Thereby, the temporal dynamics of soil structure alteration is deemed to be important for essential ecosystem functions of soil but very little is known about it. A major reason for this knowledge gap is the lack of methods to study soil structure turnover directly at microscopic scales. Here we devise a conceptual approach and an image processing workflow to study soil structure turnover by labeling some initial state of soil structure with small garnet particles and tracking their fate with X-ray microtomography. The particles adhere to aggregate boundaries at the beginning of the experiment but gradually change their position relative to the nearest pore as structure formation progresses and pores are destructed or newly formed. A new metric based on the contact distances between particles and pores is proposed that allows for a direct quantification of soil structure turnover rates. The methodology is tested for a case study about soil compaction of a silty loam soil during stepwise increase of bulk density (ρ = {1.1, 1.3, 1.5} g/cm^3). We demonstrate that the analysis of mean contact distances provides genuinely new insights about changing diffusion pathways that cannot be inferred neither from conventional pore space attributes (porosity, mean pore size, pore connectivity) nor from deformation analysis with digital image correlation. This structure labeling approach to quantify soil structure turnover provides a direct analogy to stable isotope labeling for the analysis of matter turnover and can be readily combined with each other.

Citation: Schlüter S, Vogel H-J (2016) Analysis of Soil Structure Turnover with Garnet Particles and X-Ray Microtomography. PLoS ONE 11(7): e0159948. doi:10.1371/journal.pone.0159948

Editor: Christophe Egles, Université de Technologie de Compiègne, FRANCE

Received: April 6, 2016

Accepted: July 11, 2016

Published: July 25, 2016

Data Availability Statement: All segmented X-ray μCT files are permanently available through the UFZ archive with data description using standardized metadata catalogue (Dublin Core) and with access via URL https://www.ufz.de/record/dmp/archive/3768/.

Funding: The authors have no support or funding to report.

Competing Interests: The authors have declared that no competing interests exist.

Introduction

Soil structure provides the pathways for matter fluxes, entails a high diversity of microhabitats and causes a heterogeneous distribution of reaction sites in soil. Through these regulatory traits it acts as a major driver for important soil functions like stabilization of soil organic matter, maintenance of biodiversity or water and nutrient cycling [1, 2]. Soil structure is not static, but continuously altered through abiotic (e.g. tillage, moisture changes) and biotic agents (e.g. bioturbation, root growth) [3]. These soil structure dynamics are also sometimes referred to as

Environmental Science & Technology

Article

Cite This: Environ. Sci. Technol. 2019, 53, 829−837

pubs.acs.org/est

Correlative Imaging Reveals Holistic View of Soil Microenvironments

Steffen Schlüter,*[,†,∥] Thilo Eickhorst,[‡] and Carsten W. Mueller[§]

[†]Department Soil System Sciences, Helmholtz-Centre for Environmental Research - UFZ, Halle, Germany

[‡]FB 2 (Biology/Chemistry), University of Bremen, Bremen, Germany

[§]TU Munich, Chair of Soil Science, Freising-Weihenstephan, Germany

Supporting Information

ABSTRACT: The microenvironmental conditions in soil exert a major control on many ecosystem functions of soil. Their investigation in intact soil samples is impaired by methodological challenges in the joint investigation of structural heterogeneity that defines pathways for matter fluxes and biogeochemical heterogeneity that governs reaction patterns and microhabitats. Here we demonstrate how these challenges can be overcome with a novel protocol for correlative imaging based on image registration to combine three-dimensional microstructure analysis of X-ray tomography data with biogeochemical microscopic data of various modalities and scales (light microscopy, fluorescence microscopy, electron microscopy, secondary ion mass spectrometry). Correlative imaging of a microcosm study shows that the majority (75%) of bacteria are located in mesopores (<10 μm). Furthermore, they have a preference to forage near macropore surfaces and near fresh particulate organic matter. Ignoring the structural complexity coming from the third dimension is justified for metrics based on size and distances but leads to a substantial bias for metrics based on continuity. This versatile combination of imaging modalities with freely available software and protocols may open up completely new avenues for the investigation of many important biogeochemical and physical processes in structured soils.

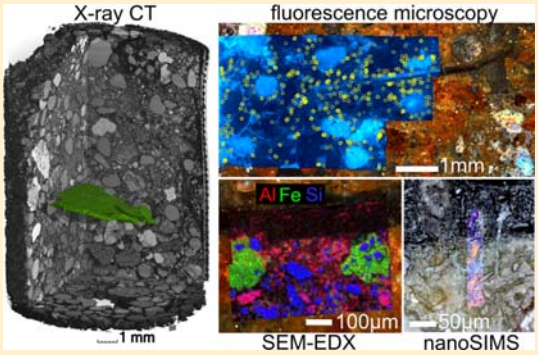

1. INTRODUCTION

Small-scale heterogeneity of environmental conditions in soil exerts a major control on carbon and nutrient cycling. Physical accessibility at the pore scale plays an important role for long-term carbon stabilization[1,2] and for microbial diversity in soil through spatial separation in diverse ecological niches.[3−5] Many microbial processes like respiration, nitrification and denitrification are known to occur in hotspots of microbial activity which are imprints of the patchy distribution of microhabitats in soil.[6] These patterns form as a result of a complex interplay between biotic and abiotic agents, so their formation cannot be understood, if individual processes are studied in isolation. This calls for a joint characterization of (i) the physical soil structure providing the pathways for matter fluxes, (ii) the chemical properties that drive local reactions in soil, and (iii) the distribution of soil biota that is both resulting from and actively changing the former.[7,8]

While the three-dimensional (3D) characterization of the physical structure of intact soil has advanced tremendously with the advent of noninvasive imaging techniques like X-ray microtomography[9−11] (μCT), 3D imaging of biogeochemical heterogeneity in opaque soil is still not achievable. Thus, it is still common practice to cut the soil into pieces, with or without prior resin impregnation, in order to apply two-dimensional (2D) microscopic and microspectroscopic imaging techniques on exposed surfaces. The combination of various biogeochemical imaging methods is an emerging field in life sciences called correlative imaging or correlative microscopy.[12,13] In contrast to the fast growing number of applications of 3D chemical imaging using fluorescence microscopy approaches, such a straightforward approach is not at hand for intact natural geological materials including opaque soil and plant−soil systems. Consequently applications in soil science are few, in particular the combination of two-dimensional biogeochemical imaging modalities with 3D noninvasive imaging. When using soil sections for 2D biogeochemical imaging, a major hurdle is to find the exact plane of the exposed surface within a bigger 3D volume. Depending on the scale gap this can turn into a search for a two-dimensional needle in the 3D haystack. One pragmatic solution is to cut or grind down the exposed surface strictly along a principle axis of the 3D image to reduce the degrees of freedom with which the 2D plane can potentially be oriented. In this way, the spatial distribution of *P. fluorescens* in fluorescence microscopy (FM) images of soil microcosms was directly related to pore space attributes measured with X-ray microtomography.[14] The more flexible approach is to pose this

Received: September 17, 2018
Revised: December 6, 2018
Accepted: December 11, 2018
Published: December 11, 2018

DOI: 10.1021/acs.est.8b05245
Environ. Sci. Technol. 2019, 53, 829−837

Geoderma 332 (2018) 10–19

Contents lists available at ScienceDirect

Geoderma

journal homepage: www.elsevier.com/locate/geoderma

Long-term effects of conventional and reduced tillage on soil structure, soil ecological and soil hydraulic properties

Steffen Schlüter[a,*], Caroline Großmann[a,b], Julius Diel[a], Gi-Mick Wu[c], Sabine Tischer[d], Annette Deubel[e], Jan Rücknagel[b]

[a] Department of Soil System Sciences, Helmholtz-Centre for Environmental Research – UFZ, Halle, Germany
[b] Department of Agronomy and Organic Farming, Institute for Agricultural and Nutritional Sciences, Martin Luther University Halle-Wittenberg, Halle, Germany
[c] DEVELOP, Helmholtz-Centre for Environmental Research – UFZ, Leipzig, Germany
[d] Department of Soil Biogeochemistry, Institute for Agricultural and Nutritional Sciences, Martin-Luther-University Halle-Wittenberg, Halle, Germany
[e] Department of Agriculture, Ecotrophology and Landscaping, Anhalt University of Applied Sciences, Bernburg, Germany

ARTICLE INFO

Keywords:
Tillage effects
X-ray tomography
Conservation agriculture
Macroporosity
Saturated hydraulic conductivity
Plow pan
Earthworm abundance

ABSTRACT

There is a long-lasting debate about the effects of tillage practices on soil structure and structure-mediated ecosystem properties like hydraulic conductivity and crop productivity. This is investigated in a long-term field experiment on tillage practices at the Westerfeld trial in Bernburg, Germany (25 years of different management). Here we combine soil structure information obtained by X-ray microtomography with bulk properties like bulk density, air capacity and saturated hydraulic conductivity, as well as integrative, ecological properties like earthworm abundance and crop yield. This study goes beyond previous studies in that the soil microstructure is investigated in two different depths, within (13–23 cm) and underneath (28–38 cm) the plow horizon. Furthermore the microstructure is investigated at two different resolutions (60 μm and 20 μm) by employing a nested sampling design.

The plowed horizon in the conventional tillage plots differs from the undisturbed soil underneath the cultivator depth (13–23 cm) in the reduced tillage plot by lower bulk density, higher air capacity, higher saturated hydraulic conductivity, higher macroporosity and pore connectivity. After 25 years of reduced tillage saturated hydraulic conductivity only marginally recovered in the abandoned plow pan (28–38 cm). Macropore density and connectivity did not change significantly as compared to the current plow pan under conventional tillage. The topsoil underneath the cultivator depth in the reduced tillage plot developed a “no-till pan”, as porosity and pore connectivity where smaller than in greater soil depths. Image-based macroporosity and laboratory-based air capacity showed good agreement.

Overall, the combination of hydraulic measurements and X-ray CT imaging of soil microstructure at different resolutions provides a comprehensive view on soil structure modification by tillage practices. The change from conventional to reduced tillage led to a compaction of soil that was not compensated by higher bioturbation as reported for other sites. This is explained by unfavorable conditions for anecic earthworms (frequent dry periods with severely impaired penetrability of the loess substrate) as well as the absence of very deep rooting, perennial crops in crop rotation.

1. Introduction

Conservation agriculture has a profound impact on soil structure and consequently on structure-mediated ecosystem functions like carbon sequestration, greenhouse gas emissions and soil water storage. The benefits of reduced tillage practices as compared to conventional plowing may be lower costs, higher carbon storage, higher energy input/output ratio, reduced erosion, more stability against compaction and lower herbicide loss (Palm et al., 2014; Tebrügge and Düring, 1999). Drawbacks associated with reduced tillage can be a risk of topsoil compaction, reduced aeration and lower soil temperature (Soane et al., 2012). With reduced tillage the absence of plowing typically leads to a loss in air capacity and an increase in bulk density and penetration resistance in the topsoil beneath the tillage depth of disc harrows or other cultivators (Abdollahi et al., 2017; Abdollahi and Munkholm, 2017; Deubel et al., 2011; Pagliai et al., 2004; Rasmussen,

* Corresponding author.
E-mail address: steffen.schlueter@ufz.de (S. Schlüter).

https://doi.org/10.1016/j.geoderma.2018.07.001
Received 20 January 2018; Received in revised form 19 June 2018; Accepted 1 July 2018

frontiers in Environmental Science

ORIGINAL RESEARCH
published: 11 April 2018
doi: 10.3389/fenvs.2018.00017

Denitrification in Soil Aggregate Analogues-Effect of Aggregate Size and Oxygen Diffusion

Steffen Schlüter[1], Sina Henjes[2], Jan Zawallich[3], Linda Bergaust[4], Marcus Horn[2], Olaf Ippisch[3], Hans-Jörg Vogel[1,5] and Peter Dörsch[6]*

[1] Department of Soil System Sciences, Helmholtz-Centre for Environmental Research-UFZ, Halle, Germany, [2] Institute of Microbiology, Leibniz University, Hannover, Germany, [3] Institue of Mathematics, TU Clausthal, Claustal-Zellerfeld, Germany, [4] Faculty of Chemistry, Biotechnology and Food Science, Norwegian University of Life Sciences, NMBU, Ås, Akershus, Norway, [5] Institute of Soil Science and Plant Nutrition, Martin Luther University of Halle-Wittenberg, Halle, Germany, [6] Faculty of Environmental Sciences and Natural Resource Management, Norwegian University of Life Sciences, NMBU, Ås, Akershus, Norway

Soil-borne nitrous oxide (N_2O) emissions have a high spatial and temporal variability which is commonly attributed to the occurrence of hotspots and hot moments for microbial activity in aggregated soil. Yet there is only limited information about the biophysical processes that regulate the production and consumption of N_2O on microscopic scales in undisturbed soil. In this study, we introduce an experimental framework relying on simplified porous media that circumvents some of the complexities occuring in natural soils while fully accounting for physical constraints believed to control microbial activity in general and denitrification in particular. We used this framework to explore the impact of aggregate size and external oxygen concentration on the kinetics of O_2 consumption, as well as CO_2 and N_2O production. Model aggregates of different sizes (3.5 vs. 7 mm diameter) composed of porous, sintered glass were saturated with a defined growth medium containing roughly 10^9 cells ml^{-1} of the facultative anaerobic, *nosZ*-deficient denitrifier *Agrobacterium tumefaciens* with N_2O as final denitrification product and incubated at five different oxygen levels (0–13 vol-%). We demonstrate that the onset of denitrification depends on the amount of external oxygen and the size of aggregates. Smaller aggregates were better supplied with oxygen due to a larger surface-to-volume ratio, which resulted in faster growth and an earlier onset of denitrification. In larger aggregates, the onset of denitrification was more gradual, but with comparably higher N_2O production rates once the anoxic aggregate centers were fully developed. The normalized electron flow from the reduced carbon substrate to N-oxyanions (e^-_{denit}/e^-_{total} ratio) could be solely described as a function of initial oxygen concentration in the headspace with a simple, hyperbolic model, for which the two empirical parameters changed with aggregate size in a consistent way. These findings confirm the important role of soil structure on N_2O emissions from denitrification by shaping the spatial patterns of microbial activity and anoxia in aggregated soil. Our dataset may serve as a benchmark for constraining or validating spatially explicit, biophysical models of denitrification in aggregated soil.

Keywords: greenhouse gas emissions, denitrification kinetics, microbial hotspots, microsites, anoxic aggregate centers, *Agrobacterium tumefaciens*, physically-based modeling

OPEN ACCESS

Edited by:
Philippe C. Baveye, AgroParisTech Institut des Sciences et Industries du Vivant et de L'environnement, France

Reviewed by:
Nobuko Katayanagi, National Institute for Agro-Environmental Sciences, Japan
Sven Marhan, University of Hohenheim, Germany

****Correspondence:***
Steffen Schlüter
steffen.schlueter@ufz.de

Specialty section:
This article was submitted to Soil Processes, a section of the journal Frontiers in Environmental Science

Received: *31 January 2018*
Accepted: *27 March 2018*
Published: *11 April 2018*

Citation:
Schlüter S, Henjes S, Zawallich J, Bergaust L, Horn M, Ippisch O, Vogel H-J and Dörsch P (2018) Denitrification in Soil Aggregate Analogues-Effect of Aggregate Size and Oxygen Diffusion. Front. Environ. Sci. 6:17. doi: 10.3389/fenvs.2018.00017

Biogeosciences Discuss., https://doi.org/10.5194/bg-2019-2
Manuscript under review for journal Biogeosciences
Discussion started: 8 March 2019

Biogeosciences Discussions Open Access EGU

Physical constraints for respiration in microbial hotspots in soil and their importance for denitrification

Steffen Schlüter[1] , Jan Zawallich[2], Hans-Jörg Vogel[1], Peter Dörsch[3]

[1] Department Soil System Sciences, Helmholtz-Centre for Environmental Research - UFZ, Theodor-Lieser-Str. 4, 06120 Halle, Germany

[2] Institute of Mathematics, TU Clausthal, Erzweg 3, Clausthal-Zellerfeld, Germany

[3] Faculty of Environmental Sciences and Natural Resource Management, Norwegian University of Life Sciences, NMBU, Aas, Norway

correspondence to: Steffen Schlüter (steffen.schlueter@ufz.de)

Abstract Soil denitrification is the most important terrestrial process returning reactive nitrogen to the atmosphere, but remains poorly understood. In upland soils, denitrification occurs in hotspots of enhanced microbial activity, even under well-aerated conditions, and causes harmful emissions of nitric (NO) and nitrous oxide (N_2O). Timing and magnitude of such emissions are difficult to predict due to the delicate balance of oxygen (O_2) consumption and diffusion in soil. To study how spatial distribution of hotspots affects O_2 exchange and denitrification, we embedded porous glass beads inoculated with either *Agrobacterium tumefaciens* (a denitrifier lacking N_2O reductase) or *Paracoccus denitrificans* (a "complete" denitrifier) in different architectures (random vs. layered) in sterile sand adjusted to different water saturations (30%, 60%, 90%) and measured gas kinetics (O_2, CO_2, NO, N_2O and N_2) at high temporal resolution. Air connectivity, air distance and air tortuosity were determined by X-ray tomography after the experiment. The hotspot architecture exerted strong control on microbial growth and timing of denitrification at low and intermediate saturations, because the separation distance between the microbial hotspots governed local oxygen supply. Electron flow diverted to denitrification in